1983

The Propagation Of Microwaves On Line-of-sight Oversea Paths

Wang-leung Ignatius Lam

CANADIAN THESES ON MICROFICHE

I.S.B.N.

THESES CANADIENNES SUR MICROFICHE

National Library of Canada
Collections Development Branch

Canadian Theses on
Microfiche Service

Ottawa, Canada
K1A 0N4

Bibliothèque nationale du Canada
Direction du développement des collections

Service des thèses canadiennes
sur microfiche

NOTICE

The quality of this microfiche is heavily dependent upon the quality of the original thesis submitted for microfilming. Every effort has been made to ensure the highest quality of reproduction possible.

If pages are missing, contact the university which granted the degree.

Some pages may have indistinct print especially if the original pages were typed with a poor typewriter ribbon or if the university sent us a poor photocopy.

Previously copyrighted materials (journal articles, published tests, etc.) are not filmed.

THIS DISSERTATION
HAS BEEN MICROFILMED
EXACTLY AS RECEIVED

AVIS

La qualité de cette microfiche dépend grandement de la qualité de la thèse soumise au microfilmage. Nous avons tout fait pour assurer une qualité supérieure de reproduction.

S'il manque des pages, veuillez communiquer avec l'université qui a conféré le grade.

La qualité d'impression de certaines pages peut laisser à désirer, surtout si les pages originales ont été dactylographiées à l'aide d'un ruban usé ou si l'université nous a fait parvenir une photocopie de mauvaise qualité.

Les documents qui font déjà l'objet d'un droit d'auteur (articles de revue, examens publiés, etc.) ne sont pas microfilmés.

LA THÈSE A ÉTÉ
MICROFILMÉE TELLE QUE
NOUS L'AVONS REÇUE

NL-339 (r. 82/08)

Canada

THE PROPAGATION OF MICROWAVES ON LINE-OF-SIGHT OVERSEA PATHS

by

Wang-Leung Ignatius Lam

Faculty of Engineering Science

Submitted in partial fulfillment
of the requirements for the degree of
Doctor of Philosophy

Faculty of Graduate Studies
The University of Western Ontario
London, Ontario
April, 1983

ABSTRACT

The Bay of Fundy, with its humid maritime climate, presents a hostile environment for the operation of microwave digital radio systems due to the frequent occurrence of multipath propagation. Therefore, a detailed knowledge of the ray path characteristics during multipath fading is of value to system and propagation path designers.

Two microwave propagation experiments were conducted on separate oversea paths across the Bay of Fundy in 1980 and 1981. A sweep frequency microwave diagnostic system operated with a frequency sweep from 9.5 to 10.5 GHz was used. The data collected provide information on various characteristics of the received ray(s). These include the amplitude, angle-of-arrival, and relative delay time of each ray. A digital radio test was also conducted during the 1981 experiment on an essentially identical propagation path.

The results from these experiments are presented to illustrate the propagation mechanisms associated with severe fading activities observed across the bay. In addition, statistics are presented on ray amplitudes, angles-of-arrival, delay times, and fade depth distributions. These results are related to the performance of the digital radio.

It is found that most of the severe fading activities result from the combined effects of atmospheric layers and the sea reflection. The properties of the sea reflected ray are discussed in detail as a function of sea surface roughness and atmospheric refractive properties. Particularly significant is the influence of atmospheric layers on the reflected ray. These layers have the effect of substantially increasing the relative delay time of the reflected ray to more than 10 nanoseconds. Auxiliary ray paths with such long delay times, which are rarely found in the literature, have significant impact on the operation of digital radio systems. In particular, the effectiveness of frequency diversity protection schemes are much reduced when these long delay ray paths are present.

ACKNOWLEDGEMENTS

I would like to express my sincere gratitude to Professor Alan R. Webster, my thesis advisor, for his excellent guidance. His efforts in organizing the experiments and his active involvement in the research are very much appreciated.

Thanks go to Mr. M.P. Pothier for the useful discussions and for the extra efforts beyond his normal duties at M.T.& T during the 1981 experiment.

Many thanks also go to Mrs. M. Meighen for her encouragement and great help in the typing; Ms. S. Frank for drawing some of the diagrams; and Mr. R.J. Haycock for his help during the preparation of the experiments.

I would also like to acknowledge the financial support provided by the Communications Research Centre, and for the use of various equipment and facilities provided by the Centre for Radio Science during the work. The close cooperation of Maritime Telegraph and Telephone and New Brunswick Telephone during the experiments is much appreciated.

TABLE OF CONTENTS

LIST OF TABLES

LIST OF FIGURES

NOMENCLATURE

a	earth radius
a_e	effective earth radius
b/s/Hz	bits per second per hertz
c	velocity of light
e	partial pressure of water vapour
e_s	saturation vapour pressure of water
f	frequency
h	height
h_o	layer height
h_D	duct thickness
h_L	layer thickness
h_M	maximum wave height
j	$\sqrt{-1}$
k	basic refractivity gradient
l	physical path length
mb	100 Pascal
n	refractive index
t	temperature
$\bar{t}(L)$	average duration of fades corresponding to level L
A1	main ray (strongest ray) amplitude
A2	second ray (weaker ray) amplitude
ADC	analog to digital converter
ADT	Atlantic Daylight Time
AGC	automatic gain control
AOA	angle-of-arrival

AOA's	angles-of-arrival
AOAI	main ray angle-of-arrival derived from intercept of phase record
AOAS	main ray angle-of-arrival derived from slope of phase record
BER	bit-error-rate
BERT	bit-error-rate test set
BPF	band-pass filter
BPSK	binary phase shift keying
CPU	central processing unit
CCIR	International Radio Consultative Committee
D	divergence coefficient
E	field strength
EPROM	erasable-programable read only memory
F_1	radius of the first Fresnel Zone
F_n	radius of the n-th Fresnel Zone
FM	frequency modulation
FSK	frequency shift keying
H	relative humidity, equal to e/e_s
IF	intermediate frequency
I/O	input-output
K	Kilo-byte
K	effective earth radius factor
L	phase path length
L	specified signal level
LOS	line-of-sight
M	modified refractive index
Mb/s	Mega-bits per second

MSL	mean sea level
M.T.& T	Maritime Telegraph and Telephone Company
N	refractivity
N(L)	number of fades corresponding to level L
N_o	ground refractivity
NU	N-units, units of refractivity
P	pressure
P	power density
P_n	probability of in-band null
P( )	probability
P(e)	error probability, same as BER
PCM	pulse-coded modulation
PSK	phase shift keying
QAM	quadrature amplitude modulation
QPR	quadrature partial response
R	reflection coefficient
R_o	reflection coefficient of perfectly smooth surface
R_d	reflection coefficient for diffuse component
R_s	reflection coefficient for specular component
RAM	random-access memory
RF	radio frequency
RX	receiver or receiving antenna
T	absolute temperature in Kelvin
TCTS	Trans-Canada Telephone System
TX	transmitter or transmitting antenna.
TTY	teletype

TWT	travelling-wave-tube amplifier
V	signal level
X-band	8.0 to 12.5 GHz frequency band
YTO	(Yttrium-Iron-Garnet)-tuned Gunn diode oscillator
ψ	ray path angle relative to local horizontal
$\delta\ell$	physical path length increment
δL	phase path length increment
ε	relative phase
ϵ	dielectric constant
ϵ_o	dielectric constant of free space
ρ	ray path radius of curvature
ρ_d	scattering coefficient for the diffuse component
ρ_s	scattering coefficient for the specular component
γ	angle of reflection, grazing angle
θ	angle subtended at the centre of the earth
θ_c	critical angle for ray trapping by duct
λ	wavelength
ω	radian frequency
π	3.14159265
Δh	anomaly thickness
$\bar{\Delta}h$	standard deviation of surface height irregularities
ΔN	layer strength, duct strength
$\Delta\theta_s$	specific change in angle-of-arrival per unit path length
$\Delta\tau$	relative time delay between rays

Chapter 1

INTRODUCTION

1.1 Background

The history of radio communications dates back to the year 1896 when Marconi first succeeded in transmitting telegraph messages across the English Channel by radio. In subsequent years, advances in radio technology resulted in the use of progressively higher frequencies for communication purposes. By the early 1950's, microwave radios were used commercially in long distance telephone networks in North America. Accompanying these advances in transmission technology were developments in modulation schemes from single channel Amplitude Modulation to multichannel Frequency Modulation techniques, resulting in more efficient spectrum utilizations. These technologies provided the basis for telecommunication networks of the last decade.

In response to the increasing demands for information exchange in the modern society, fundamental changes in the structure of the telephone system are currently being made worldwide. Digital transmission systems, because of their cost advantages, flexibility in multiplexing, ease of interconnection and expansion, and consistent transmission quality under noisy situations, are replacing conventional

analog systems as the backbone of the telephone network. At the present time, microwave digital radio systems operating in the 2, 6, 8, and 11 GHz bands are in common use. In the Canadian 8 GHz common carrier frequency band, the allocated channel bandwidths are 40 MHz. Typical systems operating in this band provide signalling rates of approximately 90 Mb/s or the equivalent of approximately 1300 voice channels.

The implementation of microwave digital radio systems presents new challenges to the radio path designer. The requirements and behaviour of wideband digital radio systems are significantly different from those of the conventional, narrowband FM analog radios. Digital radios, because of the modulation schemes and the wide bandwidth, are particularly susceptible to the effects of frequency selective multipath fading, namely, in-band amplitude and group delay distortions. Furthermore, for proper synchronization and framing purposes, a pulse stuffing technique is usually employed in digital radios. Consequently, the radio is always operating at full bandwidth independent of the actual amount of loading on the system. On the other hand, the operating bandwidth of an analog FM radio is directly proportional to the system load. Since severe multipath fading occurs more often during the night and in the early morning when system loading is usually light, its effects are less detrimental to the operation of conventional analog radio systems.

The above problems are further compounded by the high performance standards that regulate the operation of digital radios. For example, one of the requirements specified by the Trans-Canada Telephone System for 8 GHz digital radio is an availability of 99.98% of the time, defined for a hypothetical reference circuit of length 6560 km. When scaled to a typical line-of-sight (LOS) microwave radio link of length 50 km, the availability is 99.99985 % of the time. This is equivalent to an allowable total outage time of 48 s per year (two way outage) or an average of 0.13 s per day. Outages due to both equipment failures and propagation impairments are included and these are usually treated with equal weight.

The characteristics of the received signal on a terrestrial line-of-sight microwave link is dependent on the refractive properties of the atmosphere and on the topographical features of the intervening terrain. The common causes of signal fading are diffraction by obstacles to the line-of-sight path, absorption by hydrometeors, and multipath propagation. The effects of diffraction fading may usually be reduced or avoided by a careful design of the propagation path. Fading due to absorption and multipath effects, however, are usually dependent on atmospheric conditions, frequency, and path length. Generally speaking, at frequencies below 10 GHz, multipath propagation is the predominant cause of severe signal fading on terrestrial microwave links.

Fading due to multipath effects occurs as a result of interference between the direct ray and one or more auxiliary rays that reach the receiving antenna via different paths. These auxiliary rays may arise from a ground reflection or from anomalous refraction and reflections from atmospheric layers. Because of the frequency selective nature of multipath fading, its effects on wideband digital radio systems are particularly severe. High bit-error-rates may result from in-band distortion effects even when the average signal level is well above the receiver threshold.

As part of the present investigation, two microwave propagation experiments were performed on separate line-of-sight, oversea paths across the Bay of Fundy in 1980 and 1981. Prior to the propagation experiments, a digital radio test was conducted by the local telephone companies on the path used in the 1980 experiment. The results of the test indicated that the performance of the digital radio installed across the bay was unacceptable due to unknown propagation effects. The experiments therefore were performed with the aim of identifying the propagation mechanisms that are associated with outages on the digital radio. In both experiments, sweep frequency records of the amplitude and phase (relative phase between two vertically spaced antennas) of the received signal were gathered. Subsequent analysis of these sweep records then gives estimates of the amplitudes, angles-of-arrival, and the

relative delay of the individual received ray(s). In addition, a digital radio was operated simultaneously with the 1981 experiment, providing information on the performance of such a system under various propagation conditions.

1.2 Objectives and Thesis Format

The main objective of the thesis is to provide a better picture of the mechanisms that are associated with microwave propagation across the Bay of Fundy. Possible explanations of some of the observed fading phenomena are proposed. The propagation results are also examined with respect to the performance of the digital radio and the events that led to digital radio outages are discussed. Because of the complex nature of the subject, a complete set of explanations is not attempted, nor are conclusive results always attained. However, it is hoped that a contribution is made to the body of knowledge associated with the propagation of radio waves through the atmosphere.

With the above objectives in mind, the thesis starts with a discussion of basic microwave propagation mechanisms in the troposphere in Chapter 2, with descriptions of some of the parameters and notations that are used in subsequent chapters. The experimental equipment is described in Chapter 3 together with a section on the configuration of

the digital radio used in the 1981 experiment. Chapter 4 contains a detailed description of the propagation experiments and the propagation paths across the Bay of Fundy. The data analysis method and the associated uncertainties in the results are discussed.

The major results of the experiments are presented in Chapters 5 to 8. The results of the 1980 and 1981 experiments are presented in Chapters 5 and 6 respectively. Explanations are offered to account for the experimentally observed ray path characteristics.

Statistical results on fade depth distributions are presented in Chapter 7. The results are compared with theoretical predictions as well as results from previous experiments. The performance of a digital radio installed across the bay during the 1981 experiment is examined in Chapter 8 in the light of the results obtained from the propagation experiments. Finally, a summary of the major findings and recommendations for future research is presented in Chapter 9.

Chapter 2

MICROWAVE PROPAGATION IN THE TROPOSPHERE

2.1 The Refractive Index in the Troposphere

The region of the lower atmosphere from ground level up to approximately 10 km height is generally referred to as the troposphere. Propagation of microwaves in this region is governed by the refractive index n of the air which is a function of the atmospheric pressure, temperature, and humidity. Since the value of n differs by only a small amount from unity, a more convenient parameter usually used is the refractivity N which is given by

$$N = (n - 1).10^6 \tag{2.1}$$

Although N is a dimensionless quantity, it is often given in N-units (NU) which represents "units of refractivity". At radio frequencies up to 30 GHz, the refractivity is given by [1]

$$N = 77.6 \frac{P}{T} + 3.73 \times 10^5 \frac{e}{T^2} \tag{2.2}$$

where P(mb) is the atmospheric pressure, T(K) is the absolute temperature, and e(mb) is the partial pressure of water vapour. The two terms in Eq. (2.2) are usually referred to as the "dry" and the "wet" components of the refractivity, respectively. The contribution of the wet

component is small at low temperatures. As the temperature increases, however, the value of N becomes very sensitive to small changes in the humidity and the temperature. This is due to the rapid increase in the saturation vapour pressure with temperature. The effect is illustrated in Fig. 2.1 which shows the variation of N with temperature t(°C) and relative humidity H(%) for an atmospheric pressure of 1000 mb. The curves for H = 0 % and H = 100 % correspond to the minimum and maximum values of N at a given temperature. For the standard atmospheric condition of P = 1013.0 mb, T = 288 K, and e = 11.9 mb (assuming a relative humidity of 70 %) the value of N is 326 NU.

The variations of pressure, temperature, and humidity in the atmosphere result in a corresponding variation of N with elevation. The relative contributions of the pressure, temperature, and humidity gradients to the N-gradient may be illustrated by differentiating Eq. (2.2) with respect to height h which gives

$$\frac{dN}{dh} = \left(\frac{77.6}{T}\right)\frac{dP}{dh} - \left(\frac{77.6P}{T^2} + \frac{7.46\times10^5}{T^3}e\right)\frac{dT}{dh} + \left(\frac{3.73\times10^5}{T^2}\right)\frac{de}{dh} \qquad (2.3)$$

For the standard atmospheric conditions specified above, Eq. (2.3) reduces to

$$\frac{dN}{dh} = 0.27\,\frac{dP}{dh} - 1.3\,\frac{dT}{dh} + 4.5\,\frac{de}{dh} \qquad (2.4)$$

In a well-mixed atmosphere, the refractivity gradient dN/dh

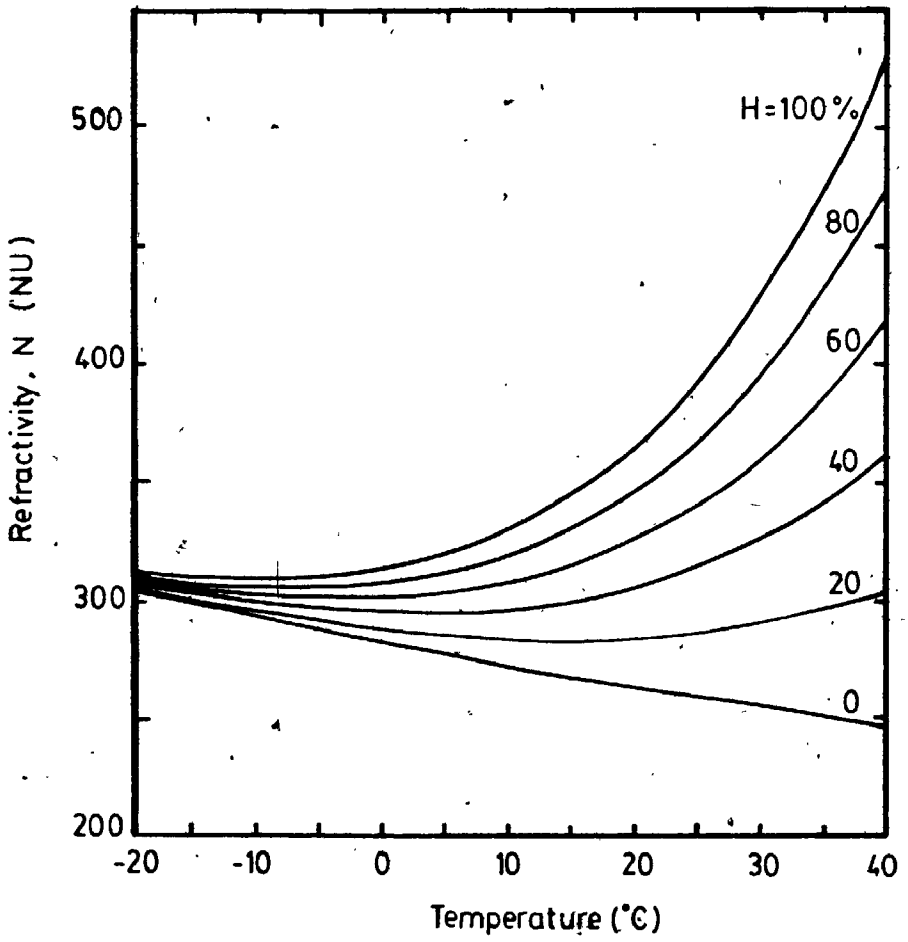

Fig. 2.1 Variation of refractivity N with temperature t and relative humidity H at a pressure of 1000 mb.

corresponds to the adiabatic lapse rate and has an essentially constant value of approximately -23 NU/km. In practice, however, the atmosphere is not well-mixed and the measured median of the mean value of dN/dh in the first kilometre above ground in most temperate regions is about -40 NU/km. In general, the variation of pressure with height accounts for roughly -30 NU/km and the contributions from the components due to the normal humidity and temperature gradients amount to approximately -17 NU/km and +8 NU/km respectively [2]. Values of the ground refractivity N and the average N-gradient observed over the first 100 m of the atmosphere at various locations in North America are tabulated in Segal and Barrington [3].

2.2 Propagation in an Atmosphere with Uniform Refractivity Gradient

As a result of the vertical gradient in the refractive index, radio waves propagating through the atmosphere generally do not travel along straight line paths. In the case of a spherically stratified atmosphere, Snell's law is modified to give the relationship

$$n(h).(h + a).\cos \psi(h) = C \qquad (2.5)$$

where n(h) is the refractive index at height h above the earth's surface, a is the earth radius, $\psi(h)$ is the ray

path angle relative to the local horizontal, and C is a constant along a ray. The local radius of curvature ρ of the ray path is given by the equation

$$\rho = - \frac{n}{(dn/dh) \cos \psi} \qquad (2.6)$$

It follows that, for rays launched at angles close to the horizontal in an atmosphere with a uniform refractivity gradient, the ray path will approximate a circular arc with curvature

$$\frac{1}{\rho} \simeq - \frac{dn}{dh} \qquad \text{for} \quad n \simeq 1 \qquad (2.7)$$

The inconveniences associated with studying the propagation of a curved ray path over a spherical earth are usually avoided by transforming the curvatures entirely to that of either the ray path or that of the earth's surface as shown in Fig. 2.2. The former case, in which a curved ray path propagates over a flattened-earth, is usually referred to as the Flattened-Earth model. In the latter case, we have straight ray paths travelling over a model earth of effective earth radius a_e which is given by

$$a_e = Ka = \left(\frac{\rho}{\rho - a} \right) a \qquad (2.8)$$

where the quantity K is called the effective earth-radius factor. A normal refractivity gradient of -40 NU/km corresponds to a K value of 4/3 which is often considered as the standard refractivity condition. The ray path radius of curvature for this condition has a value four

(a) Real earth model: • actual earth radius, a
• ray path radius of curvature, ρ

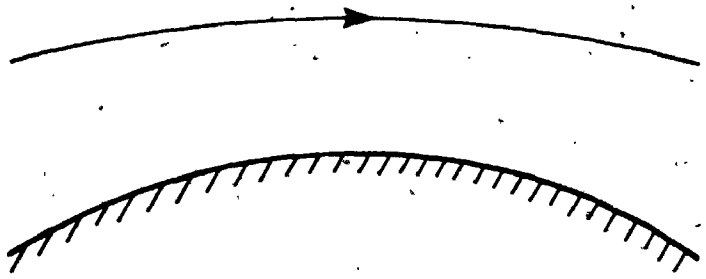

(b) Flattened-earth model:
• flattened-earth
• ray path effective radius of curvature, ρ_e

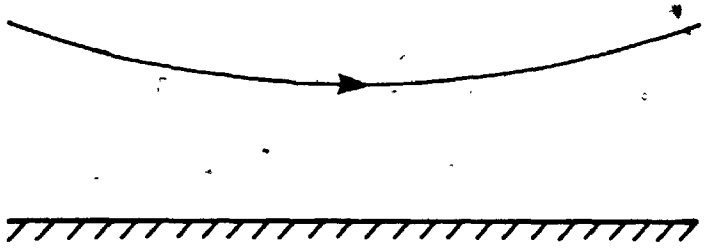

(c) Straight ray path model:
• straight ray path
• effective earth radius, a_e

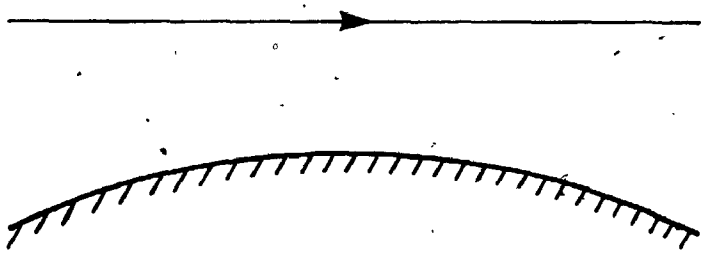

Fig. 2.2 Models for representing ray path propagating over earth surface.

times the earth radius ($\rho = 4a$) and the ray therefore is refracted away from the earth surface on a flattened-earth representation.

For values of dN/dh more negative than -40 NU/km, the ray is refracted more towards the earth's surface and the condition is described as superrefractive. The opposite situation in which dN/dh is less negative than -40 NU/km is described as subrefractive.

The diurnal and seasonal variations in the refractivity gradient give rise to corresponding changes in the ray path radius of curvature. This in turn leads to changes in the angle-of-arrival (AOA), in the vertical plane, of the received ray path. The variations in ray path angle-of-arrival were studied by various workers [4]-[8], and angle ranges of up to 0.9 deg have been reported. In the case of narrow beam antennas (beamwidth less than 1 deg), variations in ray path AOA may lead to signal loss due to antenna decoupling [7], [8].

In general, the observed range in angle-of-arrival is dependent on the path length and Webster [9] suggested the use of a parameter "specific change in angle-of-arrival $\Delta\theta_s$" which is defined as the change in angle-of-arrival per unit path length. The relationship

$$\Delta\theta_s = -2.86 \times 10^{-5} \cdot \Delta\left(\frac{dN}{dh}\right), \quad \text{deg/km} \qquad (2.9)$$

where $\Delta\left(\frac{dN}{dh}\right)$ is a given change in the refractivity gradient producing $\Delta\theta_s$, was suggested for use in

estimating the value of $\Delta\theta_s$ for LOS microwave paths.

2.3 Ray Tracing and the Modified Refractive Index

A common technique often used in microwave propagation studies is that of ray tracing based on geometrical optics. This involves the calculation, by using Eq. (2.6), of the ray paths followed by rays launched at various launch angles from a transmitting antenna. The resultant ray path may then be plotted using either a flattened-earth or a straight ray path representation after the appropriate transformations. In this thesis the flattened-earth representation is used because ray paths corresponding to different refractivity profiles may be plotted and compared on the same flattened-earth terrain profile. This approach also allows for logical representations of ray paths under multipath propagation conditions.

In applying the ray tracing technique, a parameter called the modified refractive index M is conveniently used instead of the refractivity N. This modified refractive index is related to N by

$$M = N + 10^6 . \ln\left(1 + \frac{h}{a}\right) \qquad (2.10a)$$

or

$$M \simeq N + 10^6 \left(\frac{h}{a}\right) \quad \text{for } h << a \qquad (2.10b)$$

and the gradient in M is given by the relationship

$$\frac{dM}{dh} = \frac{dN}{dh} + 157 \quad , \quad \text{NU/km} \qquad (2.11)$$

When conditions are such that any ray launched horizontally will travel parallel to the earth's surface, the value of dN/dh is -157 NU/km. According to Eq. (2.11), the value of dM/dh is zero for such propagation conditions.

For positive values of dM/dh, the N-gradient is less negative than -157 NU/km and the ray is refracted away from the flattened-earth. Conversely, dM/dh is negative for dN/dh more negative than -157 NU/km and the ray is refracted towards the flattened-earth. The condition $dM/dh < 0$ is usually used for identifying the occurrence of a radio duct.

The ray tracing technique used in this thesis work is that developed by Webster [10]. The ray tracing geometry is shown in Fig. 2.3 in which ψ_1 and ψ_2 are the ray path angles relative to the local horizontal. The technique uses the angle θ subtended at the centre of the earth as the independent variable. The propagation path is then subdivided into an integer number of increments each with subtended angle $\delta\theta$ at the centre of the earth. Starting at one end of the propagation path and for successive points on a ray path, the local ray path radius of curvature is calculated using Eq. (2.6) with the appropriate value of the local refractive index. The new values of ψ_2, R_2, and $\delta\ell$ are then obtained by simple

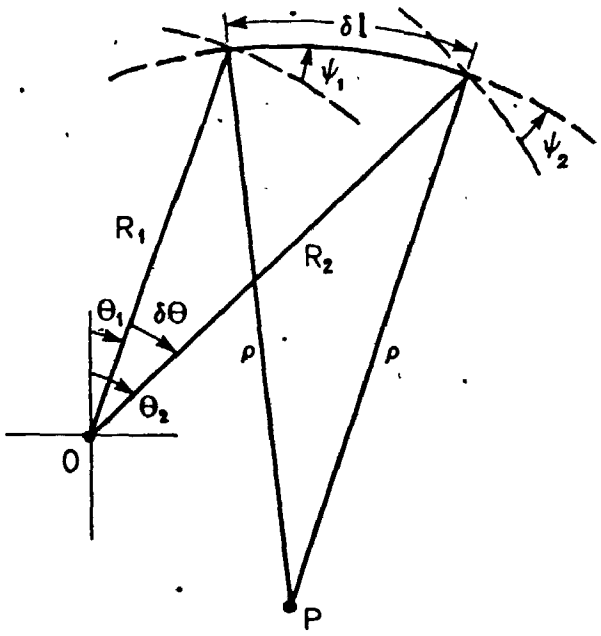

O... centre of earth
P... local centre of curvature of ray path

Fig. 2.3 The Ray Tracing geometry.

geometry. The ray path corresponding to any given launch angle is calculated and plotted by repeating the above procedures. Furthermore, the phase path length L may be obtained by summing the individual phase path length increments δL with

$$\delta L = n.\delta \ell \qquad (2.12)$$

where n is the refractive index and $\delta \ell$ is the physical path length increment.

In the case of the atmosphere having a non-uniform refractivity profile, an analytic expression is used for modelling the refractive index structures associated with atmospheric layers. This has the advantage, over the common approach of using a piecewise linear model, of allowing smooth and continuous changes in N which may be considered a better representation of the situation in reality. Furthermore, the characteristics of the layer may be varied by changing the associated parameters in the analytic expression. The modelling of layers is discussed in more detail in Section 2.4.3 on the ducting phenomenon.

Using the ray tracing technique, the parameters that may be investigated include: (a) the number of possible ray paths joining the transmitting and the receiving antennas, (b) the ray path amplitudes, (c) the ray path angles-of-launch and angles-of-arrival, and (d) the relative delays. In estimating the ray path amplitudes, it is assumed that the refractive index is horizontally

homogeneous. The power density P at the receiver is then calculated based on

$$P \propto \left.\frac{\delta\psi}{\delta h}\right|_{\delta\psi \to 0} \qquad (2.13)$$

2.4 Propagation in an Atmosphere with Non-uniform Refractivity Gradient

2.4.1 Anomalous Propagation

In general, the conditions in the atmosphere are such that a uniform refractivity profile is not maintained over the height range for tropospheric propagation. In addition, changes in the refractivity profile may occur over time due to climatic changes and the effects of diurnal heating and cooling cycles. These conditions may lead to various anomalous propagation phenomena. For example, more than one propagation path may exist between the transmitting and receiving antennas -- a condition which is called multipath propagation.

The additional paths may be caused by a reflection from the ground or by reflection or refraction due to atmospheric layers. Since the different signals travelled along separate paths, they arrive at the receiving antenna with different amplitudes, phases, and path delays. The constructive and destructive interference of these signals result in frequency selective fading.

According to the conditions under which they exist, multipath propagation may be classified into two distinct types. The first type occurs under conditions of a relatively stable and stratified atmosphere when the multipath is due to the influence of layers or ducts. The second type occurs under turbulent conditions and is associated with regions of atmospheric inhomogeneity. In this section, it is assumed that ground reflections do not play any part. The effects of ground reflections are discussed in Section 2.5.

2.4.2 Effects of Atmospheric Layers

Under certain meteorological conditions in a stratified atmosphere, layered structures may be formed within which exist large negative refractivity gradients. The formation of such structures are closely associated with temperature inversions and excessive humidity gradients. Some of the atmospheric processes responsible for such conditions are advection, subsidence, evaporation, ground heating, and radiation cooling [11].

Before proceeding with the discussion of the effects of layers on radio propagation, the parameters for describing these layers will be defined. A refractivity gradient more negative than -157 NU/km, i.e. $dM/dh \leq 0$, is a necessary condition for the occurrence of a duct. The N- and M-profiles for an idealized duct, together with the duct parameters, are shown in Fig. 2.4. For a horizontally

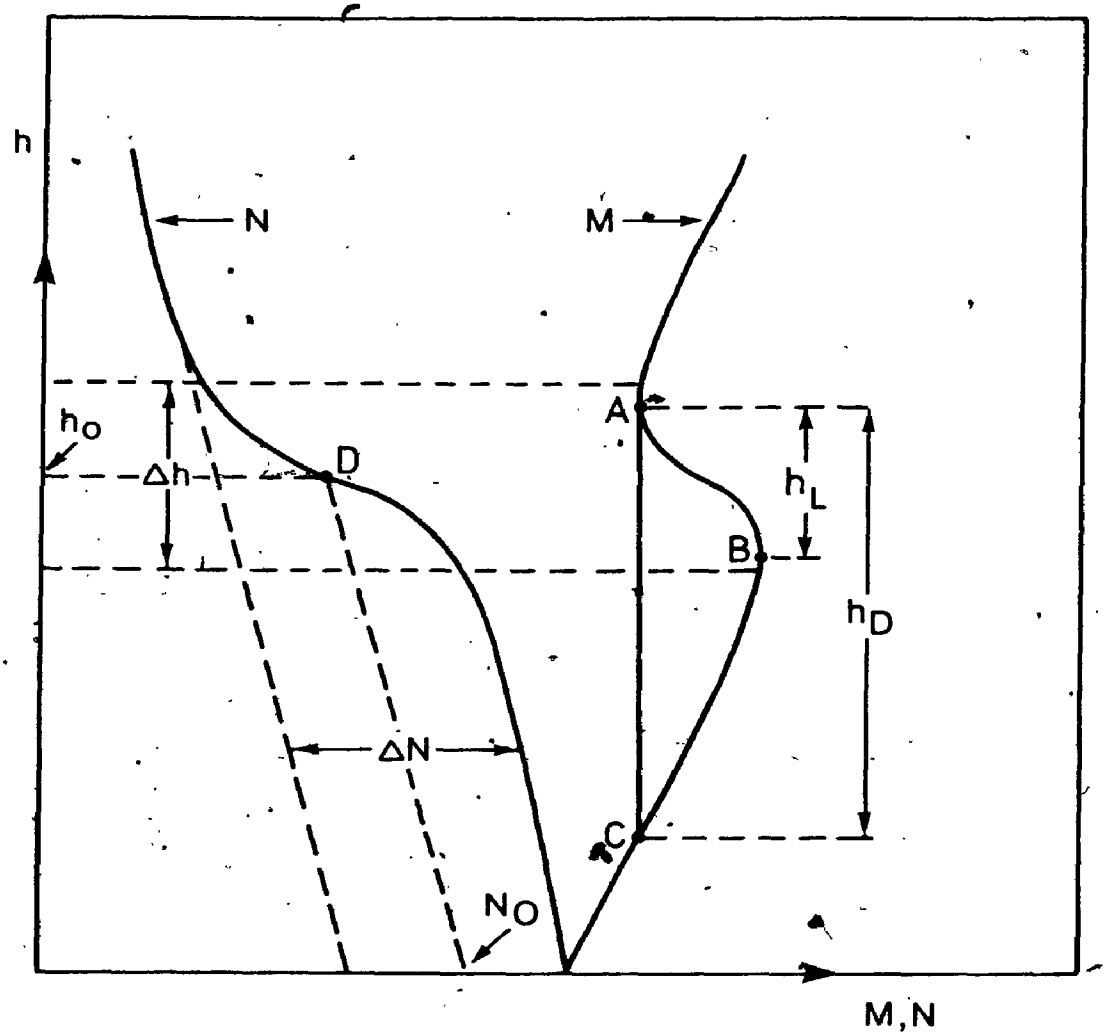

Fig. 2.4 The M- and N- profiles for an idealized elevated duct.

homogeneous duct, A and C mark the duct boundaries and h_D is the duct thickness. Within the height range AB the M-gradient is negative (this is sometimes called the ducting layer [12]) and h_L is the layer thickness. The duct strength is defined as the total N-change associated with the duct and is given by ΔN in NU. The duct may be modelled by the analytic expression

$$N = N_o + kh + \frac{\Delta N}{\pi}.\arctan\frac{[12.63(h-h_o)]}{\Delta h} \quad ; \text{ NU} \qquad (2.14)$$

The corresponding N-gradient is obtained by differentiating Eq. (2.14) which gives

$$\frac{dN}{dh} = k + \frac{\Delta N}{\pi}.\frac{12.63\ \Delta h}{(\Delta h)^2 + [12.63(h-h_o)]^2} \quad ; \text{ NU/km} \qquad (2.15)$$

In these equations, the ground refractivity N_o and the basic refractivity gradient k describe the underlying N-profile in the absence of the duct. The anomaly thickness Δh is defined as the height range between points at which the change in N has reached 90 percent of its final value. Finally, h_o is the height at the centre of the change.

The expressions in Eqs. (2.14) and (2.15) are identical to those used by Webster [10]. Basically similar forms of these expressions are also employed by Chang [13] for duct modelling. The choice of the analytic functions is partly arbitrary and it provides a useful tool for investigating the propagation effects of ducts. Although it is implicit in the expression that the N-change

associated with a duct is symmetrical, in the absence of detailed N-profile data, the assumption is considered a valid starting point for modelling such ducts. More complicated profiles may be synthesized by simple addition of the effects of more than one layer.

Numerous studies on duct structures have been reported by various workers [14]-[17] of which the papers by Sheppard [14] and Ikegami et al. [16] are particularly detailed. Most of the available information on duct properties, however, are from isolated events. Nevertheless, a general idea may be gained of the possible values of various duct parameters such as the height of occurrence h_o, duct strength ΔN, and anomaly thickness Δh. Some of the reported values are listed in Table 2.1. The general observation is that ducts may occur at any height from ground level up to a few kilometres. The duct strength was rarely observed to exceed about -40 NU but the value of Δh may range from a few metres to several hundreds of metres. Duct occurrence probabilities and average values of duct thickness and elevation are also tabulated for regions in North America in Segal and Barrington [3].

Ducts may be classified into ground-based ducts and elevated ducts. An elevated duct is shown in Fig. 2.4. When the ducting layer (region AB) occurs at ground level, the duct is a ground-based duct.

Table 2.1 Some reported values of duct parameters including height of occurrence h_o, duct strength ΔN, and anomaly thickness Δh.

Reference	Duct parameters reported		
	h_o (m)	ΔN (NU)	Δh (m)
Sheppard [14]	0 - 20	-20	50
	100	-40	200
	200	-30	200
Lane [15]	1100	-25	150
	1200	-40	300
	400	-10	100
Gossard [17]	2750	-25	500
	20	-30	40
	10	-20	5

One of the main characteristics of ducted propagation, or ducting, is the trapping of radio waves that are launched within a critical angle from inside the duct. To explain the mechanism for ducting, it is recalled from Section 2.3 that in a region where dM/dh is negative, rays are bent towards the flattened earth and vice versa. On examining Fig. 2.4 it is seen that within an elevated duct, dM/dh has opposite signs in the adjacent regions AB and BC. Rays that are launched at angles within a critical value $\pm\theta_c$ therefore are bent towards the other region where ray bending will occur in the reverse direction. The net result is that the radio wave is guided or trapped within the duct and can propagate over long distances with low loss. This is illustrated in Fig. 2.5 in which representative rays launched both within and outside the duct are shown. It is noted that by reciprocity, and based on ray theory, rays launched from outside the duct cannot be trapped within the duct, assuming an ideal duct which is horizontally homogeneous. In practice, however, weak coupling into the duct can occur through a mechanism called duct leakage. A full wave solution for explaining duct leakage may be found in Chang [13]. The importance of duct leakage is proportional to the path length. Over the short distances usually involved in LOS communication systems, the amount of duct leakage is small and ray theory is adequate in the majority of cases.

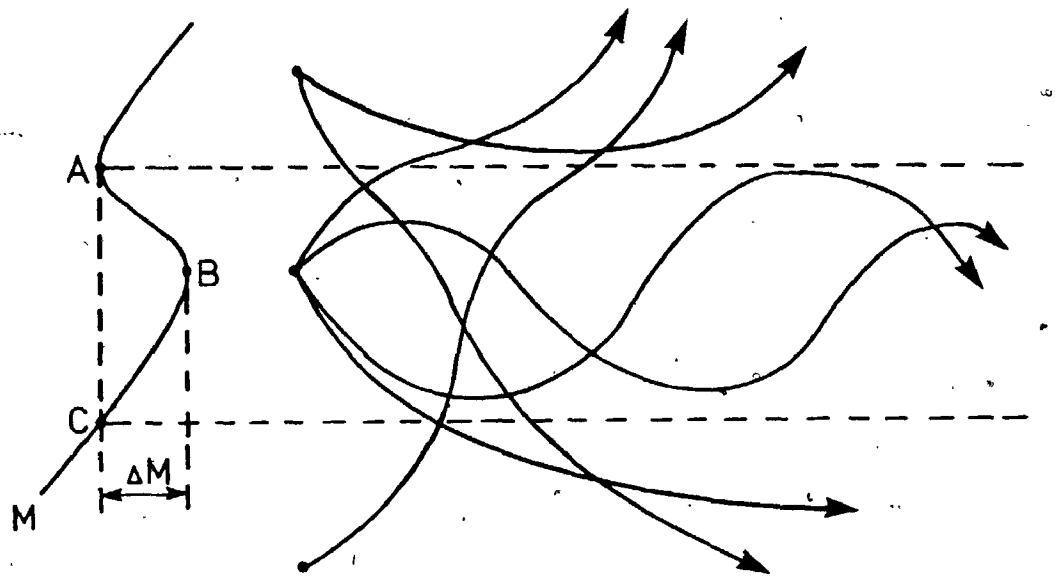

Fig. 2.5 Representative rays launched from various points relative to a propagation duct.

An estimate of the critical angle for ray trapping is given in Dougherty and Hart [12] as

$$\theta_c = \theta_{co} = (2.|\Delta M|)^{\frac{1}{2}} \; ; \text{ mrad; for } y = 0 \qquad (2.16)$$

$$\theta_c(y) = \theta_{co}\left(1 - \frac{y}{h_L}\right)^{\frac{1}{2}} \qquad \text{for } 0 \leq y \leq h_L \qquad (2.17)$$

$$\theta_c(y) = \theta_{co}\left(1 + \frac{y}{h_D - h_L}\right)^{\frac{1}{2}} \qquad \text{for } (h_L - h_D) \leq y \leq 0 \qquad (2.18)$$

where y is the displacement of the radio source from B, and h_L and h_D are the layer thickness and the duct thickness respectively.

In order for ducting to occur, the ducting layer AB must be maintained over a height of many wavelengths. The requirement was examined qualitatively by using a mode theory of tropospheric propagation in Booker and Walkinshaw [18]. For ground-based ducts, an estimate of the maximum radio wavelength $\lambda_{max}(m)$ which can be trapped by a duct of anomaly thickness $\Delta h(m)$ is given by [11], [19]

$$\lambda_{max} = 2.51 \times 10^{-3} \left(\frac{\Delta N}{\Delta h} - 0.157\right)^{\frac{1}{2}} . \Delta h^{3/2} \qquad (2.19)$$

where ΔN is the change in the refractivity (absolute value) over the height Δh . Consider as an example a duct with ΔN = 20 NU and Δh =100 m, the value of λ_{max} is 0.52 m. Therefore the minimum radio frequency above which the radio wave can be trapped by the duct is approximately 580 MHz.

As a result of radio wave trapping, the presence of ducts leads to several important propagation anomalies. These are illustrated by the effects associated with a

"typical" duct with parameters $\Delta N = -20$ NU, $\Delta h = 100$ m, and located at a height of $h_o = 250$ m. An underlying gradient of -40 NU/km was assumed and the ground refractivity in the absence of the duct is 300 NU. Using the ray tracing approach and assuming a horizontally uniform duct, the ray paths for various rays launched from above, within, and below the duct are shown in Figs. 2.6 (a) to (c).

In Fig. 2.6(a), the radio source is located above the duct. As mentioned above, trapping does not occur except for weak coupling into the duct through leakage. However, a radio-hole effect is observed in region A which is caused by a defocussing mechanism due to the duct. Substantial flat fading may occur as a result of the defocussing mechanism.

Rays launched from a source located within the duct are shown in Fig. 2.6(b). Again the radio-hole effect is observed in region A while in regions labelled B the propagation is essentially normal with one received ray path. Ducting is observed and as a result, multipath propagation occurs in regions labelled C.

For a radio source located below the duct, the ray paths are shown in Fig. 2.6(c). Again trapping is not possible except for weak coupling into the duct. In the absence of ground reflections, multipath propagation is not supported. The radio-hole effect observed at A in this case is a result of insufficient antenna height for the long distances considered and not due to the presence of

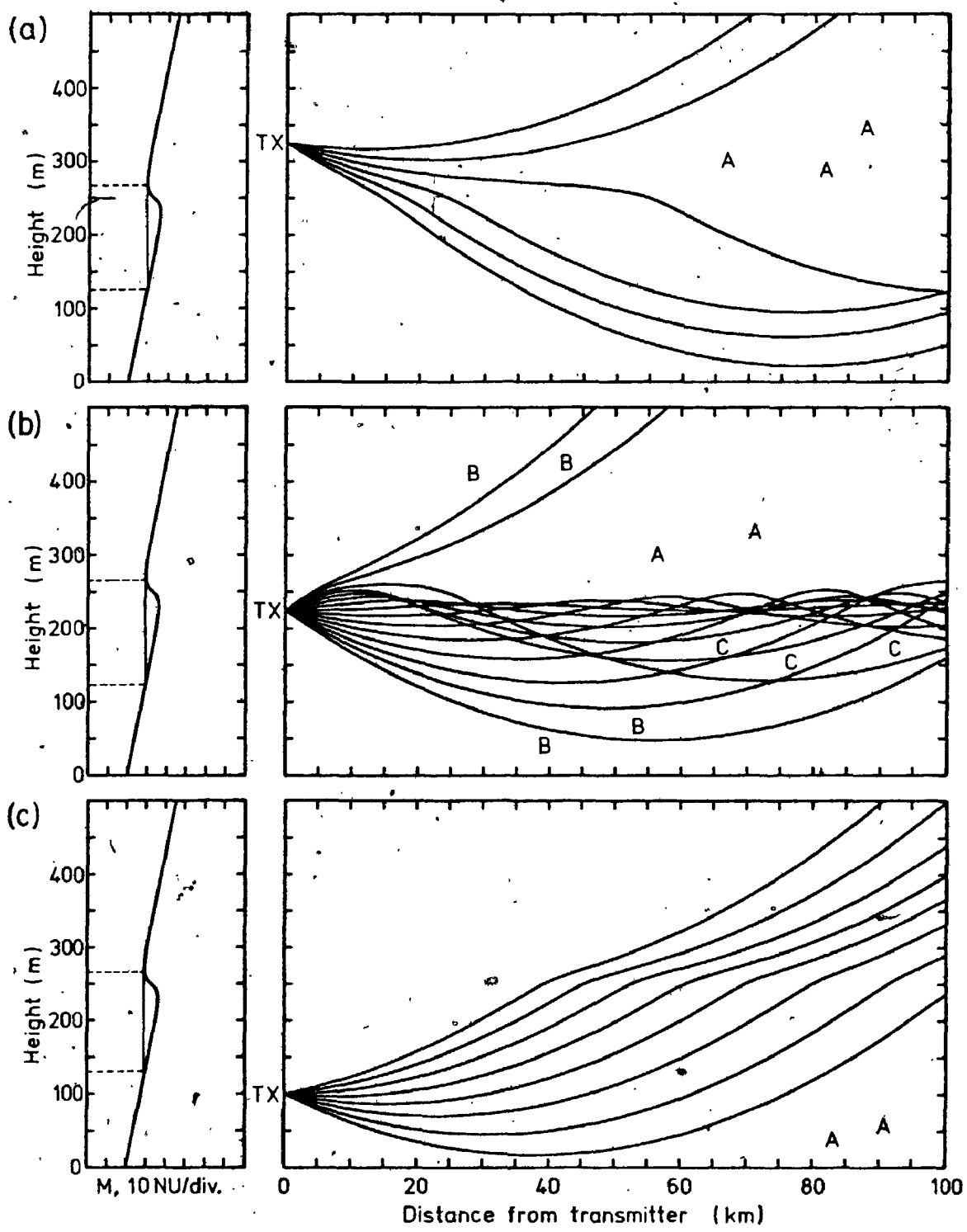

Fig. 2.6 Propagation in the presence of a duct.
(a) rays launched from above the duct.
(b) rays launched from within the duct.
(c) rays launched from below the duct.

the duct.

2.4.3 Multipath Propagation in a Turbulent Atmosphere

A type of multipath fading may occur when the atmosphere is turbulent but not well-mixed. Regions of inhomogeneity in the refractivity gradient may cause rapid and random fluctuations in both the amplitude and received phase of the resultant signal.

To understand the mechanism for such fading, consider for the moment that a small region of unusually high refractivity gradient occurs slightly above the mid-point of the main ray path. The atmosphere is assumed to have a uniform refractivity gradient everywhere except for this small region. The rays passing through this region, in the absence of the inhomogeneity, normally do not terminate at the receiving antenna. However, due to the abnormal gradient, extra ray bending occurs in this region and the result is that additional rays may reach the receiving antenna, with amplitudes and phases different from those of the nominal ray. Now if there exist more than one such region distributed randomly along the propagation path, the resultant signal would be the vector sum of a large number of signals each with randomly varying amplitude, phase, and relative delay time.

Due to the random nature of the mechanism involved, a statistical approach is more suitable for describing this type of fading. When conditions are such that: (a) there

exist a large number of interfering vectors, (b) the phase of each interfering vector is uniformly distributed, and (c) the amplitude of the vectors are normally distributed about zero amplitude, then the amplitude of the resultant of the vectors is described by the Rayleigh distribution [20], [21]. The functional form of the Rayleigh distribution is

$$P(A \leq L) = 1 - \exp(-L^2/\alpha) \tag{2.20}$$

where $P(A \leq L)$ is the probability that the amplitude A of the resultant signal is below a given level L, and α is the mean square value of A.

In general, the conditions required for a Rayleigh type fading is not always satisfied. A more general distribution function was proposed by Nakagami [22] in which the shape of the function may be varied by changing an empirical parameter m. The function describes the Nakagami m-distribution and it includes the Rayleigh distribution as a special case.

Rapid but mild fading observed on most propagation paths is often attributed to a Rayleigh type mechanism [20] although its effects are more pronounced on long, especially trans-horizon, paths.

2.5 Terrain Effects on Radio Wave Propagation

2.5.1 Path Clearance and the Fresnel Zone

Adequate clearance of the ray path above the underlying terrain is required on a LOS propagation path. If sufficient clearance is not allowed for, signal fading due to terrain blockage will occur through a diffraction mechanism. Path clearance may be quantified by using the concept of Fresnel Zones.

Consider a point along a LOS propagation path. According to Huygen's principle, the field received at the receiving antenna is a sum of the fields emitted by all the Huygen's sources distributed on a surface perpendicular to the path. The radiation from the sources that are further away from the LOS path travelled through greater distances and therefore are delayed in phase. The loci of points for which the phase lags are exactly integral multiples of half-wavelength are given by

$$F_n = \left[\frac{n\lambda d_1 d_2}{d_1+d_2}\right]^{\frac{1}{2}} \qquad (2.21)$$

where F_n (m) is the radius of the n-th locus, λ(m) is the radiation wavelength, and d_1(m) and d_2(m) are the distances of the point on the ray path from the transmitting and receiving antennas.

The region enclosed by F_{n-1} and F_n is called the n-th Fresnel Zone and radiation from sources located on successive Fresnel Zones are in phase opposition. Most of

the power received at the receiving antenna is contributed by the first few Fresnel Zones. The clearance h(m) of a propagation path is often expressed as a normalized clearance $k = h/F_1$ where F_1 is the radius of the first Fresnel Zone. In this thesis path clearances are written in the form kF_1.

Diffraction loss curves for diffraction by a single obstacle are shown in Fig. 2.7. For a given path clearance, diffraction loss due to a knife-edge obstacle has a minimum value.

The path clearance on a LOS path depends on the amount of ray bending which in turn is affected by the N-gradient in the atmosphere. Since the latter quantity can assume a wide range of values, proper path design must ensure that adequate clearance is maintained for all the anticipated values of dN/dh occurring on the path.

2.5.2 Reflection from terrain structures

In LOS microwave propagation, the underlying terrain acts as a surface that scatters the incident radio energy back into the atmosphere. The resultant field due to this scattering may be considered as the sum of two components, namely, the specular component and the diffuse component.

The specular component is a result of reflection from the surface and has coherent phase. Most of this reflected energy originates from the part of the surface which is contained within the first Fresnel Ellipse. For most

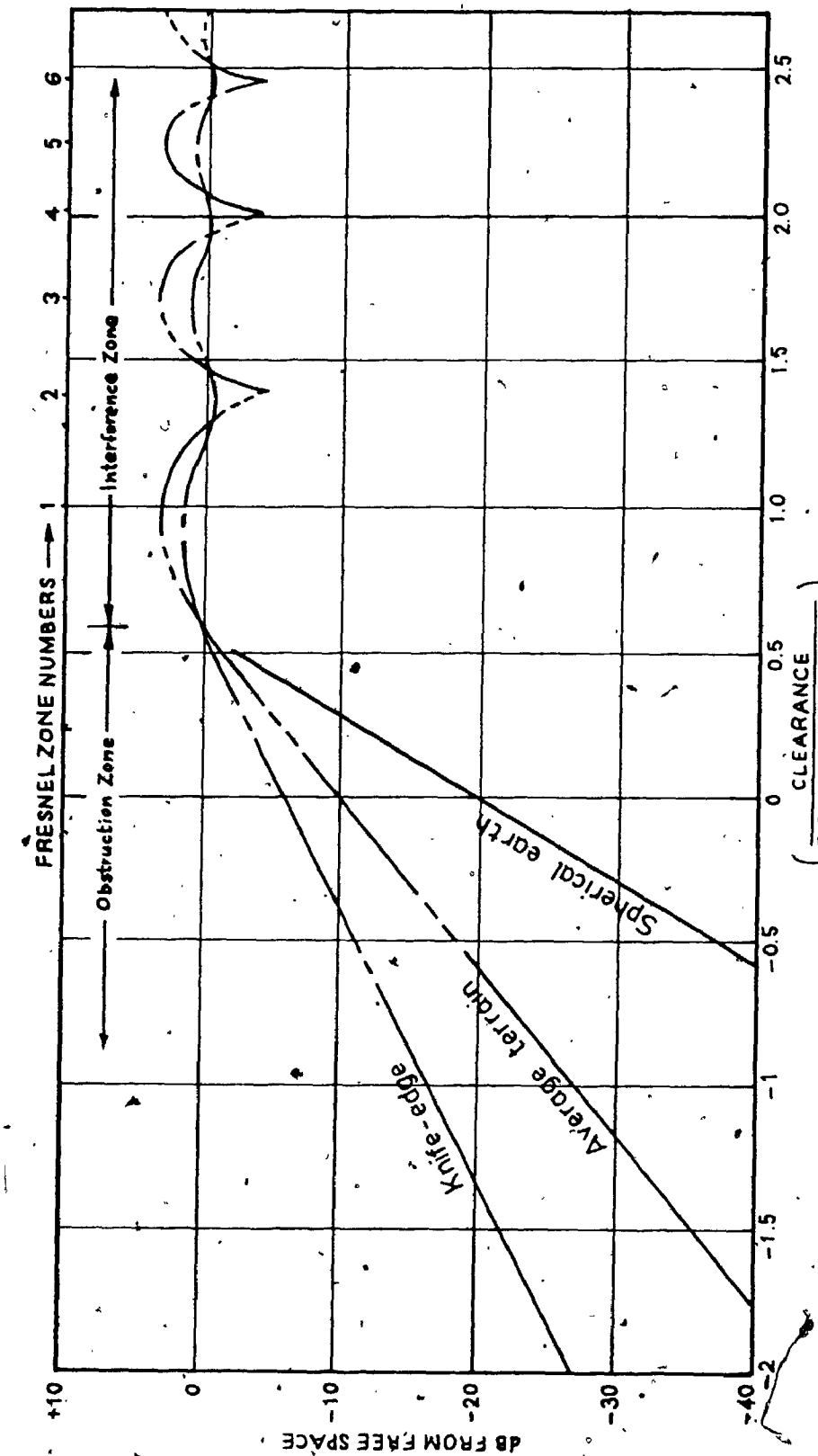

Fig. 2.7 Diffraction loss versus terrain clearance.

symmetrical LOS paths, the distances from the reflection point to the transmitting and the receiving antennas are usually much greater than the semi-axes of the first Fresnel Ellipse, especially at microwave frequencies. When this condition applies, the semi-axes F_{1X} and F_{1Y} of the first Fresnel Ellipse for a curved earth are given by (see Appendix 1)

$$F_{1X} \simeq \frac{D}{\sin\gamma}\left[\frac{\lambda R_1 R_2}{(R_1 + R_2)}\right]^{\frac{1}{2}} \tag{2.22}$$

and

$$F_{1Y} \simeq \left[\frac{\lambda R_1 R_2}{(R_1 + R_2)}\right]^{\frac{1}{2}} \tag{2.23}$$

where λ is the wavelength, R_1 and R_2 are the distances from the reflection point to the two ends of the path, γ is the reflection angle (sometimes also called the grazing angle), D is the divergence coefficient due to earth curvature, and the subscripts X and Y denote the axes parallel and perpendicular to the path.

Unlike the specular component, the energy of the diffuse scattering component originates from over the entire area in between the two ends of the propagation path, unless highly directive antennas are used. The phase of this component is incoherent and its amplitude is Rayleigh distributed [24]. Therefore, fast fluctuations in amplitude usually are observed for the diffuse component.

In general, both specular reflection and diffuse scattering exist simultaneously although one of which may be dominant, depending on the terrain profile and the

surface roughness characteristics. The effects of either of the two components may be quantified by defining a parameter called the Reflection Coefficient R such that

$$R = \frac{E_2}{E_1} \tag{2.24}$$

where E_1 and E_2 are the field strengths of the incident and the scattered fields, and the reflection coefficient takes on values $R = R_s$ and $R = R_d$ for the specular and the diffuse components respectively. These are discussed in more detail in Chapter 5.

In the discussion of multipath propagation in Section 2.4, ground reflections were not considered in order that atmospheric effects may be well illustrated. The effect of ground reflections, when supported by the underlying terrain, is to reflect energy back into the atmosphere and thus cause extra ray paths to be received.

Chapter 3

THE EXPERIMENTAL EQUIPMENT

3.1 Introduction

The equipment used in the propagation experiments consists of a Microwave Diagnostic System and a Data Acquisition System. Propagation measurements, in the form of sweep frequency amplitude and phase records, were made through the use of the Microwave Diagnostic System. The sweep frequency records, together with time information, were gathered by the Data Acquisition System and recorded on magnetic tape in digital form. These systems are described in Sections 3.2 and 3.3 respectively.

In the 1981 experiment, a digital radio test was carried out simultaneously with the propagation experiment. The configuration of the digital radio used by the telephone companies is described in Section 3.4.

3.2 The Microwave Diagnostic System

3.2.1 General Description

The microwave diagnostic system used in the propagation experiments was designed to provide measurements of the received ray path parameters on a

propagation path. In the case of a single received ray, the parameters are the amplitude and angle-of-arrival of the received ray path. In the case of multipath propagation, the parameters include the number of received ray paths, the amplitude and angle-of-arrival of the individual rays, and the relative time delay between the individual rays.

The basis of the microwave diagnostic system is the sweep frequency phase-swept interferometer. The system was developed and a prototype was built at the Centre for Radio Science, the University of Western Ontario. The experimental equipment has an operating amplitude range of 40 dB and is capable of providing measurements of ray path angle-of-arrival and relative time delay variations with accuracies of better than $\pm$0.1 deg and $\pm$0.05 nsec respectively. The following sections summarize the major features of the microwave diagnostic system. More detailed descriptions may be found in Webster et al. [25], Ueno [26], and Webster and Ueno [7].

3.2.2 Principle of Operation

Consider the case of one distinct ray path, the application of the phase-swept interferometer in the measurement of the angle-of-arrival is shown in Fig. 3.1. The incoming signal is received on two antennas which are spaced a distance D apart in the plane containing the required angle-of-arrival. This results in two signals of

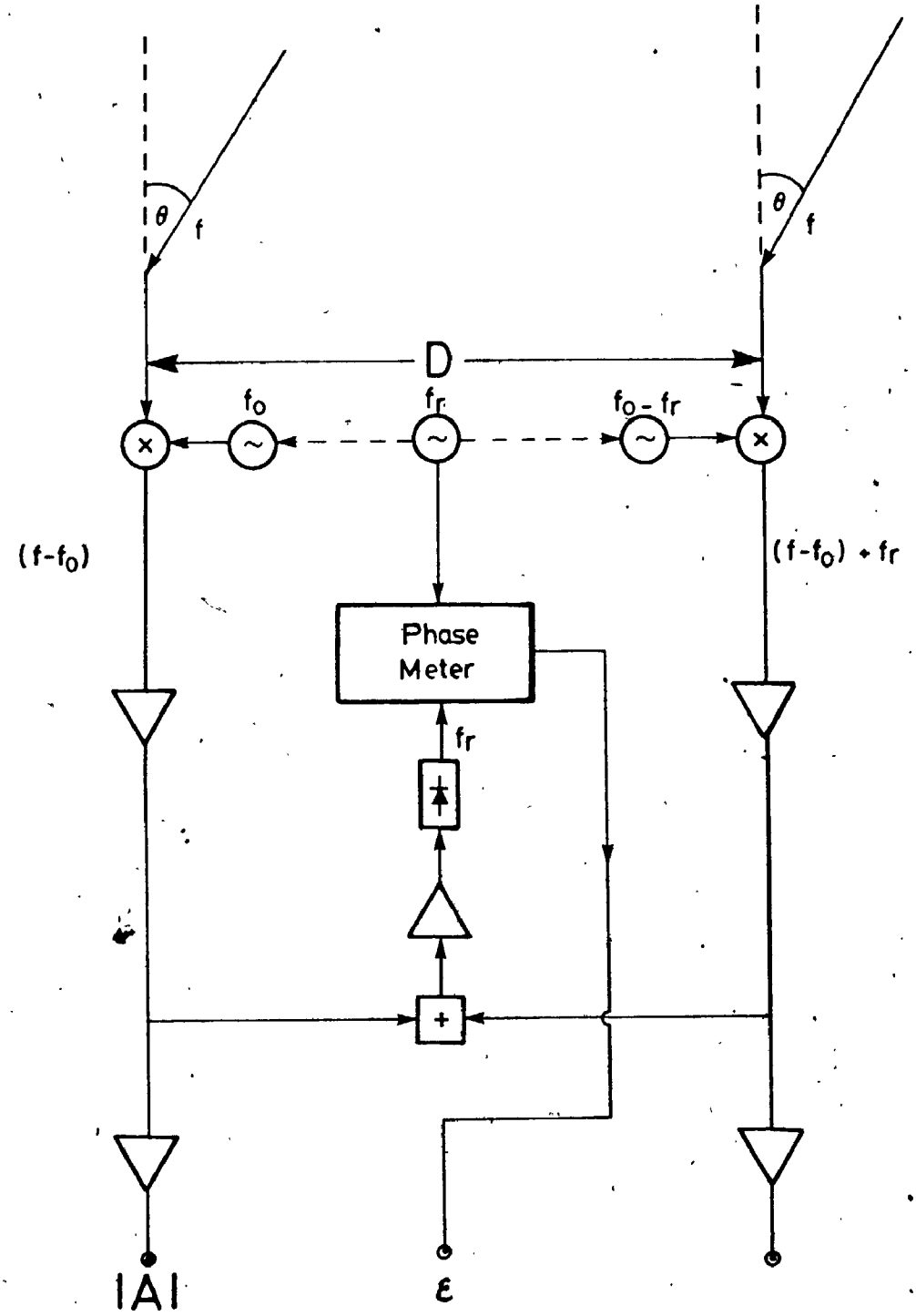

Fig. 3.1 The phase-swept interferometer [7].

the same frequency but with a phase difference ϕ given by

$$\phi = \frac{2\pi f D \sin\theta}{c} \simeq \frac{2\pi f D \theta}{c} \qquad (3.1)$$

for θ small, where f is the radio frequency (RF) and θ is the angle-of-arrival of the incident ray. These two signals are heterodyned with two local oscillator signals of frequencies f_o and $(f_o - f_r)$, where f_r is the frequency of a reference signal used for generating the above local oscillator frequencies and $f_r << f_o$. The resulting IF signals, at frequencies $(f - f_o)$ and $(f - f_o + f_r)$ may also be considered as having the same frequency $(f - f_o)$ but with a time varying phase difference of $(2\pi f_r t + \phi)$, thus accounting for the term "phase-swept interferometer". The addition of these IF signals with subsequent detection and filtering results in a signal of frequency f_r which has a phase ε, measured by a phase meter, relative to the reference signal given by [26]

$$\varepsilon = \frac{2\pi f D \theta}{c} + \phi_o \qquad (3.2)$$

where ϕ_o is a constant including an arbitrary phase shift through the system. An unambiguous measure of the angle-of-arrival is obtained by sweeping the radio signal frequency f, thus

$$\frac{d\varepsilon}{df} = \frac{2\pi D \theta}{c} \qquad (3.3)$$

provided that care is taken to ensure that ϕ_o is not sensitive to variations in frequency. The slope of the

measured phase ε versus frequency f thus gives a direct measure of the ray path angle-of-arrival.

The sweeping of the radio frequency is also useful for identifying the relative path (or time) delay in the case of multipath propagation. This may be illustrated by considering the two path situation shown in Fig. 3.2. The vector addition of two signals of amplitudes 1 and r with relative time delay of $\Delta\tau$ results in a signal $A(\omega)$ given by

$$A(\omega) = 1 + re^{j\omega.\Delta\tau} = |A(\omega)|e^{j\phi(\omega)} \tag{3.4}$$

where $\omega = 2\pi f$, and $|A(\omega)|$ and $\phi(\omega)$ are the amplitude and relative phase of the composite signal given by

$$|A(\omega)| = [1 + r^2 + 2r.\cos(\omega.\Delta\tau)]^{\frac{1}{2}} \tag{3.5}$$

and

$$\phi(\omega) = \tan^{-1}\left[\frac{r.\sin(\omega.\Delta\tau)}{1 + r.\cos(\omega.\Delta\tau)}\right] \tag{3.6}$$

The amplitude of the composite signal versus frequency therefore is periodic as shown in Fig. 3.3 and the period Δf is related to the relative time delay by

$$\Delta\omega.\Delta\tau = 2\pi \tag{3.7}$$

or

$$\Delta\tau = \frac{1}{\Delta f} \tag{3.8}$$

The relative amplitude and relative time delay of the ray paths may thus be derived from the sweep frequency amplitude record by a Fourier Transform technique.

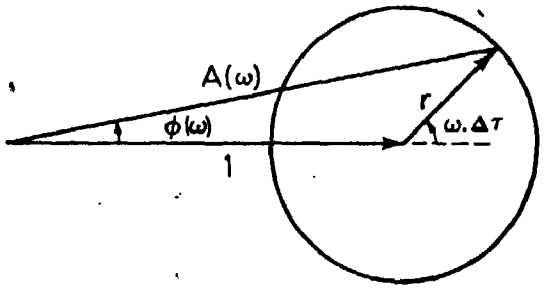

Fig. 3.2 Vector addition of two signals with a relative time delay of $\Delta\tau$.

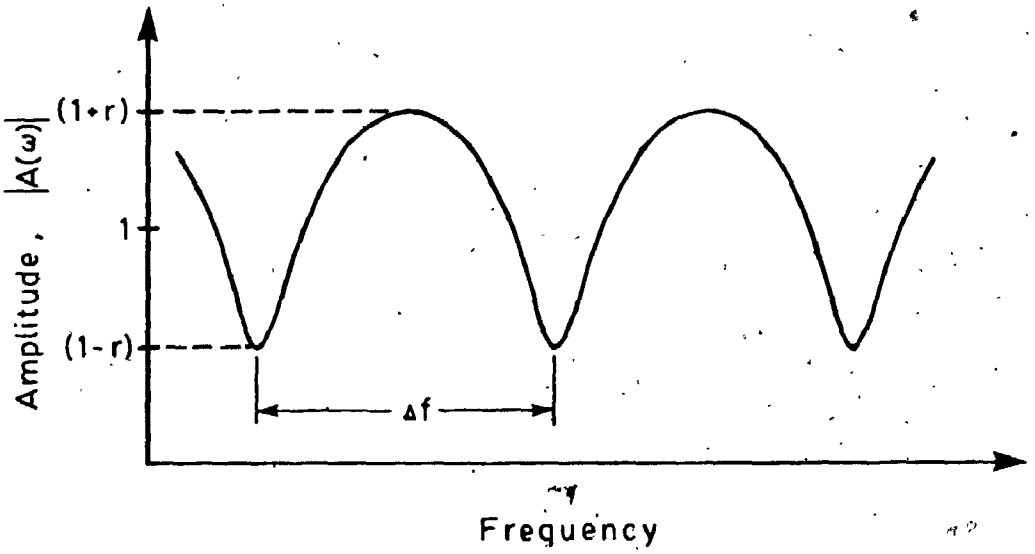

Fig. 3.3 Amplitude characteristics of the resultant of two signals with relative time delay of $\Delta\tau$.

To obtain the angle-of-arrival of the individual ray paths in a two path situation, one observes that the phase meter output ε is now the relative phase difference between the composite signals on the two receiver channels. The analysis in this case is not as straightforward because the measured phase ε is a function of both the relative delay and the angle-of-arrival of the individual rays. An example of the sweep frequency amplitude and phase records simulated for a two path situation is shown in Fig. 3.4. Computer simulations revealed that, for such cases, the angle-of-arrival of the stronger path is still given by the general slope of the phase record. To estimate the angle-of-arrival of the second path, however, a trial-and-error synthesis technique has to be used. This involves the estimation of the angles-of-arrival by synthesizing the experimentally observed sweep frequency phase pattern. Although very accurate angle-of-arrival values may be obtained in this manner, the process is rather time consuming.

The above analysis may similarly be extended to situations with more than two received ray paths. The data analysis procedure is similar to that for the two path situation, with the relative amplitudes and relative time delays estimated by a Fourier Transform technique and the angles-of-arrival derived from pattern synthesis. In such cases the pattern will be considerably more complex and consequently will require more time for its analysis.

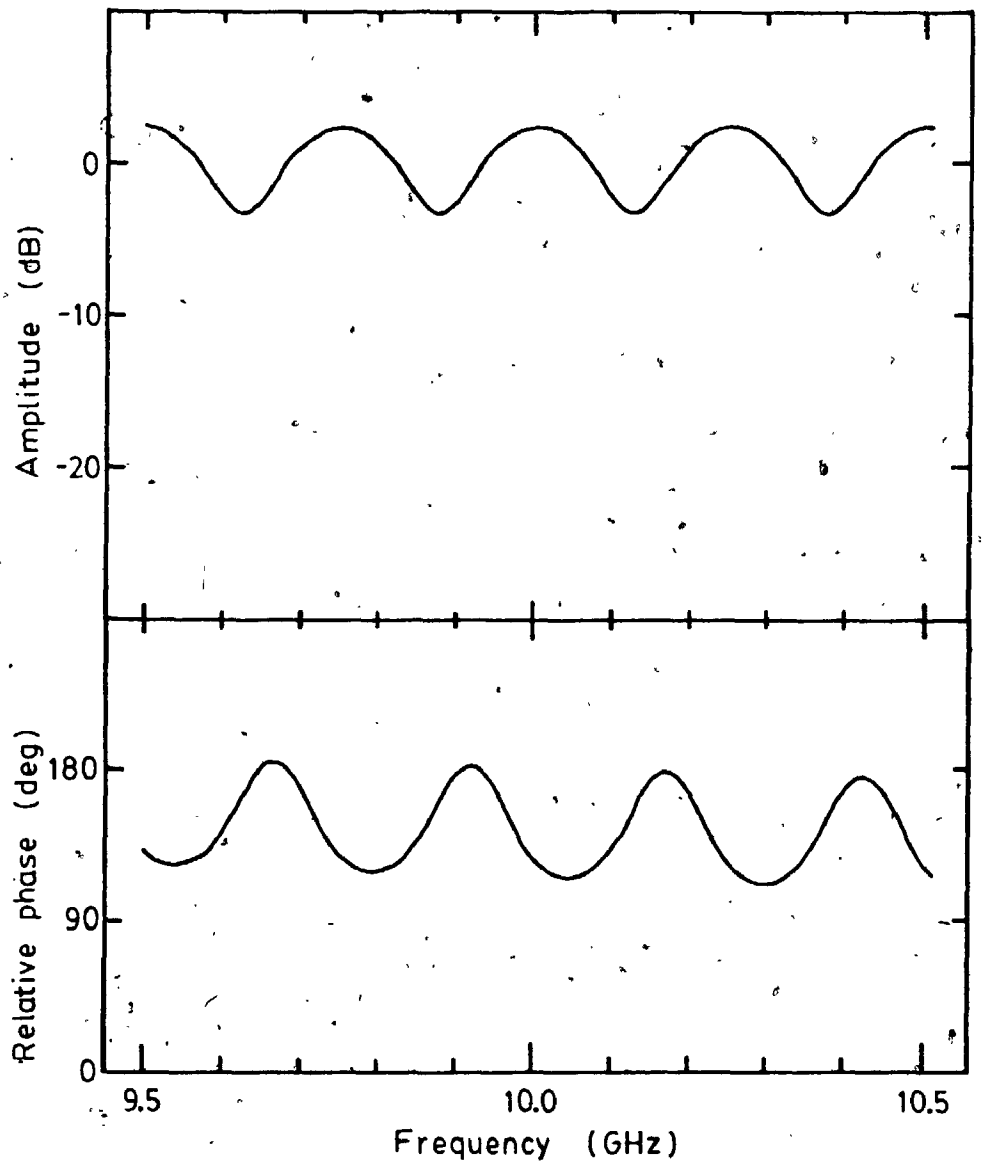

Ampl. (dB)	AOA (deg)	Delay (ns)
0.0	-0.20	-
-10.0	-0.40	4.0

Fig. 3.4 Synthesized sweep frequency amplitude and phase record for two received ray paths.

3.2.3 Equipment Details

The experimental diagnostic system was designed to operate at X-band (8.5 to 12.0 GHz) frequencies. To measure relative time delays in the 1 to 10 nsec range and ray path angles-of-arrival in the range ±1 deg, a frequency sweep of 1 GHz is required and the receiving antennas are spaced 3 m apart.

The block diagram of the diagnostic system transmitter is shown in Fig. 3.5. The transmitter transmits a CW signal that is swept in frequency through a 1 GHz band every 10 seconds. The sweep has a duration of 1.28 sec and is accomplished via 64 discrete frequency steps which are spaced at 16 MHz intervals. The microwave source is a YIG (Yttrium-Iron-Garnet) - Tuned Gunn diode Oscillator (YTO) the output frequency of which is controlled by auxillary sweep control circuitry. The latter also generates a sweep start marker signal which is used to frequency modulate the YTO to mark the start of each sweep for receiver synchronization. To obtain the required power levels, the output from the YTO is amplified by a travelling-wave tube (TWT) amplifier. The amplified signal is transmitted on a parabolic dish antenna and the transmitted signal level is maintained constant throughout the sweep by automatic gain control (AGC) using a PIN-diode modulator.

The diagnostic system receiver shown in Fig. 3.6 consists of two essentially parallel receiver channels in an interferometer arrangement. The first local oscillator

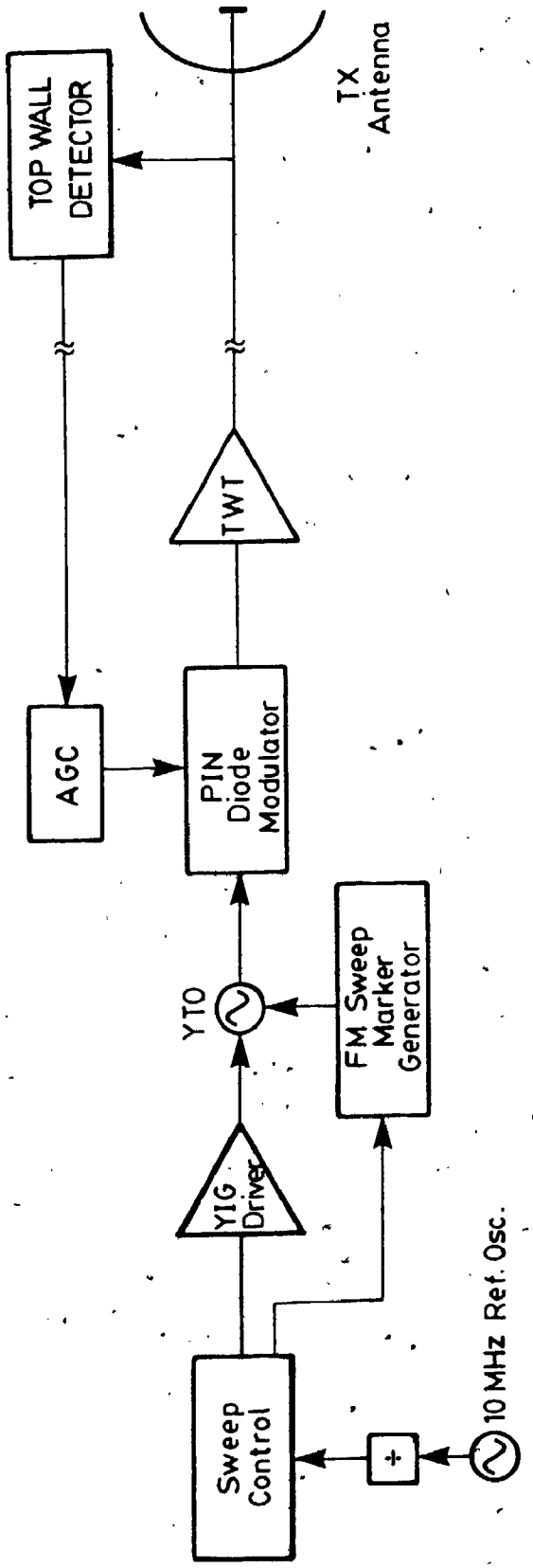

Fig. 3.5 Block diagram of the Diagnostic System transmitter

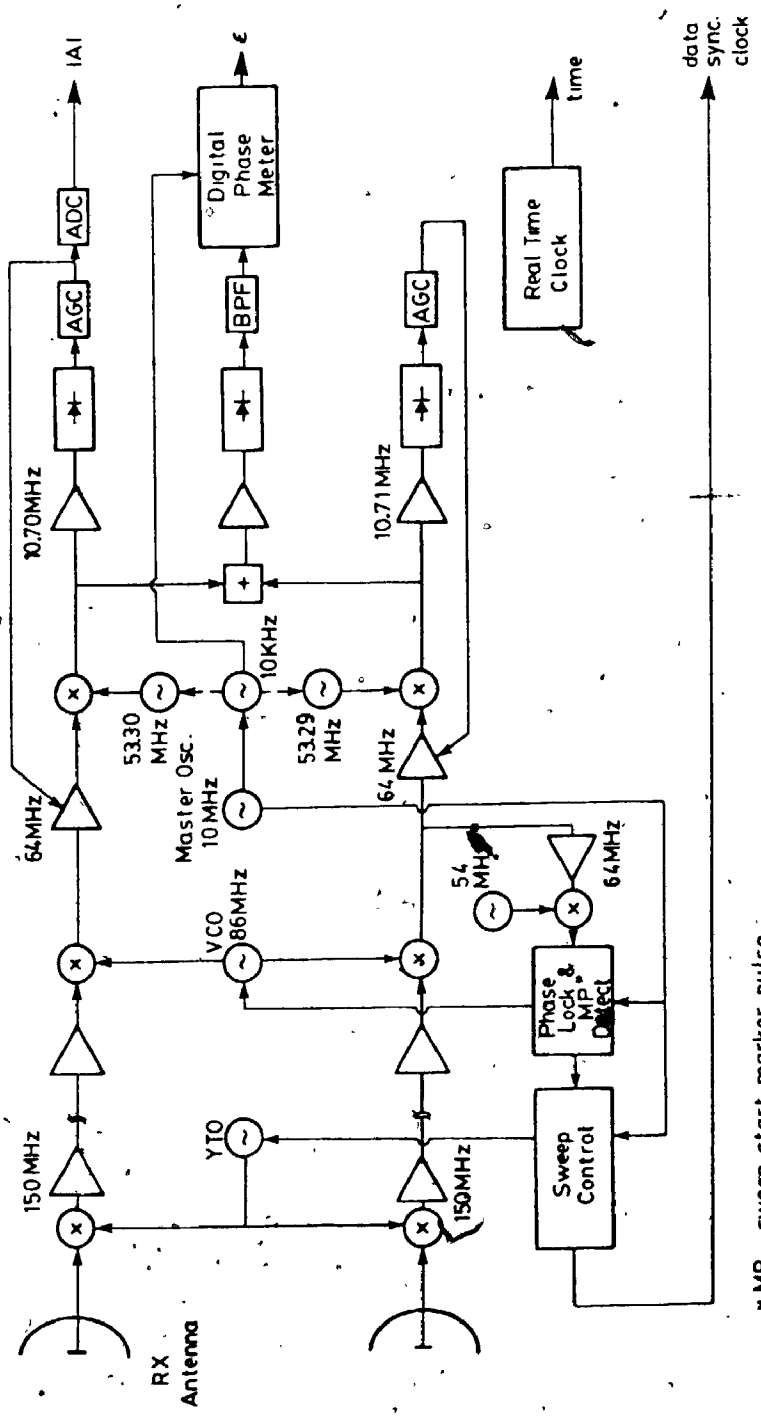

Fig. 3.6 Block diagram of the Diagnostic System Receiver

is a YTO the output sweep frequency of which is synchronized to the received signal (through the FM sweep start marker) but offset by the first intermediate frequency (IF) at all times. This is used to down convert the RF signal on each channel, at each frequency step, to the first IF of 150 MHz through the use of waveguide mixers. After amplification, a phase locking technique is employed to convert the signals to the accurate second IF of 64 MHz. Since the same local oscillator signals and identical circuitry are used for the down conversions in both channels, the phase information in the two signals is preserved.

After amplification, the second IF signals are down converted once more to the third IF using two individual local oscillator signals at 53.30 and 53.29 MHz. The frequency separation of these two local oscillator signals are maintained accurately at 10 KHz by phase locking with the reference 10 KHz signal that is supplied to the phase meter. The resulting third IF signals, at 10.70 and 10.71 MHz respectively, are maintained at constant levels by automatic gain control. For phase measurements as described in the previous section, signals from the two channels are added, detected, and filtered to produce a 10 KHz signal. The phase of this signal relative to the reference 10 KHz signal is measured by a 8-bit digital phase meter. The signal amplitude on one of the receiver channels is also measured by monitoring the AGC levels and

is made available in 8-bit digital form through the use of an analog-to-digital converter (ADC).

A sweep clock signal is available to the data acquisition system for synchronizing the data collection during a sweep. Finally, the real time is provided by a hardware clock.

The transmit antennas used in the 1980 and 1981 experiments were 4-ft diameter and 8-ft diameter parabolic antennas respectively. The receive antennas in both cases were 2-ft diameter parabolic antennas. A summary of the diagnostic system parameters is given in Appendix 2.

3.3 The Data Acquisition System

3.3.1 General Description

A data acquisition system was assembled to control the collection of data from the diagnostic system and its subsequent recording on magnetic tape. High storage capacity, reliability in field operations, and adaptability for data acquisition in other experiments are the guidelines that were followed in the design of the system.

To accommodate the large amount of data (approximately 1.2 MByte per day, 8 bit per byte) and for compatibility with other computer installations, the data is recorded on magnetic tape using a 9-track digital tape recorder. The recording density is 800 bpi and the tapes are recorded in

IBM-NRZI format which is used widely throughout the computer industry. Using 2400-ft tapes, the system is capable of providing uninterrupted recording of data from the diagnostic system for more than ten days. Furthermore, the system is capable of automatically resuming the recording process on power-up in the event of a power failure.

3.3.2 System Configuration

The configuration of the data acquisition system is shown in Fig. 3.7. The heart of the system is a S-100 Bus oriented microcomputer that coordinates the data collection and recording processes. The standard S-100 System Bus carries all the address, data, and status signals, as well as the unregulated supply voltages. The Central Processing Unit (CPU) is based on the Intel 8080 microprocessor and is operated at a clock rate of 2 MHz. The user interface for basic computer operations is provided by a set of front panel switches and CPU status indicator lights.

System memory consists of 16K of Random Access Memory (RAM) and 4K of Erasable-Programmable Read Only Memory (EPROM). The basic machine software consists of a machine monitor program that occupies 3K of EPROM and was adapted from a monitor program developed for use on another Intel 8080 based microcomputer [27]. To implement the data acquisition, recording, and data tape formatting functions, additional software was developed which occupies 1K of

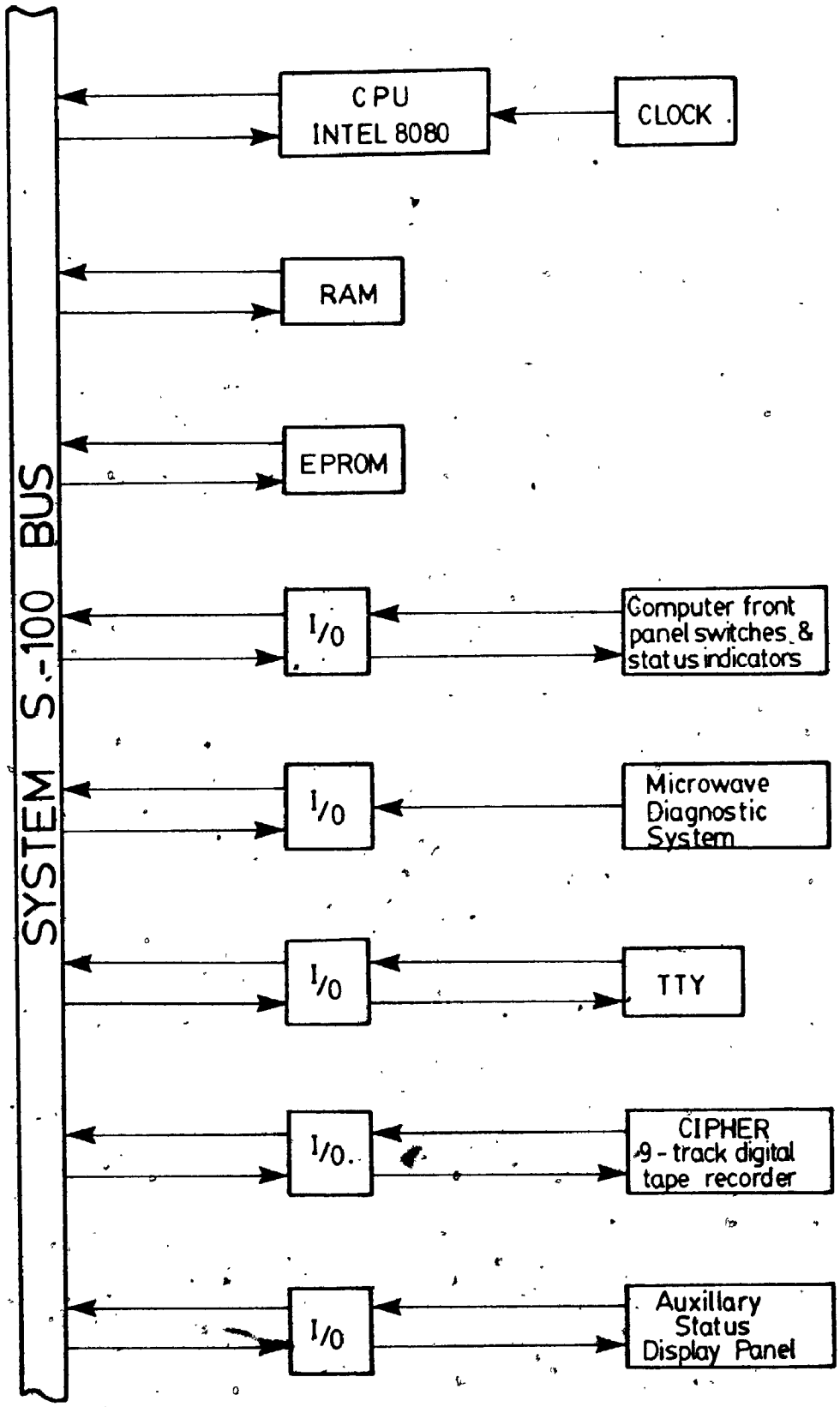

Fig. 3.7 Configuration of the Data Acquisition System.

EPROM. A memory map for the microcomputer system is shown in Appendix 3.

Interfacing between external equipment and the microcomputer is provided by a number of parallel and serial input-output (I/O) ports. Two complete parallel I/O ports are used for data communication with, and for the control of, the 9-track digital tape recorder. An asynchronous serial I/O port is used for interfacing an external video terminal or teletype. In addition, an auxiliary parallel I/O port is reserved for manual override and the display of various tape recorder and diagnostic system functions and status.

The interface with the microwave diagnostic system requires a total of eight parallel input ports for the amplitude, phase, and time data. Since such an interface board was not available at reasonable cost, a S-100 Bus compatible interface board was constructed to implement this function.

A summary of the I/O port allocations in the microcomputer is given in Appendix 3. Also, a list of the manufacturers that supplied the various component boards described above is included.

3.4 The Digital Radio

3.4.1 General Description

A commercial digital radio was used in the 1981 digital radio experiment. The RD-3 radio is a part of the DRS-8 Digital Radio System manufactured by Northern Telecom. The radio operates in the 8 GHz frequency band and was designed to carry a 91.04 Mb/s bit stream (two DS-3 bit streams of 44.736 Mb/s each) over a 40 MHz (RF bandwidth) channel. For telephone transmission applications, this is equivalent to 1344 PCM voice channels per radio channel. The modulation employed in the radio is Quadrature Partial Response Signalling (QPRS) and it provides a signalling speed of 2 b/s/Hz.

The digital radio was protected against outages by both space and frequency diversity techniques. The space diversity protection is provided by two vertically spaced antennas (Main and Diversity antennas) together with the associated RF sections and an adaptive in-phase IF combiner. For frequency diversity protection, the Main and Protection channel frequencies used in the test are 7.78611 GHz and 7.86759 GHz. In the experimental configuration, the radio had the advantage of a 1x1 system (one Main and one Protection channel) but in a developed system, the one protection channel will be used for the protection of up to four regular channels. The improvement in performance due to frequency diversity will therefore be

less in a fully developed system than the experimental configuration. This point should be borne in mind in the interpretation of the results from the digital radio experiment.

3.4.2 Equipment Details

For the purpose of the experiment, the baseband signal used for modulating the transmitted signal is a Pseudo-Random Binary Sequence provided by a Pseudo-Random Data Generator. The experimental receiver equipment block diagram is shown in Fig. 3.8. The radio consists of two essentially identical receivers for the Main and Protection channels.

Within each of the receiver channels, the two RF signals from the Main and Diversity antennas are converted to IF and combined by an adaptive in-phase combiner. The combined signal is then conditioned by a linear delay equalizer and an adaptive linear amplitude equalizer that equalizes in-band amplitude slopes. This resulting signal is subsequently demodulated by a digital demodulator.

The output bit stream from the Main and Protection channel demodulators are fed to a CE-4B Automatic Protection Switch which controls the switching of the signal between the Main and Protection channels. One of the DS-3 signals (consisting of the transmitted pseudo-random data sequence) from the Protection Switch, for the purpose of the experiment, was monitored by a

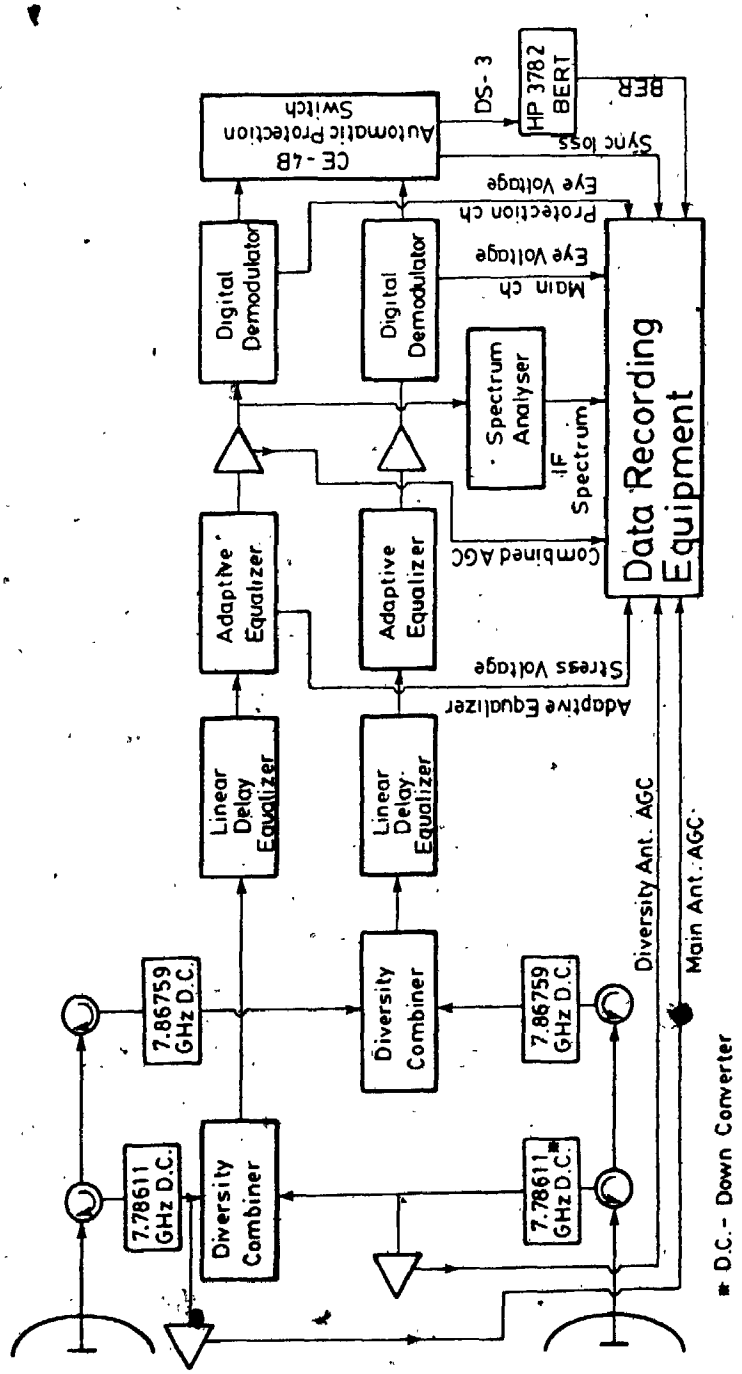

Fig. 3.8 Block diagram of the Digital Radio Receiver.

Hewlett Packard model HP-3782 Error Detector which performed Bit-Error-Rate (BER) measurements on the signal.

Also shown in Fig. 3.8 are the various parameters that were monitored in the experiment. Most of the monitored parameters were obtained from the Protection channel (including the Main, Diversity, and Combined AGC levels, the IF Spectrum, the adaptive equalizer stress voltage, and the demodulator Eye Voltage) in order to eliminate loading effects on the Main frequency channel. In addition, the Main channel Eye Voltage, the Sync-loss, and the BER count were also recorded.

The data recording equipment consisted of a low speed (1 mm/min) 6-channel paper chart recorder and a microprocessor based magnetic tape digital recorder. The paper chart recorder provided continuous records of the above-mentioned AGC levels, the two Eye Voltages, and the adaptive equalizer Stress Voltage. During periods when outages were observed, these parameters, together with the Sync-loss, BER, and the IF Spectrum, were recorded on the magnetic tape digital recorder with a higher resolution.

The antennas used in the digital radio experiment were 12-ft parabolic antennas that have antenna gains of 46.8 dB. The antenna beamwidths at 8 GHz are 0.73 deg between 3 dB points or 1:17 deg between 10 dB points.

Chapter 4

THE PROPAGATION EXPERIMENTS

4.1 Introduction

The Bay of Fundy is a 50 km wide ocean inlet that separates the provinces of New Brunswick (NB) and Nova Scotia (NS). In addition to being noted for having the highest tides in the world, it is also known to radio engineers as a particularly "difficult" propagation path. Frequent outages on LOS microwave communication systems installed on paths across the bay were usually attributed to unknown or anomalous propagation conditions. Although the fading mechanisms were not well understood, the topographical features and the meteorological conditions associated with the maritime climate were believed to have given rise to these propagation anomalies.

Two microwave propagation experiments were conducted across the Bay of Fundy during 1980 and 1981 to study the propagation mechanisms associated with microwave fading on LOS links. In addition to reasons mentioned above, the choice of the Bay of Fundy as the site for the experimental study was further prompted by plans in the New Brunswick Telephone Company (NB.Tel) and the Maritime Telegraph and Telephone Company (M.T.& T) to install a wideband digital radio system across the bay as a part of the Trans-Canada

Telephone System (TCTS). The susceptibility of wideband digital radio systems to propagation distortions is well known [28], [29]. In a test performed in 1979, it was found that the performance of a digital radio installed on a route across the Bay of Fundy was unacceptable due to unknown propagation distortions [30]. A better knowledge of the propagation mechanisms during severe fading conditions, particularly regarding their effects on wideband digital radio systems, therefore is needed.

The first experiment was performed during the period from 5th September to 3rd November, 1980. The propagation path was from Aylesford, NS to Otter Lake, NB (see Fig. 4.1) and the equipment used was a microwave diagnostic system which was discussed in Chapter 3. During the period from 31st July to 3rd September, 1981, the second experiment was conducted on a slightly different propagation path from Otter Lake, NB to Nictaux South, NS. In addition to the diagnostic system, a digital radio was installed by the telephone companies and operated simultaneously on an essentially identical propagation path in this second experiment.

This chapter describes the various experimental details. The characteristics of the propagation paths are discussed with reference to the path profiles and the average meteorological conditions in the region. The received signal characteristics under normal conditions are predicted based on the above considerations. In

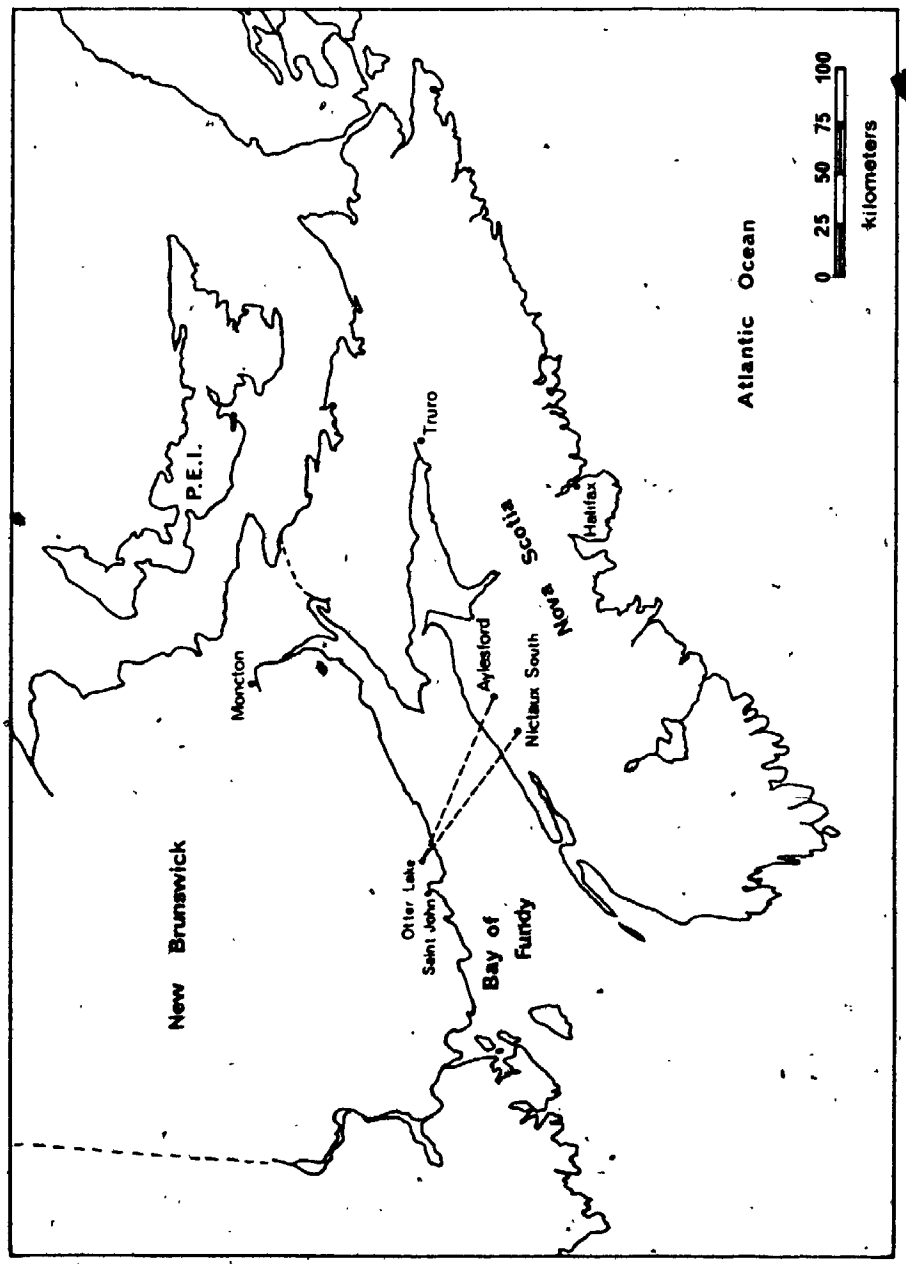

Fig. 4.1 The propagation paths across the Bay of Fundy.

Section 4.4 various aspects of the data analysis process are discussed, as well as the accuracies of the ray path parameter estimates obtained from the sweep frequency data.

4.2 The Propagation Path in the 1980 Experiment

The propagation path in the 1980 experiment is an over-water path of length 80.025 km (see Fig. 4.1) between Aylesford and Otter Lake. A major portion of the telephone voice traffic between the Atlantic coast and other parts of Canada is carried on 4 GHz narrowband analog radio links established on this path. The same path was proposed to be included as part of the TCTS digital network. A digital radio test was carried out in 1979 by the telephone companies to determine the feasibility of installing a digital radio on this link. The results indicated that the digital radio did not provide acceptable performance [30].

Detailed parameters of the propagation path are given in Appendix 4 and the path profile is shown in Fig. 4.2 together with the ray paths drawn for a constant refractivity gradient, dN/dh, of -40 NU/km (corresponding to K = 1.34). Two strong ray paths -- a direct and a sea reflected ray, are possible at least under normal conditions. Although potential terrain blockages for the sea reflection exist at two points along the path (points A and B at 3.45 and 16.85 km from Otter Lake respectively),

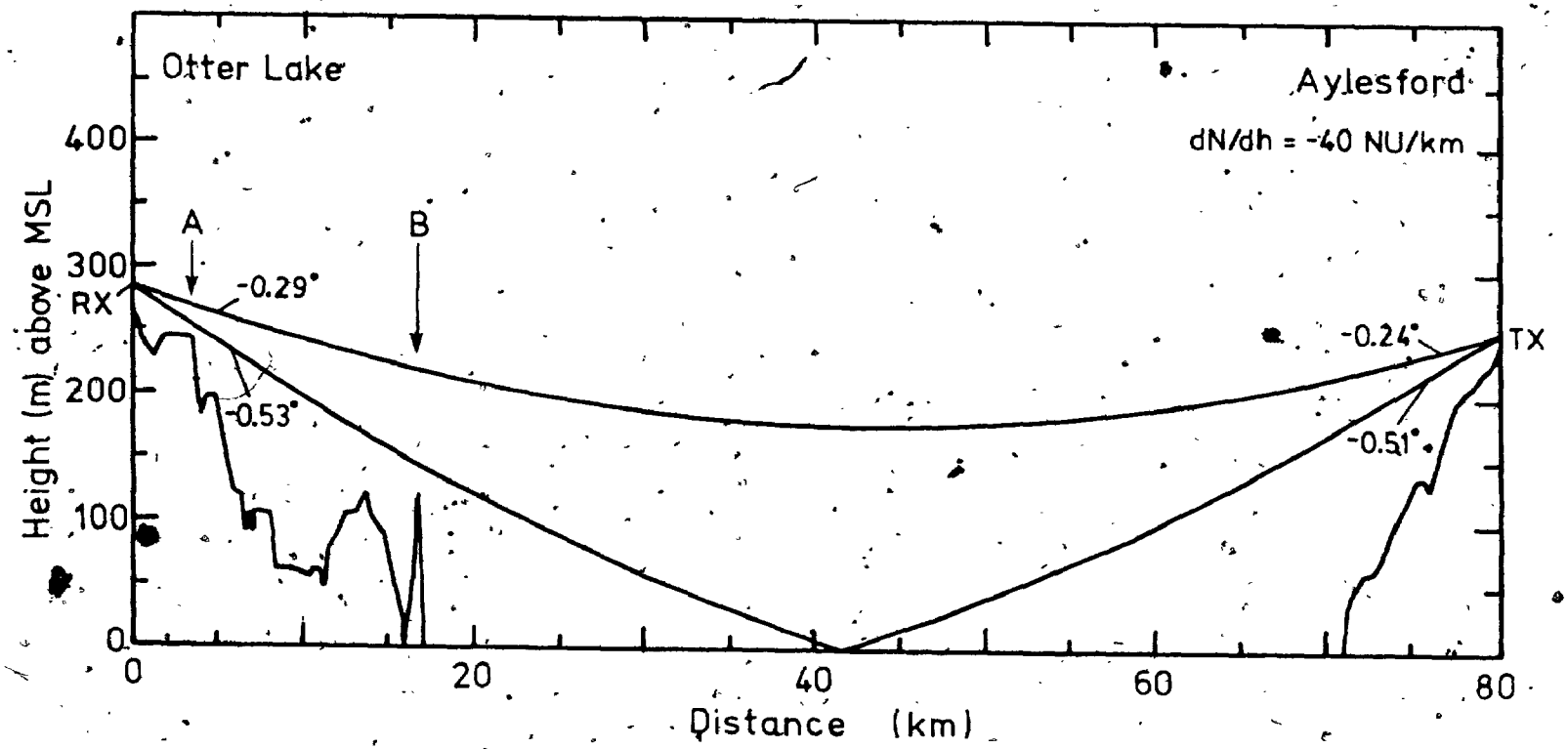

Fig. 4.2 Path profile for the Aylesford - Otter Lake propagation path.

they are not effective under normal conditions. Including an average tree height of 12 m for this geographical area, the elevations of the blockage points are 256 m and 134 m above mean sea level (MSL). For a normal gradient of -40 NU/km and at a frequency of 10 GHz, the clearances for the sea reflected ray at these locations were estimated as $-0.3F_1$ and $0.5F_1$ respectively, where F_1 is the radius of the first Fresnel Zone at the corresponding points.

Before further results from ray tracing are discussed, one quantity of importance is the expected range of dN/dh values for this geographical area. In estimating this range, use was made of published values from the Tropospheric Refractivity Atlas for Canada [3]. Since the probability distribution curves of the refractivity gradient were not available for the Bay of Fundy, the values were projected using the data available for two nearby locations; namely, Portland, Me, and Sable Island, NS. The seasonal distributions of the refractivity gradient for these locations are shown in Fig. 4.3. Based on these published values, the range of dN/dh values for 99.8 % of the time was estimated as $-340 < dN/dh < 245$ NU/km during the period from September through November. Also available from the same source are the seasonal variations of the surface refractivity for the above locations and these are shown in Fig. 4.4. Based on these statistics, an average surface refractivity value of 340 NU is assumed for the Bay of Fundy.

(a) Portland, ME.

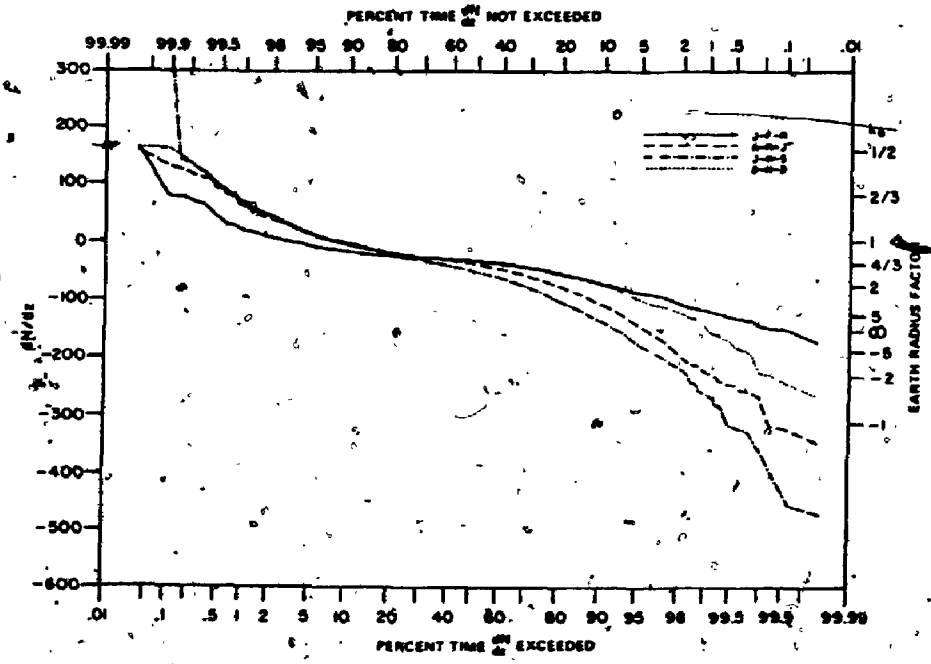

(b) Sable Island, NS.

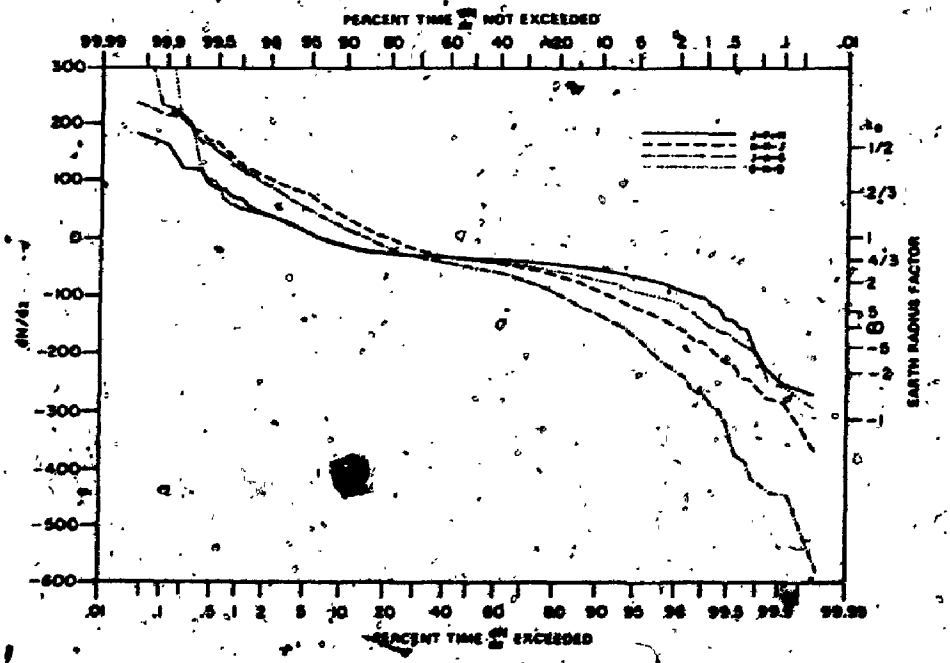

z--height above ground

Fig. 4.3 Seasonal probability distribution of ground-based refractivity gradients for (a) Portland, Me., and (b) Sable Island, N.S. [3].

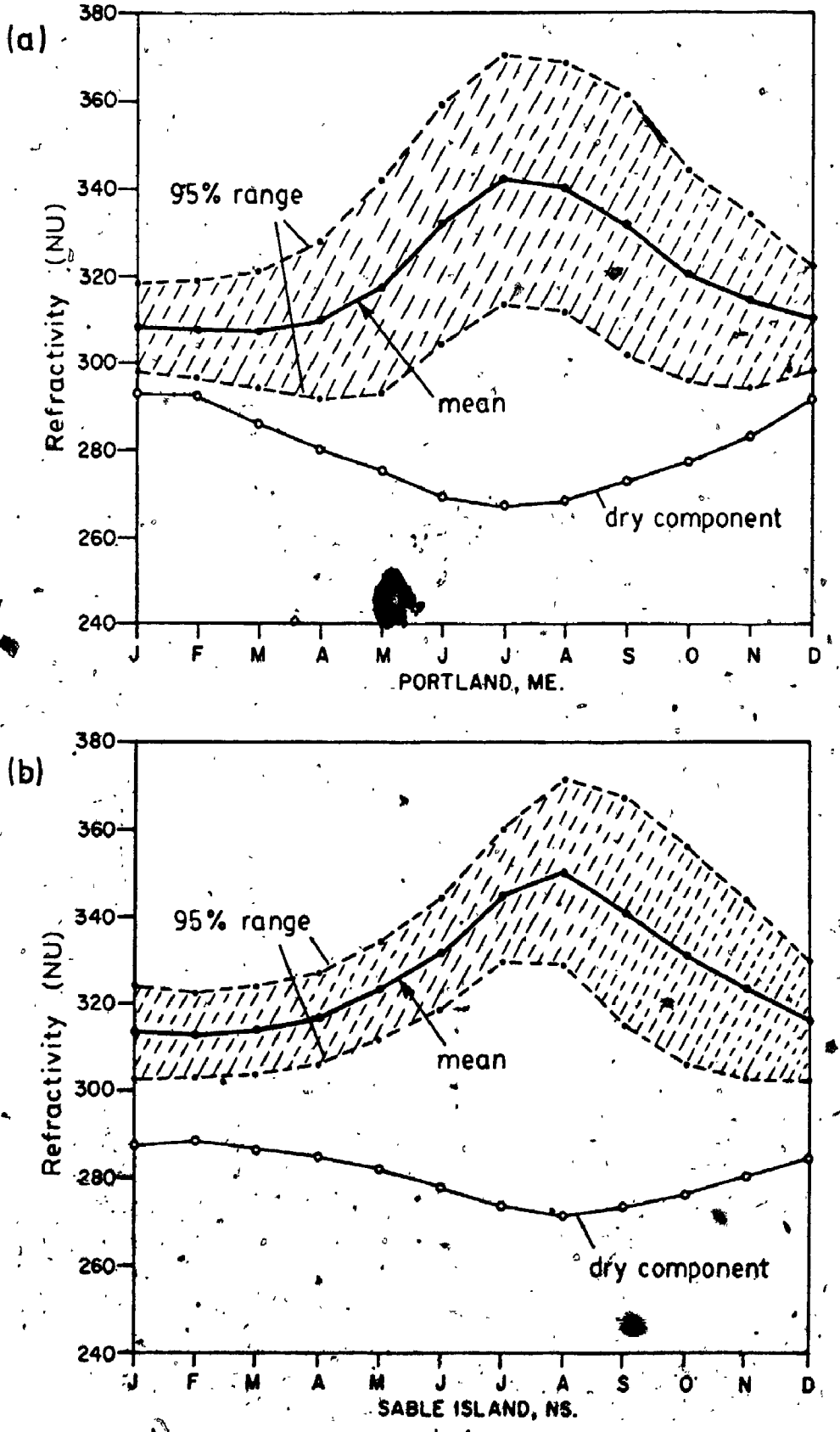

Fig. 4.4 Seasonal behaviour of the surface refractivity for: (a) Portland, Me., and (b) Sable Island, N.S. [3].

Having obtained a bound on the range of dN/dh values expected in this area, the results from further ray tracing may be discussed. The results of ray tracing performed for three representative values of dN/dh are shown in Fig. 4.5. It is observed that the terrain blockage to the sea reflection is not effective except for the more positive values of the refractivity gradient. These results are summarized in Fig. 4.6 in which the amplitudes of the direct and reflected rays were estimated by ray tracing while taking into account the diffraction losses due to terrain blockage; a perfect sea reflection and average terrain characteristics at the diffraction points were assumed. Furthermore, since two obstacles were involved (points A and B in Fig. 4.2), the diffraction losses were estimated based on a procedure proposed by Deygout [31] for dealing with multiple knife-edge diffraction. Using an attenuation of 20 dB as the criterion, the blockage to the sea reflected ray is adequate only for values of dN/dh less negative than approximately -35 NU/km.

In addition to the ray path amplitude characteristics, the angle-of-arrival estimates are also of importance. In the 1980 experiment, the transmitter was located at Aylesford and the receiver at Otter Lake. The angles-of-arrival at Otter Lake are shown in Fig. 4.6. By applying Eq. (2.9) the range in angle-of-arrival for 99.8 % of the time was estimated as 1.34 deg. One consequence of this latter observation is that a limit should be imposed

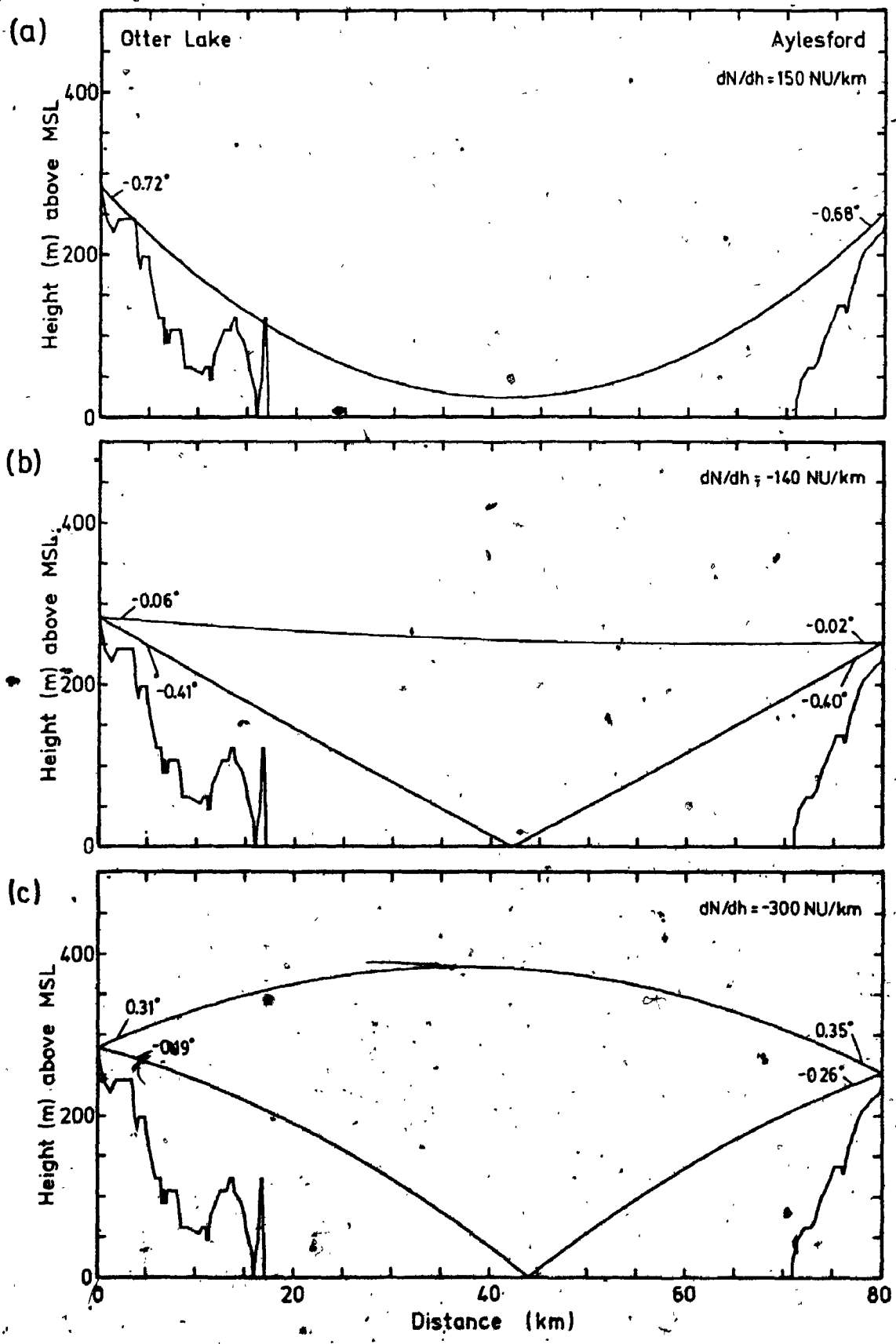

Fig. 4.5 Ray Tracing on Aylesford - Otter Lake path for three representative values of the refractivity gradient.

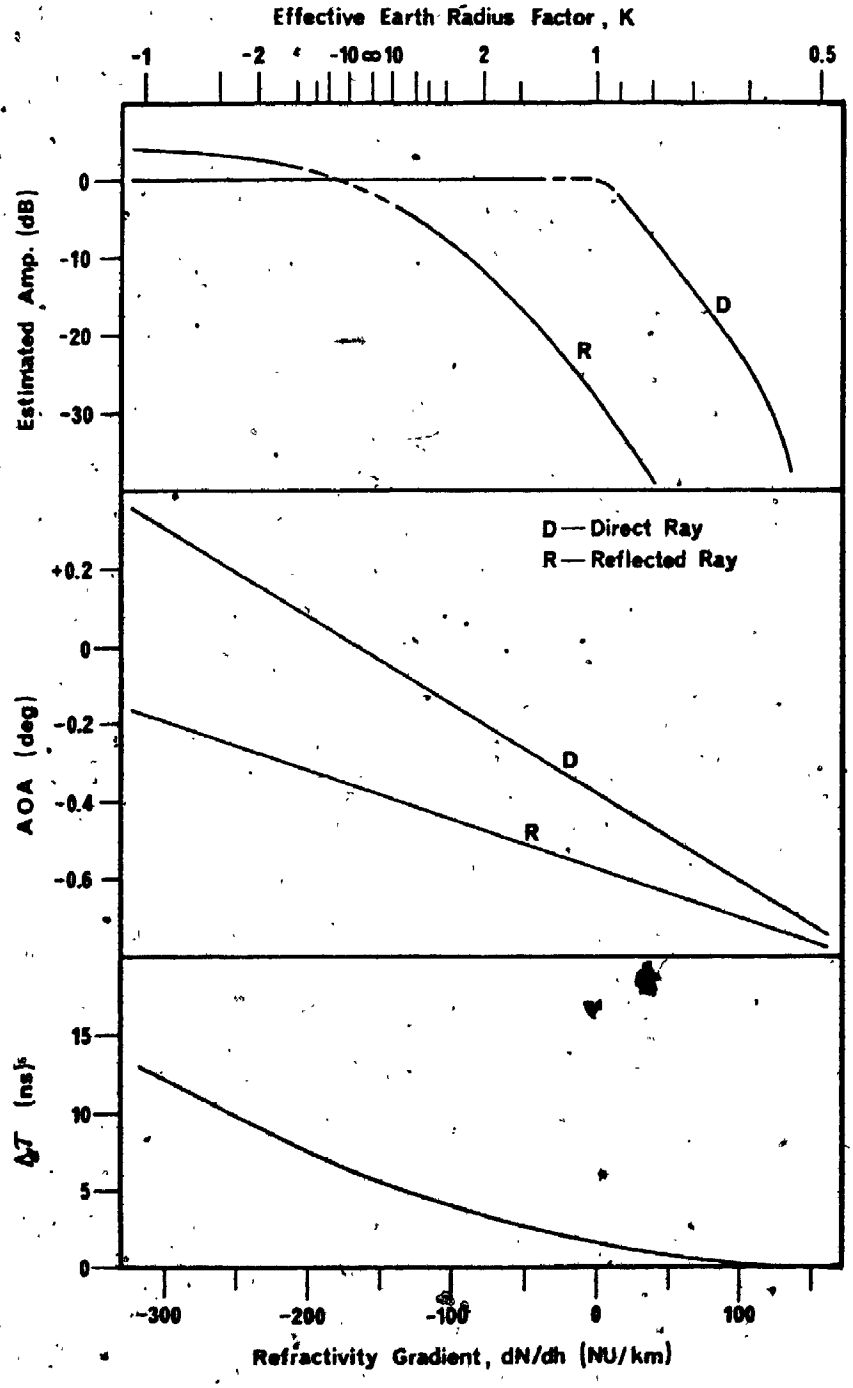

Fig. 4.6 Ray path characteristics for Aylesford - Otter Lake path under conditions of uniform refractivity gradient.

on the maximum size (minimum beamwidth) of the antennas used on this propagation path. Furthermore, since the difference in angle-of-arrival of the direct and the sea reflected rays under normal conditions is of the order of 0.25 deg, angle discrimination (through the use of simple narrow-beam antennas) cannot be used effectively for eliminating the sea reflection.

For a normal gradient of -40 NU/km, the received signal was estimated to be composed of a direct ray of "normal" amplitude and a reflected ray from the sea which is roughly -19 dB in amplitude relative to the direct ray (an average tree height of 12 m was assumed in estimating this value). The time delay of this reflected ray relative to the direct ray was estimated as approximately 2.5 nsec.

4.3 The Propagation Path in the 1981 Experiment

Based on the results obtained from the 1979 and 1980 experiments, an alternate route across the Bay of Fundy was chosen and its suitability for inclusion in the TCTS was investigated in the 1981 experiment. The experimental path from Otter Lake to Nictaux South (see Fig. 4.1) is 80.375 km in length and the various path parameters are shown in Appendix 4. The path profile, together with the ray paths drawn for a constant refractivity gradient of -40 NU/km, is shown in Fig. 4.7. One of the main reasons

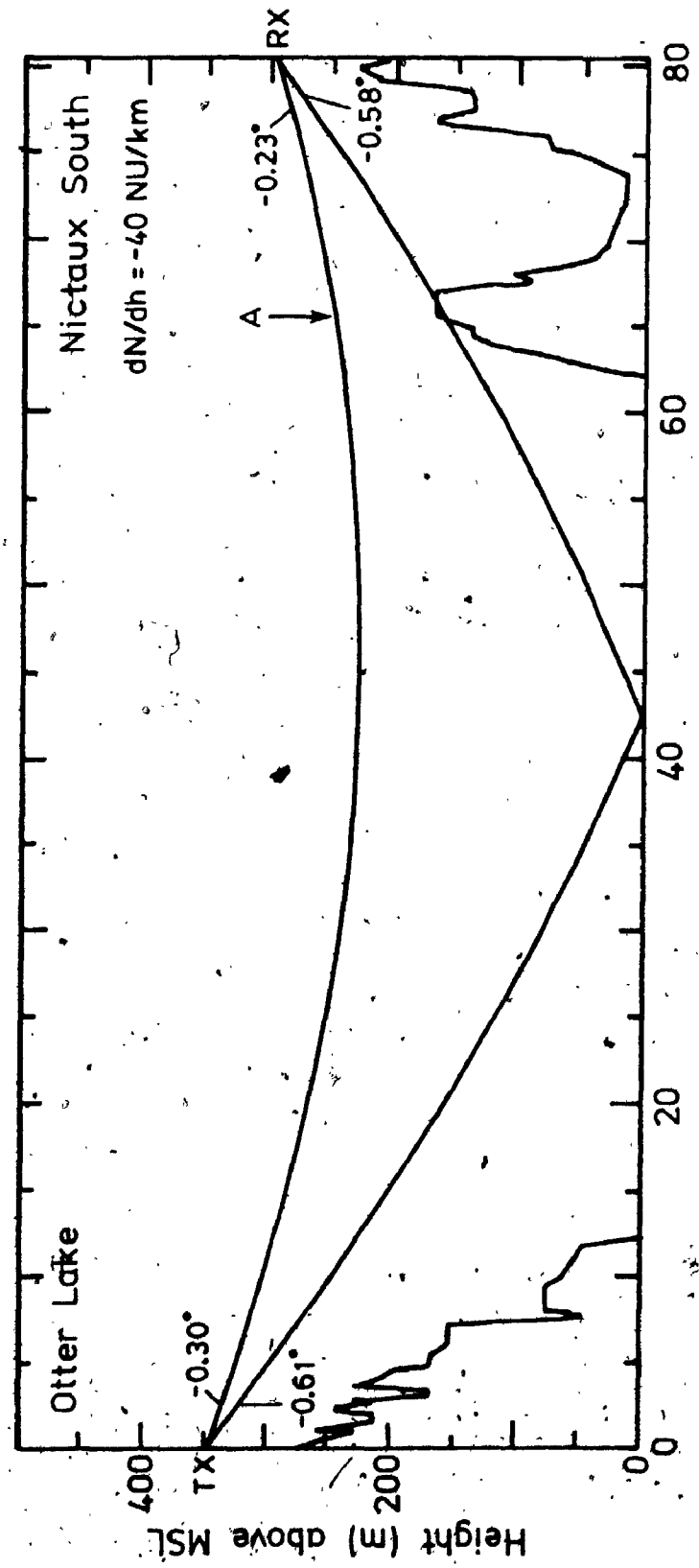

Fig. 4.7 Path profile for the Otter Lake - Nictaux South propagation path.

for the choice of this propagation path is the better blockage to the reflected ray. The blockage offered by North Mountain (labelled A in Fig. 4.7) has an elevation of 179 m (including an average tree height of 12 m) above MSL. At a frequency of 10 GHz and for a normal gradient of -40 NU/km, the clearance for the sea reflection at this location was estimated to be $-1.0F_1$.

The range of dN/dh values for 99.8 % of the time for this path is expected to be similar to that for the Aylesford - Otter Lake path and the same should be true for the average surface refractivity. However, the 1981 experiment was performed during the month of August. Taking into account the seasonal variations, the 99.8 % range in dN/dh was estimated from Fig. 4.3 as $-430 < dN/dh < 260$ NU/km. Again, ray tracing for three representative values of dN/dh are shown in Fig. 4.8 from which it may be observed that North Mountain does provide a better blockage to the reflected ray. The results are summarized in Fig. 4.9 which was derived in a similar manner as for Fig. 4.6 presented for the Aylesford - Otter Lake path, although in this case there is only one diffraction point at North Mountain. Using the same criterion of 20 dB attenuation, the blockage to the sea reflected ray is adequate for values of dN/dh greater than -105 NU/km.

As for the ray path angle-of-arrival characteristics at the receiver site at Nictaux South, the predicted values

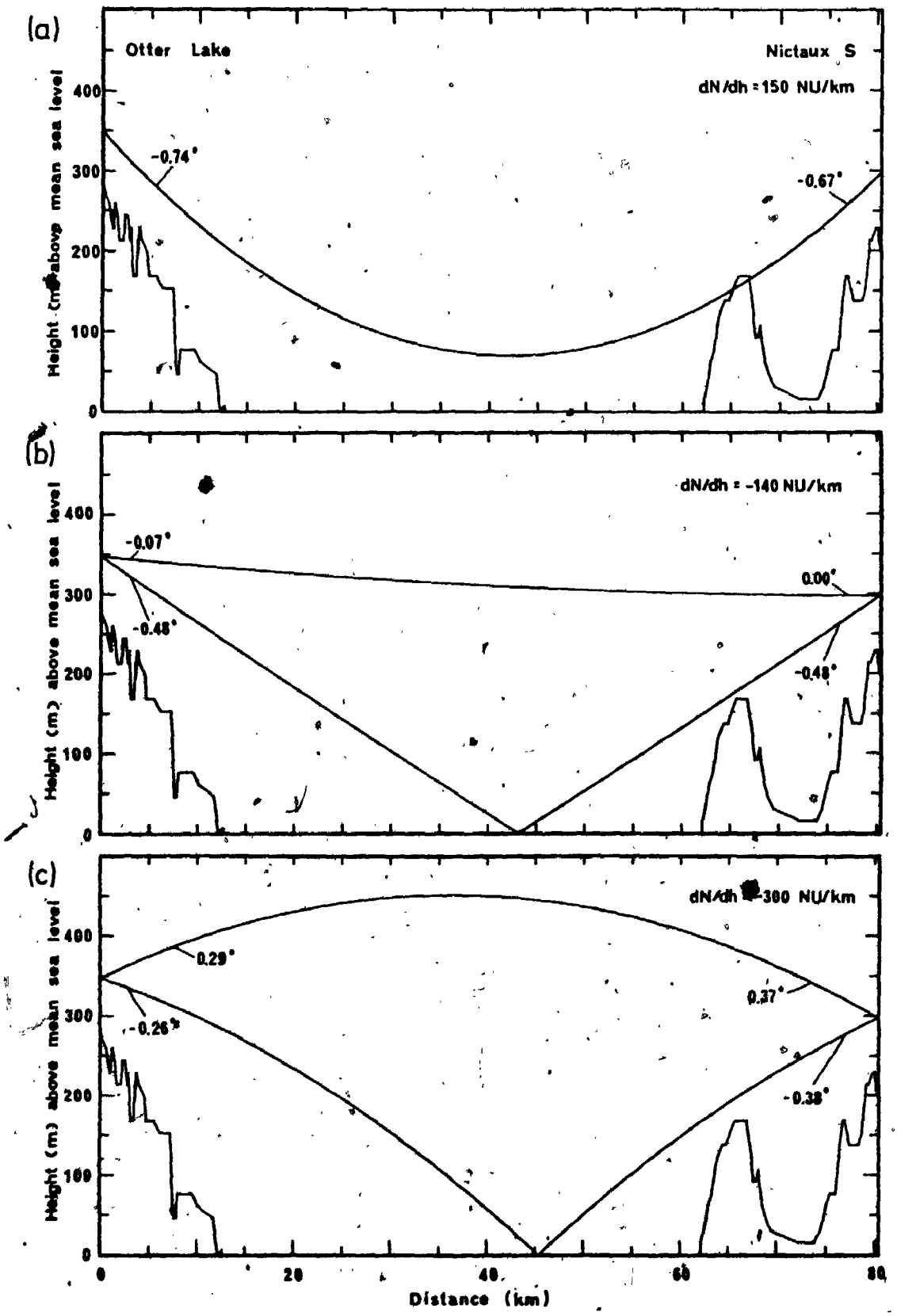

Fig. 4.8 Ray Tracing on the Otter Lake - Nictaux South path for three representative values of the refractivity gradient.

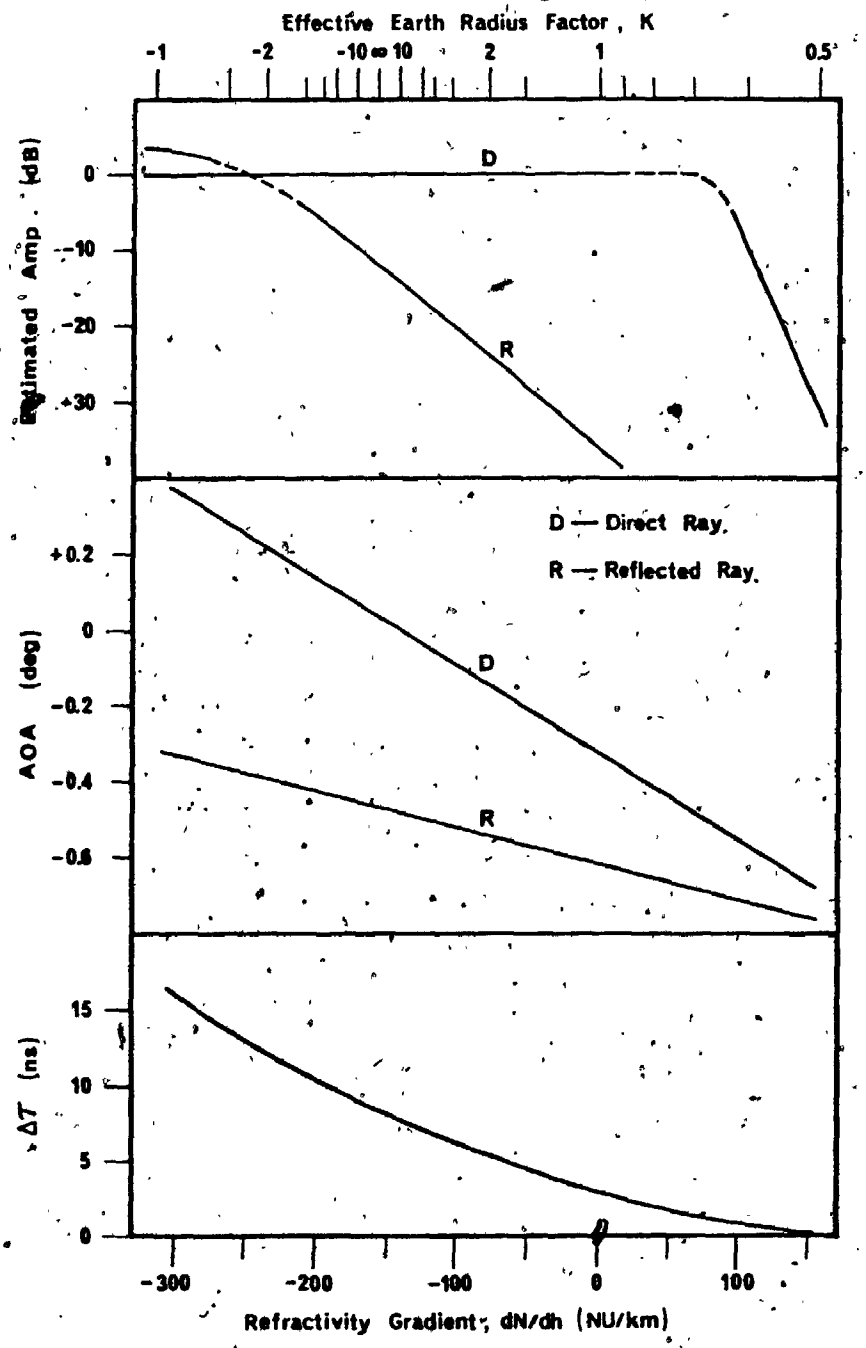

Fig. 4.9 Ray path characteristics for the Otter Lake - Nictaux South path under conditions of uniform refractivity gradient.

are shown in Fig. 4.9. Again by applying Eq. (2.9) the 99.8 % range in main ray angle-of-arrival was estimated as 1.6 deg. Although the difference in angle-of-arrival between the direct and sea reflected rays (of the order of 0.35 deg under normal conditions) is larger than the value for the Aylesford - Otter Lake path, angle discrimination is still not useful for eliminating the sea reflection.

The received signal for a normal gradient of -40 NU/km for this propagation path is estimated to be composed of a direct ray of normal amplitude and a reflected ray which is roughly -30 dB in amplitude relative to the direct ray, with a time delay between the two rays of approximately 4.5 nsec. The larger delay value in this case being explained by the higher transmitting and receiving antenna elevations.

4.4 Data Analysis

4.4.1 Data from the Propagation Experiments

Because of the large volume of experimental data available, the raw data tapes from the field experiments were organized and reformatted into random-access files on a PDP-10 computer, on which the majority of the data analysis work was performed. This facilitates the easy access and fast retrieval of the data simply by specifying the appropriate time information.

As described in the section on the microwave diagnostic system, the sweep frequency amplitude and phase records do not give direct measurements of the various received ray path parameters. Therefore, the processing of the raw data includes a spectral analysis of the sweep frequency amplitude records to estimate the ray path amplitudes and relative delay time; and a linear regression analysis of the phase record to estimate the main ray angle-of-arrival.

In using the spectral analysis method for estimating the ray path amplitudes and delay time, a few important points should be noted. The major considerations in the design of the data analysis routines are reliability and efficiency. Since a large data base is involved, it is essential that reliable and accurate results be produced by an efficient analysis routine so as to minimize computing costs. Based on these requirements and the results of trial runs using different methods, it was concluded that, for the particular application, the Smoothed Periodogram approach [32] is a suitable choice. A block of zeroes is attached to each 64-point amplitude record and a 128-point FFT is performed. Frequency averaging is then applied to the squared amplitude spectrum to give the estimated power spectrum. This frequency averaging is necessary for reducing the effects of leakage and to reduce the variance [32], [33]. The second ray amplitude and delay time is obtained from the power spectrum while the main ray

amplitude is obtained from the average value of the original sweep record (see Fig. 3.3).

There is an added complication in estimating the ray path amplitudes using the above method. In Fig. 3.3 it is seen that the sweep frequency amplitude data resulting from two ray paths are quasi-sinusoidal. As a result, the above method gives values that are not equal to the actual ray path amplitudes. However, it is shown in Appendix 5 that the desired ray path amplitudes may be obtained from the above estimated values by proper scaling. This correction was included in the analysis routine. The routine was carefully tested using synthesized data and some of the results are summarized in Figs. 4.10(a) and (b) which also give an idea of the errors involved in the amplitude estimates. The largest errors are involved when the ray paths are close in amplitude (less than 3 dB difference) and the delay is short. The uncertainties in the ray path amplitude estimates in such cases are approximately $\pm$1.5 dB. However, the accuracy improves rapidly with increases in the delay time and the differential amplitude. For example, when the ray paths differ in amplitude by more than 5 dB, the uncertainties in the amplitude estimates are less than $\pm$0.5 dB. As for the delay time estimate, the tests show that the accuracy is better than $\pm$0.1 ns for delay times longer than 1.5 ns. It is also noted that because of limitations due to a finite frequency sweep range, ray paths with delay times less than approximately

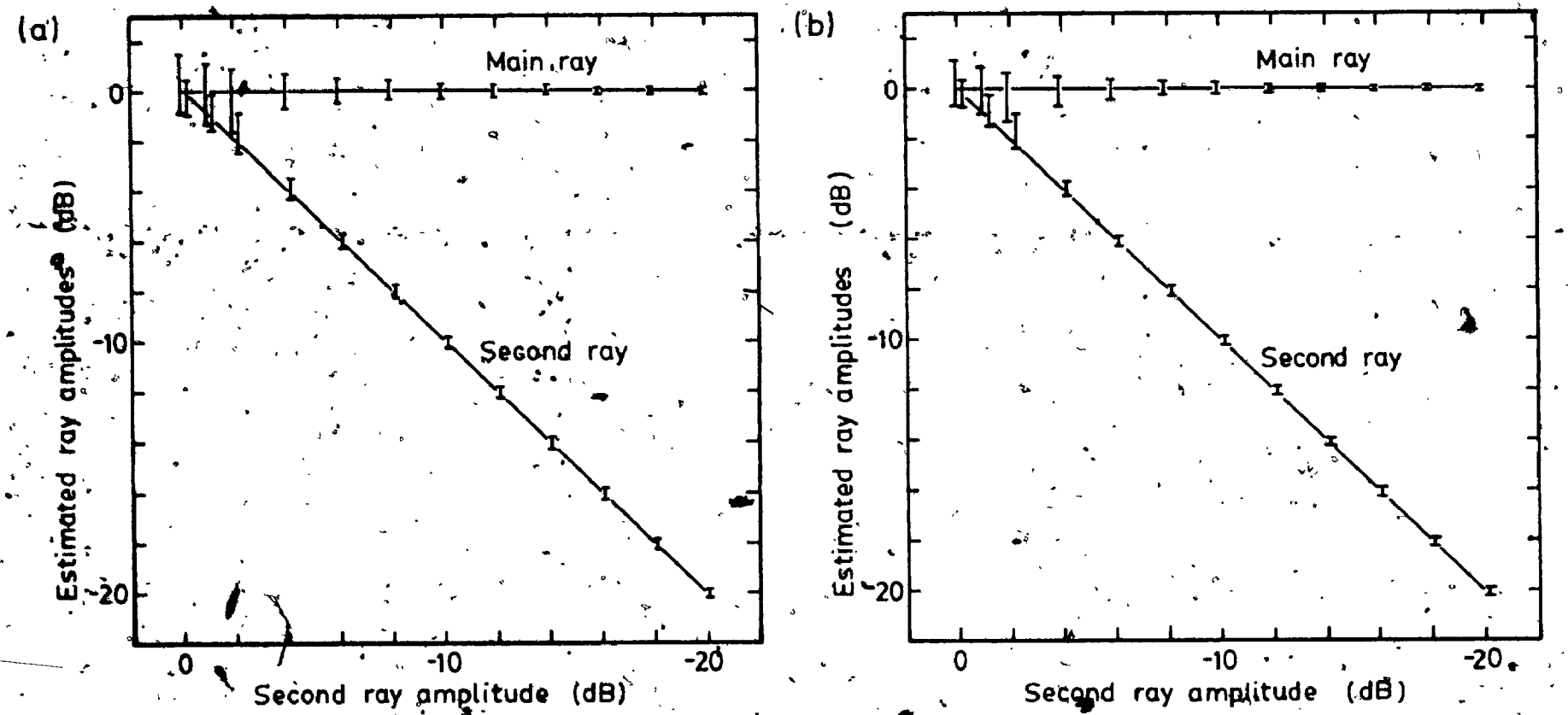

NB. 1) Main ray amplitude = 0 dB
2) Relative delay: $2 < \Delta\tau < 8$ ns
3) the vertical bars indicate the error bounds.

NB. 1) Main ray amplitude = 0 dB
2) Relative delay: $3 < \Delta\tau < 4$ ns

Fig. 4.10 Estimation of ray amplitudes using the analysis routine, the vertical bars are the error bounds of the estimated amplitudes.

2

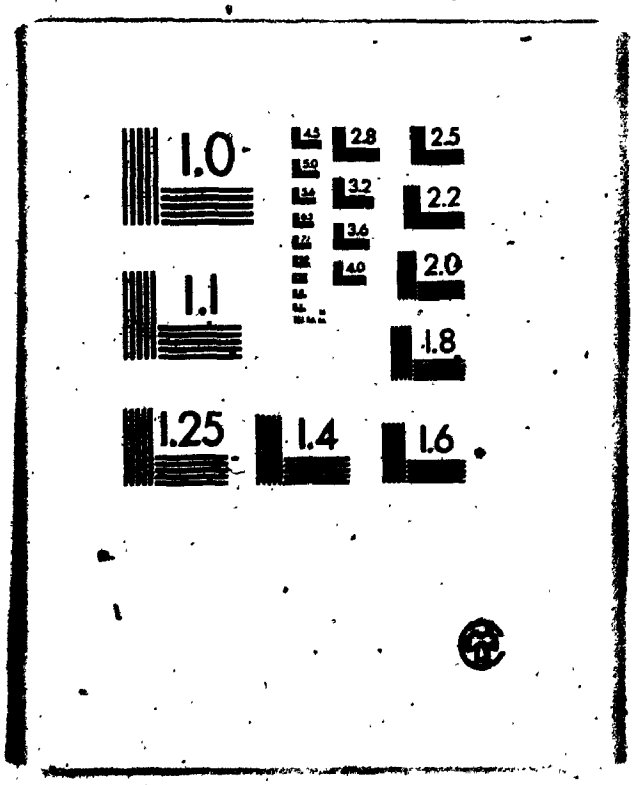

1.5 ns are not resolved.

A few points in relation to the analysis of the phase record required to produce the main ray AOA are also noteworthy. It has been pointed out in Chapter 3 that the main ray AOA is given by the general slope of the phase record even in multipath situations. The analysis method therefore involves filtering the phase record (to remove variations due to the second ray) and estimating the AOA from the slope of the filtered phase record. Tests performed on the analysis routine indicate that the main ray AOA estimated by this method is better than ± 0.05 deg provided that the second ray amplitude is less than -10 dB relative to the main ray and the delay time is greater than approximately 3 ns. Again the limitation was imposed by the finite frequency sweep range.

This latter limitation presents an even greater problem when short delay ray paths (less than 0.5 ns) are present. The slope of the phase record is significantly affected by even a low amplitude short delay ray. The effect is illustrated in Figs. 4.11(a) to (d) in which the amplitude and phase records are synthesized for various conditions for the frequency range 0 to 15 GHz. The range monitored by the diagnostic system (from 9.5 to 10.5 GHz) is also indicated. Fig. 4.11(a) shows the amplitude record for a single ray of amplitude 0 dB. The phase record is shown for various AOA values. Figs.4.11(b) to (d) were synthesized with two ray paths of amplitudes 0 and -10 dB.

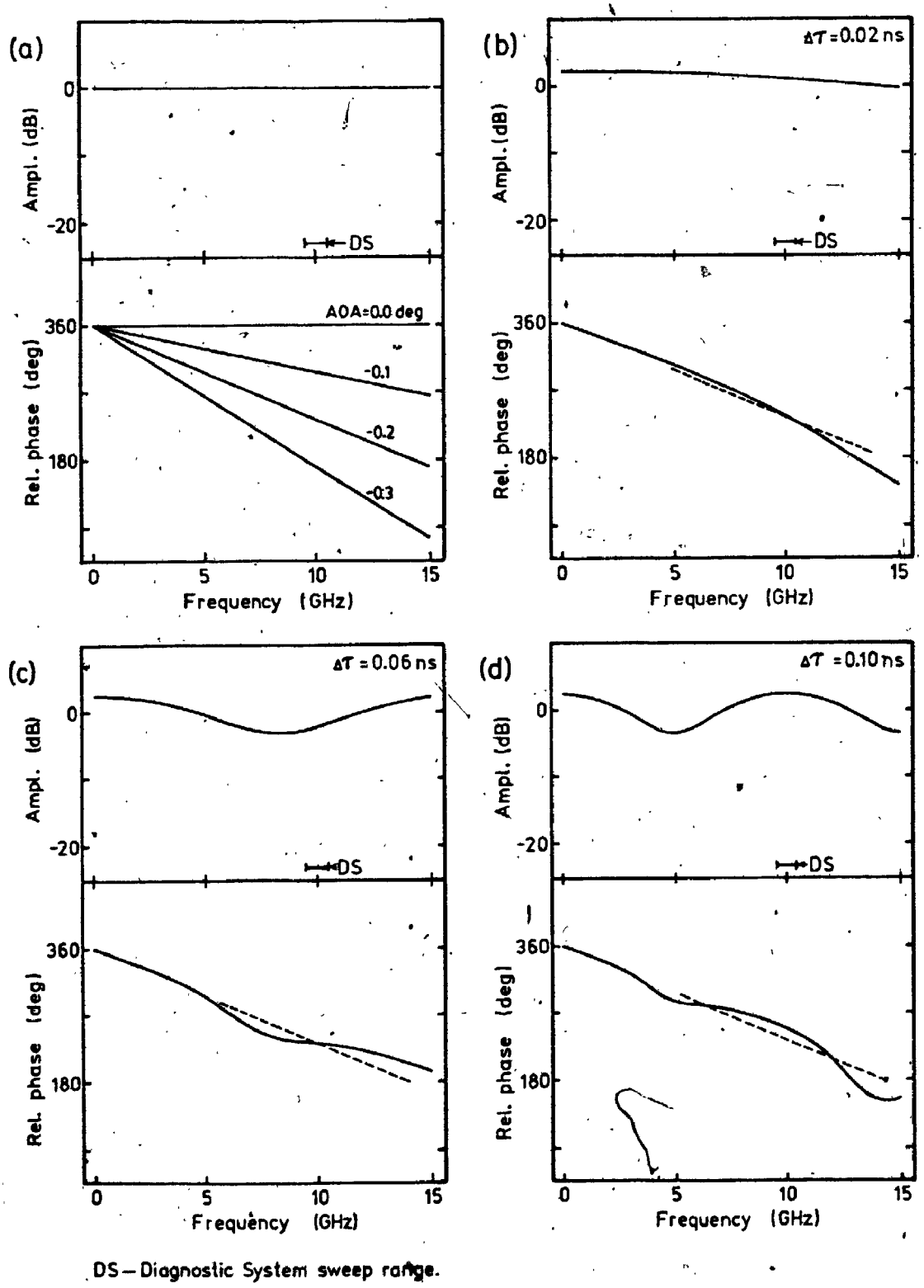

Fig. 4.11 Effects of short delay ray paths on the sweep frequency records; the broken lines show the ideal phase records if the short delay ray path is absent.

The main and second ray AOA's are -0.2 and -0.1 deg respectively. The relative delay of the weaker path is 0.02, 0.06, and 0.1 ns for Figs.4.11(b), (c), and (d) respectively. The results shown in these figures are summarized in Fig. 4.12. Also shown in these figures (broken curves) are the records which ideally should be obtained if the short delay path is absent. It is seen that spurious variations in the phase record slope is introduced by the presence of short delay rays. The intercept values, however, are only mildly affected and in fact give a reasonable estimate of the main ray AOA with an uncertainty of less than $\pm$0.05 deg. For this reason, both the slope and intercept of the filtered phase records are presented in this thesis. Spurious variations in the phase record slope due to short delay ray paths may readily be identified since there will be no corresponding variations in the intercept value. It is also noted that the intercept is related to the main ray AOA by Eq. (3.2) -- a 59.7 deg change in the intercept value at 9.5 GHz corresponds to a 0.1 deg change in the main ray AOA.

The above error bounds are not valid if significant variations in the various ray path parameters occur in the duration of a sweep, or when a strong third ray path with short relative delay is present. The results from the data processing routine may be erroneous in such cases, but these errors can be identified readily from a time plot of the various parameter estimates. The actual ray path parameters may

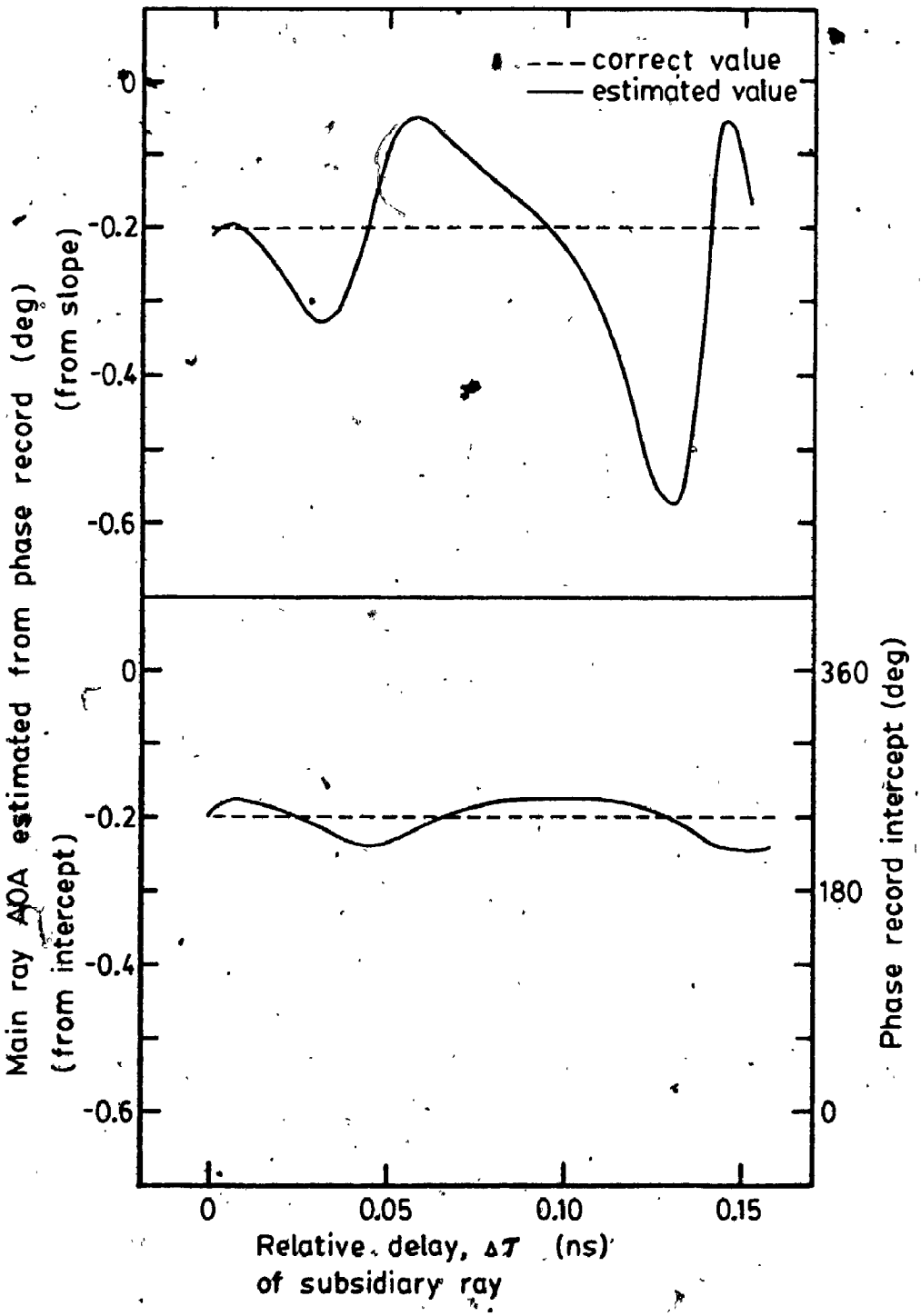

Fig. 4.12 Spurious variations in estimated main ray AOA due to short delay second ray path.

then be obtained by using an iterative process of pattern synthesis as described previously. This latter technique may also be used to obtain more accurate estimates of the ray path parameters when desired. The accuracies obtained using such a technique are better than ±1 dB, ±0.05 nsec, and ±0.05 deg for the relative amplitudes, relative delay time, and the angles-of-arrival respectively.

4.4.2 Data from the Digital Radio Test

The data supplied by the telephone companies on the performance of the digital radio are mainly in the form of low speed paper chart records. The parameters included were the Main AGC, Diversity AGC, and Combined AGC levels of the Protection channel, the Main and the Protection channel Eye Voltages, and the adaptive equalizer Stress Voltage for the Protection channel.

The main information required for the digital radio is an indication of its error probability performance. For this purpose, the eye voltage is a suitable parameter [34], [35]. This voltage indicates the amount of opening in the eye diagram. Without going into excessive detail, an open eye diagram corresponds to an error free digital signal at the output of the demodulator, while a closed eye diagram is an indication of system degradation usually caused by inter-symbol interference [34].

Using the eye voltage as the indication, the chart records from the digital radio test were examined. The

time periods when eye closures occurred were noted. The propagation data obtained during these periods were then isolated for further analysis.

Chapter 5

MICROWAVE PROPAGATION ACROSS THE BAY OF FUNDY - AYLESFORD TO OTTER LAKE

5.1 Introduction

The results from the 1980 propagation experiment are presented in this chapter and are examined with respect to the signal characteristics predicted in Chapter 4. Based on the experimental results, the major aspects of microwave propagation from Aylesford to Otter Lake are discussed.

In order to reduce the data processing to manageable proportions, representative 24-hour periods were selected from the large data base using the available continuous analog records. The resulting data from ten days selected in this way were analysed to produce the ray path characteristics of the two strongest received rays. These characteristics include the main ray amplitude and AOA, and the second ray amplitude and relative delay time. Although detailed discussions are presented only for selected periods containing significant and representative results, it is felt that additional insight may be gained from a cursory examination of the ray path characteristics for the entire period. It is for this purpose that the major ray path characteristics for the entire ten days are included in graphical form in Appendix 6.

5.2 General Experimental Observations

In the first propagation experiment the microwave diagnostic system was operated from 5th September (day of year -- 249) to 3rd November (Day 308). The fact that the period did not correspond to the fading season (which usually extends from May through August) is reflected in the comparatively modest amount of fading activities observed.

A cursory examination of the chart records collected during the experiment was performed on an hourly basis. The general observation is that less than 10 percent of the time exhibits severe fading activities. Furthermore, approximately 90 percent of the observed fading activities occurred during the month of September.

Although numerous equipment problems were encountered during the experiment, a large amount of data was collected. A representative set of data from 10 days was selected as the data base for the 1980 experiment. This includes data collected in the beginning (Day 250), in the middle (Day 258, 259, 260, 263, 264), and towards the end (Day 295, 296, 297, 298) of the experiment.

Each hour is further classified as belonging to one of two categories, namely, non-fading data and fading data. More specifically, the fading data contains all the data from the hours in which fades greater than 10 dB were recorded. In this thesis, such an hour is referred to as a

"Fading Hour". The rest of the data then constitutes the non-fading data base.

Based on the above criterion, a time chart showing the amount of fading activity for the ten selected days was constructed and this is shown in Fig. 5.1. The main feature is that fading was more pronounced in the first half of September. Only one fading hour was observed in the four consecutive days presented for October. These features are, in fact, very representative of the actual situation.

In the total data base of 239 hours, there are 55 fading hours. Propagation conditions associated with non-fading and fading periods are presented in the following sections. It is noted that the amplitude reference (0 dB) is taken as the median amplitude of the main ray calculated from the non-fading data base.

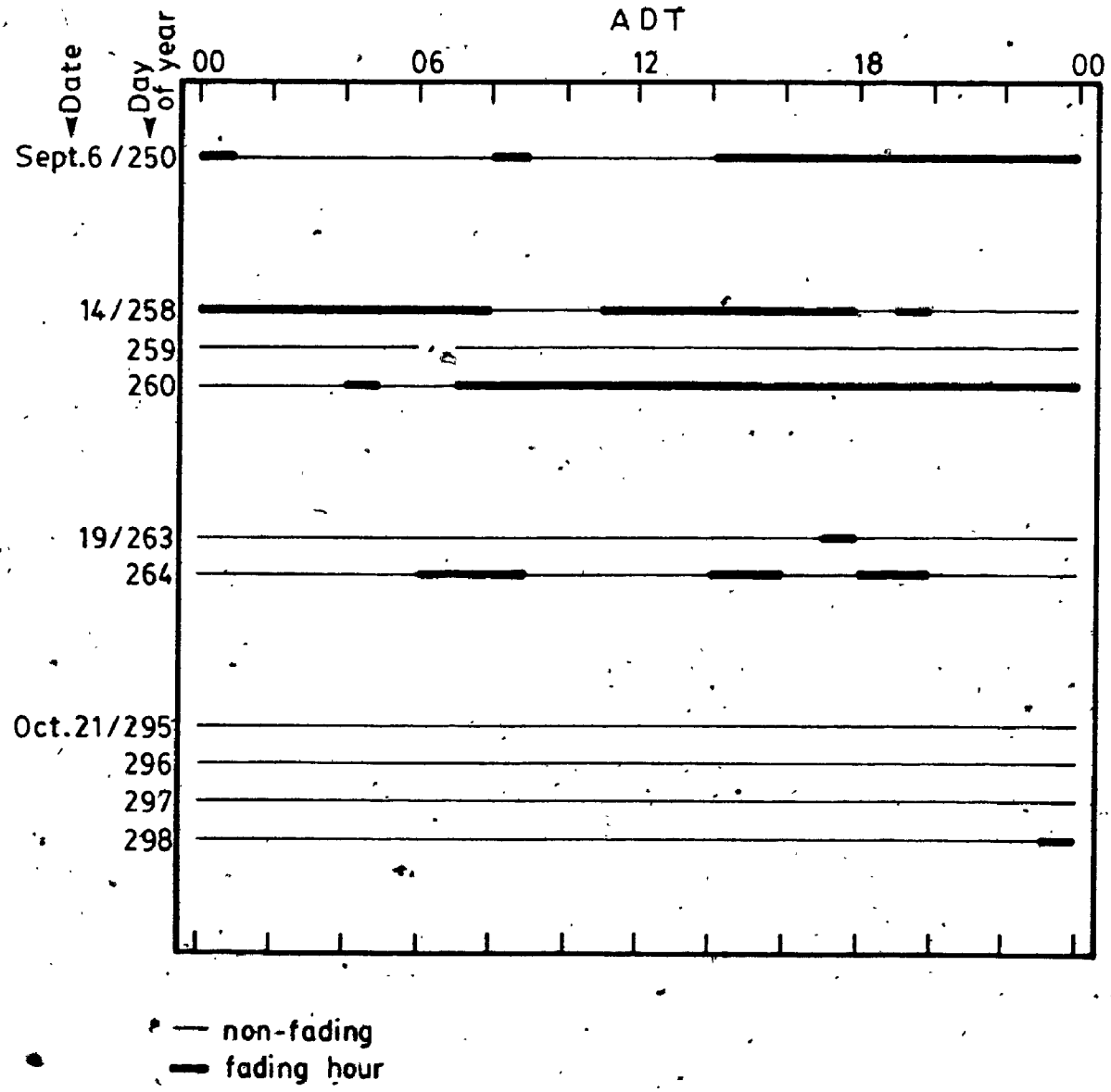

Fig. 5.1 Time chart of selected experimental observations for the 1980 experiment.

5.3 Propagation During Non-fading Periods

5.3.1 Ray Amplitudes and Delay Times

In the ten days selected in the 1980 experiment, six days (259, 263, 295, 296, 297, 298) contain little or no fading (see Fig. 5.1). To illustrate the propagation conditions observed during these periods, the data from Day 295 is used.

A typical sweep frequency record from the diagnostic system is shown in Fig. 5.2 together with the ray path parameters obtained by the pattern synthesis method. Two ray paths are identified. The amplitude and AOA of the main ray are 0.4 dB and -0.27 deg respectively. The corresponding values for the weaker ray (the sea reflected ray) are -11.6 dB and -0.48 deg. The delay time of this ray is 2.95 ns relative to the direct ray. Except for the amplitude of the second ray, the values fit in well with the values predicted in Section 4.2. The reflected ray amplitude of -11.6 dB, however, is considerably higher than the predicted value of -19 dB for a uniform gradient of -40 NU/km.

The various ray path characteristics on Day 295 are plotted in Fig. 5.3 from which several prominent features may be noted. First, the main ray amplitude is very stable with a value of 0 dB. The second ray amplitude, however, has a value that varies between -10 and -25 dB. The delay time of the second ray relative to the main ray is also

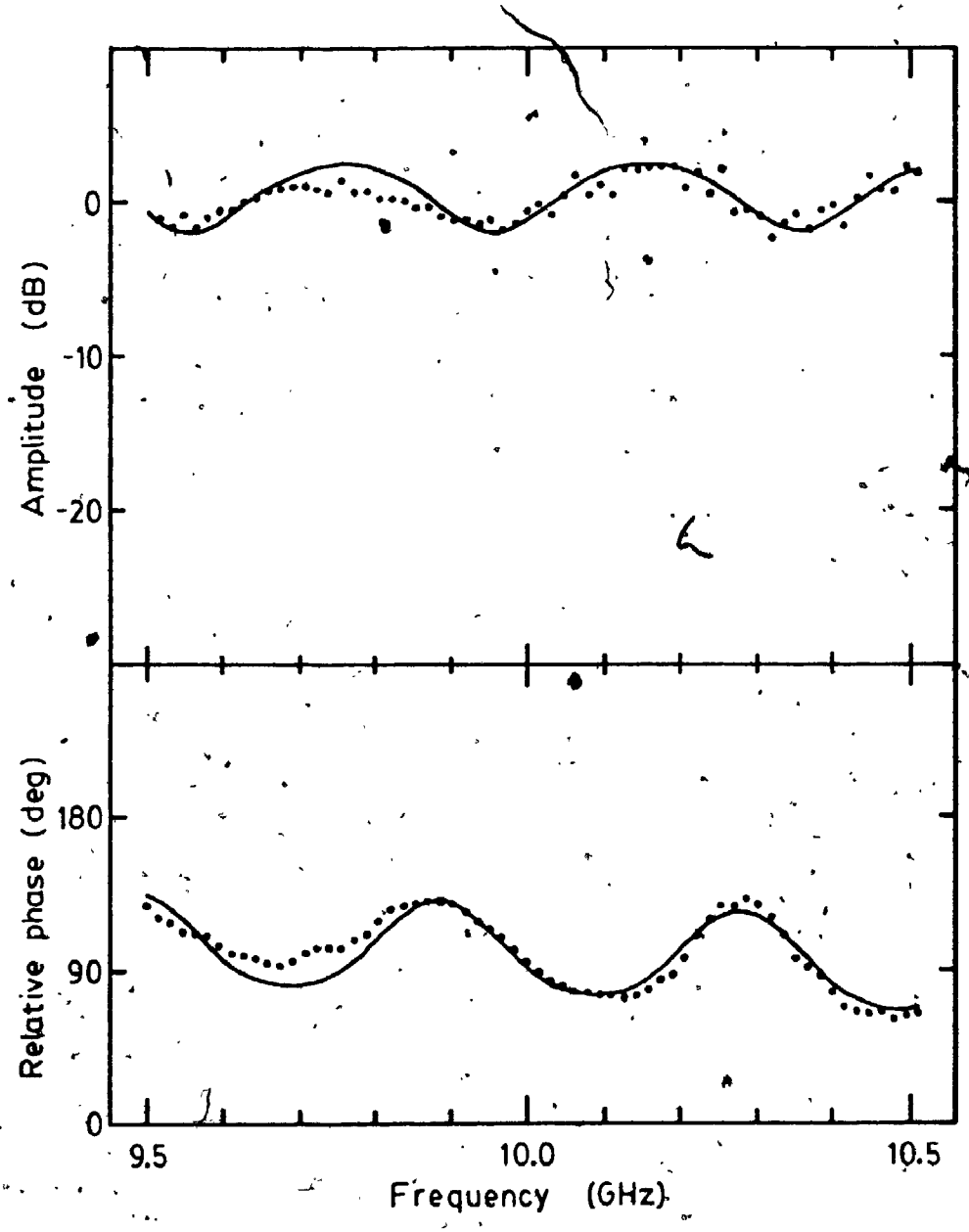

Ampl. (dB)	AOA (deg)	Delay (ns)	
0.4	-0.27	-	
-11.6	-0.48	2.5	— reflected ray

Fig. 5.2 Experimental (dotted) and synthesized data record at 12:00:01 ADT on Day 295.

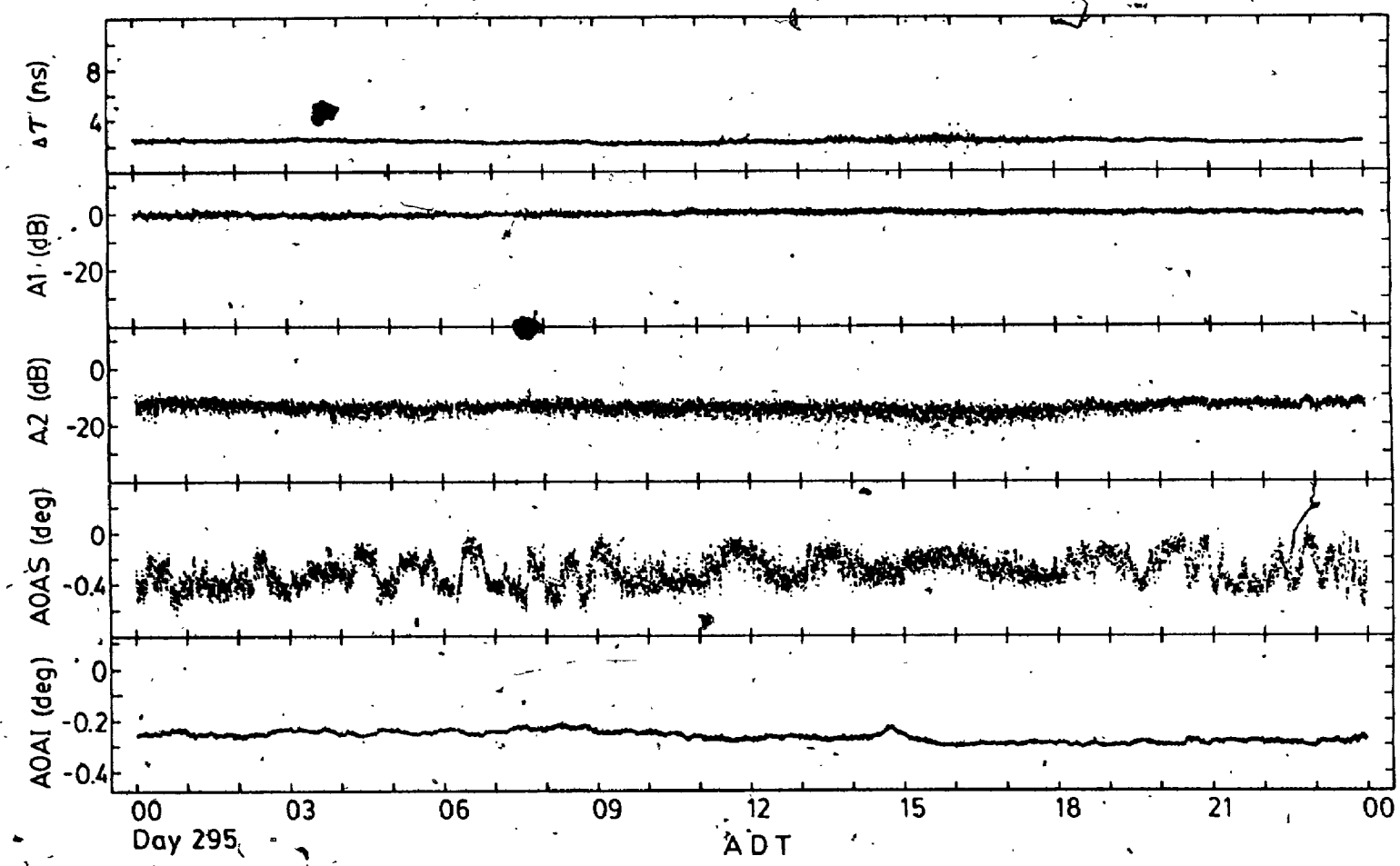

$\Delta\tau$ - relative delay time.
A1/A2 - main (1) and second (2) ray amplitude.
AOAS / AOAI - estimates of main ray AOA from slope (S) and intercept (I).

Fig. 5.3 Ray path characteristics on a non-fading day (295) in the 1980 experiment.

stable with a value of between 2 and 3 ns.

These ray path characteristics occur frequently during non-fading periods and almost identical behaviour was observed for Day 263, 295, 296, 297, 298 (see Appendix 6). The distributions of the main and second ray amplitudes and the delay time were computed for the non-fading data base and these are shown in Figs. 5.4(a) to (c). The ray path characteristics observed on Day 295 are well illustrated in these distribution curves. The median amplitudes of the main and second rays (in this case these correspond to the direct and reflected rays respectively) and the median delay time are 0 dB, -12.6 dB, and 2.3 ns respectively.

The amount of variation in the ray path characteristics is indicated by the standard deviation about the mean values. The standard deviation computed for the direct and reflected ray amplitudes and the relative delay time are 1.3 dB, 2.4 dB, and 0.3 ns respectively. The larger spread in the reflected ray amplitude is noted.

The above experimental values are summarized in Table 5.1 where they are compared with the values predicted in Section 4.2. It is seen that the measured median values of the direct ray amplitude and the delay time correspond well with the predicted values. However, the median reflected ray amplitude of -12.6 dB is more than 6 dB higher than the predicted value of -19 dB.

To explain this large measured value, it is noted that the reflected ray amplitude is controlled by three factors:

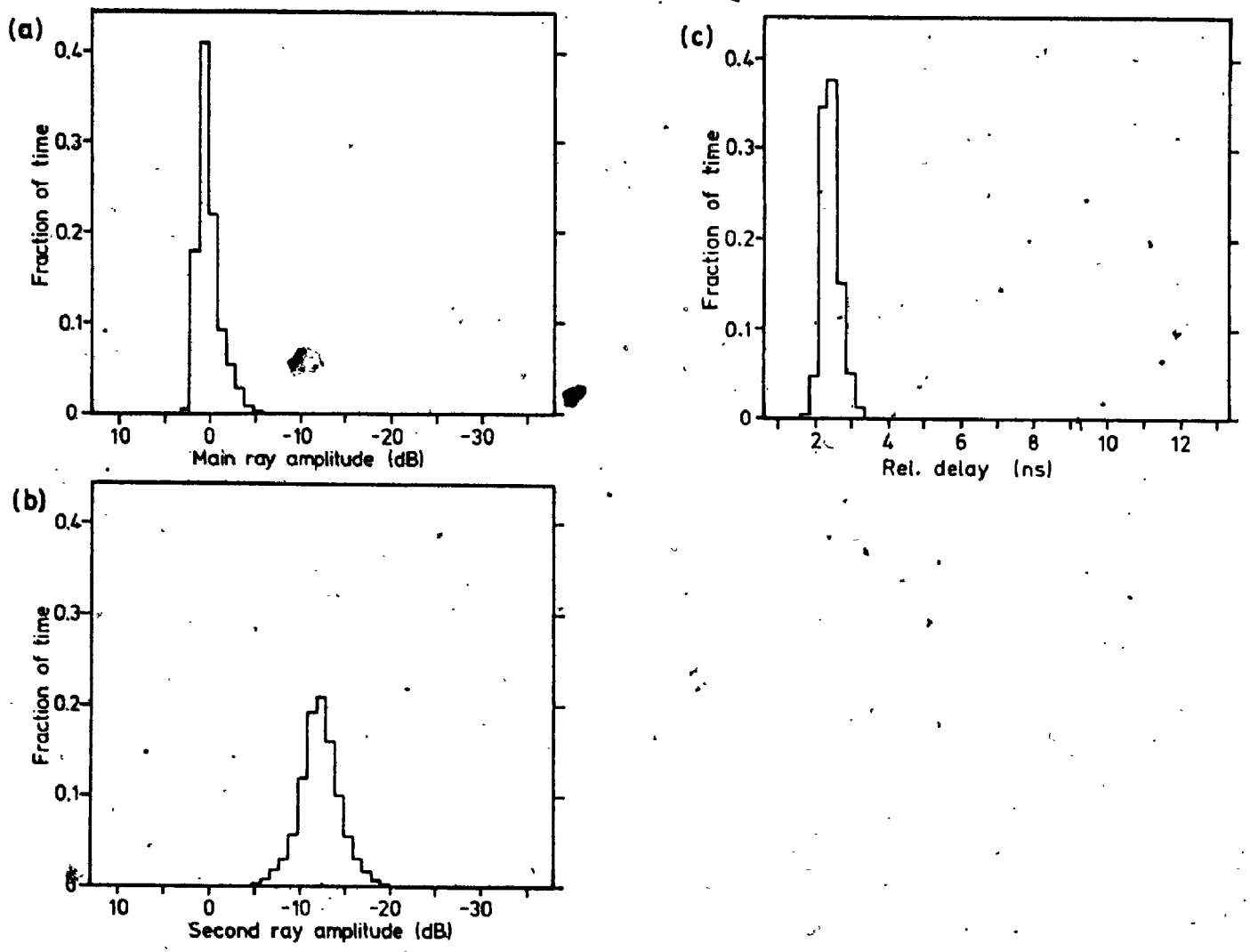

Fig. 5.4 Distributions of the ray amplitudes and relative delay time for the 1980 non-fading data.

Table 5.1 Experimental and predicted ray path characteristics for the 1980 non-fading data

Ray Path Parameter	Predicted value	Experimental	
		median value	standard deviation
Direct Ray			
Amplitude, dB	0.0	0.0	1.3
AOA, deg	-0.29	-	-
Reflected Ray			
Amplitude, dB	-19.0	-12.6	2.4
AOA, deg	-0.53	-	-
Delay, ns	2.5	2.3	0.3

(a) reflection loss, (b) divergence loss, and (c) diffraction loss. In estimating the reflected ray amplitude a perfect sea reflection was assumed, i.e. the reflection loss is zero. The divergence loss due to the curvature of the earth amounts to approximately 3 dB under normal conditions and is included in the ray tracing process. The more significant and uncertain component, however, is the loss due to diffraction by the underlying terrain. In this case, point A (see Fig. 4.2) is the main diffracting structure. In calculating the diffraction loss, an average tree height of 12 m (as used by the telephone companies for the path design) was included. The estimated loss is 16 dB which is entirely due to the tree height (the radius of the first Fresnel Zone at A is 10 m). There is in fact no diffraction loss for a tree height less than 4 m.

An additional point to note is that the path profile data was obtained from contour maps [36] with height intervals of 15.24 m (50 ft). The uncertainties in the actual height of the terrain is again of the order of the first Fresnel Zone radius. These considerations well illustrate the importance of accurate path surveys when diffraction effects are dominant. In the present case, the immediate conclusion is that the actual height of the terrain (including trees) at point A is of the order of 5 m or so less than the value used in the diffraction loss estimation, thus resulting in the low predicted amplitude

of the reflected ray.

5.3.2 Main Ray Angle-of-Arrival

One parameter which has not been considered so far is the main ray AOA. In Section 4.4, it is noted that the presence of a short delay (less than 1 ns) ray path has the effect of causing spurious variations in the slope of the phase record, which would otherwise give the main ray AOA. Such erroneous behaviour is observed in the results for Day 295. The phase record intercept, on the other hand, shows much less contamination due to short delay paths and consequently is used for estimating the main ray AOA.

The distribution of the phase record intercept was computed for the non-fading data base and the results are summarized in Figs. 5.5(a) and (b). Although a calibration of the intercept value versus the absolute AOA is not available due to practical difficulties, it is known that the intercept is linearly related to the main ray AOA (Section 4.4). To relate the intercept value to the actual AOA, an assumption was made that the median value of the intercept corresponds to the expected direct ray AOA for a normal gradient of -40 NU/km. Based on this assumption, the AOA scale and the corresponding N-gradient scale were constructed and these are shown in Figs. 5.3 and 5.5. This approach in interpreting the phase record slope and intercept results is used for both experiments.

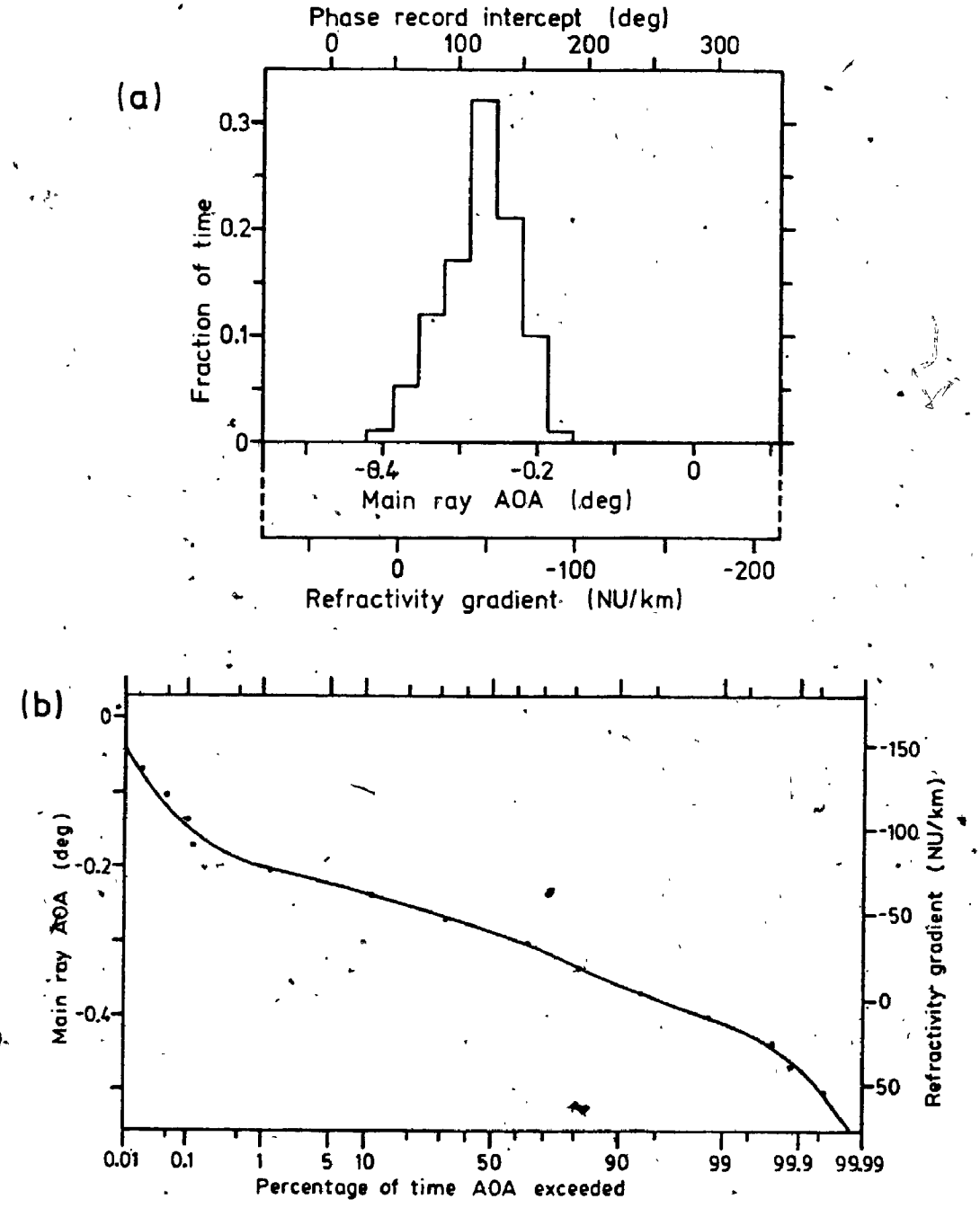

Fig. 5.5 Distribution of the main ray AOA for the 1980 non-fading data.

For the 184 non-fading hours in the 1980 data base, the results in Fig. 5.5 show that the 99.8 % range in direct ray AOA is 0.32 deg. The corresponding 99.8 % range for the refractivity gradient is $-102 < dN/dh < 40$ NU/km, which is equivalent to $2.9 < K < 0.8$.

It is also noteworthy that, based on the above results, the 99.8 % range in delay time of the reflected ray is $1.0 < \Delta\tau < 4.2$ ns (estimated from ray tracing). The experimentally observed 99.8 % range in delay time for the same period is $1.1 < \Delta\tau < 3.3$ ns, which is in fair agreement with the range estimated from the AOA results. These observations suggest that the method of interpreting the phase record intercept to give the main ray AOA is valid. It also serves as evidence that, at least during the non-fading hours, the atmosphere is well represented by a uniform N-gradient model.

5.3.3 Refractivity Gradient Variations

Some insight on variations in the overall N-gradient in the Bay of Fundy may be gained by a close examination of the ray path characteristics given in Appendix 6. In relation to this point, it is noted from Fig. 4.6 that a decrease in dN/dh will cause increases in the reflected ray amplitude, the direct and reflected ray AOA, and the delay time. The converse is also true. Furthermore, because the overall N-gradient is a function of the bulk properties in the atmosphere, its value is not expected to change too

rapidly, say, in time frames of less than a few hours. These features may be used as a means of identifying genuine variations in the N-gradient in the atmosphere.

A good example of these N-gradient variations occurred during the period from 16:00 ADT on Day 259 to 08:00 ADT on Day 260 (see Fig. 5.6). During this period, gradual increases in the amplitude and delay time of the reflected ray, and the AOA of the direct ray, were observed. This appears to have been caused by a gradual increase in the N-gradient (more negative) which preceeds the onset of more rapid fading activities in the latter half of the day (see Appendix 6).

From the ray path parameters, the N-gradient was estimated as approximately normal (-40 NU/km) at 16:00 ADT on Day 295. However, a more negative value of about -80 NU/km appears to have been responsible for the ray path characteristics at 08:00 ADT. The change in N-gradient of -40 NU/km occurred over a time span of close to 10 hours. Although variations in the N-gradient of this magnitude were not frequently observed during the experiments, possible large variations due to seasonal climatic changes should not be disregarded.

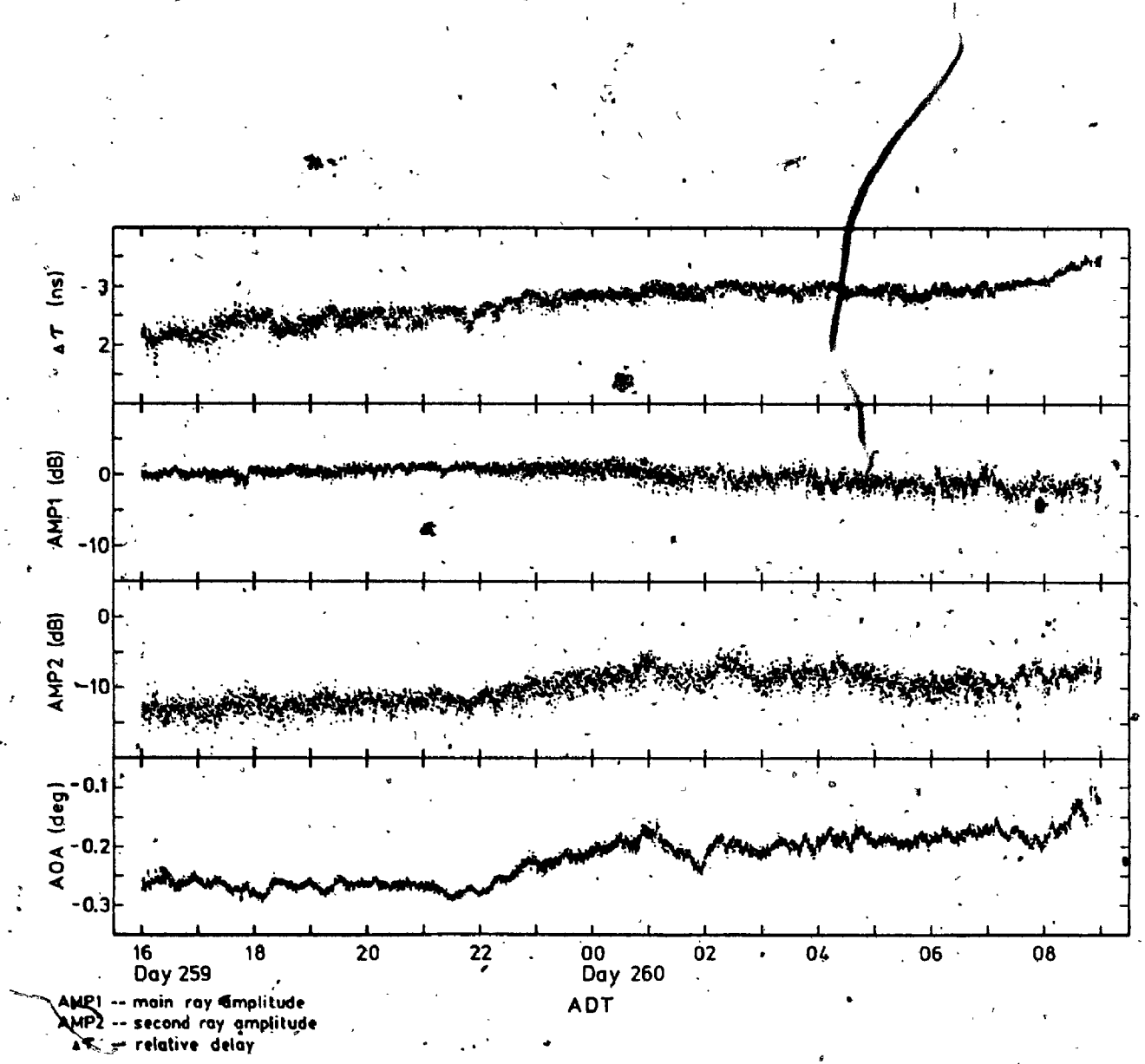

Fig. 5.6 Variations in ray path characteristics due to a suspected variation in the overall refractivity gradient.

5.4 The Sea Reflection

5.4.1 Reflection Coefficient

In the results presented so far, the sea reflected ray is observed to be rather persistent in its presence as an important component of the received signal. The properties of this reflected ray are discussed in this section.

In Chapter 2, it was noted that the resultant scattered field from a rough surface (in this case the sea surface) is made up of a specular reflection and a diffuse scattering component. The specular reflection component is first examined. The reflection phenomenon is quantified by the Reflection Coefficient R_s such that

$$R_s = \rho_s D R_o \tag{5.1}$$

where ρ_s is the scattering coefficient for the specular component, D is the divergence coefficient due to reflection from a curved earth, and R_o is the reflection coefficient of a smooth sea. The parameter R_o is a function of the angle of reflection (sometimes called the grazing angle) and of the material properties of the reflecting surface and is given by [24]

$$R_o^+ = \frac{Y^2 \sin\gamma - (Y^2 - \cos^2\gamma)^{\frac{1}{2}}}{Y^2 \sin\gamma + (Y^2 - \cos^2\gamma)^{\frac{1}{2}}} \tag{5.2}$$

and

$$R_o^- = \frac{\sin\gamma - (Y^2 - \cos^2\gamma)^{\frac{1}{2}}}{\sin\gamma + (Y^2 - \cos^2\gamma)^{\frac{1}{2}}} \tag{5.3}$$

where R_o^+ and R_o^- are the reflection coefficients for

vertical and horizontal polarizations respectively, and γ is the angle of reflection. Y is the normalized admittance of the medium given by

$$Y = \left(\frac{\varepsilon_r}{\mu_r}\right)^{\frac{1}{2}} \qquad (5.4)$$

where ε_r and μ_r are the relative complex dielectric constant and the relative magnetic permeability of the medium. The value of R_o therefore is complex and is a function of the wavelength and the reflection angle γ. The magnitude and phase of R_o is shown in Fig. 5.7 as a function of λ and γ. On most microwave LOS paths (the present one included), γ is usually of the order of 0.5 deg or less, thus giving a value of $R_o = -1$ for both polarizations.

As for the Divergence Coefficient D, this is a function of the earth curvature and the link geometry, and is given by [24]

$$D \simeq \left[1 + \frac{2r_1 r_2}{a_e.(r_1 + r_2).\sin\gamma}\right]^{-\frac{1}{2}} \qquad (5.5)$$

where r_1 and r_2 are the distances from the reflection point to the end terminals of the path, and a_e is the effective earth radius. The divergence loss is taken into account in the ray tracing technique used in this work. For the Aylesford - Otter Lake propagation path under normal refractivity conditions, the value of D calculated using Eq. (5.5) is 0.69. This corresponds to a divergence loss of approximately 3 dB.

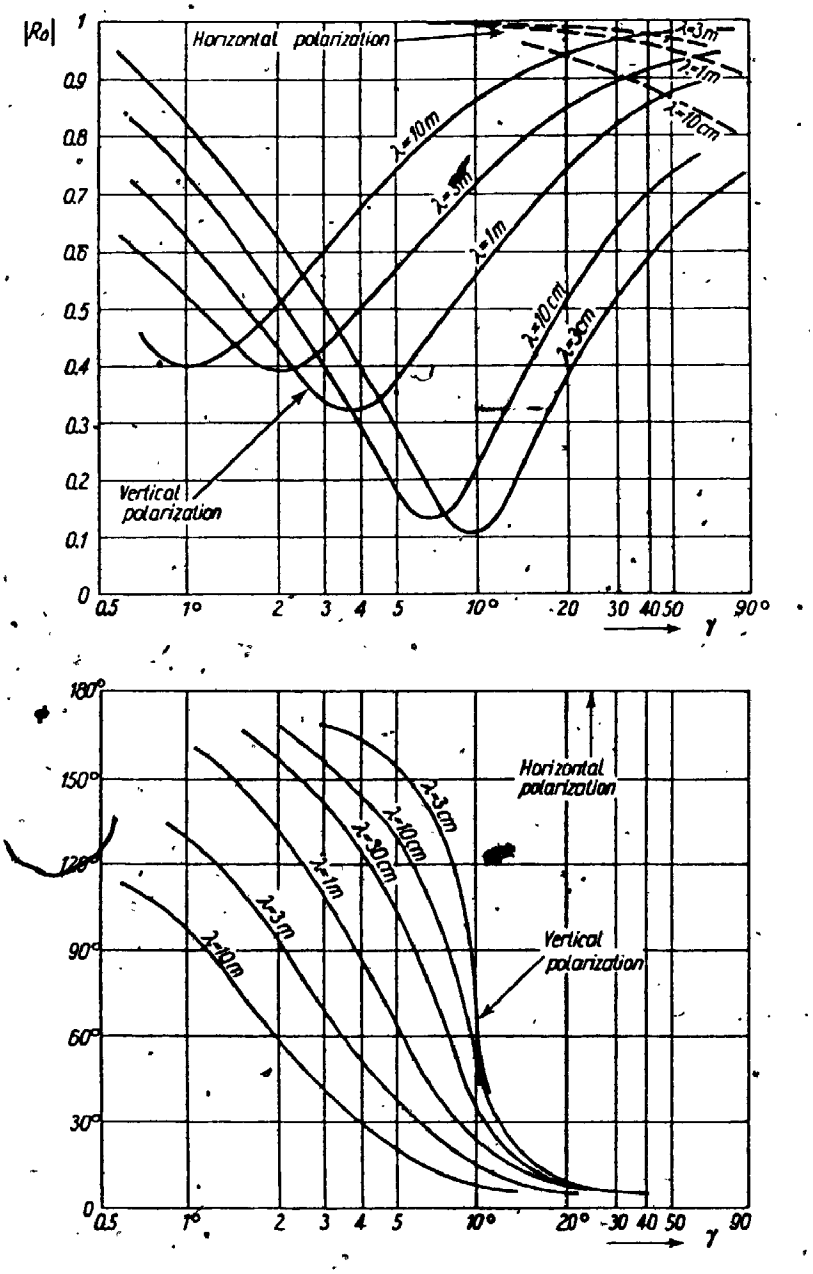

γ---reflection angle

Fig. 5.7 The magnitude $|R_o|$ and phase ϕ of the reflection coefficient of a very smooth sea. $\varepsilon/\varepsilon_o = 80$, $\sigma = 4$ mho/m. [24].

5.4.2 The Reflecting Area

Before discussing the scattering coefficient ρ_s, it is useful to gain an idea of the dimensions of the area responsible for the specular reflection. This is the region that is bounded by the first Fresnel Ellipse. The dimensions of this ellipse is given by Eqs. (2.22) and (2.23). For the Otter Lake - Aylseford path, the reflection point under normal conditions is located approximately 42 km from Otter Lake and the reflection angle is 0.25 deg. At a frequency of 10 GHz, the lengths of the semi-axes of the first Fresnel Ellipse are given by

$$F_{1X} \simeq \frac{0.69}{\sin(0.25)} \left[\frac{0.03 \times 42 \times 38 \times 10^6}{80 \times 10^3}\right]^{\frac{1}{2}} = 3.9 \text{ km} \quad (5.6)$$

and

$$F_{1Y} \simeq \left[\frac{0.03 \times 42 \times 38 \times 10^6}{80 \times 10^3}\right]^{\frac{1}{2}} = 24.5 \text{ m} \quad (5.7)$$

where X and Y denote the dimensions parallel and perpendicular to the path respectively. It should be noted that the axes of the ellipse are $2F_{1X}$ and $2F_{1Y}$ in length.

5.4.3 Effects of Sea Surface Roughness

To calculate the reflection coefficient using Eq. (5.1), one requires the scattering coefficient ρ_s for the area bounded by the first Fresnel Ellipse. ρ_s is a function of the roughness or irregularity of the reflecting surface. By assuming a Gaussian model for the surface height distribution, Beckmann and Spizzichino [24] derived

the value of ρ_s as

$$\rho_s^2 = \exp -(\Delta\phi)^2 \tag{5.8}$$

where ρ_s represents the root-mean-square (r.m.s.) value of the scattering coefficient. The parameter $\Delta\phi$ is given by

$$\Delta\phi = \frac{4\pi.\Delta h.\sin\gamma}{\lambda} \tag{5.9}$$

where Δh is the standard deviation of the height of the surface irregularities and γ is the reflection angle.

The variation of the scattering coefficient (expressed in decibels) versus Δh and γ is shown in Fig. 5.8 for a frequency of 10 GHz. For the sea surface, Δh is interpreted as the standard deviation of the wave height and it was suggested that [24]

$$h_M = 4.66\ \Delta h \tag{5.10}$$

where h_M is the maximum observed wave height.

The sea state, and therefore the wave height, is dependent on various factors such as the wind speed and ocean currents and thus is highly variable. A commonly used numerical scale for measuring sea state is the World Meteorological Organization Code 75 and this is shown in Table 5.2 [37]. Furthermore, an estimate of the percentage occurrence of wave height for the ocean as a whole is given in Table 5.3 [37]. It is observed that the wave height exceeded for 50 % of the time is approximately $h_M' = 1.4$ m

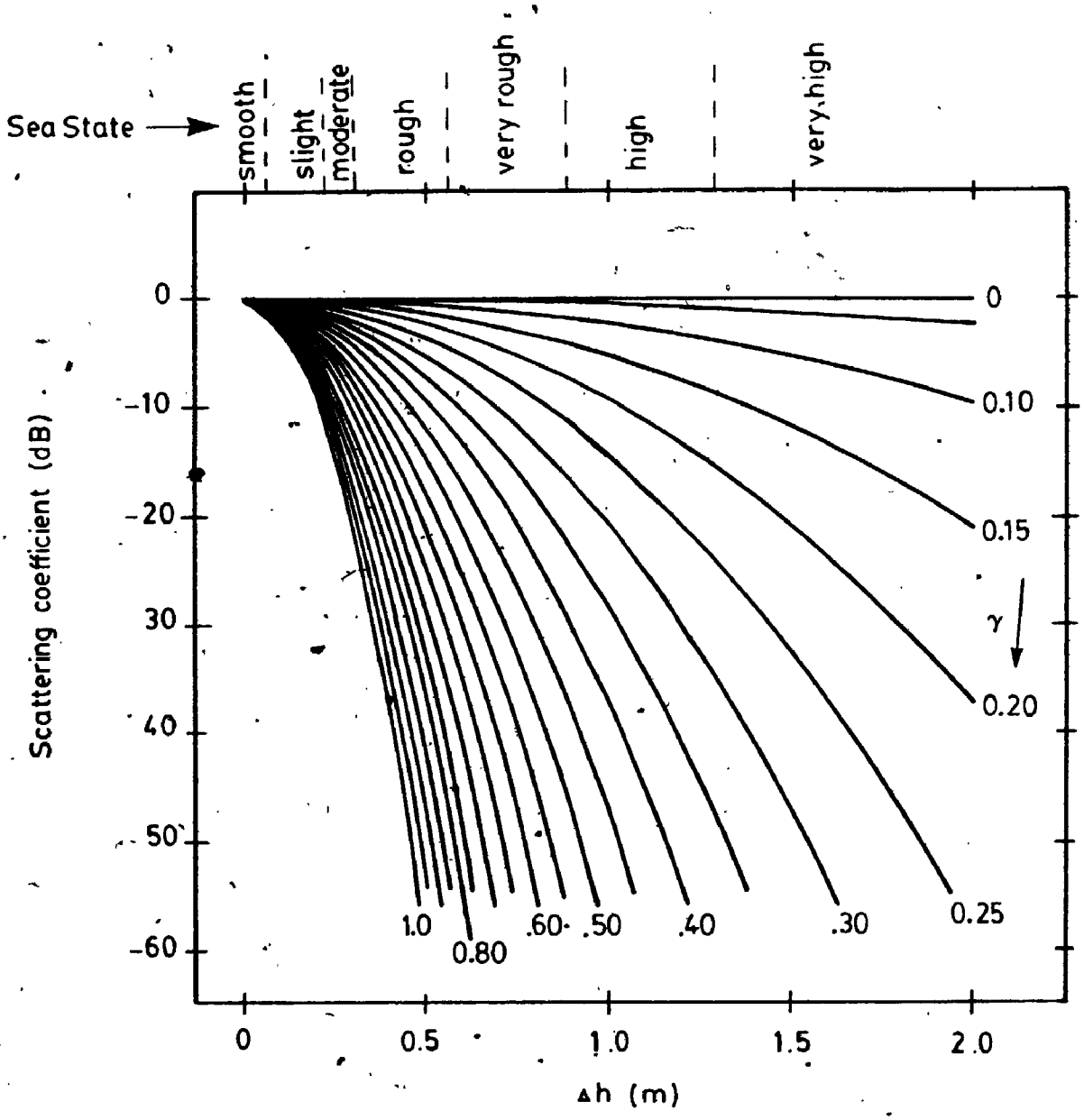

γ ...reflection angle (deg)
Δh... standard deviation of wave height

Fig. 5.8 The scattering coefficient as a function of Δh for different values of γ at a frequency of 10 GHz.

Table 5.2 World Meteorological Organization (WMO) Sea-state Scale [37]

Sea-state number	WMO Code 75 wave height (m)	Description
0	0	Calm
1	0 - 0.1	Smooth
2	0.1 - 0.5	Slight
3	0.5 - 1.2	Moderate
4	1.2 - 2.4	Rough
5	2.4 - 4.0	Very rough
6	4.0 - 6.1	High
7	6.1 - 9.1	Very high
8	9.1 - 13.7	Precipitous
9	over 13.7	Confused

Table 5.3 Percentage occurrence of wave heights for the ocean as a whole [37]

Wave height (m)	Frequency of occurrence, %
0 - 0.9	20
0.9 - 1.2	25
1.2 - 2.1	20
2.1 - 3.7	15
3.7 - 6.1	10
Over 6.1	10

(equivalent to $\Delta h = 0.3$ m).

For reflection angles of between 0.25 and 0.5 deg under normal refractivity conditions, Fig. 5.8 then gives the median value of the scattering coefficient in the range from -2 to -8 dB. Since $|R_o| = 1$ for a smooth sea, the median scattering coefficient is also the median value (negated) of the reflection loss for the sea reflection.

The effect of a change in sea state on the reflection loss may be illustrated by considering a rough sea with the wave height increased to $\Delta h = 0.5$ m. The reflection loss in this case is seen to increase to the range of 4 to 16 dB depending on the grazing angle. A case of a decreased reflected ray amplitude due to a rough sea appears to have occurred on Day 297 (see Appendix 6). The reflected ray amplitude was depressed from its normal value by more than 5 dB in the afternoon. Since the decreased amplitude was not accompanied by changes in the other ray path characteristics, it does not appear that the change was caused by atmospheric effects. The explanation that the decreased amplitude was caused by a rough sea is supported by an entry of "windy" in the log-book of the experiment for the particular day (condition observed at the Otter Lake site). In addition, average and maximum wind speeds of 22.5 km/h and 30 km/h were recorded at a nearby weather station located at Saint John Airport, compared with the monthly average wind speed of 13.1 km/h.

The effect of wave height variations on the reflected ray amplitude usually is not observed in isolation but is superimposed on changes due to other causes such as N-gradient variations. For example, a change in the refractivity gradient will cause variations in the path clearance of the reflected ray, as well as a change in the reflection angle and thus the reflection loss. The individual effects therefore are not observed in isolation.

5.4.4 Diffuse Scattering Component

Thus far, the emphasis has been placed on the specular reflection component. It appears that the observed behaviour of the reflected ray is quite well accounted for by the specular component alone. It is noted that for the diffuse scattering component, we have

$$R_d = \rho_d R_o \qquad (5.11)$$

where R_d and ρ_d are the reflection coefficient and scattering coefficient for the diffuse component, and R_o is the reflection coefficient of a smooth surface. The value of ρ_d was suggested to lie within the range of 0 to 0.35 [24]. When observed at a single frequency, the effect of the diffuse component is to produce rapid fluctuations in the reflected ray. Since the direct and reflected ray amplitudes are obtained from sweep frequency data, the effect of the diffuse component (which has random phase) is expected to be averaged out within a sweep and consequently

is not expected to affect the estimated ray amplitudes.

5.5 Propagation During Fading Periods

5.5.1 Results on Day 250

Most of the fading activities in the ten selected days occurred on Days 250, 258, and 259 (see Fig. 5.1). The results from Days 250 and 258 are used to illustrate the mechanisms responsible for fading on the Aylesford - Otter Lake path.

The ray path characteristics for Day 250 are plotted in Fig. 5.9. During the first half of the day, the delay time decreases slowly from 3.5 ns to less than 2 ns at noon. The reflected ray amplitude also shows a similar decrease. The direct ray does not exhibit a similar decrease but mild fading of a few decibels is observed. An examination of the individual sweep records reveals that the mild fading was caused by the presence of a short delay (less than 0.5 ns) and weak ray path. The short delay ray path is suspected to be of atmospheric origin. Unfortunately, as described in Chapter 4, the ray path characteristics of such short delay rays are outside of the ranges resolvable by the experimental equipment due to a finite frequency sweep range. Its presence, however, is confirmed by examining the behaviour of the slope and intercept of the phase record. Once again, spurious

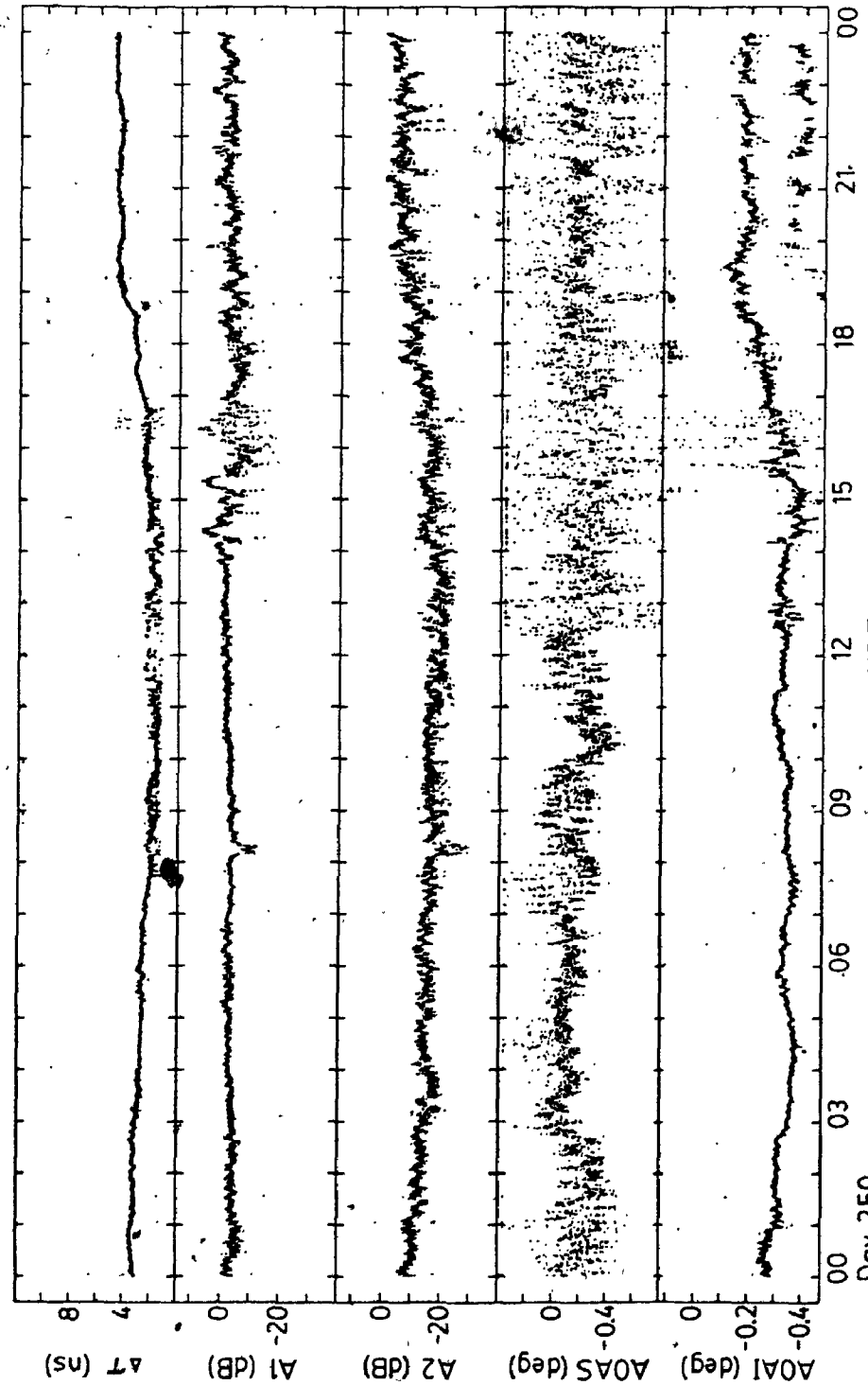

Δτ - relative delay time.
A1/A2 - main (1) and second (2) ray amplitude.
AOAS / AOAI - estimates of main ray AOA from slope (S) and intercept (I).

Fig. 5.9 Ray path characteristics on a fading day (250) in the 1980 experiment.

variations in the phase record slope is observed which was not caused by genuine variations in the main ray AOA.

Apart from the short delay rays, the decrease in the amplitude and delay time of the reflected ray from 00:00 to 12:00 ADT suggests an increasing refractivity gradient (more negative). This preceeded the fast and substantial fading which started at 14:00 ADT and continued through midnight.

Two different types of fading behaviour may be observed during the above period. The first type occurred from 14:00 to 17:00 ADT. The reflected ray amplitude and delay time are not much different from the normal values. However, the main ray path shows rapid and substantial fading and enhancement. These are attributed to the presence of a large amplitude short delay atmospheric ray path. This observation is not unique and was more frequently observed in the 1981 experiment. Detailed discussions of these atmospheric ray paths are delayed to Chapter 6 since they are better illustrated by the 1981 results. For the present, it is noted that the additional ray path was caused by the presence of an atmospheric layer occurring at a height such that both antennas are within the layer.

A different type of fading mechanism seems to be operative from 17:00 ADT to midnight on Day 250. The amount of fading of the direct ray is slightly reduced compared with the preceeding period. At the same time, the

reflected ray shows an increase in amplitude of nearly 10 dB and at times even exceeds the direct ray in amplitude to become the main ray path. This latter behaviour is well illustrated by the AOA value as indicated by the phase record intercept from 20:00 ADT to midnight. Recalling from Chapter 3 and 4 that the AOA obtained from the phase record by the analysis routine is that of the stronger (main) ray, one observes that during the time period the main AOA indicates two distinct values. The values of -0.17 and -0.4 deg correspond to the AOA of the direct and the reflected rays respectively.

In addition to the amplitude and AOA characteristics, a significant and gradual increase in the delay time from 2.5 to 5 ns is observed between 16:00 and 18:00 ADT, after which the delay time is stable at approximately 5 ns.

Several sweep frequency records were examined in detail and two representative ones are shown in Figs. 5.10 and 5.11 together with the ray path parameters obtained by pattern synthesis. The record shown in Fig. 5.10 for 18:04:56 ADT shows that the direct ray has a reduced amplitude of -5 dB but an approximately normal AOA of -0.23 deg. For the reflected ray, increases in both the amplitude and delay time are observed. More extreme behaviour is shown in Fig. 5.11 for 21:00:06 ADT when a large reflected ray amplitude is accompanied by elevated AOA values and a delay time of 4.7 ns.

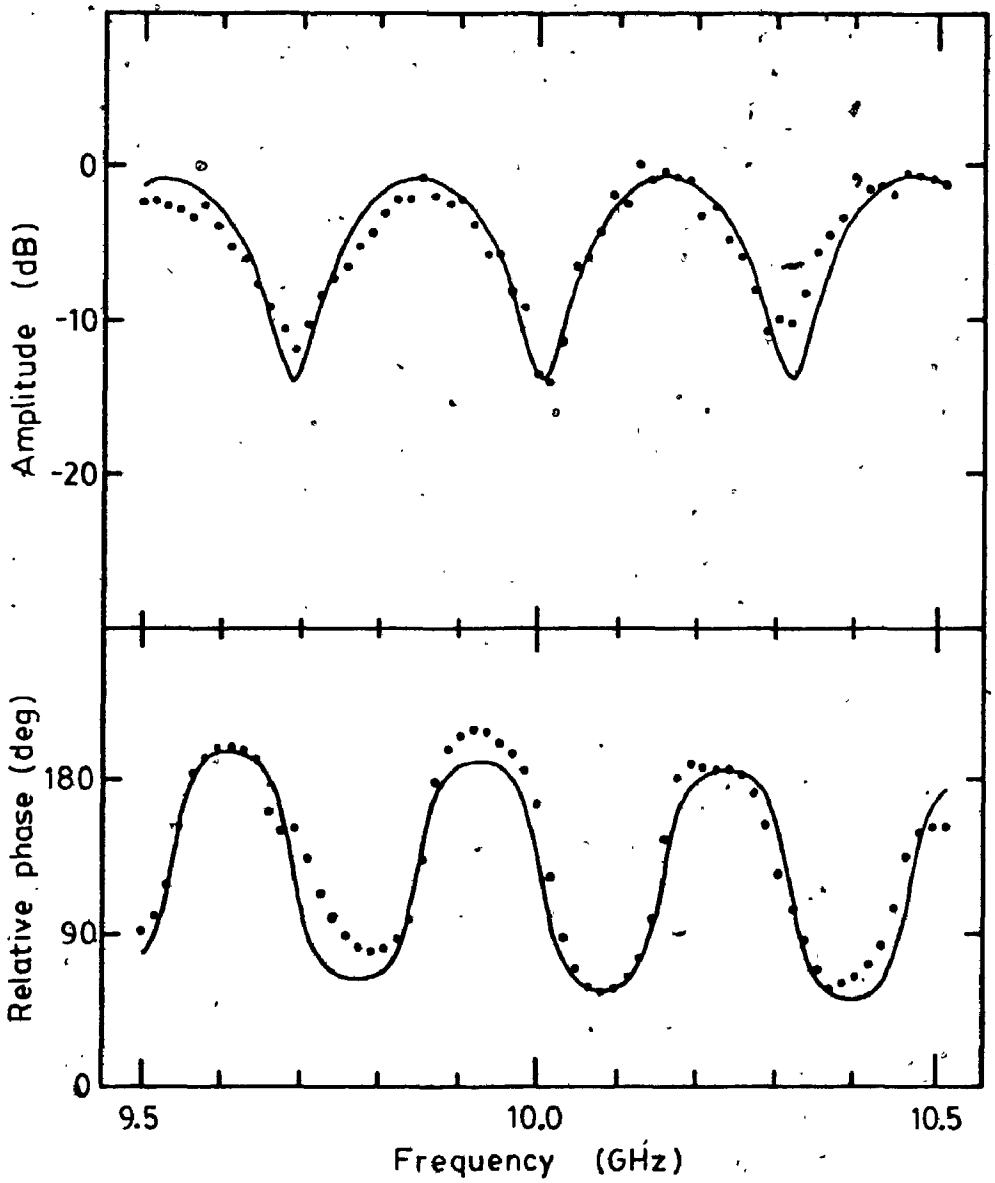

Ampl.(dB)	AOA (deg).	Delay (ns)	
-5.1	-0.23	-	
-9.0	-0.52	3.3	— reflected ray

Fig. 5.10 Experimental (dotted) and synthesized data record at 18:04:56 ADT on Day 250.

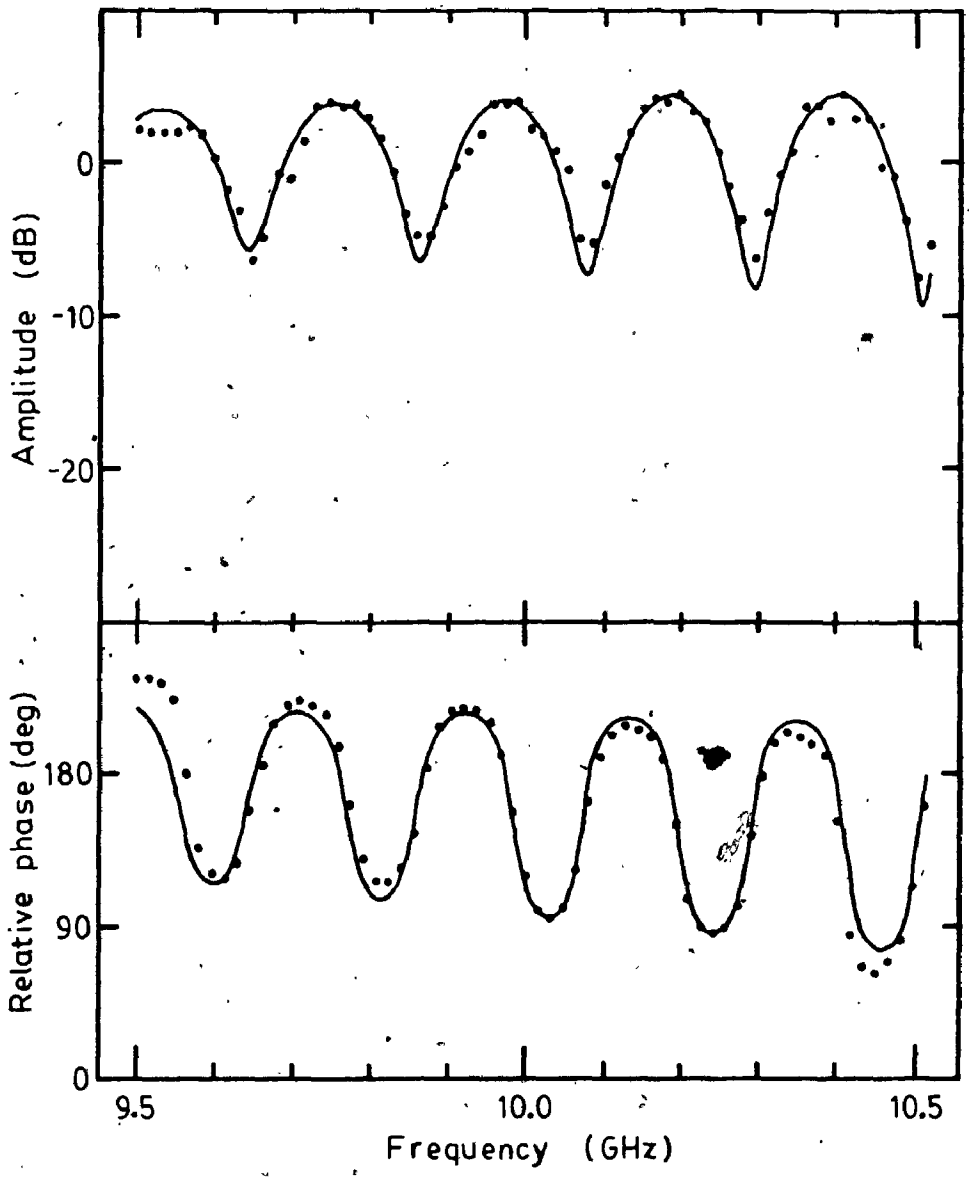

Ampl. (dB)	AOA (deg)	Delay (ns)	
-4.8 → -4.5 *	-0.17	-	
0.1	-0.41	4.7	— reflected ray

* amplitude of direct ray changing during sweep.

Fig. 5.11 Experimental (dotted) and synthesized data record at 21:00:06 ADT on Day 250.

These ray path characteristics are consistent with an atmospheric layer occurring below the antennas. To illustrate the point, an atmospheric layer with parameters $\Delta N = -15$ NU, $\Delta h = 100$ m, and $h_o = 150$ m is used. The ray paths under such conditions are shown in Fig. 5.12. The effect of the layer on the main ray is to decrease the amplitude (radio-hole effect) and to raise the AOA. As for the reflected ray, the increase in amplitude is explained by the increased clearance at the diffraction point (by approximately 4 m or $0.5F_1$). Furthermore, the delay time is increased substantially due to an enhanced refractive index below the layer. These results are summarized in Table 5.4.

From the above discussions, it is noted that the ray path characteristics before 17:00 ADT are associated with a layer at a height such that both antennas are within the layer boundaries, while those after 19:00 ADT are associated with a layer below the antennas. It therefore appears that the layer descended in height during the intervening period. The explanation appears to be valid as illustrated by the gradual increase in the delay time, the reflected ray amplitude, and the direct ray AOA.

Further evidence supporting the presence of a layer is obtained from the meteorological data recorded at the weather station at Saint John Airport (elevation 109 m above MSL) located 10 km south-west of the Otter Lake antenna site. The hourly temperature and wind speed

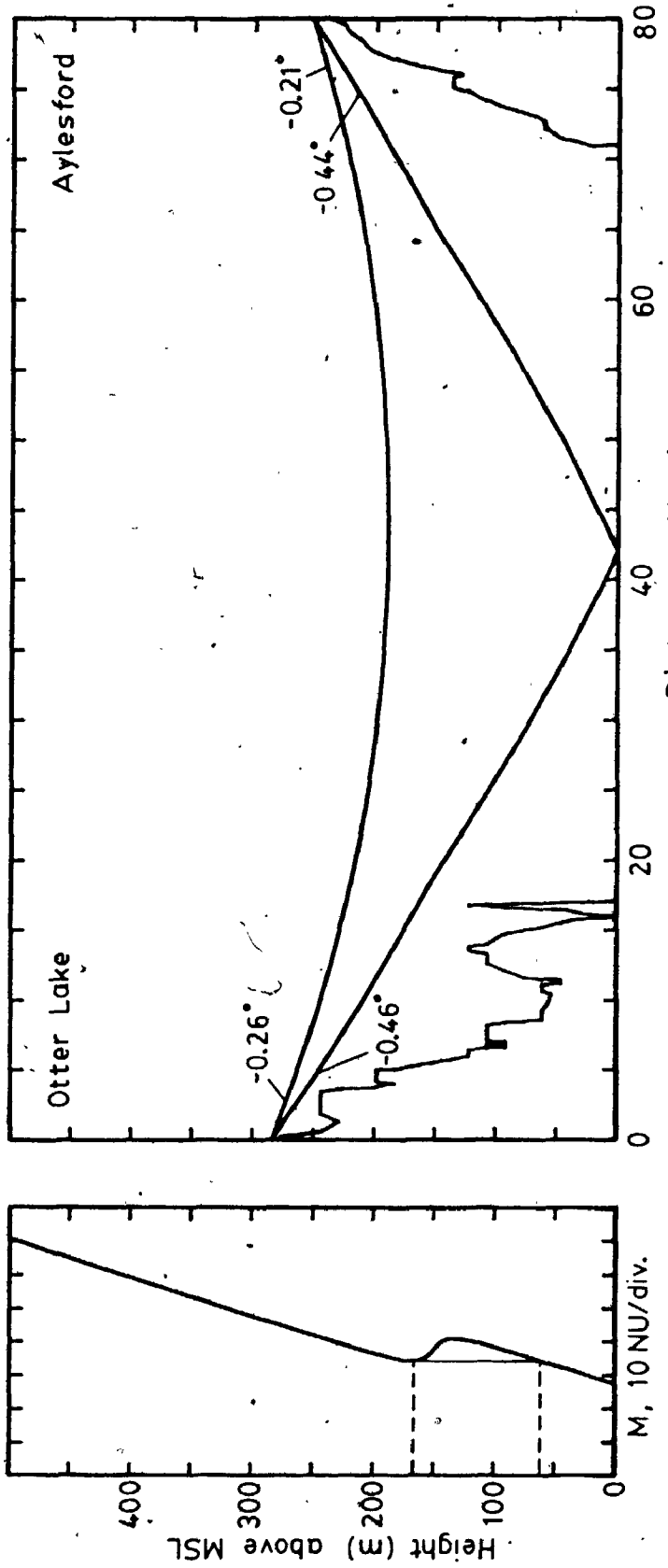

Note. 1) Basic N-profile: $N_o = 340$ NU, $dN/dh = -40$ NU/km
2) Atmospheric layer: $\Delta N = -15$ NU, $\Delta h = 100$ m, $h_o = 150$ m

Fig. 5.12 Propagation on the Aylesford - Otter Lake path when an atmospheric layer is present below the antennas.

Table 5.4 Comparison of experimental results and ray path parameters estimated with ray tracing for a layer present below the antennas

Ray Path Parameter	Experimental Day 250 18:04:56 ADT	Experimental Day 250 21:00:06 ADT	Ray Tracing with duct
Direct ray			
Amplitude, dB	-5.1	-4.7	-2.7
AOA, deg	-0.23	-0.17	-0.26
Reflected ray			
Amplitude, dB	-9.0	0.1	-4.0
AOA, deg	-0.52	-0.41	-0.46
Rel. delay, ns	3.3	4.7	4.8

Note: 1) AOA's at Otter Lake

2) reflected ray amplitudes are estimated assuming that the experimental median amplitude of -12.6 dB is the value for 4/3 - earth.

3) duct parameters: $\Delta N = -15$ NU
$\Delta h = 100$ m
$h_o = 150$ m

through the day are shown in Fig. 5.13. The onset of rapid fading at 14:00 ADT is marked by the increase in temperature in the afternoon, which is followed by a rapid decrease of almost 7° C in 6 hours . The stable layer at 19:00 ADT also correlated well with the wind speed which decreased gradually to calm conditions at 21:00 ADT. Both these conditions are favourable to the formation of atmospheric layers.

At this point it is important to note that a model of an atmospheric layer which is horizontally uniform, with well defined boundaries and well behaved values of dN/dh, is at best a simplified picture of the real situation. However, it is seen that the use of such a model does allow the gross and important features of the received ray paths to be explained. Temporal variations of the actual ray path parameters are readily introduced by localized turbulent air masses. Descriptions of such turbulent structures in the form of thermal plumes may be found in McAllister et al. [38]. These thermal plumes are reported to have horizontal dimensions that range from 70 to 840 m. The occurrence of such turbulent structures therefore can have significant effects on the ray path characteristics, recalling that the radius of the first Fresnel zone at mid path is of the order of only 25 m.

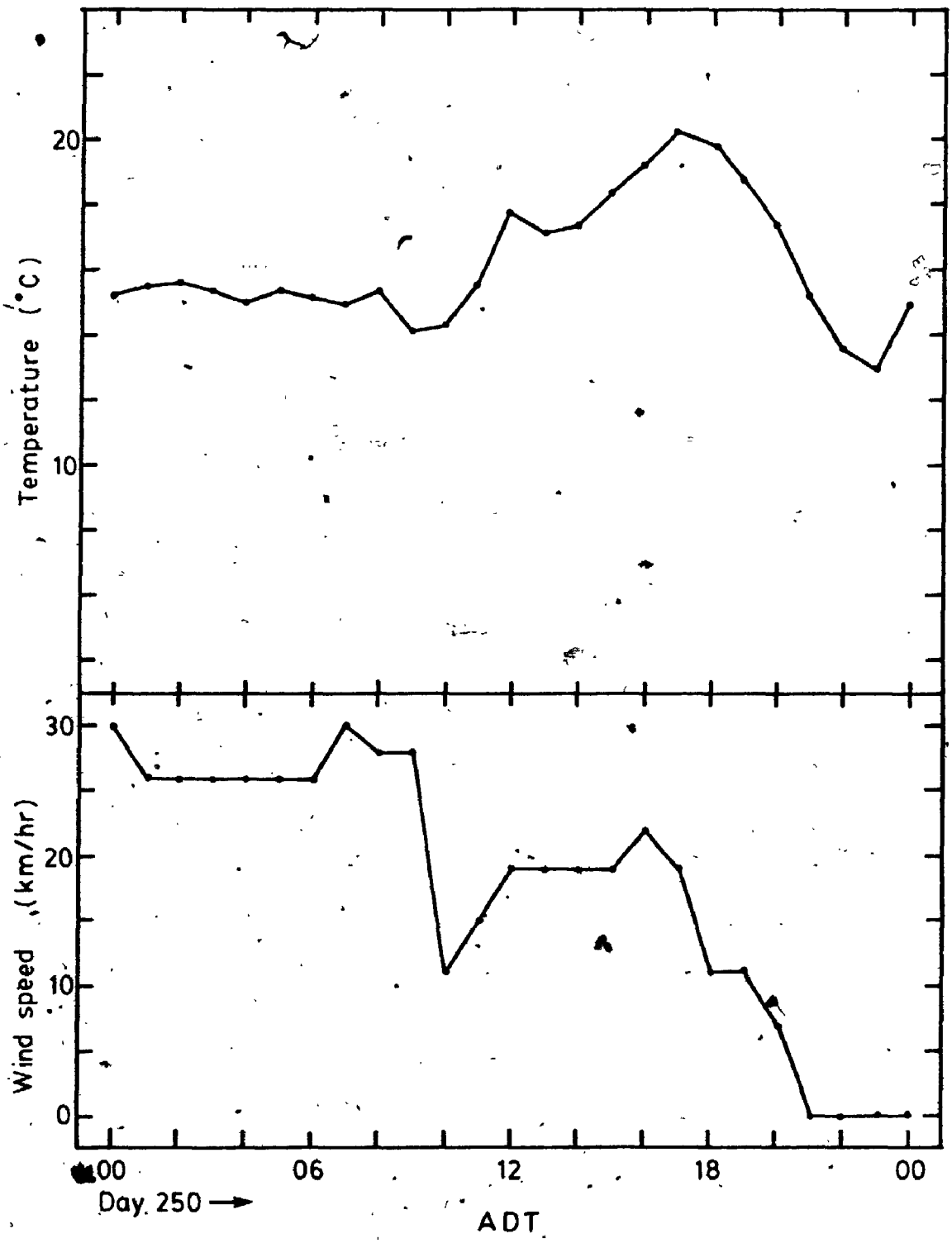

Fig. 5.13 Temperature and wind speed observed at Saint John Airport on Day 250.

5.5.2 Results on Day 258

The fading observed on Day 258 is also of interest. The ray path characteristics on this day are summarized in Fig. 5.14. The corresponding meteorological data is shown in Fig. 5.15 for the period from mid-day on Day 257 to mid-day on Day 258. In addition, it is noted that a total of 36.6 mm of rain was recorded on Day 258 at Saint John Airport starting at 07:10 ADT. In studying these results, the good correlation of the propagation results with the meteorological data is noted. First, heavy fading occurred from midnight to 07:00 ADT on Day 258. The fading characteristics are similar to those observed on Day 250 and are thus explained by the presence of a layer. Again the wind condition was reported to be calm. The rapid fading stopped at 07:00 ADT with the temperature increase at sunrise and when the wind started to develop.

A different type of fading was observed for the rest of the day. The simultaneous fading of both the direct and reflected rays (of up to 10 dB below the normal values) was caused by rain attenuation.

5.6 Ray Path Statistics

Using as data base the data from the 55 fading hours, the distributions of the main and second ray amplitudes and the delay time were computed. The results are presented in

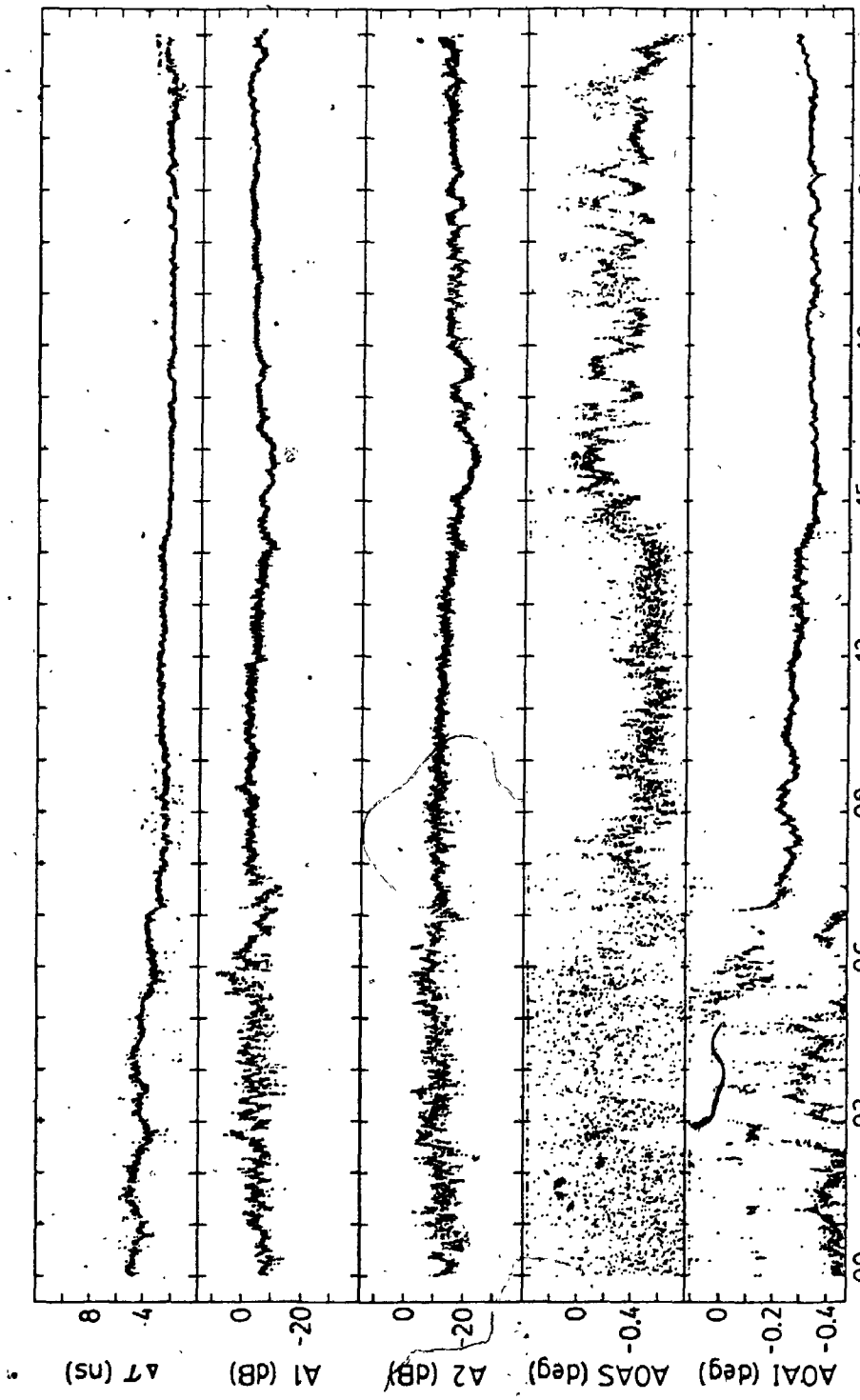

Δτ - relative delay time.
A1/A2 - main (1) and second (2) ray amplitude.
A0AS / A0AI - estimates of main ray AOA from slope (S) and intercept (I).

Fig. 5.14 Ray path characteristics on a fading day (258) in the 1980 experiment.

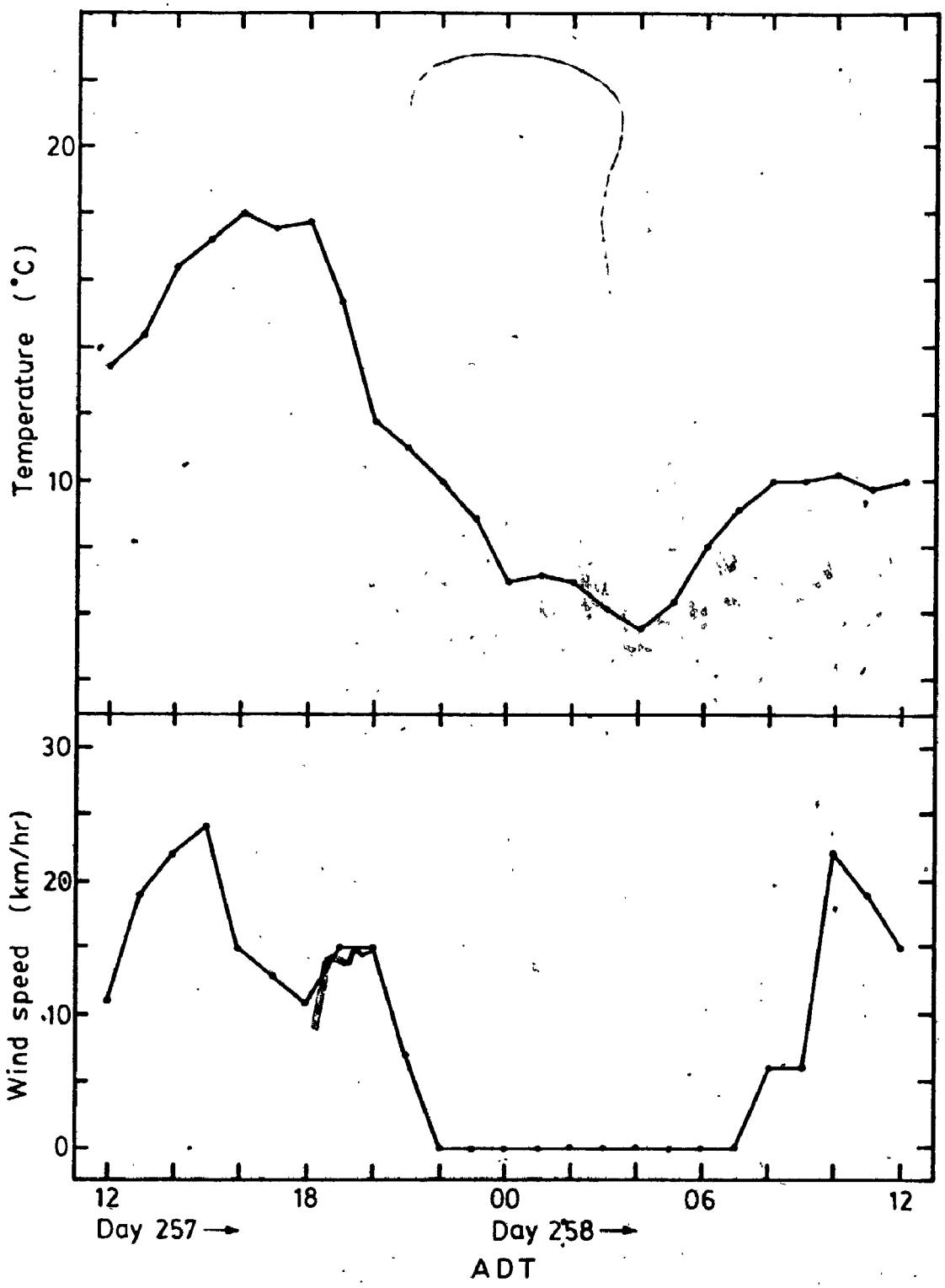

Fig. 5.15 Temperature and wind speed observed at Saint John Airport on Days 257 and 258.

Figs. 5.16(a) to (c).

It is first noted that the main and second ray amplitude during fading hours has median values of -3.1 dB and -10.2 dB, compared with the values of 0 dB and -12.6 dB during non-fading periods. These results fit in with the model that the heavy fading on this link was caused by atmospheric layers the effects of which are: (a) to decrease the direct ray amplitude by defocussing, (b) to increase the reflected ray amplitude by increasing the terrain clearance and reducing the divergence loss, and (c) to increase the relative delay of the reflected ray due to an enhanced refractive index below the layer.

The ray path characteristics for non-fading and fading periods are compared by plotting the distributions on Normal Probability coordinates. This presentation also has the effect of emphasising the tail ends of the distributions. The delay time distribution is shown in Fig. 5.17. The higher probability of occurrence of large delay time values during fading is particularly significant.

The ray path amplitude distributions for the non-fading and fading data are compared in Figs. 5.18(a) and (b). Also plotted in Fig. 5.18(a) is the theoretical distribution of the resultant amplitude of a constant vector plus a Rayleigh-distributed vector [39], the mean power of the Rayleigh vector being -14 dB relative to the power in the constant vector. The main ray amplitude

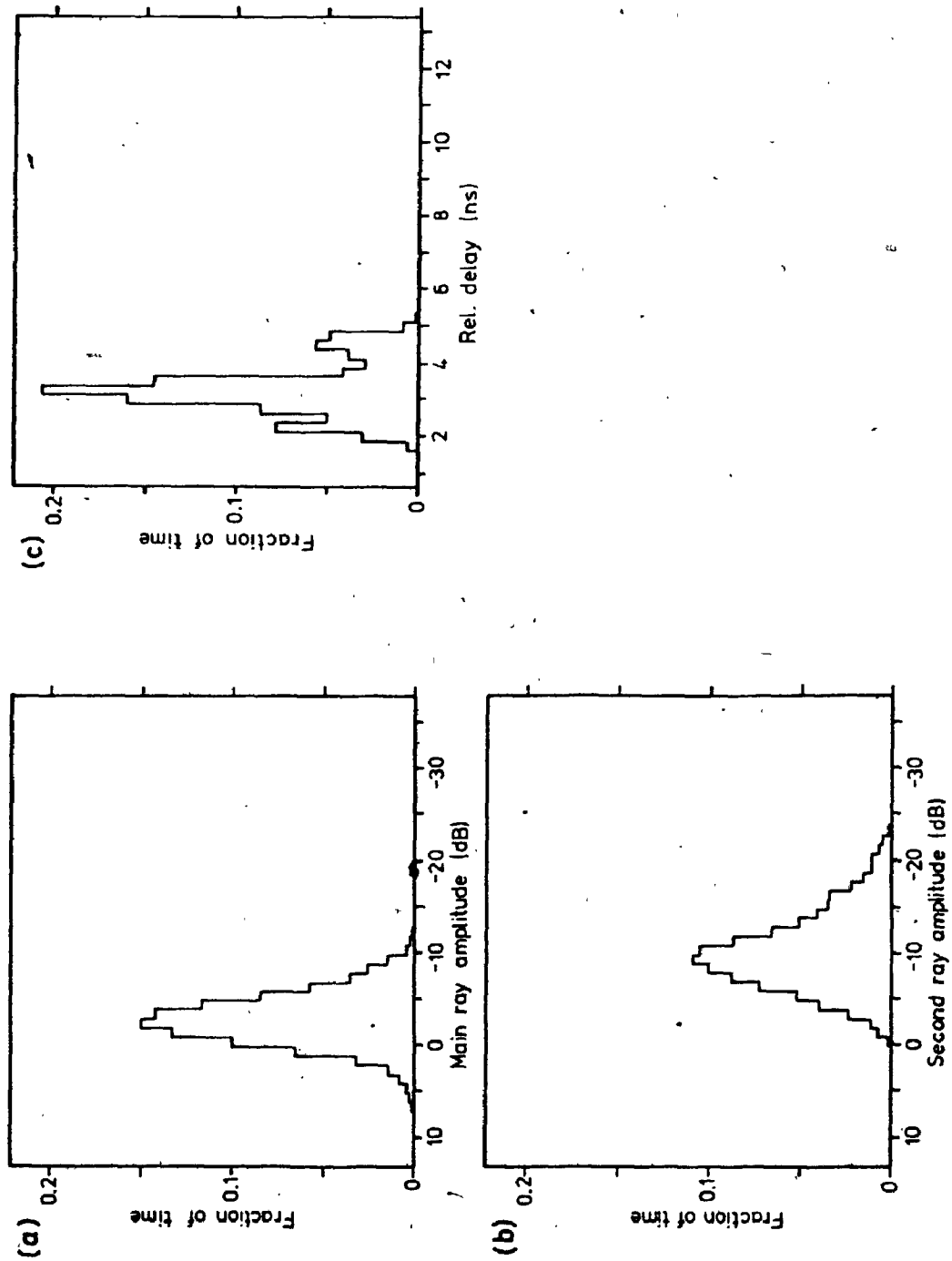

Fig. 5.16 Distributions of the ray amplitudes and relative delay time for the 1980 fading data.

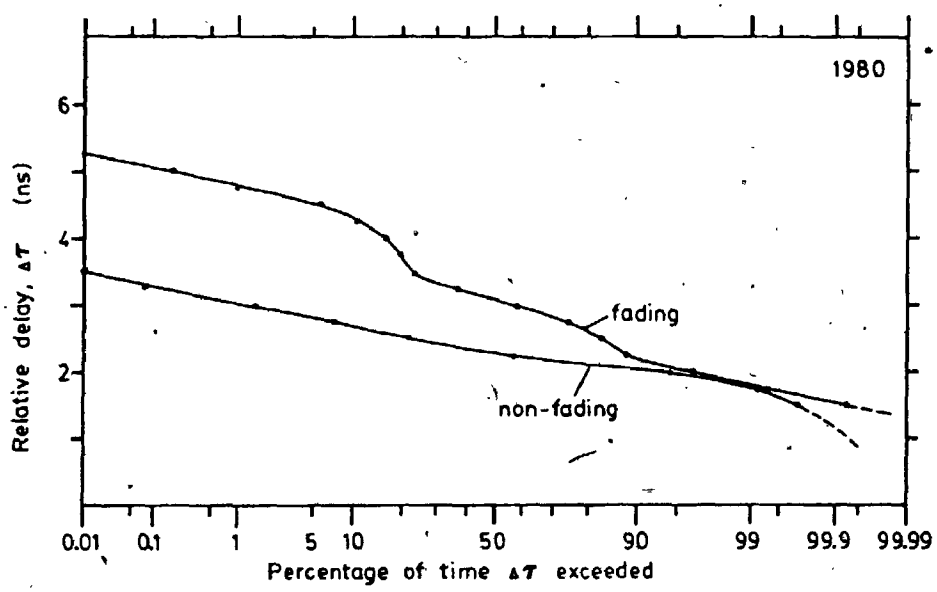

Fig. 5.17 Distributions of the relative delay time (second ray relative to the main ray) for the 1980 non-fading and fading data plotted on Normal Probability paper.

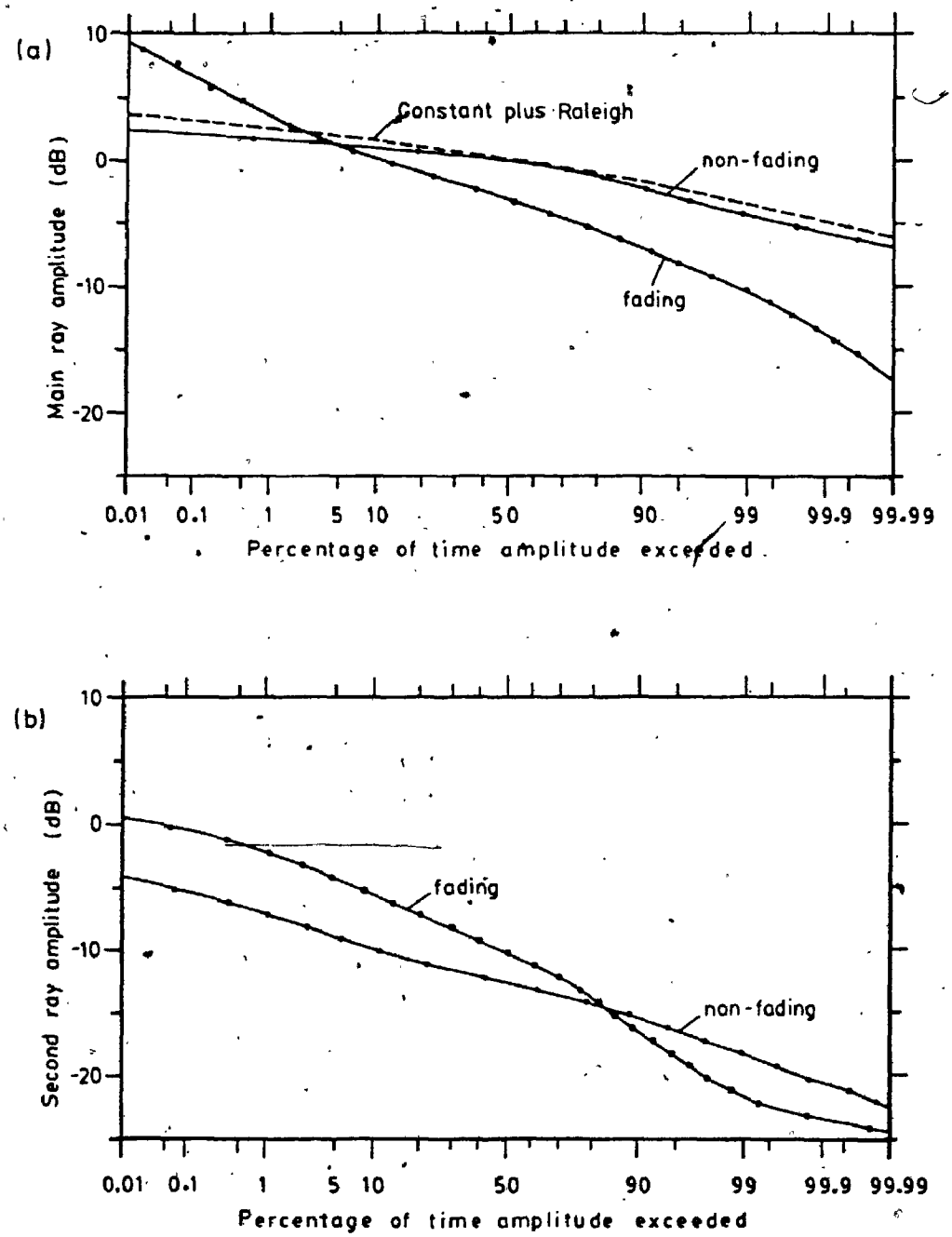

Fig. 5.18 Distributions of ray amplitudes for the 1980 non-fading and fading data plotted on Normal Probability paper.

distribution for the non-fading data closely approximates that of the Constant Plus Rayleigh distribution. This suggests that the mild variations in the direct ray amplitude during non-fading periods are due to random multipath interference occurring in a turbulent atmosphere of the type discussed in Section 2.4.3.

Different statistics are observed for the main ray during fading periods, with enhancements of up to 9 dB and fades of -15 dB. These statistics suggest strongly that the fading was caused by large amplitude but short delay rays (ΔT less than 1 ns). In these cases, the main ray amplitude is in fact the resultant of the direct ray interfering with the auxiliary ray(s). Furthermore, at least part of the fading was caused by the defocussing effect due to a layer occurring below the antennas. It is also noted that the main ray amplitude distribution during fading is approximately log-normal within the 1 % and the 99 % limits. The median amplitude of the main ray for the fading data is decreased by 3 dB relative to the non-fading value, while the median amplitude of the reflected ray is increased by 2.4 dB during fading.

The statistics of the reflected ray amplitude for the non-fading data follows closely that of a log-normal distribution. The theoretical basis for a log-normal distribution is not clear. It has been stated that "... if a positive physical magnitude X obeys a log-normal law, it can be interpreted as being the product of a great

number of independent variables" [40]. In Meyer and Mayer [41] the log-normal distribution is said to arise from a theory of elementary errors combined by a multiplicative process. In the present context, it is noted that the variation in amplitude of the reflected ray is in fact a function of several factors, these include: (a) diffraction by the intervening terrain, (b) atmospheric turbulence, (c) wave height and thus surface roughness variations, and (d) variations in divergence loss. A variation in the value of dN/dh, for example, is manifested in corresponding changes in (a), (c), and (d) due to a change in the reflection angle. Whether such an explanation can account for the log-normal behaviour of the reflected ray is not certain. However, it is interesting to note that a log-normal amplitude distribution was also observed in sea-clutter (or sea-echo) returns in high resolution radars [37], [42].

5.7 Summary

During non-fading periods, the ray path characteristics indicate that the atmosphere may be well modelled with a uniform refractivity gradient. Although the sea reflection is present most of the time with a median amplitude of -12.6 dB and a median delay time of 2.3 ns, significant fading activities were not observed

during the month of October in 1980.

From a consideration of the direct ray AOA, the 99.8 % range of the refractivity gradient for the non-fading data was found to be $-102 < dN/dh < 40$ NU/km. The 99.8 % range in the direct ray AOA is 0.32 deg.

The sea reflection was considered in detail and it was found that except under very rough sea conditions, the reflection loss due to surface roughness is limited to a few decibels.

During fading conditions, the ray path characteristics appear to indicate that heavy fading on the Aylesford - Otter Lake path was caused by a combination of a sea reflection plus the effects due to atmospheric layers. This is considered further in Chapter 6.

Chapter 6

MICROWAVE PROPAGATION ACROSS THE BAY OF FUNDY - OTTER LAKE TO NICTAUX SOUTH

6.1 Introduction

The results from the 1981 propagation experiment are presented in this chapter. These results are compared with the predicted ray path characteristics presented in Chapter 4. The experimental results are used to illustrate various aspects of microwave propagation across the bay from Otter Lake to Nictaux South. It is noted that the main difference of this propagation path from that of the first experiment is that a good blockage of the reflected ray is offered by a mountain ridge called North Mountain.

All the usable data gathered in the 35-day experiment were included in the data base and were processed. The approach taken is the same as that for the 1980 experiment and the major ray path characteristics for the entire period are included in Appendix 7. Once again only selected periods containing representative results are presented.

6.2 General Experimental Observations

In the 1981 experiment, the diagnostic system equipment was operated from 31st July (Day 212) to 3rd September (Day 246) -- a period which included one of the worst fading months of the year in this geographical region. The digital radio test was conducted during the same period. Of the total time of 809 hours during this period, 777 hours of data were collected all of which are included in the data base. No data were collected in the remaining 32 hours due to events such as equipment maintenance, power outages, and equipment malfunction.

A time chart of the experiment showing the amount of fading activity is shown in Fig. 6.1. In sharp contrast to the 1980 results, the number of fading hours totalled 366 which is equivalent to 47 % of the time. The occurrence of fading hours on a per day basis is shown in Fig. 6.2(a). Over half of the fading hours occurred within three distinct periods (marked by arrows in Fig. 6.2(a)) in 11 days. The same is observed for the digital radio test results summarized in Fig. 6.2(b) which shows the hours when digital radio performance was degraded. Most of these occurred in only five days during the 35-day period. These observations suggest that severe fading in this geographical region is closely associated with changes in meteorological conditions that take place over periods of a few days. It is noted that the amplitude reference (0 dB)

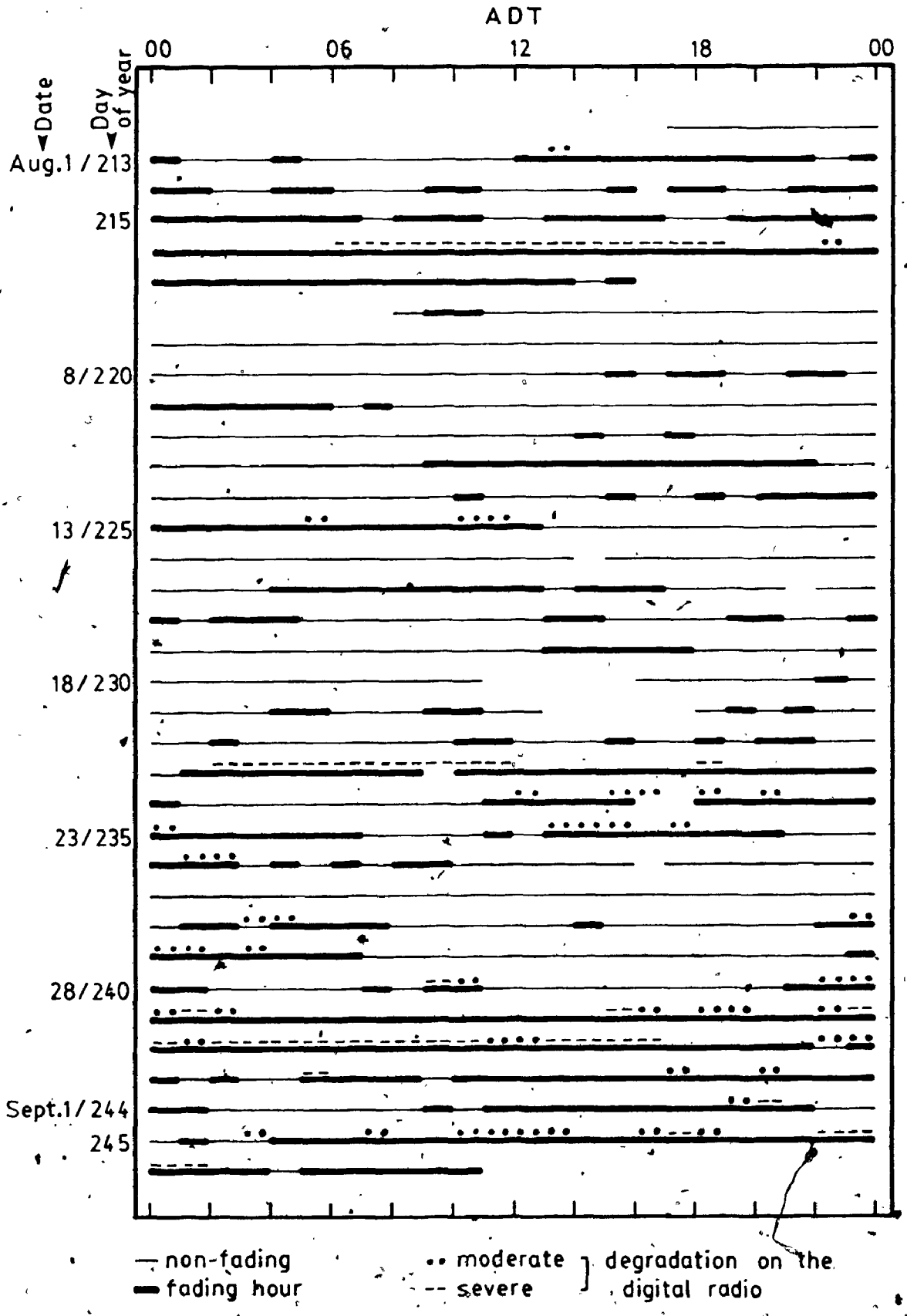

Fig. 6.1 Time chart of experimental observations for the 1981 experiment.

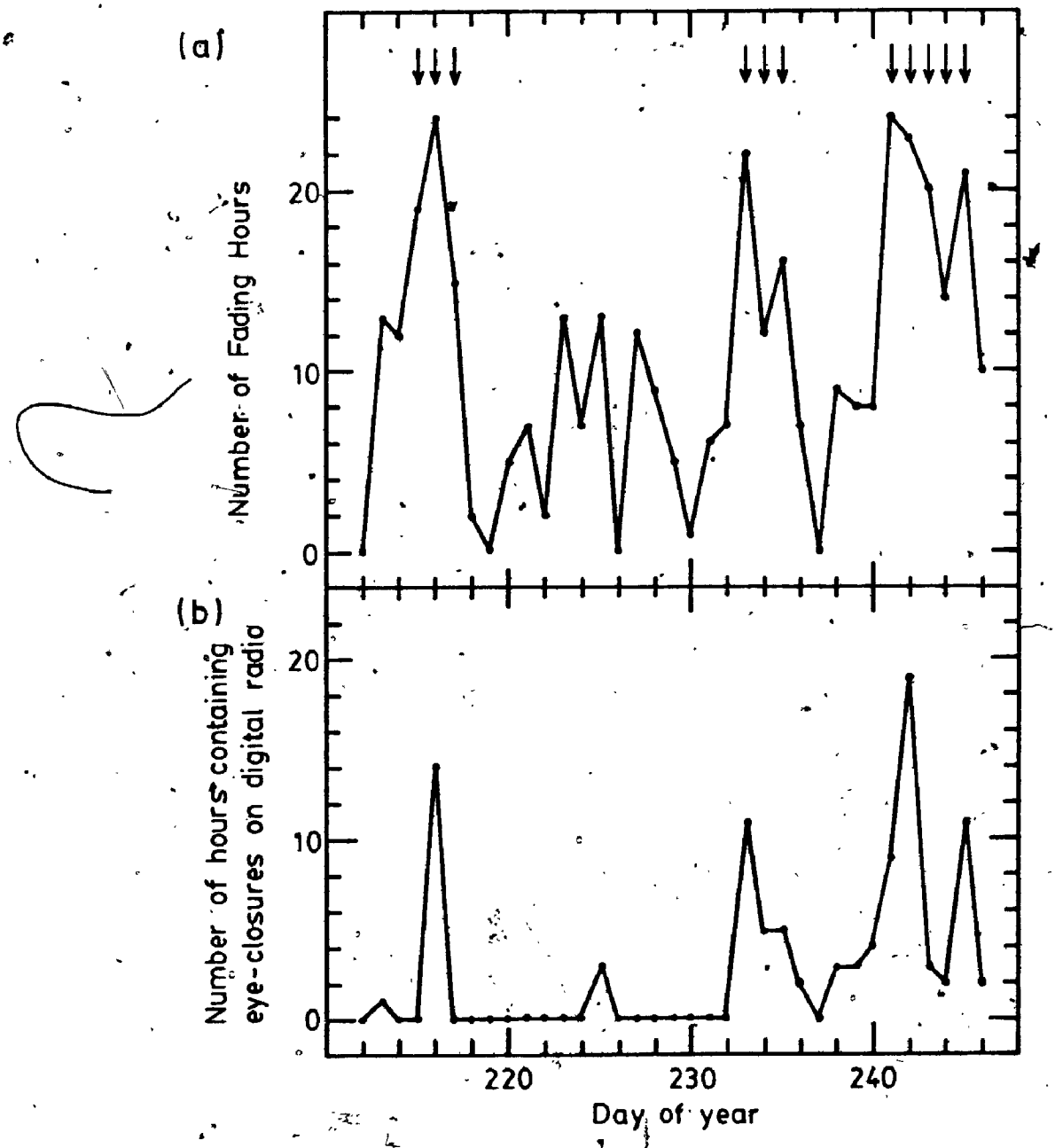

Fig. 6.2 Summary of 1981 experimental results on a per day basis. The arrows mark three distinct periods with heavy fading.

for the results presented in this chapter is the median amplitude of the main ray calculated from the 1981 non-fading data base.

6.3 Propagation During Non-Fading Periods

Out of the 35-day period, only three days (Days 219, 226, and 237) contained no fading hours. The results obtained on Day 219 are used to illustrate the propagation conditions during non-fading periods.

From ray tracing it was predicted that two ray paths, a direct and a reflected ray, would still be observed under normal conditions despite the better blockage. The amplitudes of the direct ray and the reflected ray were estimated as 0 dB and -30 dB respectively, with a relative delay time of 4.5 ns between the two rays.

The ray path characteristics for Day 219 are summarized in Fig. 6.3. The direct ray has a normal amplitude and is stable throughout most of the day. The slope of the phase record, however, shows substantial though slow variations particularly at 01:15 and 06:00 ADT. These variations were not caused by genuine AOA variations since corresponding variations are not observed in the intercept values. Again, this suggests the existence of a low amplitude and short delay ray path. As was pointed out in Section 4.4.1, the presence of such ray paths has little

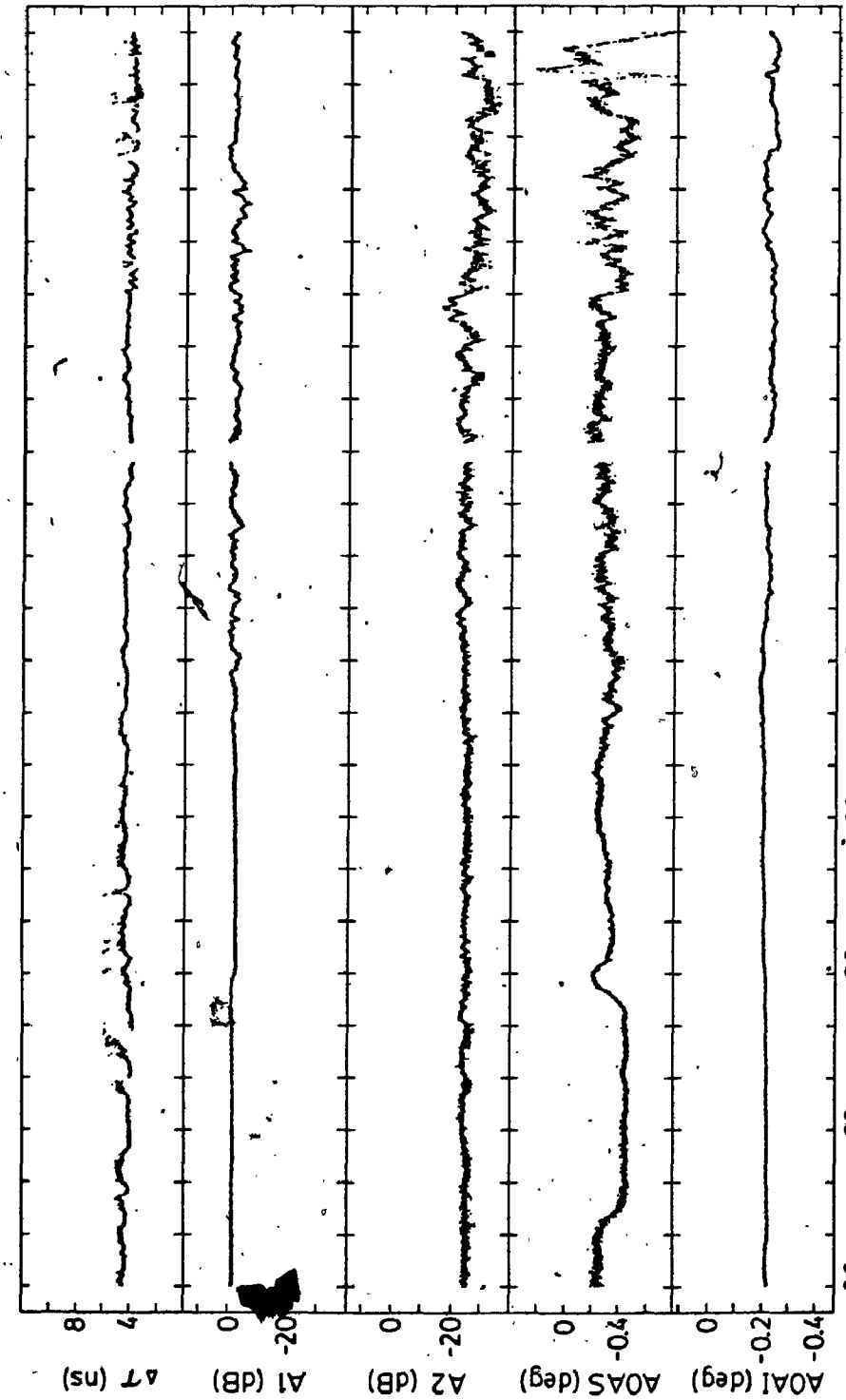

Δτ - relative delay time.
A1/A2 - main (1) and second (2) ray amplitude.
AOAS / AOAI - estimates of main ray AOA from slope (S) and intercept (I).

Fig. 6.3 Ray path characteristics on a non-fading day (219) in the 1981 experiment.

effect on the main ray amplitude and the phase record intercept. However, the phase record slope is very sensitive to these ray paths. One very good example of this is found at 23:00 ADT. A large swing in the phase record slope is observed while a corresponding change is not seen in the intercept value. The slope and intercept values are plotted on an expanded scale in Fig. 6.4. The large excursion in the phase record slope appears to have been caused by a ray path the delay of which was varying in time similar to the effect illustrated in Fig. 4.12.

As for the reflected ray, it has a fairly stable amplitude of approximately -25 dB and a delay of 4.5 ns. These values compare favourably with the predicted values although the reflected ray amplitude is again higher than the predicted value by 5 dB. A typical sweep frequency record is shown in Fig. 6.5. Because the reflected ray is more effectively blocked by North Mountain, only mild fluctuations are displayed across the 1 GHz sweep range. It is also noted that the main and reflected ray AOA values of -0.25 deg and -0.5 deg compare well with the values of -0.23 deg and -0.58 deg predicted for a uniform N-gradient of -40 NU/km (see Chapter 4).

The distributions of the direct and reflected ray amplitudes and the delay time were computed using all the non-fading data as the data base. The results are presented in Figs. 6.6(a) to (c). Median values of the direct and reflected ray amplitudes and the delay time are

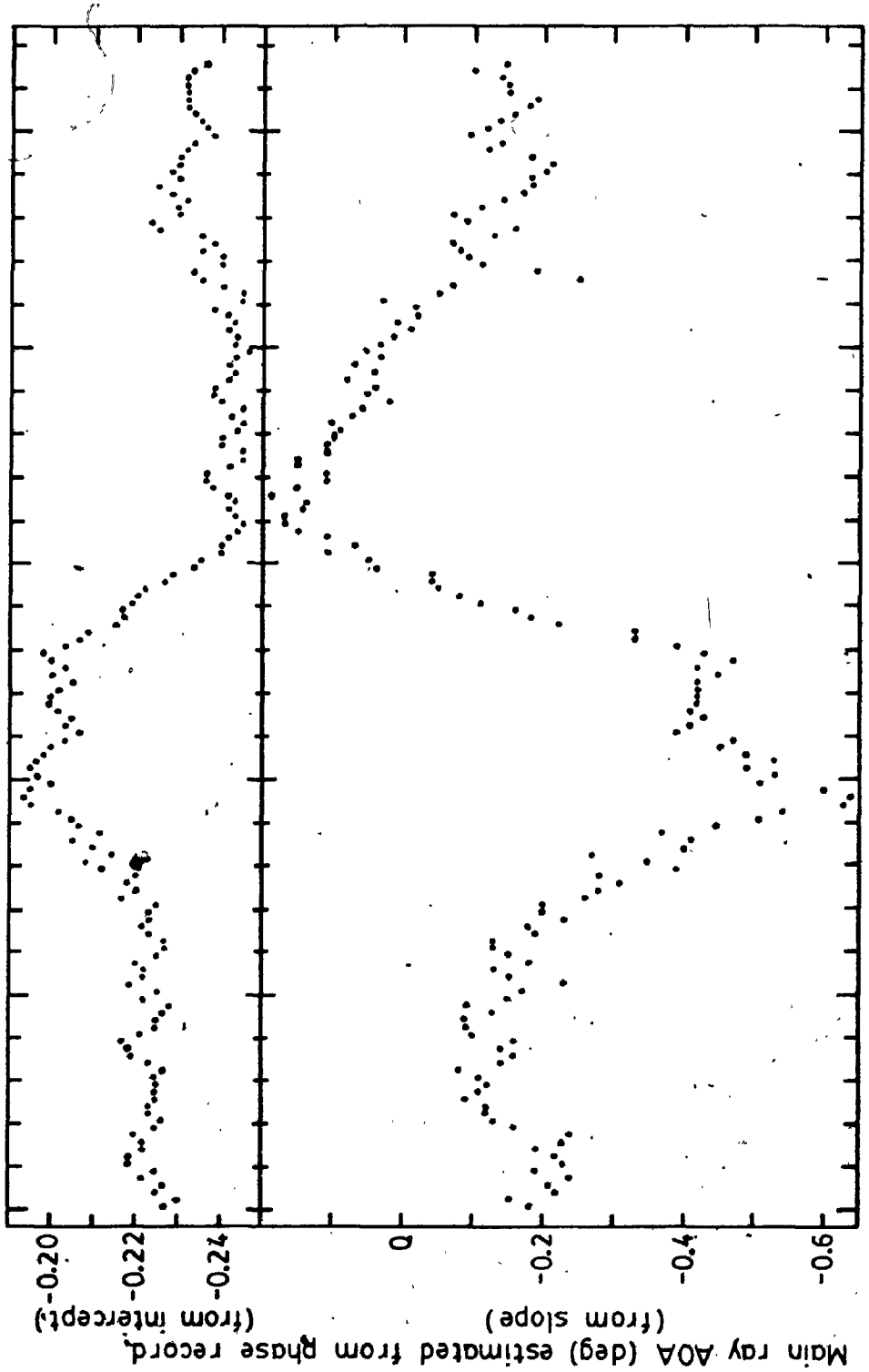

Fig. 6.4 Spurious variations in the phase record slope caused by the presence of a short delay ray with a slowly varying delay time.

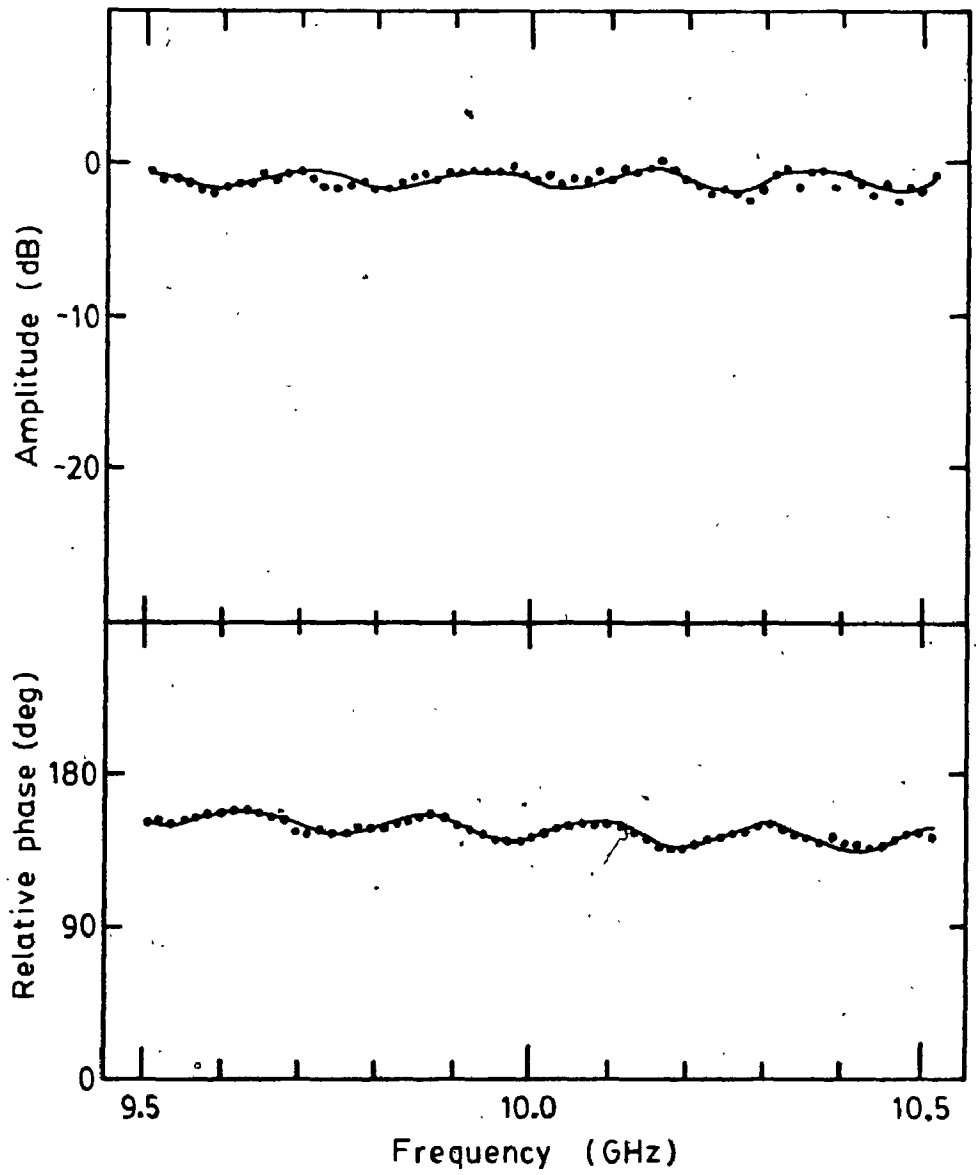

Ampl.(dB)	AOA (deg)	Delay (ns)	
-1.1	-0.25	-	
-25.0	-0.50	4.5	— reflected ray

Fig. 6.5 Experimental (dotted) and synthesized data record at 00:00:05 ADT on Day 219.

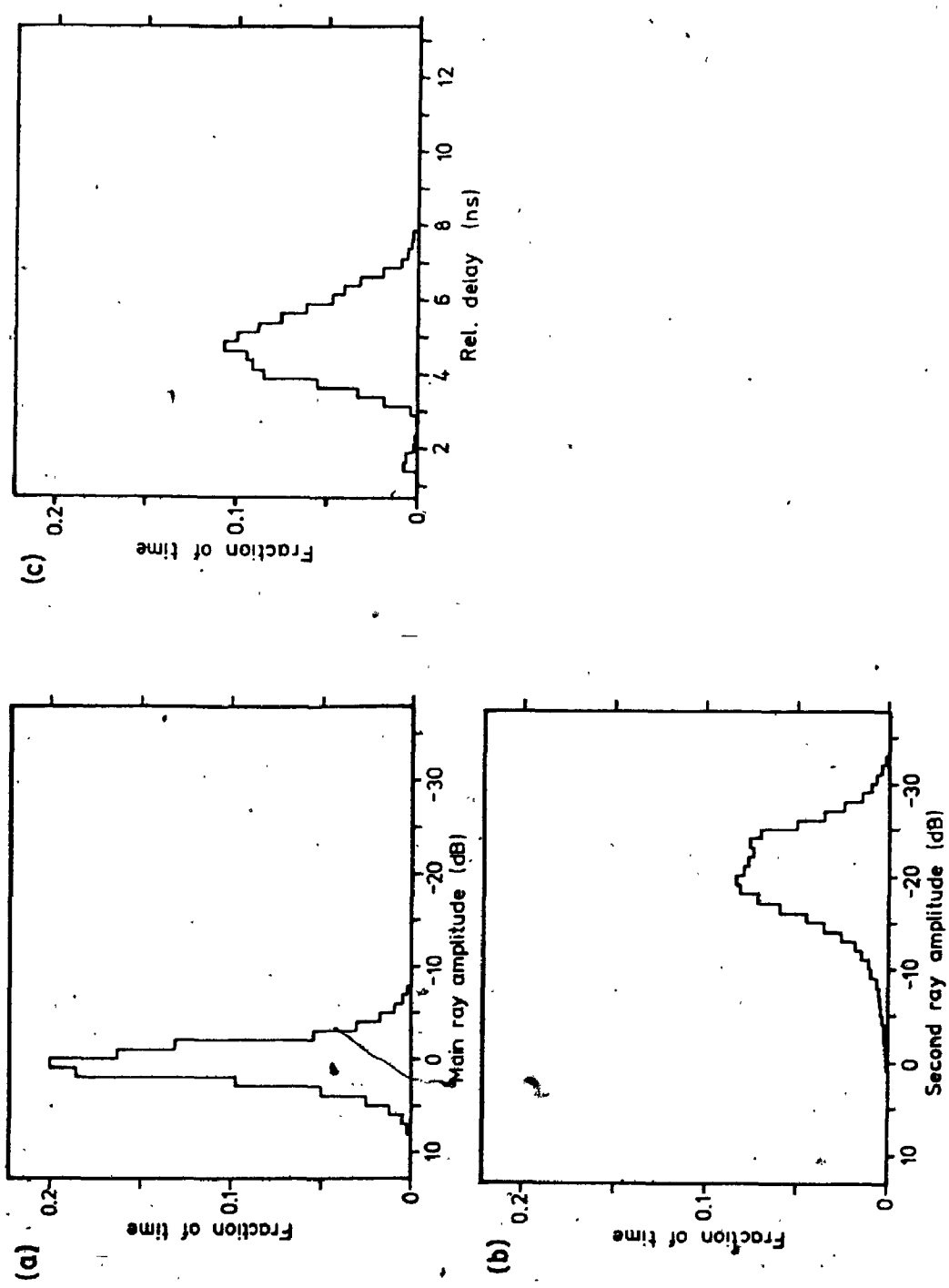

Fig. 6.6 Distributions of the ray amplitudes and relative delay time for the 1981 non-fading data.

0 dB, -20.9 dB, and 4.7 ns respectively. The corresponding values of the standard deviation from the mean are 2.3 dB, 5.0 dB, and 1.0 ns respectively.

These results illustrate a few important points. First, North Mountain does provide a more adequate terrain blockage to the sea reflection, at least under normal conditions. This resulted in a much reduced median amplitude of the reflected ray of -20.9 dB (compared with a median amplitude of -12.6 dB for the first experiment). This median amplitude, however, is 9 dB higher than the predicted value of -30 dB. As was the case for the first experiment, this discrepancy is attributed to two major causes. The first of these is the uncertainty in the height of North Mountain (including the average tree height of 12 m) used in the diffraction estimate. In any event, the results from both experiments do suggest that the assumed equivalent tree height of 12 m is too high a value. Furthermore, it is also suspected that the diffracting terrain structures in both cases are closer in characteristics to that of a knife-edge than was assumed for average terrain [23]. The second major cause of the discrepancy arises from the fact that the predicted ray path characteristics were based on a median N-gradient of -40 NU/km. Since the experiment was performed during a summer month in a region with Maritime climate, it is not inconceivable that the median gradient may be more negative than -40 NU/km, thus resulting in a higher amplitude of the

reflected ray due to increased path clearance at North Mountain. Such appears to be the case on Day 237 when higher than normal values of the delay time, direct ray AOA, and reflected ray amplitude are evident (see Appendix 7).

An estimate of the range of the overall refractivity gradient encountered on this propagation path, during the non-fading periods of a worst fading month, may be obtained by studying the range in the observed direct ray AOA. The direct ray AOA was obtained from the phase record intercept by the same method used for the 1980 results. The distribution of the AOA for the non-fading data base is shown in Figs. 6.7(a) and (b).

The distribution gives the 0.1 % and the 99.9 % values of the direct ray AOA as -0.42 deg and 0.05 deg respectively. The 99.8 % range in AOA therefore is 0.47 deg. This translates to a 99.8 % range in N-gradient of $-161 < dN/dh < 40.2$ NU/km (or $-40 < K < 0.8$).

The 99.8 % range in AOA of 0.47 deg is seen to be quite small compared with the range of 1.6 deg estimated with Eq. (2.9) and using dN/dh values obtained from Segal and Barrington [3]. The apparently large estimated AOA range is explained by the fact that the 99.8 % values in dN/dh obtained from Segal and Barrington are tabulated for the first 100 m in the atmosphere. The actual propagation path, however, dictates that the direct ray path lies within the height range from 100 to 400 m above MSL. While

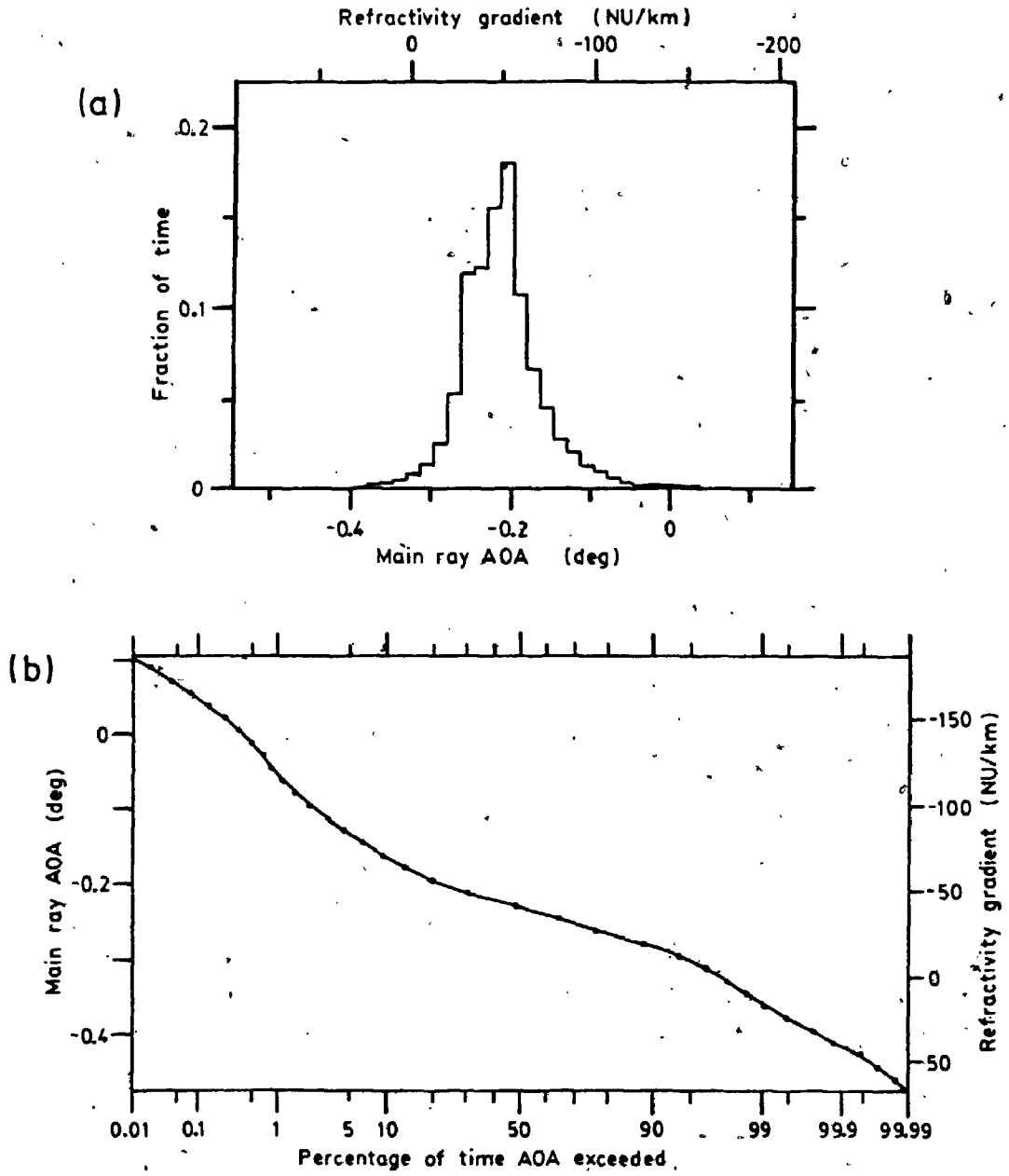

Fig, 6.7 Distribution of the main ray AOA for the 1981 non-fading data.

the extreme N-gradients used are not unreasonable at heights close to the surface of the bay, it seems less likely that such extreme gradients are maintained over the full height range in consideration.

6.4 Anomalous Propagation

Although the propagation conditions during fading are highly variable, certain ray path characteristics appear to be commonly observed during these fading periods. This point is illustrated by the results obtained from Days 225 (13th August) and 242 (30th August).

A plot of the ray path characteristics for Day 225 is shown in Fig. 6.8. The most noticeable feature is that the delay time of the reflected ray shows a gradual increase from a normal value of 4 ns to more than 8 ns., it then decreases slowly back to the normal value in the afternoon. The same is observed for the main ray AOA which is raised from its normal value of -0.23 deg to 0.1 deg. The highest AOA also occurs when the delay time is maximum.

Substantial enhancement and rapid fading in the main ray amplitude are observed in the morning. On the other hand, the reflected ray amplitude is substantially increased -- by more than 15 dB above its normal value, during the time from 09:00 to 12:00 ADT.

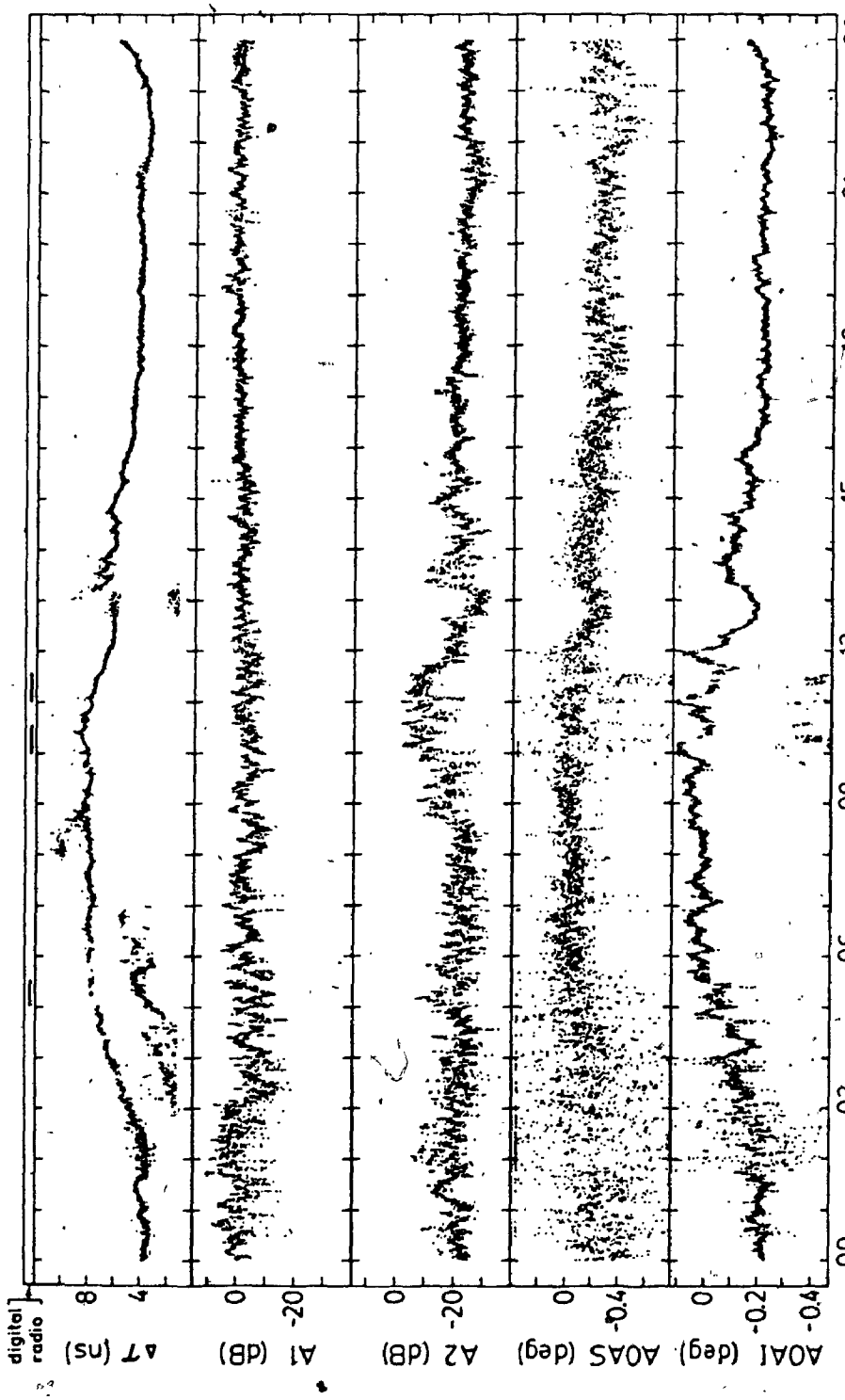

Δτ - relative delay time
A1/A2 - main (1) and second (2) ray amplitude
AOAS / AOAI - estimates of main ray AOA from slope (S) and intercept (I).

Fig. 6.8 Ray path characteristics on a fading day (225) in the 1981 experiment.

These observed ray path characteristics are in fact very similar to those observed for the 1980 experiment. Recalling the effects of atmospheric layers which were discussed in Section 5.5.1, it is seen that the gross ray path features of: (a) decreased main ray amplitude, (b) elevated main ray AOA, (c) increased reflected ray amplitude, and (d) substantially increased delay time, may all be explained by postulating an atmospheric layer occurring below the antennas. The long delay time of more that 8 ns in this case is accounted for by the increased antenna heights in the Otter Lake - Nictaux South path.

The fading observed on Day 225 is in fact an example of relatively mild fading in the 1981 experiment. The fading only caused mild degradation on the digital radio performance (at 05:00, 10:00, and 11:00 ADT). The worst fading day during the experiment is Day 242 when the operation of the digital radio was severely impaired.

The ray path characteristics for Day 242 are shown in Fig. 6.9. The relative delay time of the reflected ray is above 6 ns during most of the day, with a maximum of greater than 10 ns at 09:00 ADT. Once again rapid fluctuations in both the main and second ray amplitudes are observed. The main ray fades at times to below -20 dB relative to its normal value (e.g. at 13:00 ADT). Furthermore, signal enhancements of as high as 10 dB above normal (e.g. at 21:00 ADT) are observed. The reflected ray, on the other hand, shows an increased signal level --

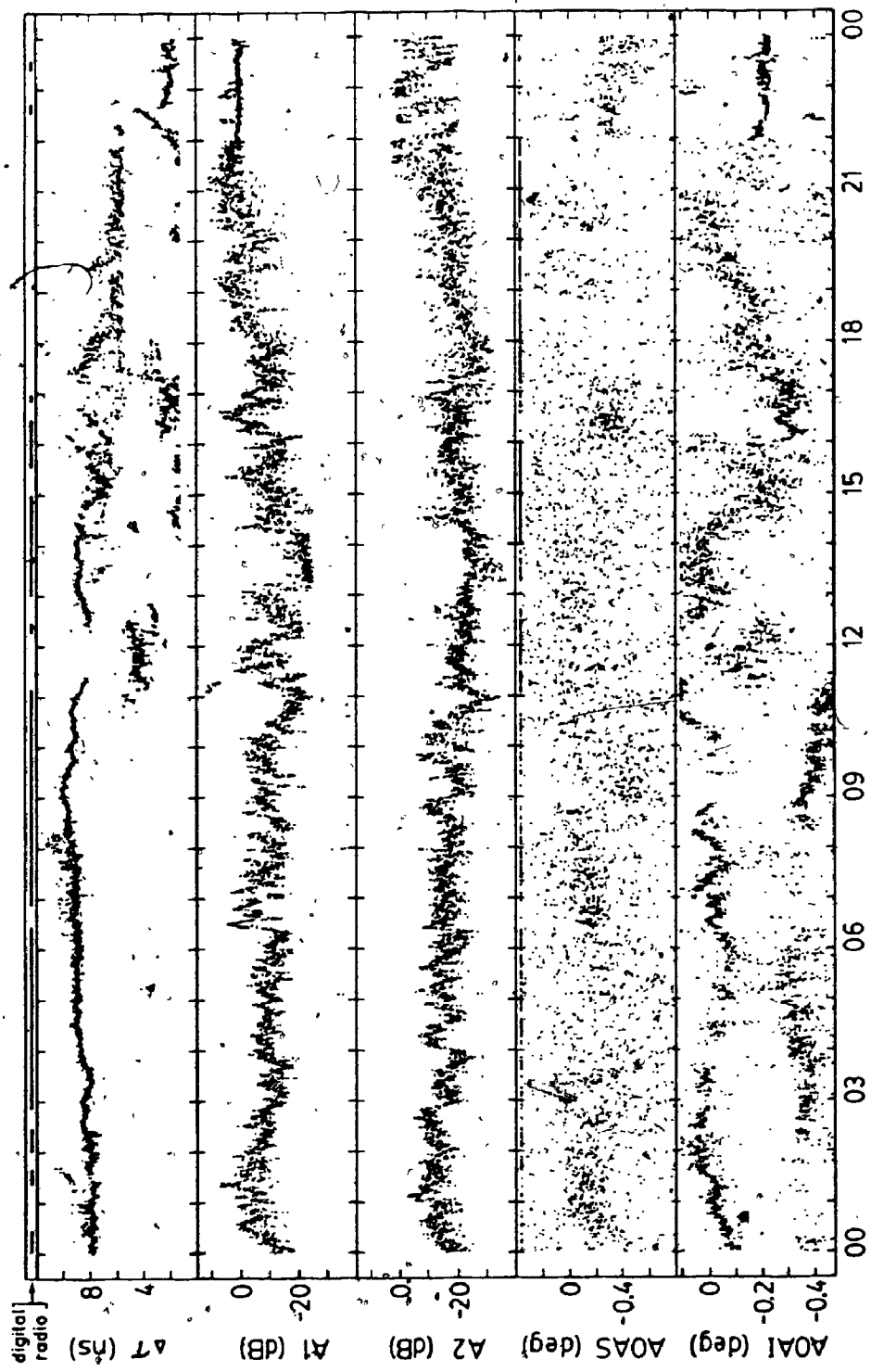

Δτ - relative delay time
A1, A2 - main (1) and second (2) ray amplitude
AOAS / AOAI - estimates of main ray AOA from slope (S) and intercept (I).

Fig. 6.9 Ray path characteristics on the worst fading day (242) in the 1981 experiment.

at times by more than 10 dB above its normal level and exceeds the direct ray amplitude to dominate as the main ray. These periods are readily identified in the AOA plot recalling that the stronger ray will dominate the AOA results. Such behaviour is observed, for example, from 02:00 ADT to 06:00 ADT, and also from 08:30 to 11:00 ADT.

A sweep frequency record obtained at 10:04:52 ADT was analysed by the pattern synthesis method and the results are shown in Fig. 6.10. A series of nine nulls is observed across the 1 GHz frequency band due to the destructive interference between the direct and the reflected rays. Two strong ray paths are identified. In particular the direct ray amplitude is reduced to -10.8 dB with an elevated AOA of 0.02 deg. The reflected ray has a much increased amplitude of -8.9 dB and a higher AOA of -0.43 deg (compared with the normal values of -20.9 dB and -0.58 deg). The delay time of 9.2 ns is also very significant.

Also shown in Fig. 6.10 are the times when severe degradation occurred on the digital radio. Very good correlations of digital radio outages with: (a) long delay times, and (b) periods when the direct ray amplitude was reduced to below the level of the reflected ray, are especially evident from 02:00 to 13:00 ADT.

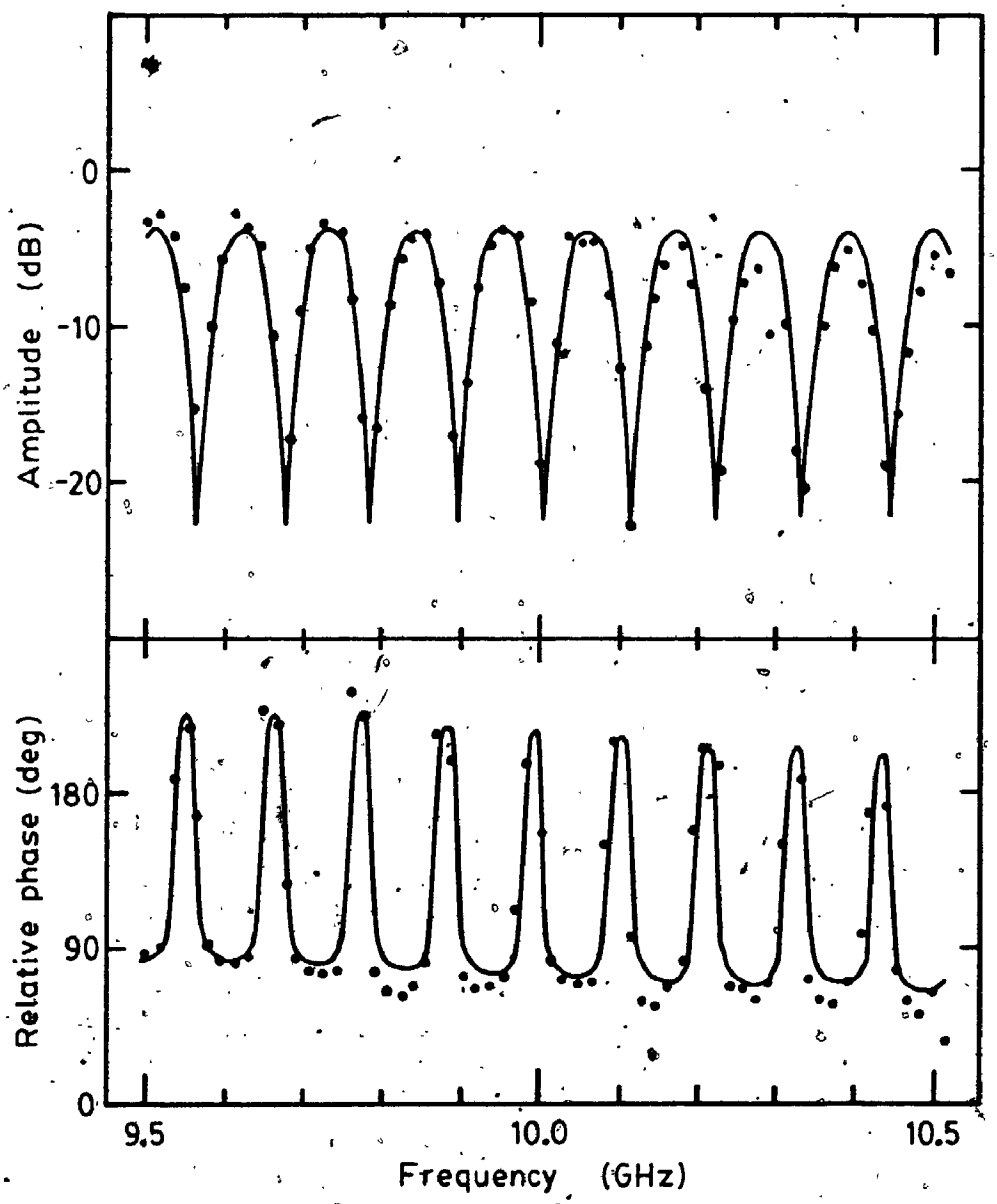

Ampl. (dB)	AOA (deg)	Delay (ns)	
-10.8	0.02	-	
-8.9	-0.43	9.2	— reflected ray

Fig. 6.10 Experimental (dotted) and synthesized data record at 10:04:52 ADT on Day 242.

6.5 Atmospheric Layers

Atmospheric layers, within which exist extreme gradients of refractivity, are the major causes of severe fading across the Bay of Fundy in both the 1980 and 1981 experiments. The influence of these layers on microwave propagation are now examined in more detail.

The occurrence of multipath propagation associated with atmospheric layers was discussed in Section 2.4.2. In the experiments presented in this thesis, there exists an added complication. In Section 5.4 various aspects of the sea reflection have been examined. It was concluded that except under very rough sea conditions, the reflected ray is fairly stable and is only attenuated by a few decibels on reflection. As is presented in the experimental results, this sea reflection plays an important role in microwave propagation across the bay, especially during periods of severe fading.

To illustrate the combined effects of atmospheric layers and the sea reflection, ray tracing was performed for the Otter Lake - Nictaux South propagation path. A layer with parameters $\Delta N = -40$ NU and $\Delta h = 100$ m was assumed. The height of the layer was varied relative to the antenna heights. The results for a low-level layer ($h_o = 200$ m), a mid-level layer ($h_o = 260$ m), and a high-level layer ($h_o = 380$ m), are shown in Figs. 6.11(a) to (c).

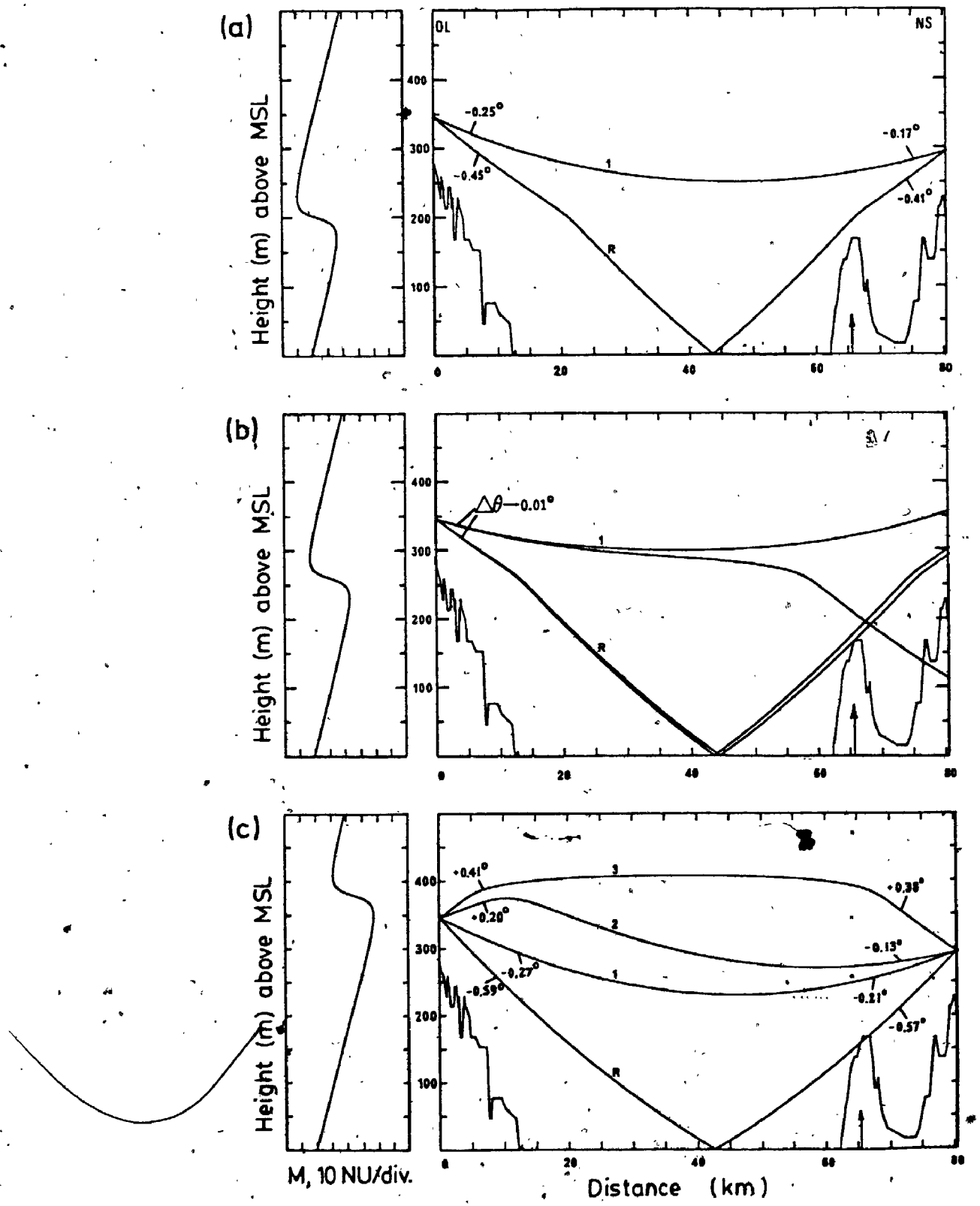

Fig. 6.11 Propagation on the Otter Lake - Nictaux South path when an atmospheric layer is present at various heights: (a) low-level layer (b) mid-level layer (c) high-level layer.

When the layer is far below both antennas, as shown in Fig. 6.11(a), its effect on the direct ray is minimal. However, the reflected ray, which is normally well blocked by North Mountain, is "lifted" due to the presence of the layer. The net result is that the clearance for the reflected ray is increased and this in turn leads to an increased amplitude. Experimental evidence of this behaviour is found in the results presented in Section 6.4 for both Days 225 (from 08:30 to 13:00 ADT) and 242 (over most of the day).

The enhanced refractive index value below the layer also has the effect of increasing the phase path length of the reflected ray. The result is a substantial increase in the relative delay time of the reflected ray. This is again frequently observed for both experiments and delay times of greater than 10 ns were found on Day 242. These long delay times have important bearings on the error performance of digital radio systems.

The same effects of increased clearance and increased delay time for the reflected ray are observed when the layer is placed just below the antennas as shown in Fig. 6.11(b). In this case there is an added effect of strong defocussing of the direct ray. This accounts for the experimentally observed reduction in the direct ray amplitude.

When the layer is present at a height above both antennas, atmospheric multipath is observed in addition to

the reflected ray as shown in Fig. 6.11(c). The atmospheric ray paths are not different from the ones described in Section 2.4.2. These ray paths are also observed in the experimental results. A detailed discussion of the behaviour of such atmospheric ray paths in relation to atmospheric layer parameters is found in Webster [43].

The above results are summarized in Fig. 6.12 which shows the effects of layer height variations on the received ray path characteristics. The important ray path behaviour of: (a) elevated direct and reflected ray AOA's, (b) increased delay time, (c) increased reflected ray path clearance, and (d) reduced direct ray amplitude due to defocussing, are noted for cases when the layer is below both antennas.

Also of interest are the ray path characteristics for the atmospheric rays labelled 2 and 3. It is seen that two atmospheric ray paths would be present for a high-level layer. Ray 2 has comparable amplitude to the normal direct ray while ray 3 can take up varying amplitudes depending on the layer height. It is also noted that these atmospheric ray paths have higher AOA's than the normal ray and their relative delay times can range from negative to positive values of up to 5 ns for the duct used in the example.

Using Fig. 6.12 as a guide, the experimental results for Days 225 and 242 are examined in further detail. During the period from 03:00 to 06:00 ADT on Day 225 (see

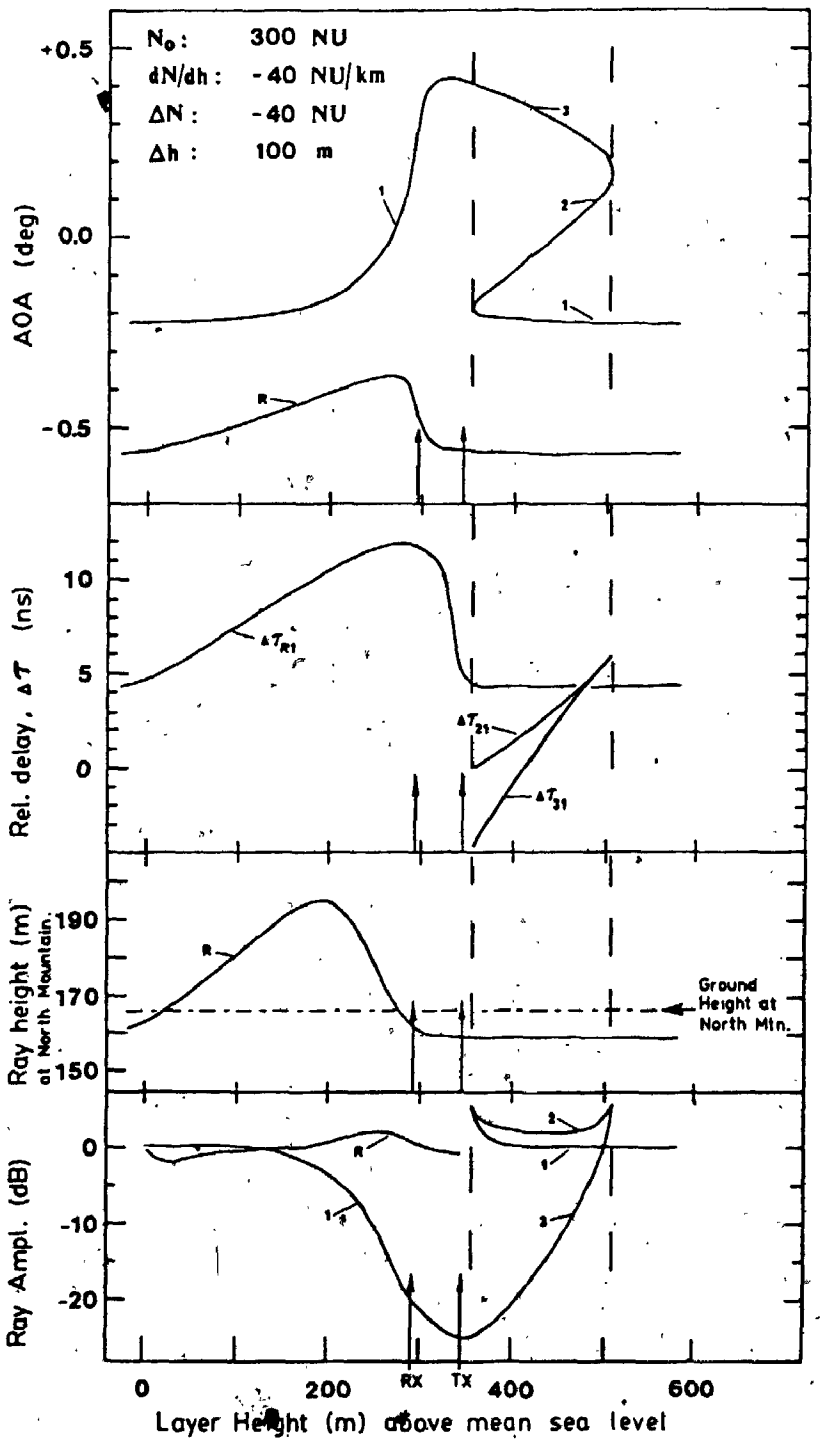

Fig. 6.12 Effects of layer height variations on ray path characteristics for the Otter Lake - Nictaux South path. R.... reflected ray. [44]

Fig. 6.8), an extra ray path (in addition to the normal direct and reflected rays) is present as is evident in the delay time characteristics. The extra ray has a delay of ~4 ns at 05:00 ADT and an amplitude which is higher than that of the reflected ray. Analysis of some of the sweep frequency records reveals that the extra ray path has an AOA of approximately 0 deg and an amplitude of -12 dB. Also, the amplitude of the normal ray was found to be -7 dB. Although the AOA's and delay time can be explained by a single layer at the height of the antennas, the reduced ray path amplitudes do suggest the presence of a second layer below the antennas thereby causing the defocussing in the two atmospheric paths.

Further insight may also be gained from the results for Day 242 shown in Fig. 6.9. First, it is observed that at 11:30 ADT, both the delay time and the amplitude of the reflected ray show a rapid drop from extraordinarily high values down to the normal values. Based on Fig. 6.12, it appears that from 08:00 to 13:00 ADT, the layer height was increasing slowly. The rapid drop in delay time at 11:30 ADT then corresponds to a layer height such that both antennas are within the layer. The results after 12:30 ADT indicate a subsequent decrease in the layer height to just below the antennas from 13:00 to 14:00 ADT, thus causing the substantial decrease in the direct ray by defocussing.

Although the model of a layer rising and falling in height seems to adequately explain the observed ray path

characteristics, it is again noted that the model of an idealized layer with well defined boundaries is at best a simplified picture. It is not inconceivable that variations in the layer height can be accompanied by changes in the layer strength ΔN as well as the anomaly thickness Δh. Furthermore, layer parameters are not expected to be horizontally homogeneous along the full length of the propagation path. Differences between the experimentally observed and the modelled ray path parameters are thus attributed to deviations in the actual atmosphere from the idealized layer structure.

A rough estimate of the layer strength ΔN commonly observed in the Bay of Fundy may be inferred from the maximum delay value of the reflected ray. This is illustrated by assuming a layer with anomaly thickness Δh = 100 m and a height which will cause maximum delay on the Otter Lake - Nictaux South path ($h_o \simeq 260$ m). The variation of the delay time versus the layer strength ΔN for this layer height is shown in Fig. 6.13. Based on this diagram, the strength of the layer that caused a maximum delay of 8 ns on Day 225 was estimated to be $\Delta N \simeq -20$ NU. Similarly, the layer observed on Day 242 was estimated to have a strength of $\Delta N \simeq -30$ NU since it caused a maximum delay of 10 ns. By the same reasoning, an examination of the ray path characteristics summarized in Appendix 7 reveals that except on one occasion (at 23:00 ADT on Day 245) the maximum delay of the reflected ray did not exceed

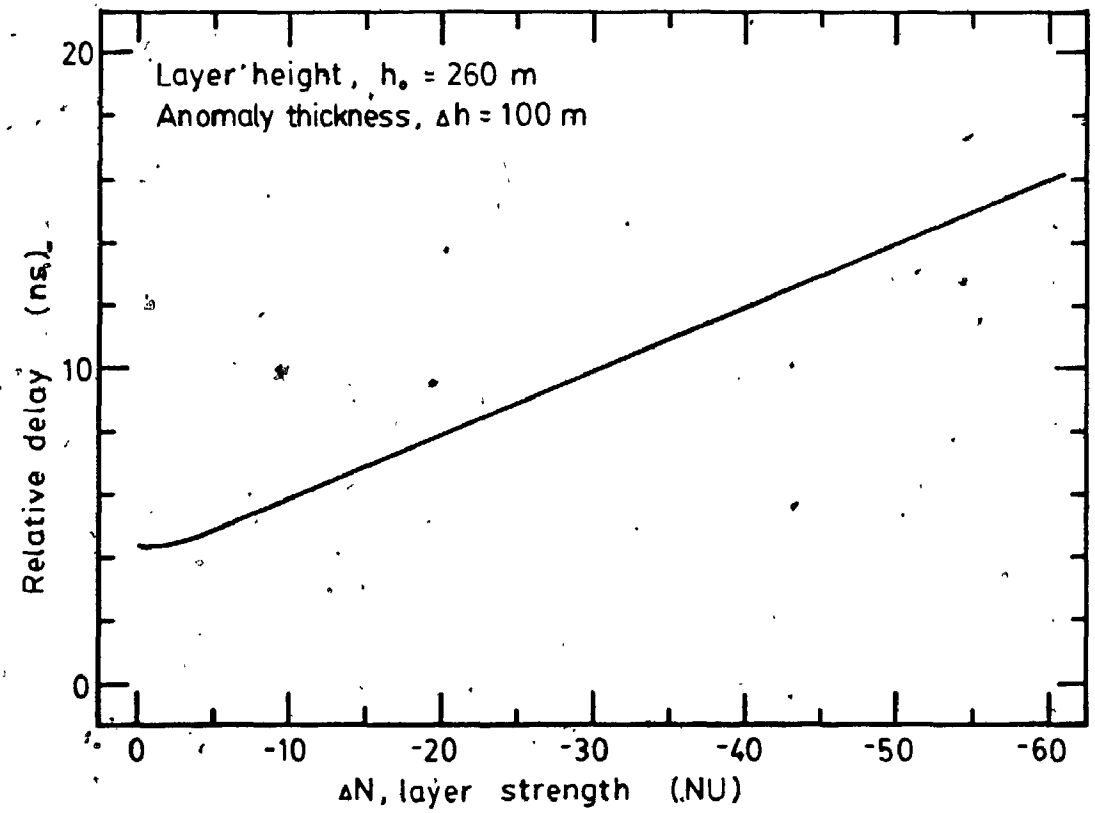

Fig. 6.13 The maximum relative delay of the reflected ray caused by a single layer with strength ΔN.

12 ns; therefore it is concluded that the layer strength of elevated layers observed in the Bay of Fundy rarely exceeds -40 NU. For the period from 23:00 ADT on Day 245 to 01:00 ADT on Day 246, the delay time has a maximum value of just above 14 ns, the corresponding layer strength was estimated to be approximately -50 NU.

6.6 Ray Path Statistics

The statistics of the main and second ray amplitudes and of the delay time during fading were computed using the 366 fading hours obtained in 1981 as the data base. The results are summarized in Figs. 6.14(a) to (c). The median amplitudes of the main and reflected ray were found to be -4.0 dB and -18.9 dB (compared with values of 0 dB and -20.9 dB respectively for the non-fading data). As was found from the first experiment, severe fading appears to be caused not merely by an increased second ray amplitude, but, more importantly, by a significant decrease in the main ray amplitude. The results also support the model that atmospheric layers, which cause fading in the main ray and enhancements in the reflected ray, are the main causes of severe fading across the Bay of Fundy.

The ray path statistics during non-fading and fading periods are compared by plotting on Normal Probability paper. The delay time statistics shown in Fig. 6.15

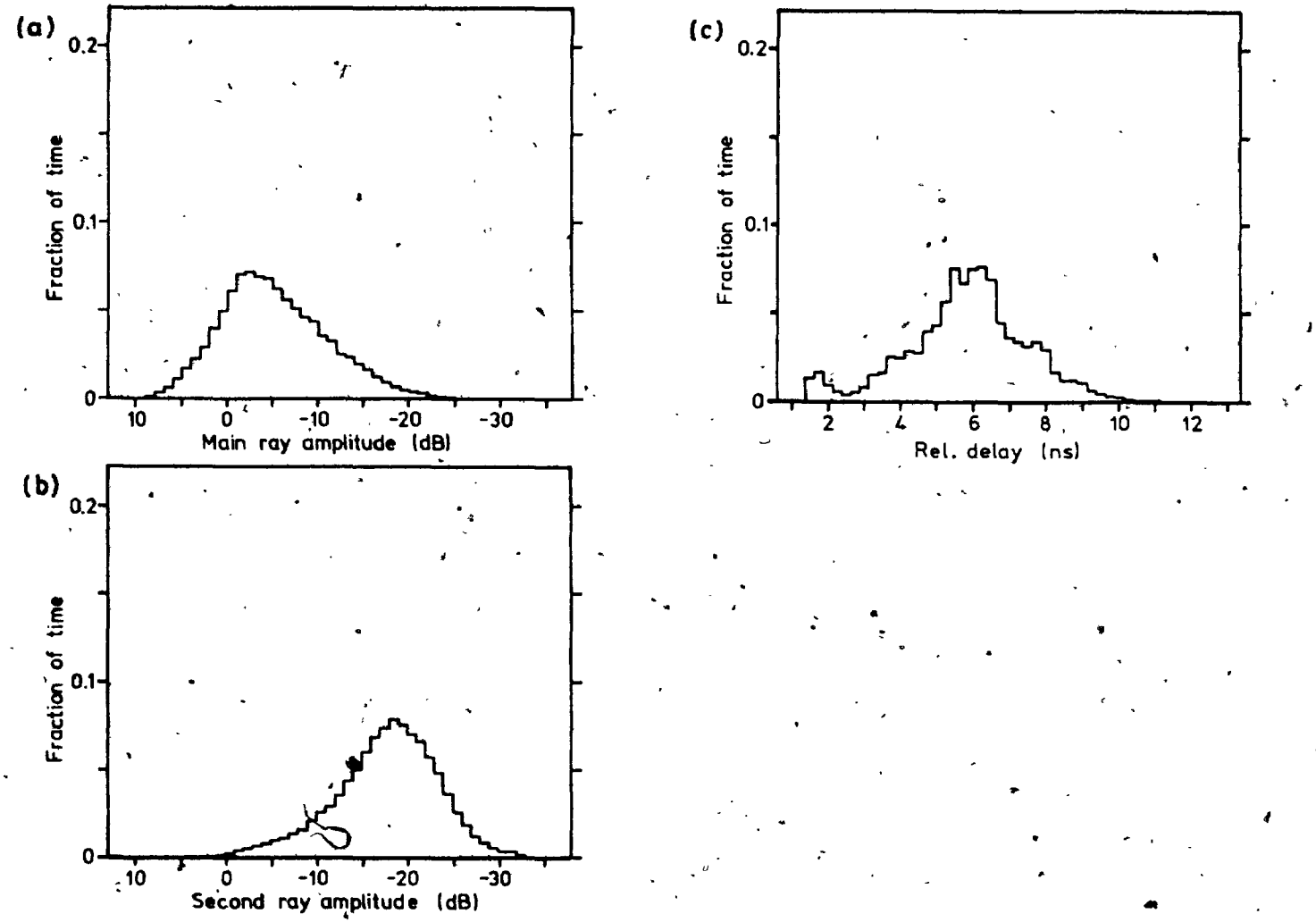

Fig. 6.14 Distribution of the ray amplitudes and relative delay time for the 1981 fading data.

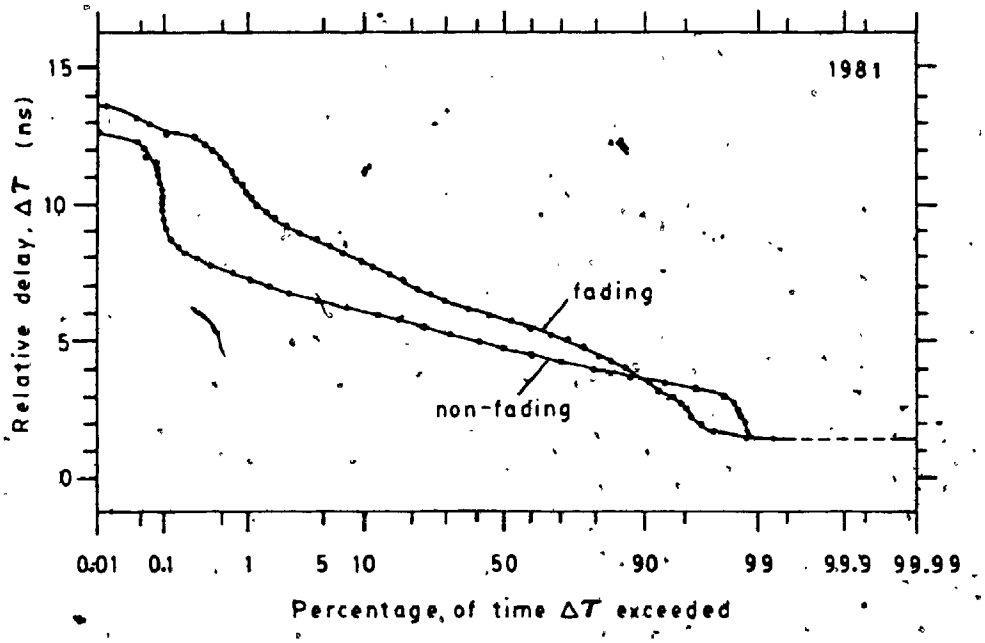

Fig. 6.15 Distribution of the relative delay time of the reflected ray in the 1981 experiment plotted on Normal Probability paper.

indicate an overall increase in the delay time during fading. The more important point is that although the median delay time is increased by only 1.1 ns for the fading data, the delay time for 0.1 % of the time is increased by almost 3 ns. The effect of long delay times on digital radio performance will be discussed in Chapter 8.

The main and second ray amplitude statistics for the non-fading and fading data are compared in Figs. 6.16(a) and (b). The theoretical distribution of the resultant of a constant vector and a Rayleigh-distributed vector (power of Rayleigh vector is -10 dB relative to the Constant vector) is plotted for comparision. The agreement between the main ray amplitude distribution for the non-fading data with the theoretical Constant Plus Rayleigh distribution is well demonstrated. As for the main ray amplitude distribution during fading periods, the occurrences of very low signal levels (less than -20 dB relative to the normal value) are noted.

For the reflected ray, it is recalled that the results in the 1980 experiment indicate a log-normal distribution during non-fading periods. The same distribution is not observed for the 1981 experiment. As for the fading data, the general increase of the second ray amplitude relative to its normal value is noted.

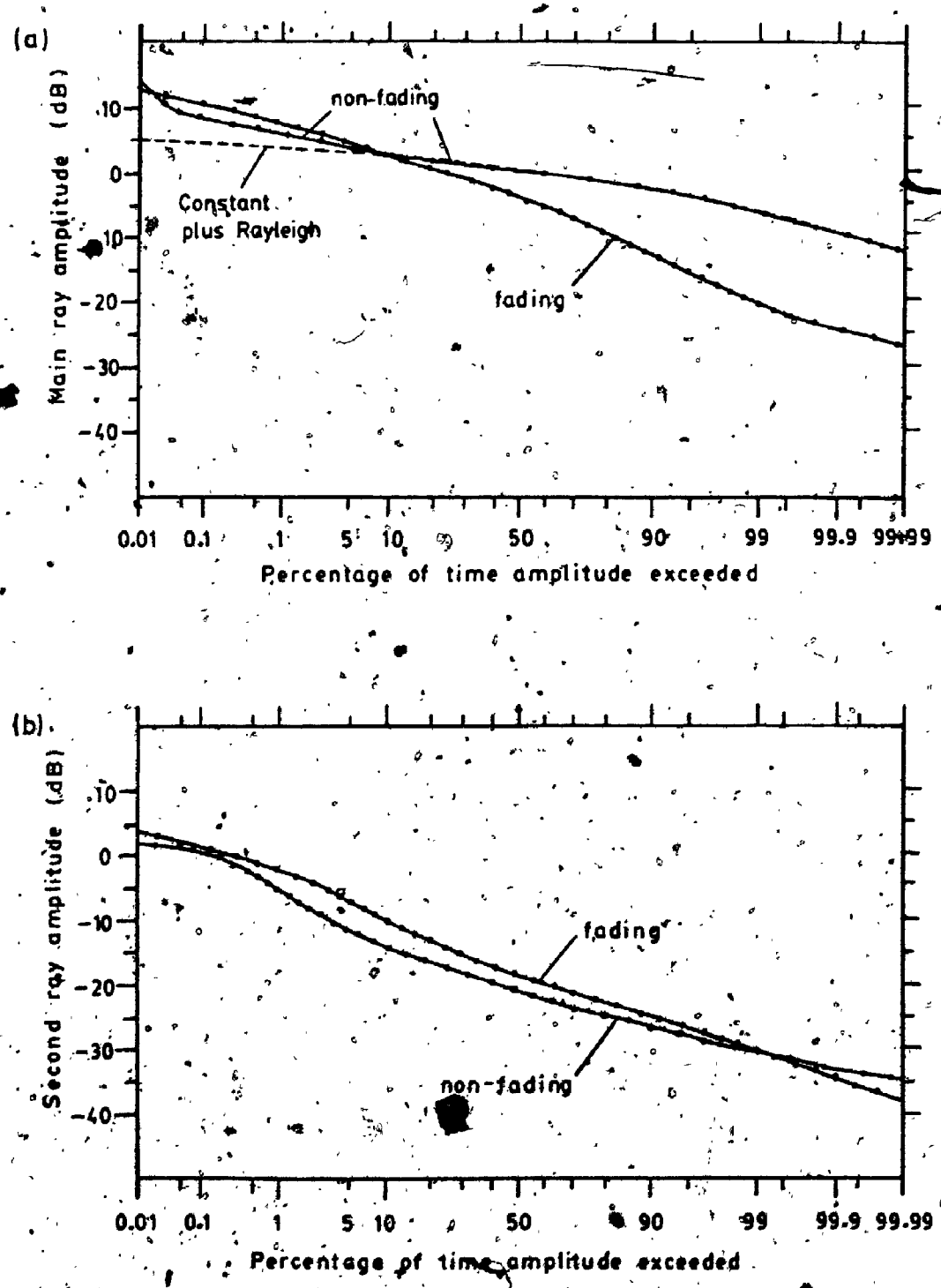

Fig. 6.16 Distributions of the ray amplitudes in the 1981 experiment plotted on Normal Probability paper.

6.7 Summary

Some aspects of microwave propagation across the Bay of Fundy have been examined with reference to the results obtained from two propagation experiments. The propagation characteristics during non-fading periods are, in most cases, well explained by a model of a uniform refractivity gradient.

Propagation conditions during fading periods are highly variable. The experimental results, however, point to two major causes of heavy fading -- namely, the sea reflection and atmosphere layers.

Although the reflected ray is effectively blocked by North Mountain under normal conditions, such is not the case during fading periods. The presence of a layer below the antennas will cause an increase in the clearance of the reflected ray at North Mountain and consequently an increased amplitude. This, combined with occasional severe defocussing in the direct ray, can lead to extremely deep fades in the received signal.

From the maximum delay time values observed during the experiment, the layer strength ΔN of most atmospheric layers in the Bay of Fundy was estimated to be less than -30 NU. Only on one occassion was a value of close to -50 NU observed.

Chapter 7

THE STATISTICS OF SIGNAL FADING

7.1 Introduction

In the design of receiving equipment and communication systems to meet certain reliability objectives, a knowledge of the statistics of signal fading is often required. For example, the statistics of fade depth distribution allows an estimate to be made of the probability of occurrence of fades which will exceed a given fade depth so that adequate receiver fade margins can be incorporated in the equipment design.

From the propagation point of view, it is informative to compare fading statistics observed on propagation paths with different path geometry and terrain characteristics. Conclusions drawn from detailed propagation studies for one particular propagation path may then be related to the fading characteristics observed on paths with similar fading statistics.

The statistics of fade depth distribution obtained for both the 1980 and 1981 experiments are presented in this chapter.

7.2 Signal Level Distributions

7.2.1 Statistical Models

The signal statistics that are of interest in propagation work are: (a) the probability $P(V \leq L)$ that the normalized signal amplitude V is below a given level L, (b) the number of fades N(L) below a given level L, and (c) the average duration $\bar{t}(L)$ of fades corresponding to a given signal level L. In addition to these fading statistics, the distribution of signal level enhancements are also of interest.

Various distribution functions are available for describing the statistical behaviour of fading signals. A function which is commonly used as a reference, with which experimental results are compared, is the Rayleigh distribution. The appropriate form for describing signal fading is given by [39]

$$P(V \leq L) = 1 - \exp(-L^2) \qquad (7.1)$$

where V is the normalized signal amplitude (usually normalized to the root-mean-square value), and L is the signal level. Eq. (7.1) is in fact a normalized form of Eq. (2.20). As discussed in Section 2.4.3, the Rayleigh distribution describes the amplitude of a resultant vector which is the sum of a large number of random interfering vectors. Each of these random vectors has an amplitude which is normally distributed about zero and a phase which

is uniformly distributed in the interval from 0 to 2π .

In line-of-sight tropospheric propagation, the conditions for a Rayleigh distribution are not always satisfied. However, it has been pointed out that the restrictive conditions under which the Rayleigh distribution was derived are sufficient but not necessary conditions for the amplitude V to be Rayleigh distributed [21], [45]. Therefore, the number of interfering signals need not be large.

In some cases the resultant signal is the sum of a Rayleigh component plus a main or direct signal. The distribution of the resultant amplitude for these cases was studied in detail by Norton et al. [39] and tables of values of the probability distribution of the amplitude of a Constant vector plus a Rayleigh-distributed vector were prepared for different values of the mean power in the Rayleigh component.

Another distribution function which is found in literature on fading statistics is the m-Distribution derived by Nakagami [22]. This is a general distribution function the shape of which may be varied to fit various experimental distributions by adjusting a parameter m. However, the practical application of this function is less common due to its somewhat more complex functional form. Nevertheless, it is interesting to note, that the m-Distribution includes the Rayleigh distribution and the one-sided Gaussian distribution as special cases.

In the design of communication systems to satisfy certain reliability requirements, the emphasis is often placed on the deep fade region. Based on a theoretical model in which the fading signal $Ve^{j\phi}$ is composed of a constant unit vector plus a resultant interfering vector $Re^{j\theta}$, such that

$$Ve^{j\phi} = 1 + Re^{j\theta} = 1 + \alpha + j\beta \qquad (7.2)$$

Lin [45] shows that, in the deep fade region, the statistics of the fading signal obey the power laws of deep fades:

$$P(V \leq L) \propto L^2 \qquad (7.3)$$

$$N(L) \propto L \qquad (7.4)$$

$$\bar{t}(L) \propto L \qquad (7.5)$$

for small L

The above relationships appear to be applicable to a wide class of fading problems with the variables R and θ either dependent or independent; θ uniformly or non-uniformly distributed; and α and β either Gaussian or non-Gaussian. The only requirement stated is that the interfering vector be described by a joint probability density function $f(\alpha, \beta)$ and that it represents the resultant of all the extraneous signals, noise, echoes, and rays. The power laws in Eqs. (7.3) to (7.5) will then hold provided that $f(\alpha, \beta)$ is a smooth function which is

neither singular nor zero at the deep fade point ($\alpha = -1, \beta = 0$).

Furthermore, Lin also shows that if $f(\alpha, \beta)$ is singular at $(\alpha = -1, \beta = 0)$, the corresponding relationships, for small L, becomes

$$P(V \leq L) \propto L^{2\mu} \qquad (7.6)$$

$$N(L) \propto L^{2\mu-1} \qquad (7.7)$$

$$\bar{t}(L) \propto L \qquad (7.8)$$

$$1 > \mu > \tfrac{1}{2}$$

From Eq. (7.6) it is seen that, for $\mu < 1$, the probability of deep fades decreases at a slower rate than the square law relationship in Eq. (7.3). The set of equations (7.6) to (7.8) thus describes fading conditions which are more severe than those which obey Eqs. (7.3) to (7.5). The most severe fading corresponds to the case when $\mu = \frac{1}{2}$ and this is said to apply to certain over-water radio links on which a strong water-reflected ray exist as a dominant component of the interfering vector.

For radio path designs, the International Radio Consultative Committee (CCIR) proposed a formula for estimating the overall probability of fading, $P(V \leq L)$, for deep fades (fade depths exceeding about 15 dB). The empirical formula for the worst fading month is [46], [47]

$$P(V \leq L) = K.Q.L^2.f^B.d^C \qquad (7.9)$$

where K and Q are factors for climatic and terrain

conditions, d is the path length in km, f is the frequency in GHz, and B and C are empirical constants which have values of 1.0 and 3.0 for the United States. Values of K and Q are also tabulated for various climatic and terrain conditions.

7.2.2 Previous Experimental Findings

The available experimental evidence appears to support the square law relationship for the amplitude distribution in the deep fade region. Babler [48] presented results at 6 GHz for an experiment performed on a 42.5 km over-land path in Atlanta which well support the square law relationship. Other studies conducted by Barnett [49] and Vigants [50] at 4, 6, and 11 GHz on a 45.9 km over-land path also produced results which are in accordance with the relationships given in Eqs. (7.3), (7.4), and (7.5). In addition, Barnett's results also support a linear frequency dependence of the fade depth distribution (see Eq. (7.9)). It is noted that the fd^3 dependence of the fade depth distribution, where f is the frequency and d is the path length, was originally derived by Ruthroff [51].

Similar results were reported for a 14 GHz experiment conducted in Denmark by Stephansen and Mogensen [52] who also presented one of the few available sets of empirical distributions of signal enhancements which follow the relationship $P(V \geq L) \propto L^{-4.5}$.

7.3 Experimental Results on Fade Depth Distributions

7.3.1 General Descriptions

The propagation experiments performed across the Bay of Fundy were not configured for the study of fading statistics. Only one sweep record was taken every 10 s. Statistics on the number and duration of fades were not generated since most fades have durations of less than 10 s. Nevertheless, statistics on fade depth distribution may be generated and compared with theoretical predictions, assuming that the 10 s sampling interval only has the effect of reducing the sample size.

The probability distribution of fade depth, $P(V \leq L)$, was generated by dividing the total number of data points of level $V \leq L$ by the total sample size. This was performed for both experiments using the signal level at the base frequency (9.5 GHz) of each sweep record. Although an averaging technique may be employed to include all data at different frequencies within the sweeps, it was decided that such a technique may create undesirable side effects due to frequency dependent factors and differences in the reference signal levels for different frequency steps within sweeps. In any event, the results do seem to indicate an adequate data base in using only the data at the base frequency, at least for the 1981 experiment which provides data for a 35-day period.

Due to less than ideal equipment alignment in the 1980 experiment, reliable results were obtained only for signal levels from 10 dB down to approximately -30 dB (both relative to the normal signal level). In the 1981 experiment, improvements made to the receiving equipment produced reliable results from 10 dB down to -36 dB relative to the normal level.

In computing the signal level distributions for both experiments, the reference 0 dB level used in each experiment are the median signal levels for the respective data bases. Furthermore, signal level distributions for the non-fading data, the fading data, and the complete data bases were computed for each experiment.

7.3.2 Signal Fading Statistics

The signal level distributions for the 1980 data are shown in Fig. 7.1 for the non-fading, fading, and the complete data bases. A regression technique was used to fit the results for fade depths exceeding 15 dB. The results indicate a square law relationship for both the fading data and the entire data base, corresponding to a value of $\mu = 1$ in Eq. (7.6).

Also plotted in Fig. 7.1 is the predicted distribution for the worst fading month using the CCIR formula given in Eq. (7.9). In comparing the experimental results with the CCIR prediction, a few points are noted. First, the 1980 experiment did not correspond to the worst fading month.

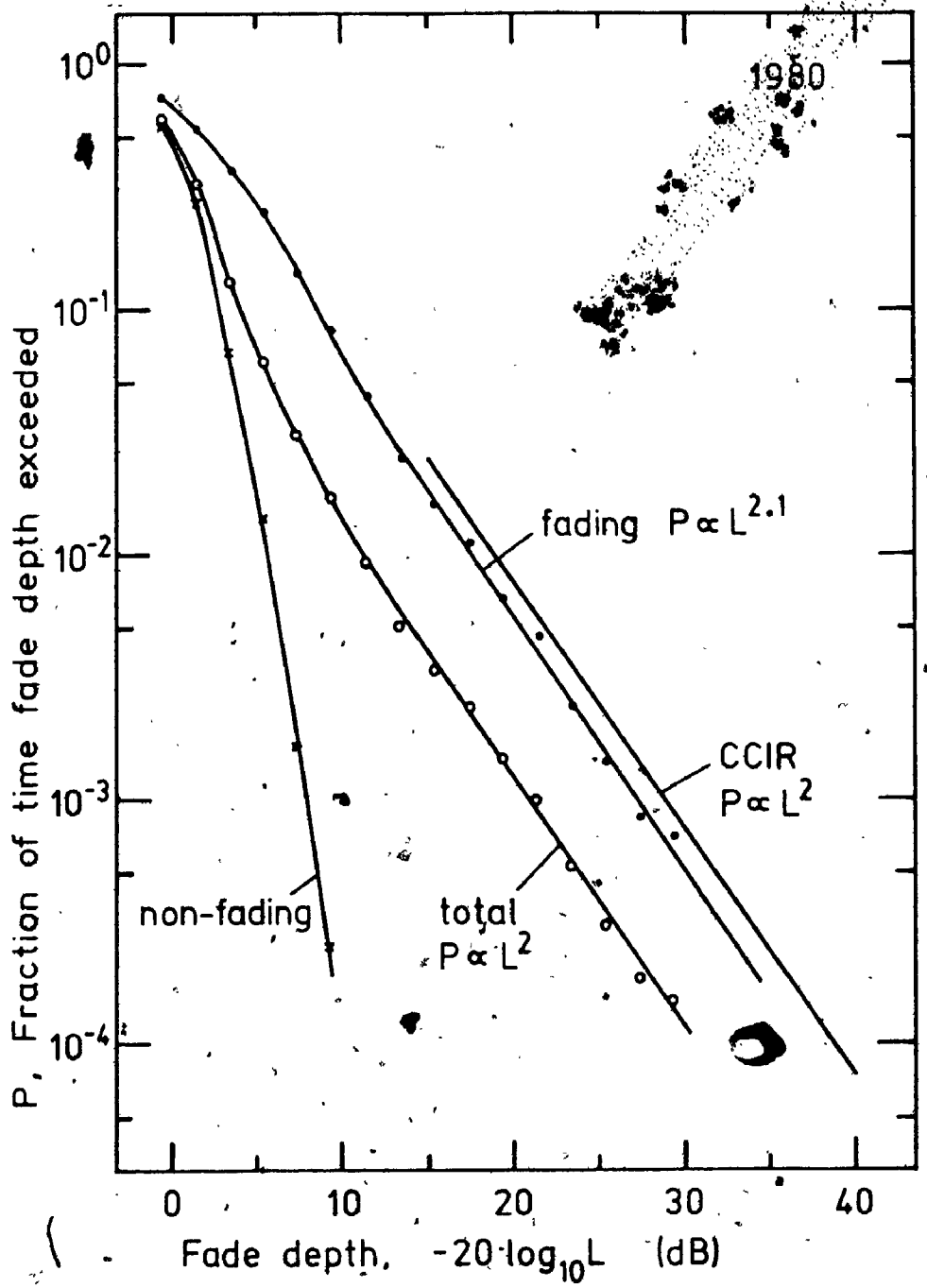

Fig. 7.1 Fade depth distributions for the non-fading data, fading data, and the total data bases in the 1980 experiment.

Second, the data base for the experiment consists of ten days of data selected not completely at random over an extended period. The empirical relationship describing the fade depth distribution for the 1980 results is

$$P(V \leq L) = 0.14\ L^{2.0} \quad \text{for } L < 0.18 \qquad (7.10)$$

The signal level distributions for the 1981 experiment are shown in Fig. 7.2. The CCIR predicted distribution (for the Otter Lake - Nictaux South path) is also included for comparision. The most important result is that a $P(V \leq L) \propto L^{1.6}$ relationship was obtained (using a regression fit for results less than -15 dB) instead of the $P(V \leq L) \propto L^{2.0}$ relationship obtained for the 1980 results. This corresponds to a value of $\mu = 0.8$ in Eq. (7.6). The fact that the limit of $\mu = 0.5$ is not attained is partly attributed to the partial blockage offered by North Mountain. Although the fading mechanism during severe fading -- namely the defocussing effect of the direct ray and the increased clearance (and thus increased amplitude) of the reflected ray, should be kept in mind when studying the results.

The CCIR prediction for fading in the worst month for this propagation path is seen to be too optimistic by a factor of 2.5 at the 30 dB fade level and 3.6 at the 40 dB level.

The empirical relationship for the fade depth distribution on the Otter Lake - Nictaux South path for the

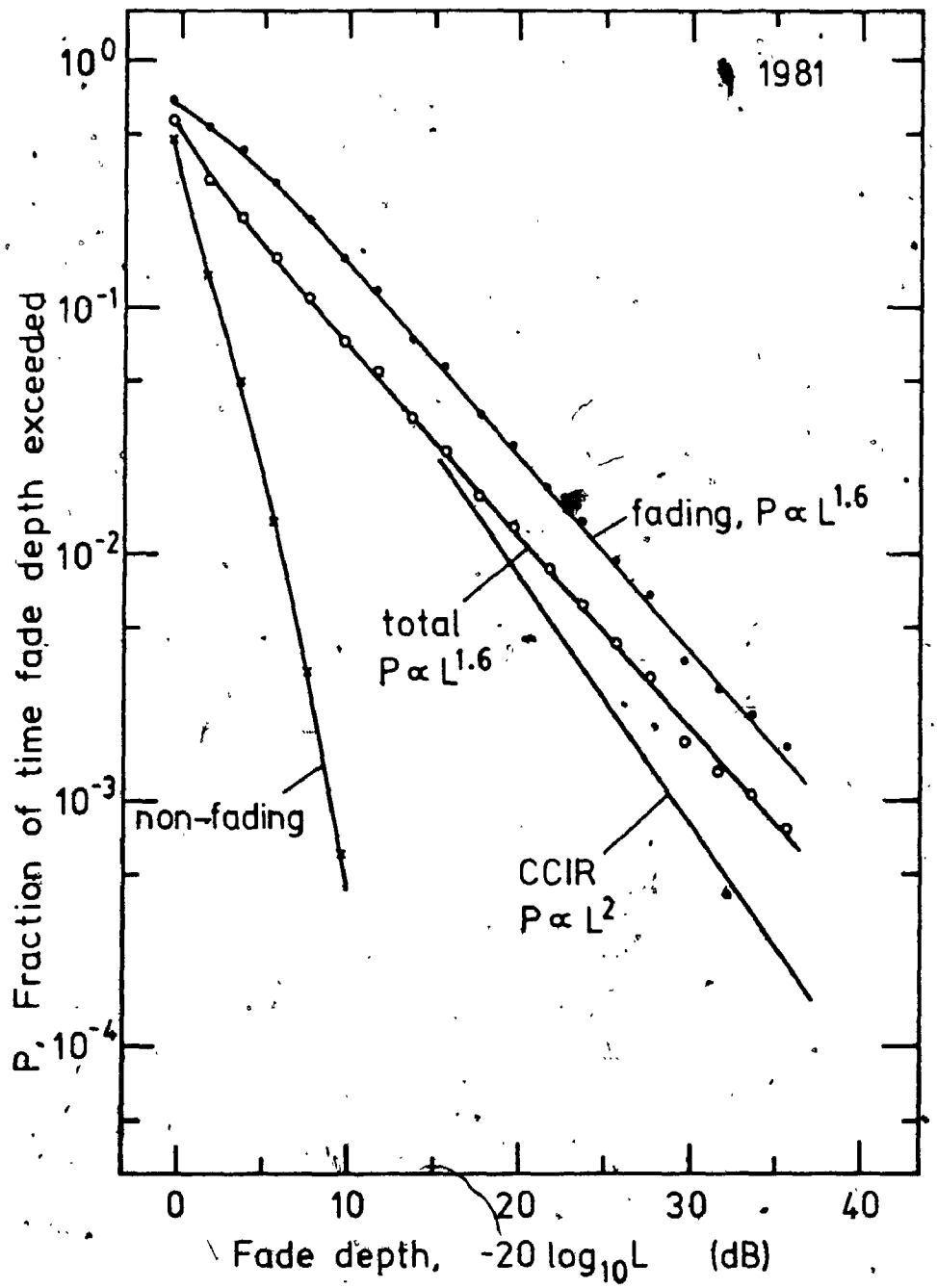

Fig. 7.2 Fade depth distributions for the non-fading data, fading data, and the total data bases in the 1981 experiments.

1981 results is

$$P(V \leq L) = 0.91\ L^{1.6} \quad \text{for } L < 0.18 \qquad (7.11)$$

7.3.3 Signal Enhancement Statistics

The statistics for signal enhancements above the median level are summarized in Figs. 7.3 and 7.4 for the 1980 and 1981 results respectively. Also plotted are the enhancement statistics given by Stephansen and Mogensen [52] for an over-land path at a frequency of 14 GHz. To allow comparison with the Stephansen and Mogensen results, the empirical relationships for signal enhancement (fitted using a regression technique) were computed. These are:

(1) Aylesford - Otter Lake, 1980

$$P(V \geq L) = 0.54\ L^{-7.8} \quad 1.25 < L < 2.8 \qquad (7.12)$$

(2) Otter Lake - Nictaux South, 1981

$$P(V \geq L) = 0.65\ L^{-3.9} \quad 1.25 < L < 2.8 \qquad (7.13)$$

(3) Stephansen and Mogensen [52]

$$P(V \geq L) = 0.059\ L^{-4.5} \quad 1.25 < L < 3.6 \qquad (7.14)$$

The much higher probability of signal enhancements in the 1981 experiment compared with the Stephensen and Mogensen results is thought to be due to more frequent occurrences of atmospheric layers in the Bay of Fundy. The more frequent occurrences of multipath propagation then lead to

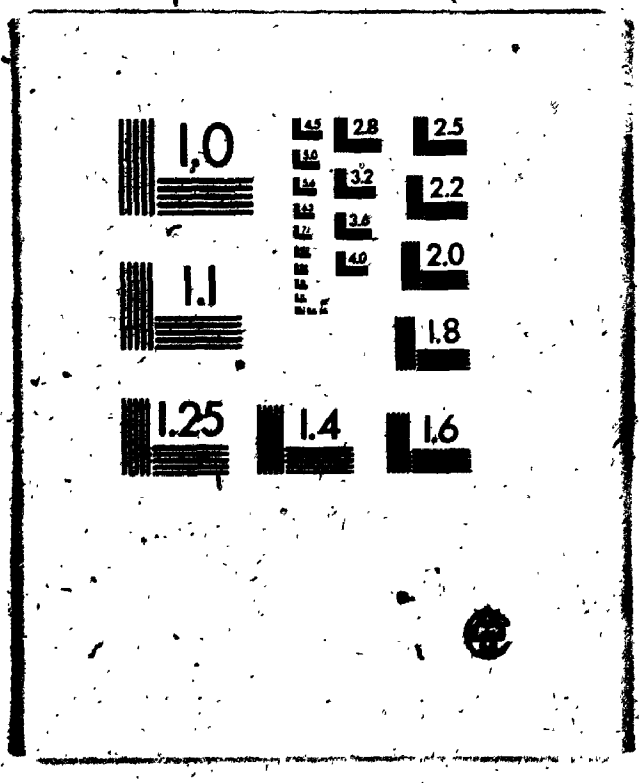

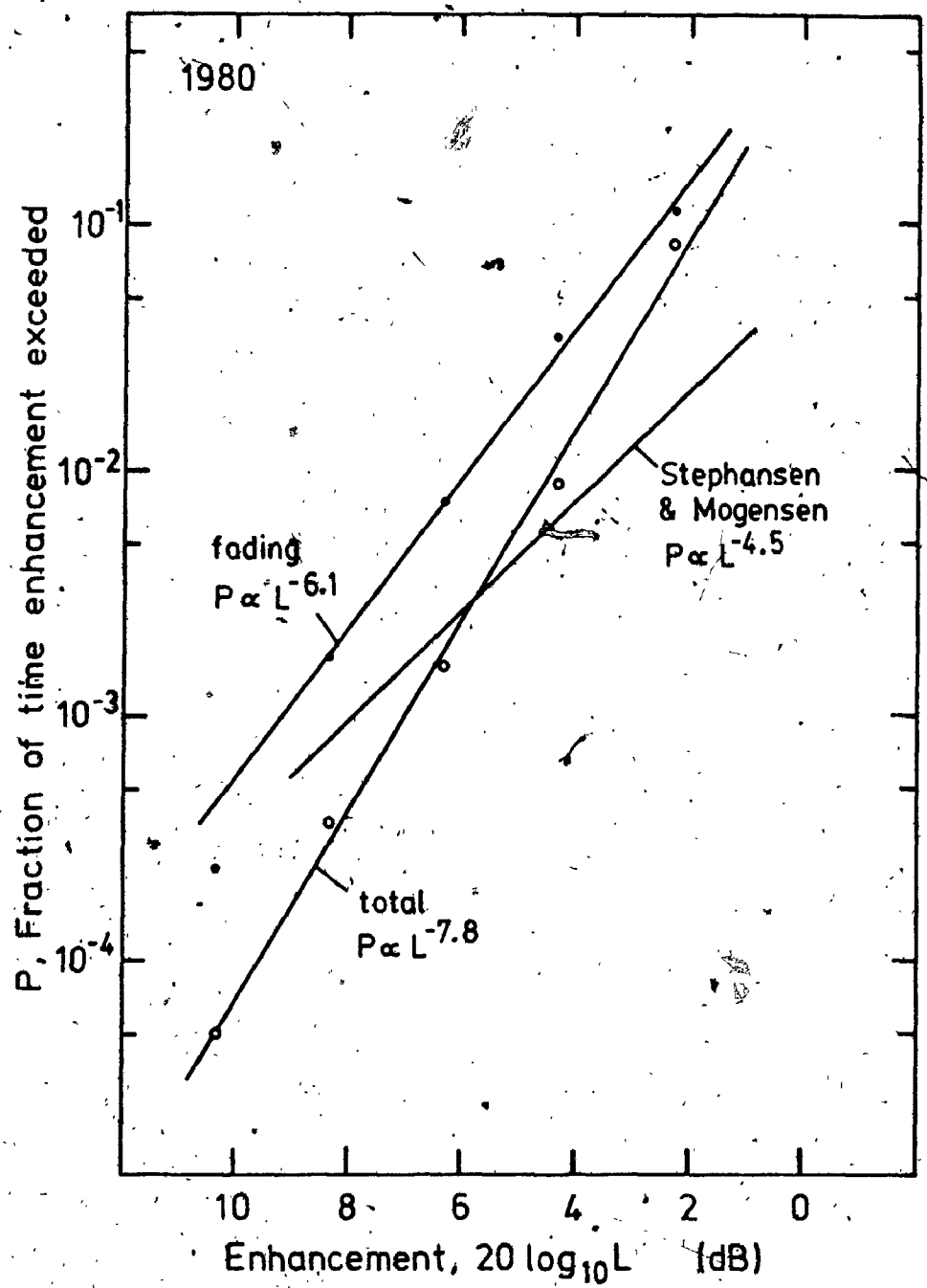

Fig. 7.3 Distributions of signal enhancement for the 1980 experiment.

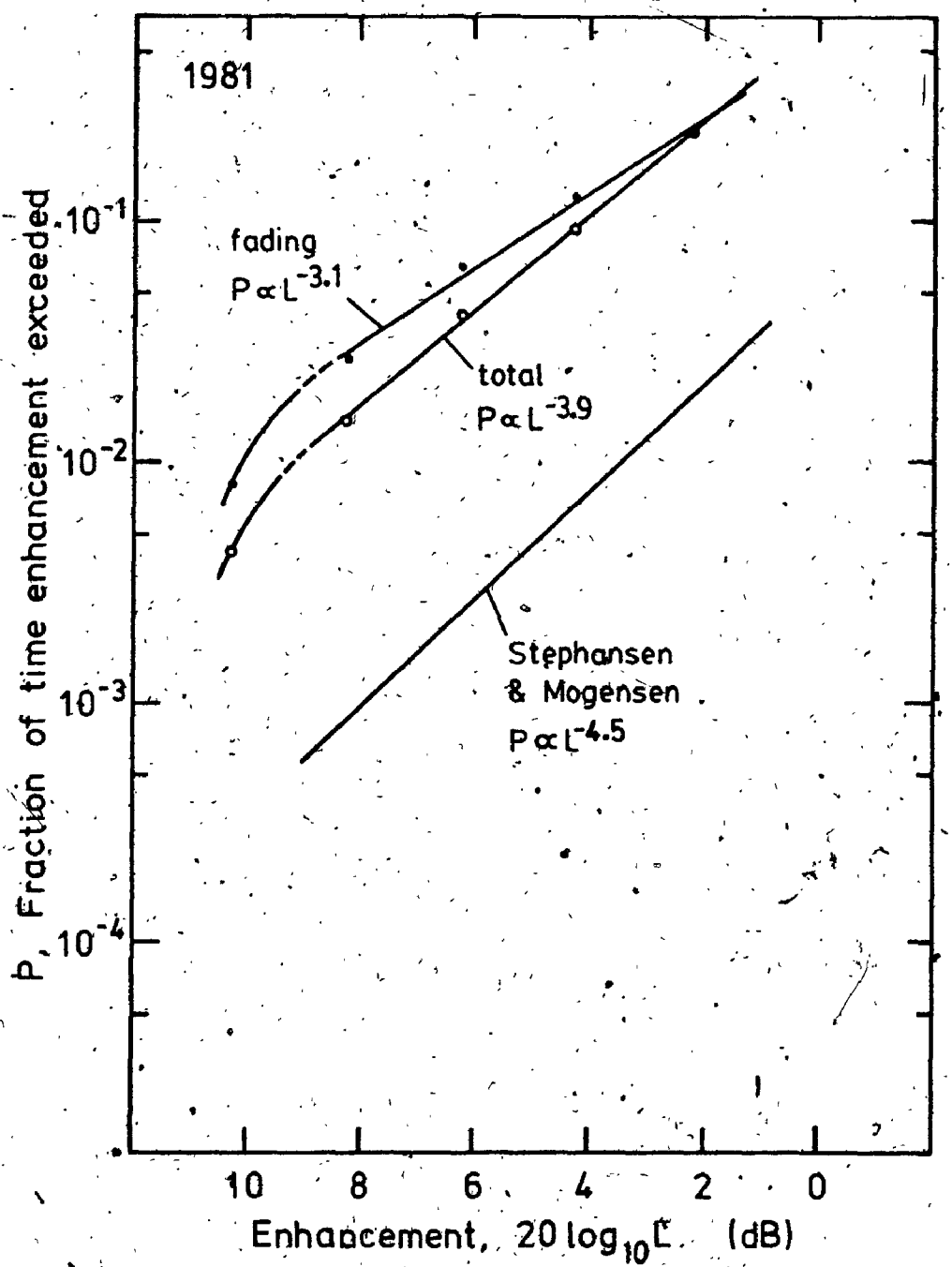

Fig. 7.4 Distributions of signal enhancement for the 1981 experiment.

a higher probability of signal enhancements.

7.3.4 Other Aspects

It is informative to plot the signal level distributions on Rayleigh Probability Coordinates so that comparisons may be made with the theoretical Rayleigh distribution. The results for both experiments are presented in Fig. 7.5. Also plotted in the same figure are the theoretical Rayleigh distribution and the Constant Plus Rayleigh distribution (power in the Rayleigh distributed vector is -6 dB relative to the constant vector). The 1980 experimental results appear to be in good agreement with the Constant Plus Rayleigh distribution. Another interesting point noted is that the shape of the distribution for the 1980 results is very similar to that presented by Albrecht et al. [53] for an 88 km path across the English Channel. The propagation path for the 5 GHz experiment across the English Channel is also open to sea reflection and comparable antenna elevations above the sea surface were used.

While the distributions for the 1980 results are well approximated by a Constant Plus Rayleigh distribution, the results for the 1981 experiment indicated fading conditions that are more severe than Rayleigh fading. Similar observations were also reported by Gudmandsen and Larsen [54] for two oversea paths in Denmark. The importance of atmospheric layers as controlling factors in signal fading

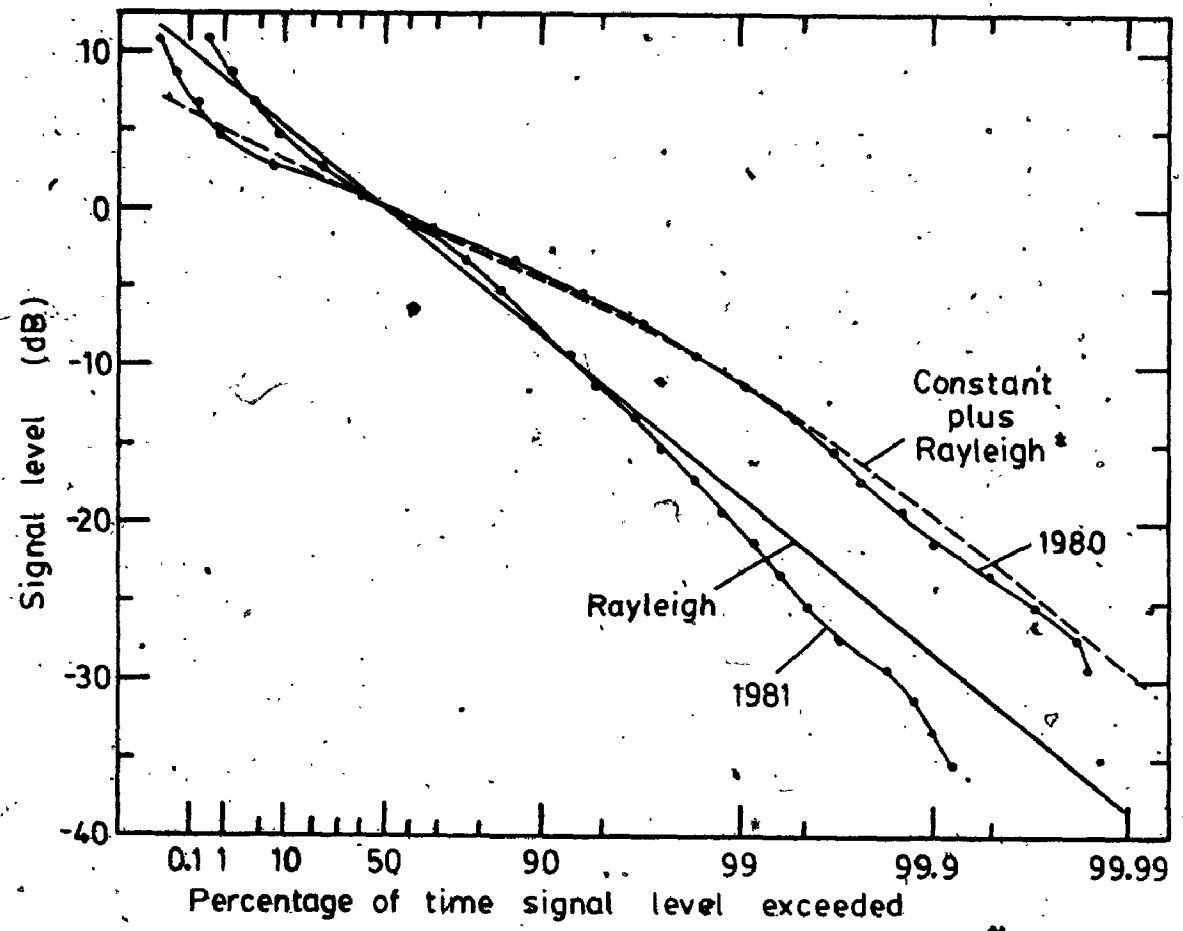

* Rayleigh vector is -6 dB in power relative to constant vector.

Fig. 7.5 Signal level distributions for the 1980 and 1981 experiments plotted on Rayleigh Coordinates.

is partly demonstrated in the 1981 results in that more severe fading was observed even with better terrain blockage to the reflected ray.

7.4 Summary

The statistics of fade depth distribution and enhancement distribution have been presented for the two propagation experiments performed across the Bay of Fundy. The distributions were compared with theoretical predictions and also with existing experimental results available in the literature.

Significant differences were observed between the results obtained from the two experiments. In particular, a $P(V \leq L) \propto L^2$ relationship is applicable to the 1980 results while $P(V \leq L) \propto L^{1.6}$ was obtained for 1981. The differences are attributed to the differences in the path characteristics as well as seasonal variations -- the 1981 experiment being performed in the fading season. The same may be said for the enhancement results which are compared with those obtained by Stephansen and Mogensen. The amount of signal enhancement observed in the 1981 experiment is substantially larger than that reported in the literature.

The overall signal level distribution for 1980 is well approximated by a Constant Plus Rayleigh distribution. For the 1981 results, the fading observed is more severe than

Rayleigh fading despite more effective terrain blockage under normal conditions.

Chapter 8

THE DIGITAL RADIO

8.1 Introduction

Microwave digital radio systems are rapidly replacing conventional analog radio systems in short-haul telephone transmission applications. Typical wideband digital radio systems occupy bandwidths of 30 MHz (in the United States) and 40 MHz (in Canada). Because of the wide bandwidth and the modulation techniques required for bandwidth efficient transmission, these radio systems are vulnerable to the distortion effects caused by frequency selective multipath fading. New approaches to the design of radio paths for digital radio links therefore are required.

A review of digital radio basics as found in the literature is given in Section 8.2 with emphasis on distortion effects associated with multipath propagation. The performance of a digital radio installed across the Bay of Fundy during the 1981 experiment is then examined in Section 8.3 in relation to the results obtained from the propagation experiments.

8.2 Microwave Digital Radio Systems

8.2.1 Background

Due to the increasing demand for the transfer of digital information, radio systems employing digital modulation techniques are finding widespread applications in telecommunications. In addition, digital radios offer economic advantages and allow for easy interfacing to digital switching and terminal equipment. In terrestrial line-of-sight communication systems used in telephone transmission applications, the predominant trend is to use digital radio equipment on new radio routes, and to overbuild them onto the existing analog system.

The complexity of digital radio systems prohibits a detailed description to be included in this thesis. Instead, relevant aspects of digital radio systems are discussed so that the performance of the digital radio installed across the Bay of Fundy may be examined in the light of the results from the propagation experiments.

The performance of a digital transmission system is usually measured in terms of the probability of error P(e) in the digital output. This P(e) term, sometimes also referred to as the Bit-Error-Rate (BER), represents a statistical average of the ratio of the average number of bits in error to the average number of transmitted bits in a sufficiently long measurement interval [34]. A commonly used gating period is 300 ms [29], [34]. An outage then is

said to have occurred on the radio system when BER $> 10^{-4}$ for a period of time longer than 300 ms.

Two other criteria which are often quoted in the literature for describing system performance are [29]: (a) the outage probability which is the probability of occurrence of a system outage, and (b) the effective system fade margin, defined as the fade depth which has the same probability as the observed outage probability.

Various modulation techniques are being used in digital radio systems, these include:

(1) Amplitude Modulation (AM) techniques, e.g. Quadrature Amplitude Modulation (QAM) and Quadrature Partial Response (QPR);

(2) Frequency Modulation (FM) techniques, e.g. Frequency Shift Keying (FSK);

(3) Phase Modulation (PM) techniques, e.g. Phase Shift Keying (PSK); and,

(4) Hybrid AM/PM techniques, e.g. Amplitude and Phase Shift Keying (APK).

A thorough comparison of these various modulation techniques is found in Oetting [55]. In most cases the choice of the modulation technique is dictated by the required spectral efficiency which is measured by the signalling speed per unit RF bandwidth (in bits/s/Hz). To improve the spectral efficiency, most high capacity digital radio systems use multi-level signals instead of binary signals, thus giving rise to multi-level modulation

schemes. In a M-ary (M-level) transmission system, each transmitted symbol represents n information bits, where $n = \log_2 M$. A typical example is 8-ary PSK which is commonly employed in digital radio systems used in the United States.

Digital radio systems employing different modulation techniques are usually compared by their P(e) performance versus the carrier-to-noise (C/N) ratio under conditions of Additive White Gaussian Noise. This is shown in Fig. 8.1 for various commonly used modulation techniques.

8.2.2 Propagation Impairments on Digital Radio Systems

The major impairment in wideband digital radio systems is in-band distortion which includes both amplitude distortion (due to an in-band amplitude null or amplitude slope) and delay distortion. The effect of in-band distortion is to cause inter-symbol interference and consequently a degradation in the P(e) performance.

Computer and laboratory simulations of P(e) degradation caused by in-band distortion have been reported in the literature [35],[56],[57]. Results of P(e) versus (C/N) for a 30 MHz bandwidth, 8-PSK digital radio as presented by Lungren and Rummler [56] are shown in Fig. 8.2. The term "in-band selectivity" in Fig. 8.2 is defined as the difference between the maximum and minimum attenuation present in the transmission channel bandwidth. The asymptotic behaviour for large (C/N) values are

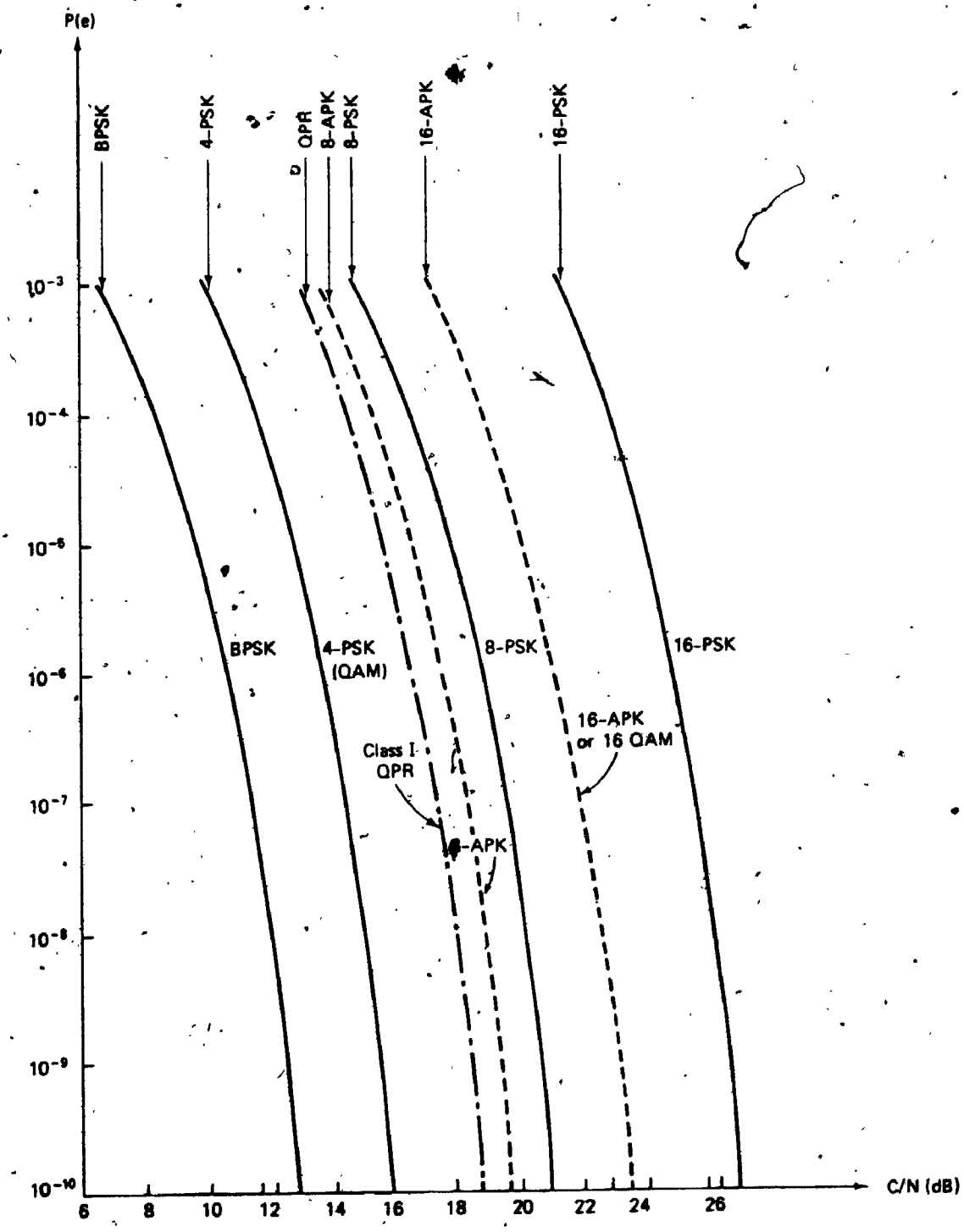

Fig. 8.1 P(e) performance of M-ary PSK, QAM, QPR, and M-ary APK coherent systems. The rms C/N is specified in the double-sided Nyquist bandwidth [34].

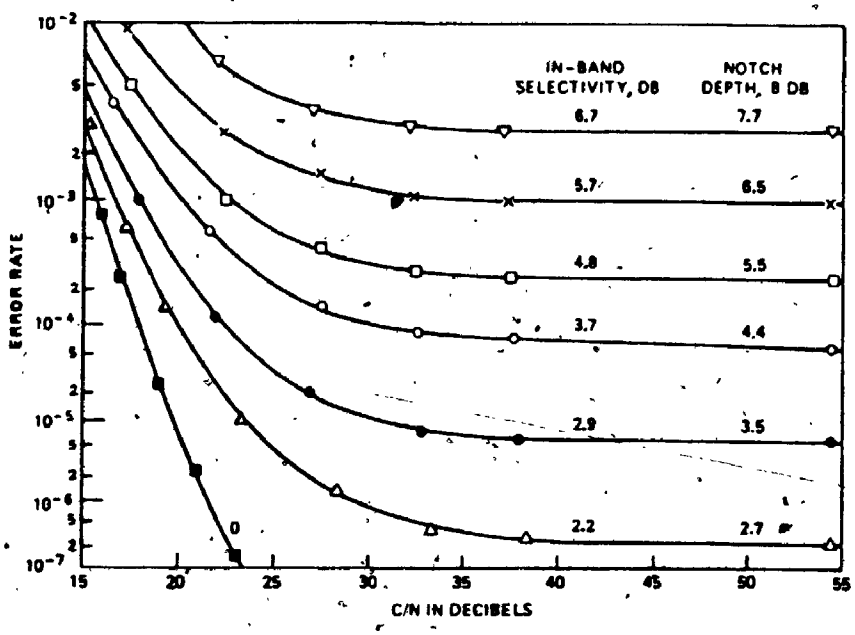

Fig. 8.2 High-speed digital radio IF dispersive fade simulations, τ = 6.3 ns, f_o = -19.8 MHz relative to the centre of the channel where f_o is the frequency at the notch [56].

particular interesting in that when in-band distortion occurs, even a large increase in the transmitted power will not significantly improve the P(e) performance.

Experimental evidence and computer simulations also suggest that of the two types of in-band distortion, the performance degradation caused by amplitude slope is much more severe than that caused by the delay slope [57], [58], [59]. In-band amplitude distortion therefore is a useful parameter for estimating the outage probability of digital radio systems [60].

At least three models have been proposed for modelling the behaviour of the transmission channel for the purpose of evaluating and simulating the performance of digital radio systems under multipath conditions.

Greenstein [35], [61] used a power series model to determine the frequency transfer function of a multipath fading channel and concluded that only two terms of the power series are required for characterizing multipath effects.

Ramadan [58] used a two ray analytic model to represent the transmission channel. Of particular interest is that, based on the two ray model, Ramadan concluded that the relative delay of the additional ray (or echo) during multipath decreases exponentially with the echo amplitude and therefore with fade depth. The conclusion was arrived at by a consideration of the physical path length of the echo and not the phase path length. It appears that the

latter would be more appropriate for such an application. As is pointed out in Webster [43], a substantial difference can exist between the actual time delay (based on the phase path length) and the value calculated based on the physical path length.

Finally, Rummler [62] used a three ray fixed delay model to examine transmission channel characteristics. Based on experimental results he concluded that, for a 30 MHz channel, a model with a fixed delay of 6.3 ns is sufficient for representing all observed channel conditions. However, the fixed delay model is not intended to represent the physical situation and should not be interpreted as such.

Different methods for estimating digital radio outage probability due to multipath propagation have also been reported [63]-[65] for systems employing various modulation techniques and operating at different bit rates. Widely different approaches are usually taken by different authors in estimating the outage probability. For example, Jakes [63] assumed independent fade depth and delay time distribution statistics, with an exponential distribution in delay time; while Rummler [65] calculated the outage on the assumption that the interference due to the transmission channel can be replaced by Gaussian Noise of the same power. In most cases, however, the pertinent conclusion seems to be that, for wideband digital radio systems without diversity protection, the estimated outage

time will exceed the outage objectives required for short-haul transmission over average terrain.

8.2.3 Space Diversity Combining and Adaptive Equalization

In order that availability objectives be met, special techniques are required to improve the performance of digital radio systems under multipath fading conditions. The two most commonly used techniques are space diversity combining and adaptive equalization.

To minimize the effects of multipath fading, space diversity protection is usually employed whereby the strongest signal available from more than one antenna is selected and fed to the receiver. However, in digital radio applications, it is undesirable to switch the radio input between the main and the diversity antennas as the switching process will introduce errors due to the discontinuity. The alternative method is to combine the signals from the main and diversity antennas by using an in-phase combining technique. The combining is usually done at the IF stage. An in-phase combiner is essentially a maximum power combiner [66]. The phase of the signal on one antenna is shifted by a calculated amount before it is combined (added) with the other signal so that the output power from the combiner is maximized. However, a maximum power combiner does not minimize in-band distortion which is the major impairment to digital radio systems.

Wang [66] pointed out that by using a maximum power combiner, a signal with a flat spectrum can combine with one which contains an in-band null (caused by the transmission channel) to produce a signal with an in-band amplitude slope. One common technique therefore is to equalize the amplitude slope from the combiner output by the use of an adaptive amplitude equalizer [59], [66], [67]. The function of such an equalizer is to produce a signal with an essentially flat spectrum.

Extensive experimental results reported by Barnett [28] and Anderson et al. [29] appear to indicate that digital radio systems, when in-phase combining and adaptive amplitude equalization techniques are incorporated, will meet required reliability objectives for short-haul transmission applications.

Both the techniques of in-phase IF combining and adaptive equalization are incorporated in the digital radio installed across the Bay of Fundy.

8.3 Performance of Digital Radio Across the Bay of Fundy

8.3.1 System Reliability Objectives

In order to comply with the requirements of the TCTS, the allowable one-way system unavailability (due to propagation impairment) allocated to the Otter Lake - Nictaux South digital radio hop is 19.5 s per year [68].

The total outage time measured during the severe fading period on Day 241 and 242 in 1981 is 72.2 s. The propagation induced outage on the two worst fading days therefore exceeded the outage time allowance for the whole year.

8.3.2 Experimental Results

The results of the digital radio test is available in the form of low speed (6 cm/h) paper chart records that contain the following parameters:

(a) Protection Channel Main AGC voltage;

(b) Protection Channel Diversity AGC voltage;

(c) Protection Channel Combined AGC voltage;

(d) Protection Channel Eye voltage;

(e) Protection Channel Adaptive Equalizer Stress voltage; and,

(f) Main Channel Eye voltage.

The eye voltage is a good indication of the P(e) performance of the digital radio [35] and consequently is used for indicating system performance degradations.

During the 809-hour period from 31st July (Day 212) to 3rd September (Day 246) in 1981, digital radio performance was observed to show degradation in 97 hours. The temporal distribution of these 97 hours is shown in Fig. 6.1. The data from the 97 hours are used as the data base in the statistical analysis the results of which are presented in Section 8.3.3.

It is seen in Section 8.3.1 that the fading conditions on Day 242 are extremely detrimental to the digital radio. The fading characteristics on Day 242 were discussed in Chapter 6. The ray path parameters and the hours when severe system performance degradation was observed on the digital radio is also shown in Fig. 6.9. Several observations pertinent to the digital radio are noteworthy.

First, a high correlation exists between long delay time and system degradation. As shown in Fig. 6.9, the performance of the digital radio is most severely degraded when the delay time is above 7 ns. Particularly dramatic is the period at 11:30 ADT (Day 242) when the drop in the delay time from 8 ns to 5 ns results in restored performance on the digital radio.

Second, a good correlation also exists between system degradation and the differential amplitude (difference between the amplitudes of the main and second rays). From 02:00 to 06:00 ADT (Day 242), and again from 08:00 to 11:00 ADT, the main and second rays are observed to be very close in amplitude. This correlation is to be expected since two rays with about the same amplitude will result in deep nulls due to interference between the rays as displayed in Fig. 6.10. These nulls, when occurring within the channel bandwidth of the digital radio, will lead to excessive in-band distortion and therefore outages.

To illustrate the combined effects of long delay and deep fades on the digital radio, the measured delay time

and the calculated maximum notch depth for a two hour period from 09:00 to 11:00 ADT (Day 242) are shown in Fig. 8.3 together with the Eye voltages and the Combined AGC voltage on the digital radio. The maximum notch depth of the amplitude nulls caused by the two strongest rays was estimated using the main and second ray amplitudes as measured by the propagation experiment.

To explain the correlation between a long delay time and digital radio outage, a simplified approach is used. Consider a two ray path situation with a relative delay of $\Delta\tau$ between the rays. The equivalent amplitude transfer function of the transmission channel is of the form shown in Fig. 3.3. The amplitude response is periodic in frequency with the nulls separated in frequency by $\Delta f = (1/\Delta\tau)$ as given in Eq. (3.8).

Consider now a wideband radio system having a bandwidth of B Hz and operating on one of the allocated radio channels as shown in Fig. 8.4. Given the condition that two rays are received, the probability, P_n, that the radio channel will contain an in-band null is given by

$$P_n = \frac{B}{\Delta f} = B.\Delta\tau \qquad (8.1)$$

For a fixed radio bandwidth, the probability of the radio channel containing an in-band null therefore is directly proportional to the delay time. The probability of a null occurring within channels of bandwidth 30 MHz and 40 MHz versus the delay time, given the condition that two ray

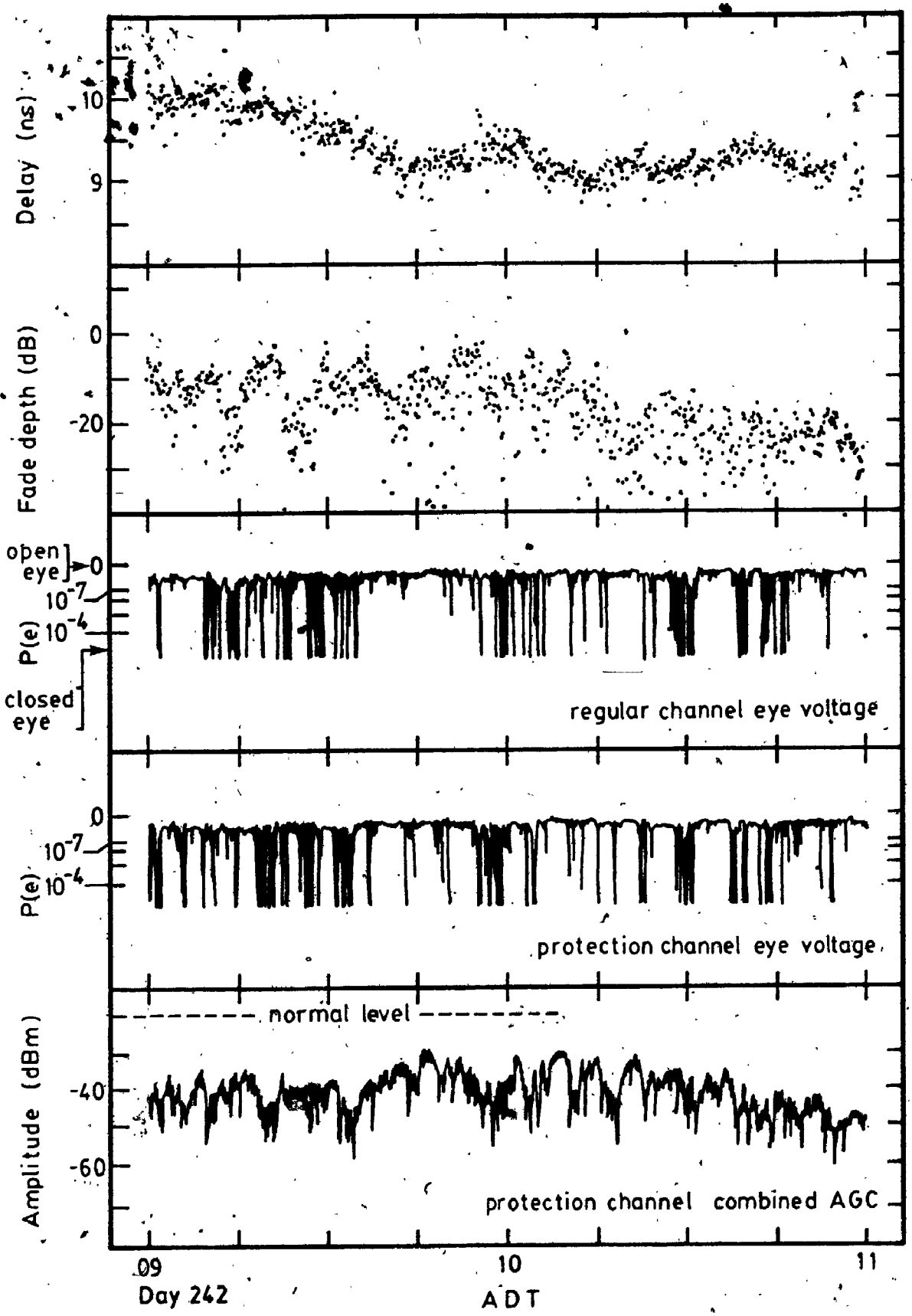

Fig. 8.3 Effect of long relative delay time on digital radio performance.

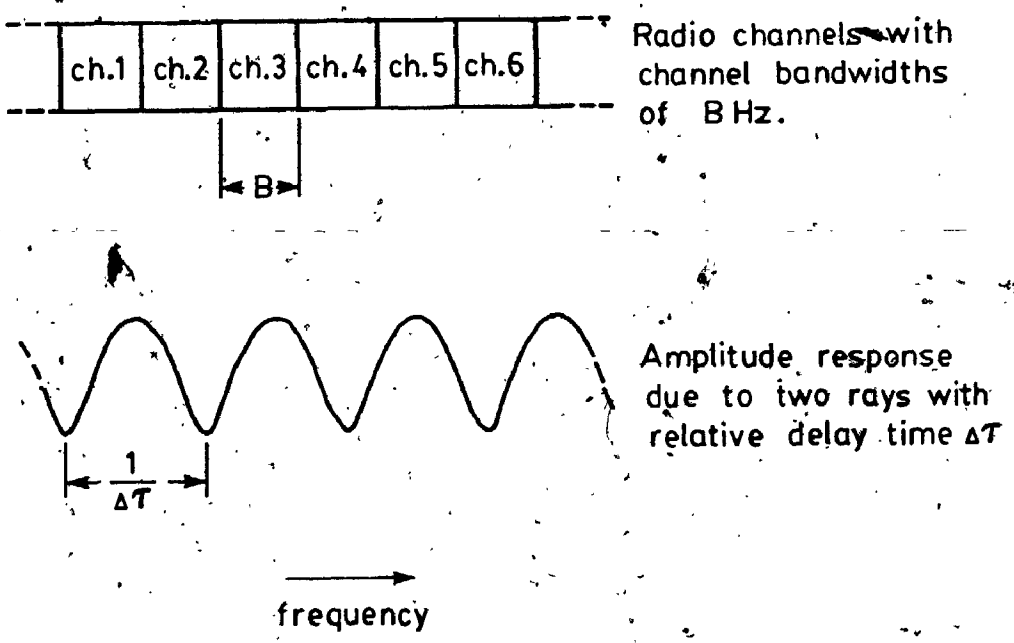

Fig. 8.4 Diagram to illustrate the probability that a particular radio channel will contain an in-band null, given the condition that two ray paths are received.

paths with relative delay $\Delta\tau$ is present, is shown in Fig. 8.5.

The digital radio used in the experiment has a bandwidth of 40 MHz. From Fig. 8.5, it is seen that for a delay time of greater than 8 ns, the probability of an in-band null is greater than 32 %.

The above simple approach has important implications in relation to frequency diversity protection schemes. It is seen that for two ray paths, the frequency separation between nulls is inversely proportional to the delay time. For the range of delay times observed in the propagation experiments, the null separation versus the delay time is plotted in Fig. 8.6. For delay times of greater than 8 ns, the null separation is less than 120 MHz. For 40 MHz bandwidth channels, then, an in-band null will occur on more than one out of three channels as shown in Fig. 8.7. Unless the frequency of the diversity protection channel is properly selected (so that nulls do not occur simultaneously on the regular and the protection channels), no improvement will be offered by switching to the protection channel. A good example is found in the digital radio experiment. The main and protection channel frequencies in the Otter Lake - Nictaux South digital radio test are 7.78611 and 7.86759 GHz -- a separation of 121.5 MHz. As a result, if a two path situation with a delay time of greater than approximately $(1/121.5\times10^{6}) = 8.23$ ns occurs with sufficient fade depth

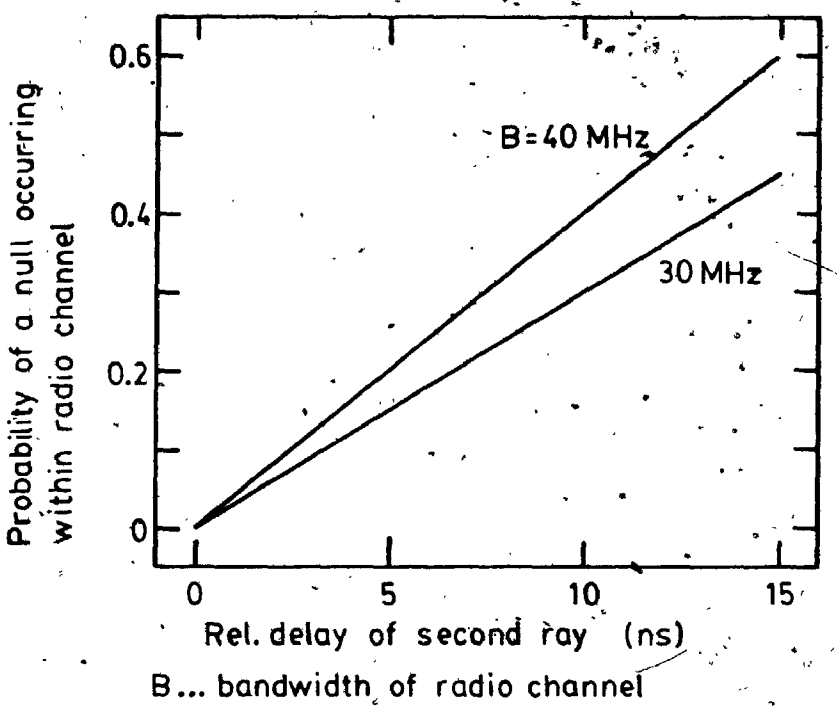

Fig. 8.5 Probability of in-band nulls versus relative delay of second ray.

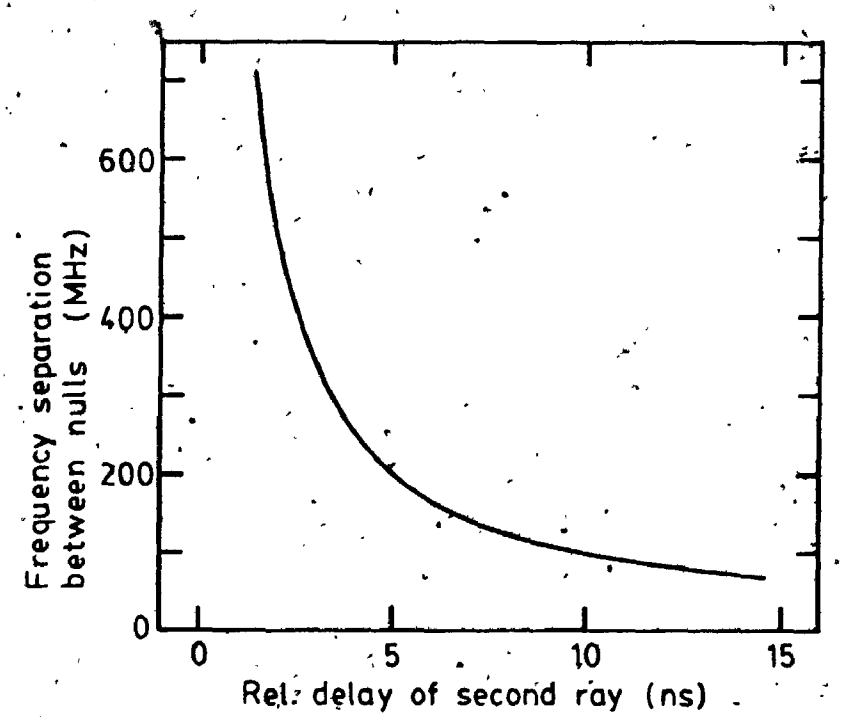

Fig. 8.6 Null separation versus relative delay of second ray.

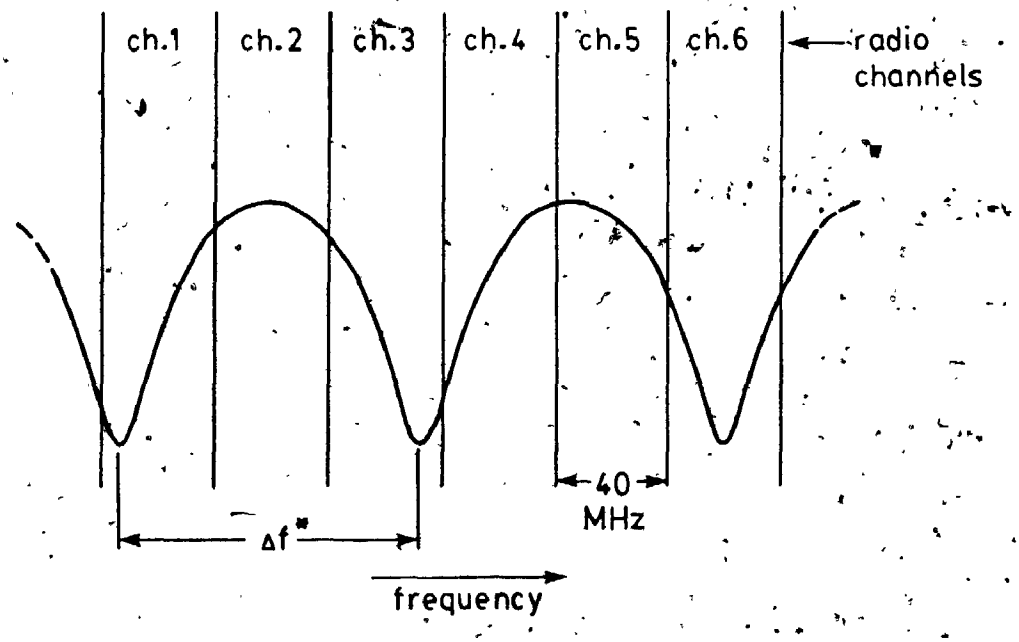

* Δf less than 120 MHz for ΔT larger than ~8.3 ns

Fig. 8.7 Occurrence of in-band nulls on adjacent radio channels with bandwidths of 40 MHz.

to cause excessive BER on the main channel, the same is likely to be occurring on the protection channel and thus a switch to the protection channel will not be successful. The situation is worst when (1xN) protection schemes are used in which one protection channel is used for protecting N regular channels. The above two path condition then will result in a situation in which several channels will suffer simultaneous outages and therefore compete for the protection channel.

8.3.3 Statistical Results

Using as data base the 97 hours when the performance of the digital radio was degraded, the distributions of the delay time, the main and second amplitudes, and the estimated maximum fade depth (cause by the two strongest rays), were computed.

The delay time distribution is shown in Fig. 8.8. The median delay time is 6.8 ns, compared with values of 4.7 ns and 5.8 ns for the non-fading and fading data bases for the same experiment. More important is that the delay time exceeded 8.25 ns for 20 % of the time for this data base, illustrating the correlation between long delay time and digital radio performance degradation.

The ray path amplitude distributions, as well as the distribution of the estimated maximum fade depth, are shown in Fig. 8.9. The median amplitudes of the main and second rays for this data base are -7.5 dB and -17.0 dB

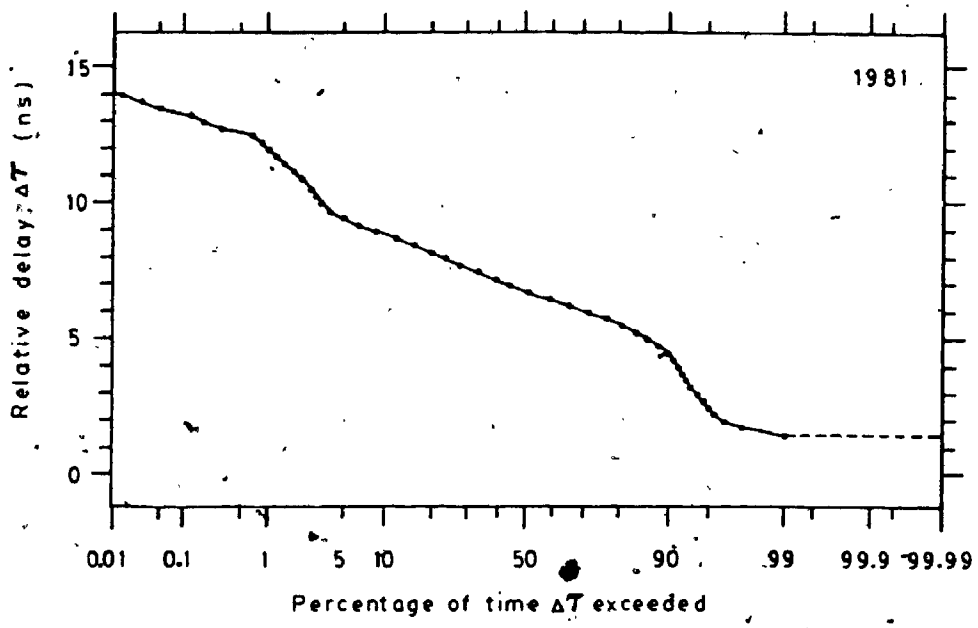

Fig. 8.8 Delay time distribution during periods when the digital radio suffered impairments.

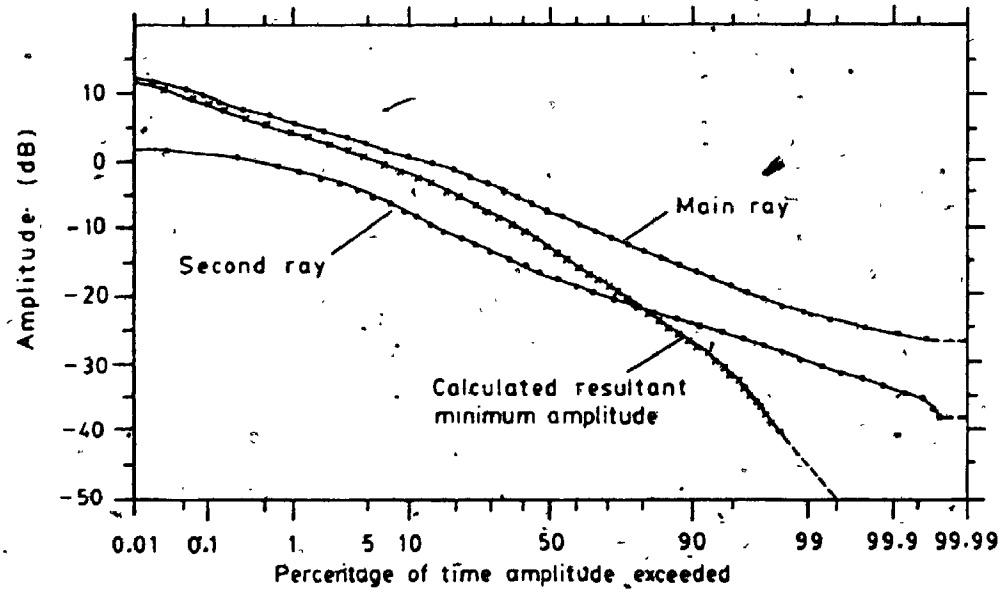

Fig. 8.9 Amplitude distribution during periods when the digital radio suffered impairments.

respectively (compared with median values of -4.0 dB and -18.5 dB for the fading data in the same experiment). These results appear to indicate that the outages on the digital radio are caused mainly by a substantial decrease in the main ray amplitude, accompanied by a relatively modest increase in the second ray amplitude.

The distribution of the maximum fade depth (minimum amplitude) caused by the main and second rays are also shown in Fig. 8.9 and it has a median value of -13 dB. The results indicate that the two rays alone can cause fades of more than 40 dB for more than approximately 2 % of the time.

Finally, it is interesting to note that although there are only 97 hours (12 % of the total data base of 777 hours) during which eye closures were observed on the digital radio, the same 97 hours contain approximately 91 % of all the long delay time values ($\geq$9 ns) recorded in the 1981 experiment. These hours also contain 70 % of all the recorded fades that are in excess of 20 dB in the 1981 experiment.

8.4 Summary

The main impairment to terrestrial microwave digital radio systems is in-band distortion. This includes both in-band amplitude distortion and delay distortion. The

degradation due to amplitude distortion is more severe than that of delay distortion. Digital radio systems which incorporate in-phase diversity combining and adaptive equalization techniques are reported to provide adequate performance on typical over-land LOS paths.

The performance of a digital radio installed across the Bay of Fundy missed the reliability objectives by a wide margin. The poor performance was found to be caused by unusually large delay time values and simultaneous severe fading. The digital radio is particularly vulnerable, in the case of two ray paths, to delay times of the second ray larger than approximately 8 ns. When additional rays are present, the significant decrease in the main ray amplitude (due to defocussing by atmospheric layers) is seen to be an important cause of digital radio failures.

When at least two ray paths exist with a delay time of more than approximately 8 ns, the effectiveness of frequency diversity protection for wideband digital radio systems is significantly reduced. Under such circumstances, the frequency of the protection channel must be carefully selected. Finally, it is noted that at least for the radio paths across the Bay of Fundy on which long delay time values are frequently observed, wide channel bandwidths (e.g. 40 MHz) appear to be rather inadequate choice. Significant improvements should result from the use of digital radio systems occupying narrower bandwidths.

Chapter 9

SUMMARY AND CONCLUSIONS

The propagation of microwave signals across the Bay of Fundy has been examined in this thesis. Two propagation experiments were performed at X-band frequencies on two separate line-of-sight paths across the Bay of Fundy. The results of the experiments provide important insight into the propagation mechanisms which are responsible for the heavy fading activities usually observed in this geographical area.

The major cause of microwave signal fading across the bay is the sea reflection. Although a specularly reflected ray is generally expected and known to exist on such over-water paths, the exact nature and ray path characteristics are not usually well understood. The experimental results indicate that, at a frequency of 10 GHz, the reflected ray is stable and suffers a reflection loss of only a few decibels, except under very rough sea conditions. Under normal conditions of a uniform refractivity gradient, the delay time of the reflected ray relative to the direct ray is of the order of 2.5 ns for the Aylesford - Otter Lake path and 4.5 ns for the Otter Lake - Nictaux South path. The larger delay value is due to the higher antenna heights in the second experiment.

The most severe fading observed across the bay was caused by the presence of atmosphere layers within which exist extreme negative gradients in refractivity. The major influence of atmospheric layers, when they occur below the antennas, are:

(1) to cause defocussing of the direct ray and therefore substantially reduce its amplitude (at times by more than 10 dB);

(2) to improve the clearance of the reflected ray above the underlying terrain and therefore increase its amplitude;

(3) to increase the relative delay time of the reflected ray; and,

(4) to raise the angles-of-arrival of both the direct and the reflected rays.

When the layer occurs at a height such that both antennas are within the layer, atmospheric ray paths are introduced. The delay times associated with such atmospheric paths are usually less than 6 ns for typical LOS paths and therefore are less detrimental to the operation of wideband communication systems.

In the presence of atmospheric layers, the delay time of the reflected ray is frequently increased to longer than 6 ns for the Aylesford - Otter Lake path and 8 ns for the Otter Lake - Nictaux South path. Delay times of higher than 14 ns were observed during one fading period. Long

delay times of this magnitude are found to be extremely detrimental to the proper operation of wideband digital radio systems. In particular, the effectiveness of frequency diversity protection under these circumstances is severely reduced.

A square law relationship for deep fades, $P(V \leq L) \propto L^2$, was obtained for the fade depth distribution of the 1980 results. The more severe fading in 1981 is reflected in a $P(V \leq L) \propto L^{1.6}$ relationship.

These then, are some of the main conclusions drawn from the propagation experiments. It is recognized that, for a subject matter of this scope and nature, the results and conclusions are not exhaustive. Several points therefore are noted for future work.

Although most of the usable data obtained from the propagation experiments have been processed, much valuable information is still contained in the original data. Further analysis of individual sweep frequency records by pattern synthesis should provide insight into various other aspects of microwave propagation. Unfortunately, the process is a rather time consuming task.

The experimental results revealed a weakness in the microwave diagnostic system in that very short delay ray paths are not resolved. Furthermore, these short delay ray paths could lead to spurious variations in the slope of the sweep frequency phase records which otherwise would yield accurate and valuable information on the individual ray

path angle-of-arrival. A different and more reliable scheme for measuring this latter parameter under multipath conditions should be developed.

Finally, it is noted that the Bay of Fundy is an ideal location for investigating various propagation effects which are associated with atmospheric layers due to the relatively frequent occurrence of layers in this region. One important aspect to be studied, for example, is the depolarization effects of such atmospheric layers. It is recommended that any such future study should be accompanied by simultaneous measurements of the vertical profiles of temperature, humidity, and refractivity in the atmosphere.

APPENDIX 1

Dimensions of the first Fresnel Ellipse on the Ground for Specular Reflection on LOS Microwave Links

Consider the reflection from a plane earth surface as shown in Fig. A1.1. The lengths of the semi-axes of the first Fresnel Ellipse are f and g. For the direction perpendicular to the path, the semi-axis g is equivalent to the line-of-sight case for propagation from A' to B as given by Eq. (2.19), thus

$$g = \left[\frac{\lambda R_1 R_2}{R_1+R_2}\right]^{\frac{1}{2}} \qquad \text{(A1.1)}$$

where λ is the wavelength. In the direction parallel to the path, the point P is located such that

$$(r_1 + r_2) - (R_1 + R_2) = \frac{\lambda}{2} \qquad \text{(A1.2)}$$

The cosine rule applied to triangle AOP gives

$$r_1^2 = R_1^2 + f^2 - 2R_1 f.\cos\gamma$$

$$= (R_1 - f.\cos\gamma)^2 + (f.\sin\gamma)^2 \qquad \text{(A1.3)}$$

For most LOS microwave links, the conditions $f \ll R_1$ and $f \ll R_2$ usually are satisfied. Applying the binomial approximation

$$(a + b)^{\frac{1}{2}} \simeq a^{\frac{1}{2}} + \frac{1}{2} a^{-\frac{1}{2}}.b \quad \text{for } a \ll b \qquad \text{(A1.4)}$$

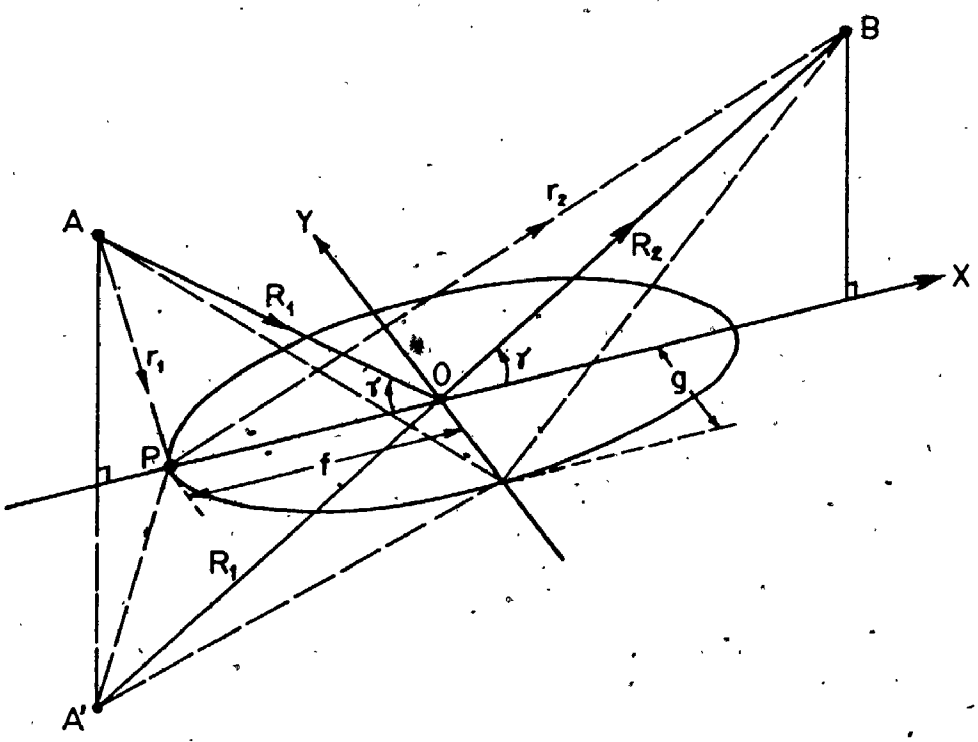

A, B... antennas at the link terminals
A'.....the image of A
O.....reflection point
γ.....angle of reflection

Fig. A1.1 The Fresnel Ellipse in the case of specular reflection on LOS paths.

to Eq. (A1.3) gives

$$r_1 = (R_1 - f.\cos\gamma) + \frac{f^2.\sin^2\gamma}{2(R_1 - f.\cos\gamma)} \qquad (A1.5)$$

For $f << R_1$, Eq.(A1.5) becomes

$$r_1 \simeq R_1 + \frac{f^2.\sin^2\gamma}{2R_1} \qquad (A1.6)$$

Similarly, triangle BOP gives, for $f << R_2$,

$$r_2 \simeq R_2 + \frac{f^2.\sin^2\gamma}{2R_2} \qquad (A1.7)$$

Combining Eqs. (A1.3), (A1.6), and (A1.7) one obtains the length of the Fresnel Ellipse

$$f \simeq \frac{1}{\sin\gamma}\left[\frac{\lambda R_1 R_2}{R_1+R_2}\right]^{\frac{1}{2}} \qquad (A1.8)$$

for reflection from a plane surface.

The case for a curved earth is not as straight forward analytically. However, the earth curvature may be accounted for by the use of a divergence coefficient, D. In the direction parallel to the path, the length of the semi-axis of the first Fresnel Ellipse for a curved earth is given by [24]

$$F_{1X} = Df = \frac{D}{\sin\gamma}\left[\frac{\lambda R_1 R_2}{R_1+R_2}\right]^{\frac{1}{2}} \qquad (A1.9)$$

The divergence coefficient, D, is given by

$$D \simeq \left[1 + \frac{2R_1R_2}{a_e.(R_1+R_2).\sin\gamma}\right]^{-\frac{1}{2}} \qquad (A1.10)$$

where a_e is the effective curvature of the earth. In the direction perpendicular to the path, the effect of earth

curvature does not appreciably affect the Fresnel Zone dimension. The length of the first Fresnel Ellipse in the perpendicular direction to the path for a curved earth is thus

$$F_{1Y} \simeq g \doteq \left[\frac{\lambda R_1 R_2}{R_1+R_2}\right]^{\frac{1}{2}} \qquad \text{(A1.11)}$$

APPENDIX 2

Summary of Diagnostic System Parameters

Transmitted power:	30 dBm
Transmit antenna:	4 ft diameter paraboloid, 1980 8 ft diameter paraboloid, 1981
Receive antennas:	2 ft diameter paraboloids vertically spaced 3 m
Frequency sweep:	9.500 - 10.508 GHz, 1980 9.505 - 10.513 GHz, 1981 64 steps, 16 MHz per step
Sweep time:	1.28 sec
Repetition period:	10 sec
Recording:	amplitude and phase digital, 8 bits each

APPENDIX 3

Details of the Data Acquisition System

A3.1 System Memory Map

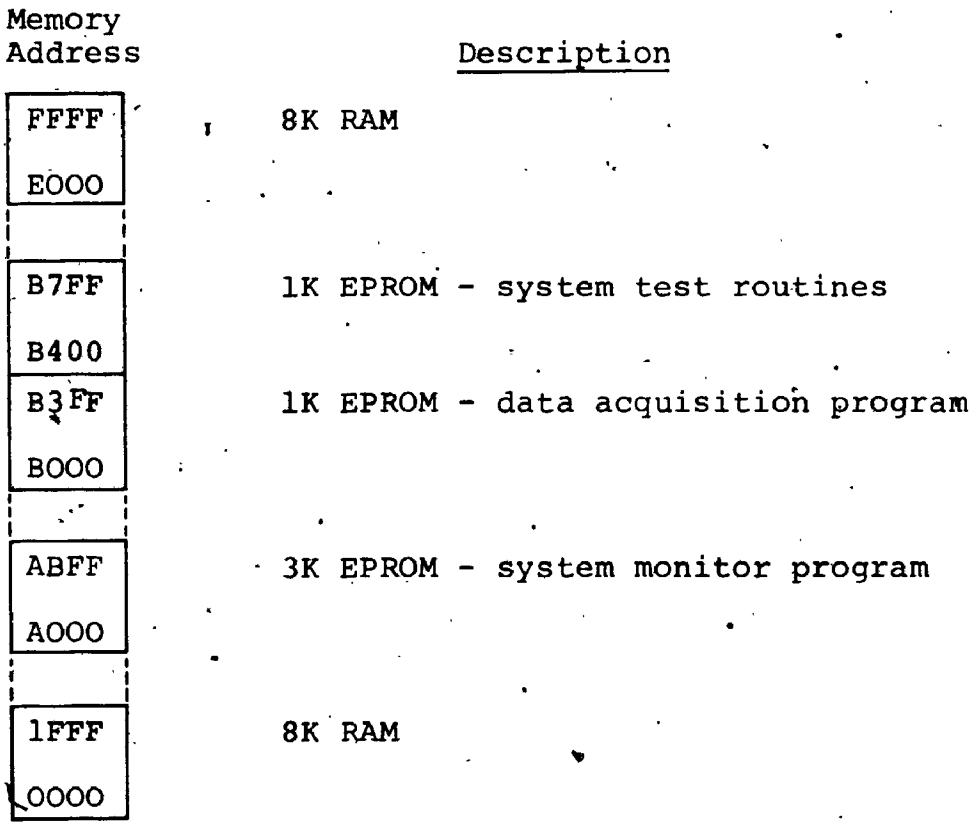

A3.2 System Input/Output (I/O) Port Allocations

Port Address	Description	
00	Cassette Interface Port	IMSAI 8080 MIO
01	Parallel I/O Port (2 x 8-bit)	
02	Serial I/O Port	
03	Control and Status of MIO board	
10		
11		
12		
13	8 x 8-bit parallel input ports for interfacing to diagnostic system	
14		
15		
16		
17		
FC	Control and Status	MITS 88-PIO
FD	Parallel I/O (1 x 8-bit)	
FF	Front Panel sense switches 1 x 8-bit parallel input port	

A3.3 System Configuration

(1) Chassis, Front Panel, and Display:

- ALTAIR 8800

(2) Central Processing Unit:

- MITS 8800

(3) Memory:

(a) RAM -- Industrial Micro Systems

I S-C00231 8K memory board, 2 units

(b) EPROM -- Econorom 2708

Godbout Electronics, Ca.

(4) Interface boards:

(a) MIO -- IMSAI 8080 MIO board

2 parallel I/O + 1 serial I/O ports

(b) PIO -- MITS 88-PIO board

1 parallel I/O port

(c) 8 x 8 bit parallel input board

APPENDIX 4

Parameters of the Propagation Paths

Year	1980	1981
Path Length	80.025 km	80.375 km
NB Site		
Location	Otter Lake	Otter Lake
Latitude	45°22'10" N	45°22'10" N
Longitude	65°46'23" W	65°46'23" W
Ground Elevation	279 m	279 m
Antenna Height (above ground)		
Diagnostic System	6 m	69 m
Digital Radio	-	79 m
NS Site		
Location	Aylesford	Nictaux South
Latitude	45°04'26" N	44°52'00" N
Longitude	64°50'30" W	65°02'10" W
Ground Elevation	239 m	216 m
Antenna Height (above ground)		
Diagnostic System	14 m	81 m
Digital Radio, main	-	79 m
Digital Radio, diversity	-	55 m
Free Space Loss @ 10 GHz	-150.5 dB	-150.5 dB

APPENDIX 5

Analysis of Sweep Frequency Amplitude Records

Consider the case of two received rays of amplitudes r_0 and r_1, with a relative delay time of $\Delta\tau$ between the rays. The resultant amplitude A is generated by the vector addition of the two signals as shown in Fig. A5.1, where $\theta = \omega.\Delta\tau$ is the phase difference between the two signals. As the frequency ω is swept the resultant amplitude varies in a quasi-sinusoidal manner as shown in Fig. A5.2. The variation of A with θ may be expressed as a Fourier series

$$A = A_0 + A_1.\cos\theta + \ldots + A_i.\cos i\theta + \ldots \quad (A5.1)$$

where A_0 and A_1 are the Fourier coefficients of the average (dc component) and the fundamental components respectively.

From Fig. A5.1, the amplitude A is given by

$$A = (r_1^2 + r_2^2 - 2r_1r_2.\cos\theta)^{\frac{1}{2}} \quad (A5.2)$$

which can be written as

$$A = (r_1^2 + r_2^2)^{\frac{1}{2}}\left[1 - \frac{2r_1r_2}{r_1^2+r_2^2}.\cos\theta\right]^{\frac{1}{2}} \quad (A5.3)$$

Eq. (A5.3) may be expressed in the form of Eq. (A5.1) by expanding the second term of Eq. (A5.3) by the binomial series and the cosine expansion formula. Equating the result with Eq. (A5.1) gives the coefficients A_0 and A_1 as

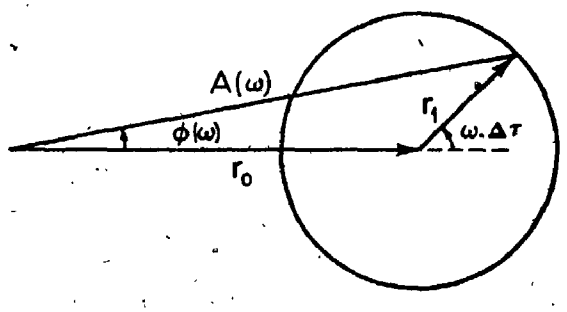

Fig. A5.1 The vector addition of two signals with a relative time delay of $\Delta\tau$.

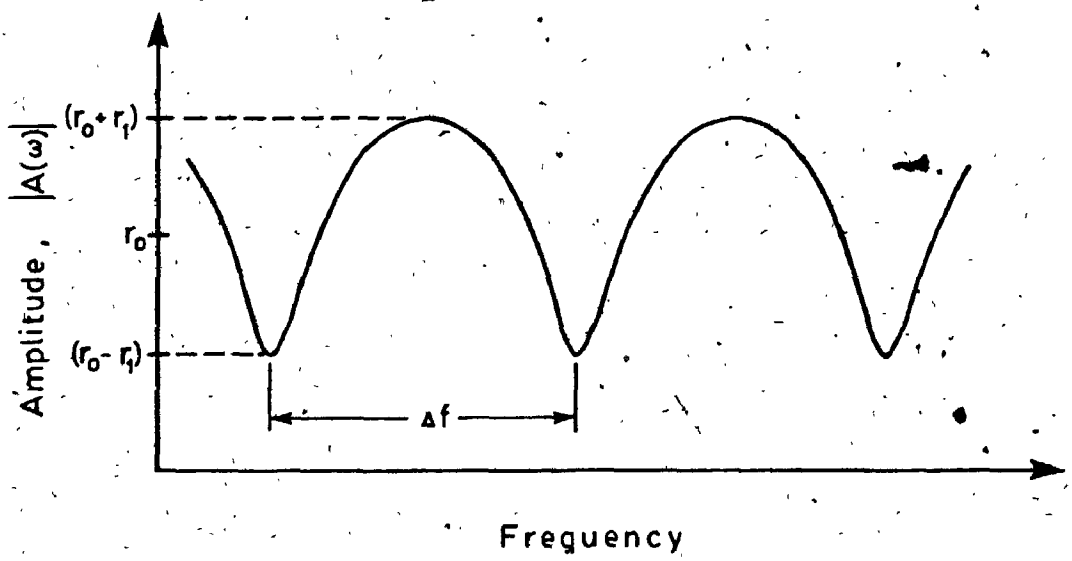

Fig. A5.2 Amplitude characteristics of the resultant of two signals with relative time delay of $\Delta\tau$.

(first five terms in each series included)

$$A_o \simeq r_o(1 + R^2)^{\frac{1}{2}}[1 - 0.0625\ k^2 - 0.0146\ k^4 - 0.00641\ k^6 - 0.00358\ k^8] \quad (A5.4)$$

and

$$A_1 \simeq r_1\left(1 + \frac{1}{R^2}\right)^{\frac{1}{2}}[0.5\ k + 0.0469\ k^3 + 0.01709\ k^5 + 0.00881\ k^7 + 0.00537\ k^9] \quad (A5.5)$$

where $k = \frac{2R}{1+R^2}$ and $R = \frac{r_1}{r_o}$.

Eqs. (A5.4) and (A5.5) are in the form

$$A_o \simeq r_o.\Delta r_o \quad (A5.6)$$

and

$$A_1 \simeq r_1.\Delta r_1 \quad (A5.7)$$

where Δr_o and Δr_1 are the scaling factors the values of which depend on the ratio R. Expressed in decibels and rearranging Eqs. (A5.6) and (A5.7) gives

$$[r_o]_{dB} = [A_o]_{dB} - [\Delta r_o]_{dB} \quad (A5.8)$$

and

$$[r_1]_{dB} = [A_1]_{dB} - [\Delta r_1]_{dB} \quad (A5.9)$$

The actual ray amplitudes r_o and r_1 therefore may be obtained from the values A_o and A_1. A_o is the average value of the sweep frequency amplitude record, and A_1 is the fundamental component obtained by a spectral analysis of the sweep record. The latter procedure also yields the relative delay time between the two signals.

The correction factors Δr_0 and Δr_1 are shown in Fig. A5.3 as functions of $(A_o - A_1)$. These are applied to

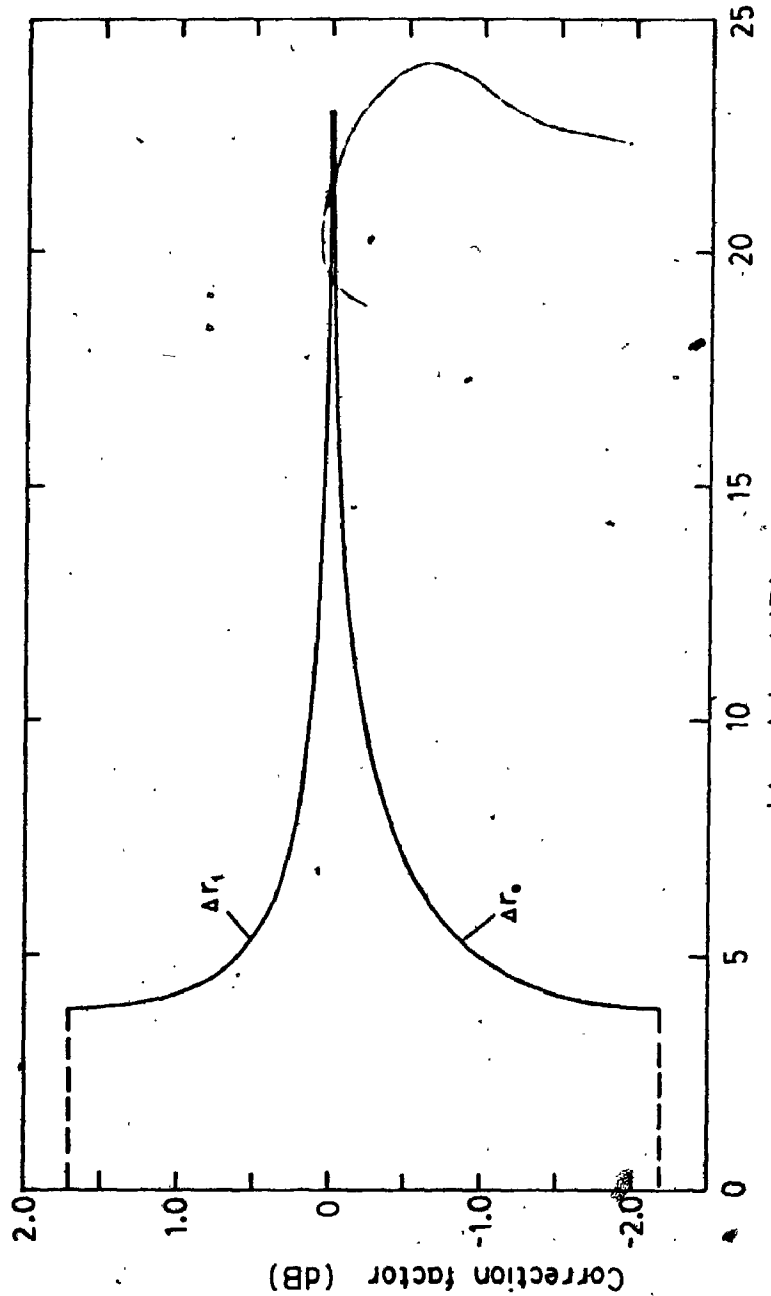

Fig. A5.3 Scale factors required to produce correct estimates of ray amplitudes.

the estimated values of A_o and A_1 by a calibration method to give estimates of r_o and r_1 which are the desired ray amplitudes. Computer simulations and tests verified the above approach and some of the results are summarized in Fig. 4.10 in Chapter 4.

APPENDIX 6

Summary of Results of the 1980 Experiment

The ray path characteristics of the two strongest rays during the ten selected days in the 1980 experiment are summarized in the following pages. These characteristics include:

(a) Relative delay time (absolute value), $\Delta\tau$, between the rays given in nanoseconds.

(b) Main ray (strongest ray) amplitude, A1, given in dB relative to the median value during non-fading periods.

(c) Second ray (weaker ray) amplitude, A2, given in dB relative to the same reference level as in (b).

(d) Main ray angle-of-arrival. Two estimates of this parameter are obtained from the relative phase records. These are:

  (i) AOAS - estimated from the slope of the phase record.

  (ii) AOAI - estimated from the intercept of the phase record.

In most cases, the correct main ray AOA is given by AOAI rather than by AOAS. This is because the value of AOAS is often contaminated by the presence of short delay rays and was included mainly for identifying the occurrence of such short delay rays.

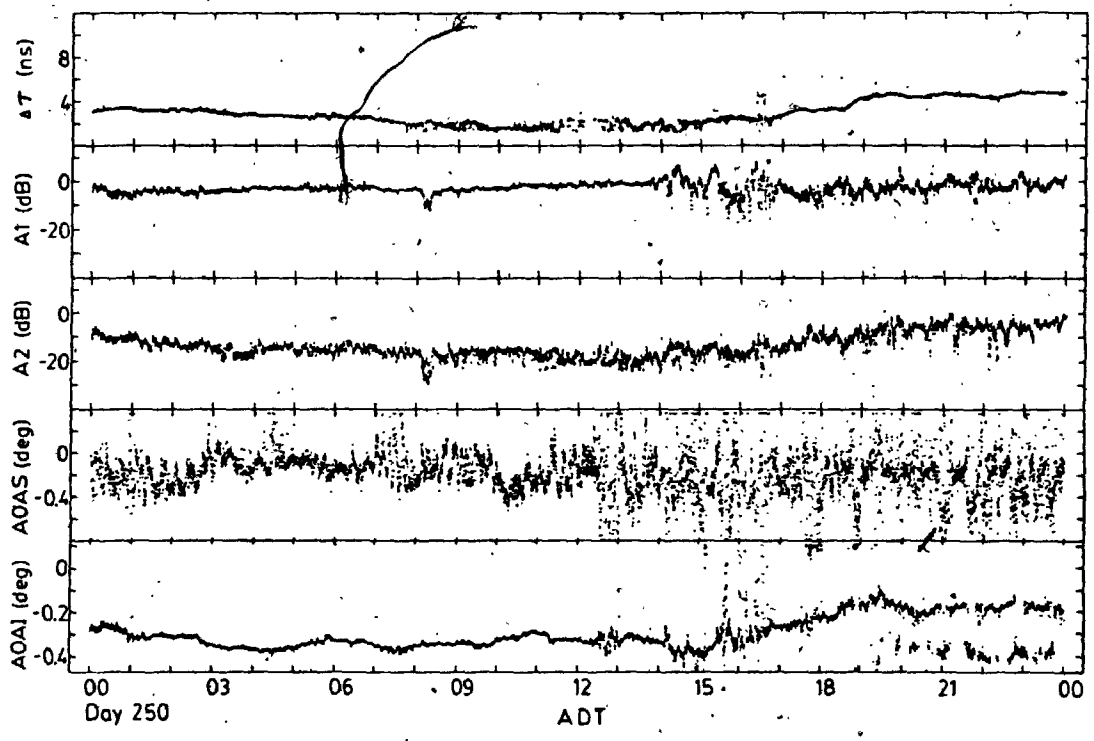
Δτ (ns)
8
4
A1 (dB)
0
-20
A2 (dB)
0
-20
AOAS (deg)
0
-0.4
AOAI (deg)
0
-0.2
-0.4
00
03
06
09
12
15
18
21
00
Day 250
ADT

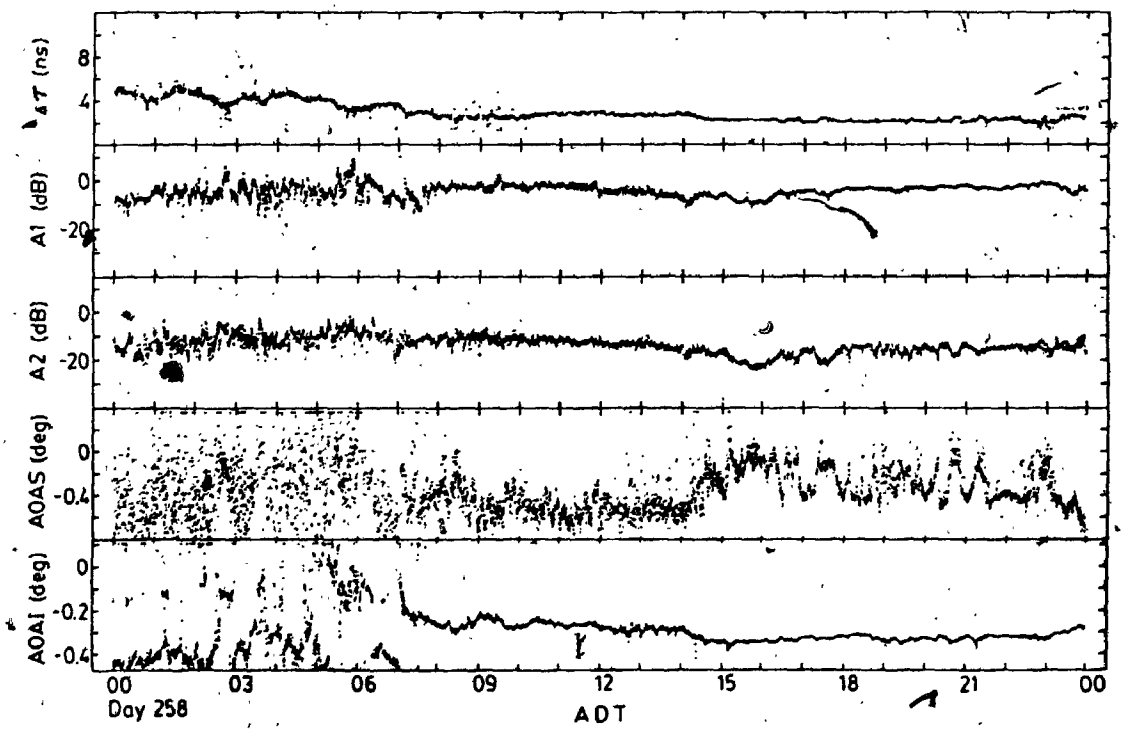
Δτ (ns)
8
4
A1 (dB)
0
-20
A2 (dB)
0
-20
AOAS (deg)
0
-0.4
AOAI (deg)
0
-0.2
-0.4
00
03
06
09
12
15
18
21
00
Day 258
ADT

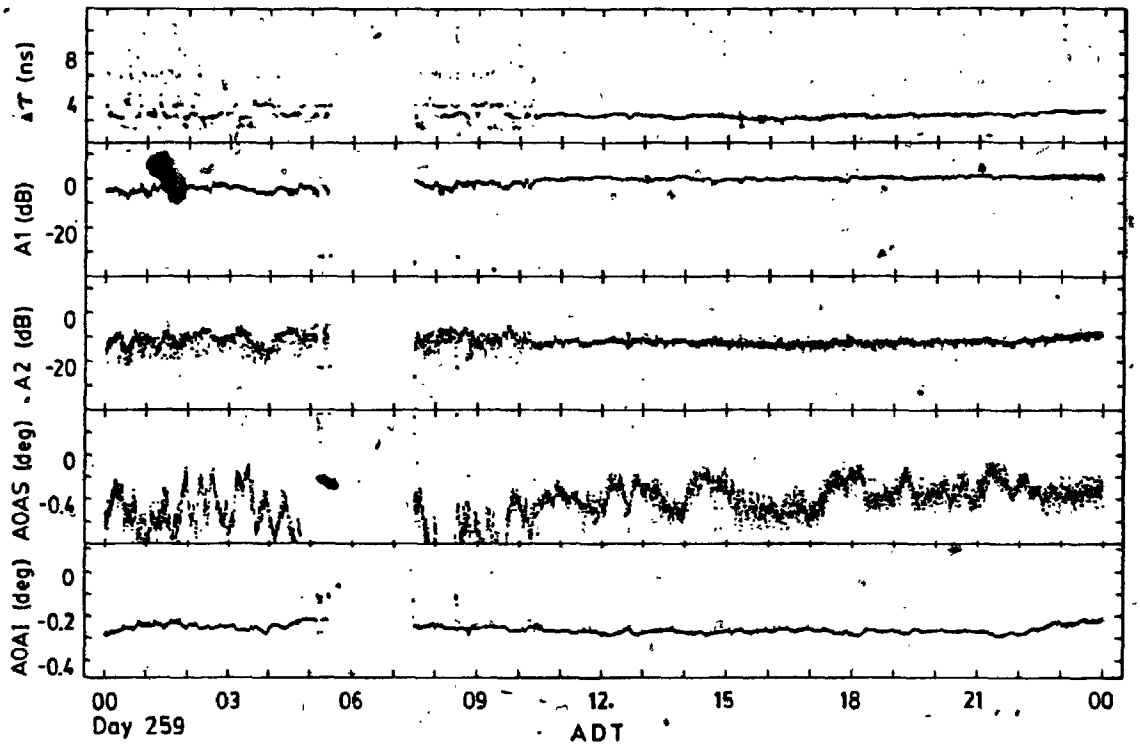
ΔT (ns)
8
4
A1 (dB)
0
-20
A2 (dB)
0
-20
AOAS (deg)
0
-0.4
AOA1 (deg)
0
-0.2
-0.4
00
03
06
09
12.
15
18
21
00
Day 259
ADT

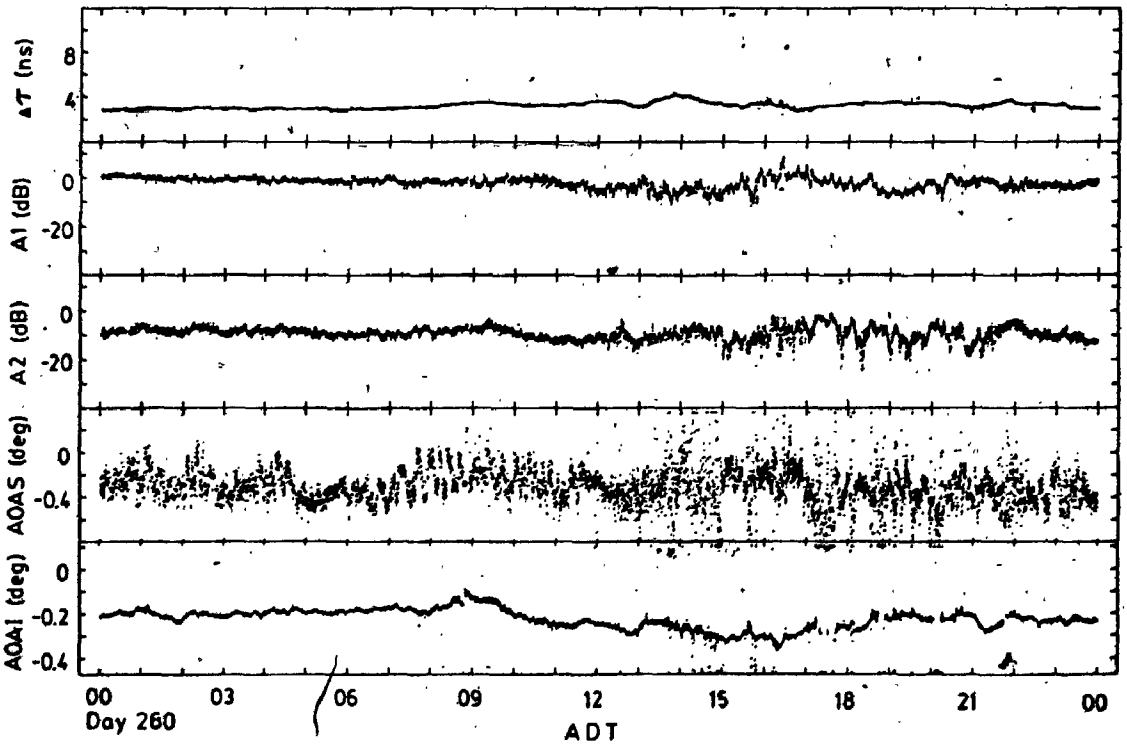
ΔT (ns)
8
4
A1 (dB)
0
-20
A2 (dB)
0
-20
AOAS (deg)
0
-0.4
AOA1 (deg)
0
-0.2
-0.4
00
03
06
09
12
15
18
21
00
Day 260
ADT

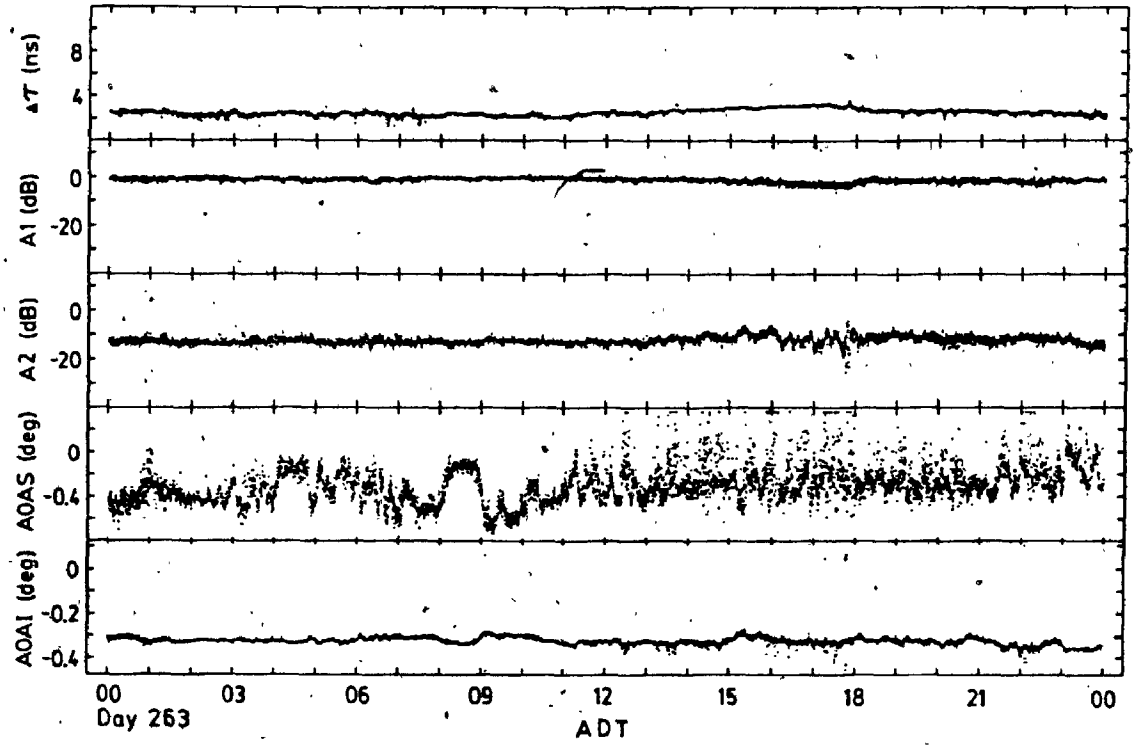
Δτ (ns)
8
4
A1 (dB)
0
-20
A2 (dB)
0
-20
AOAS (deg)
0
-0.4
AOAI (deg)
0
-0.2
-0.4
00
03
06
09
12
15
18
21
00
Day 263
ADT

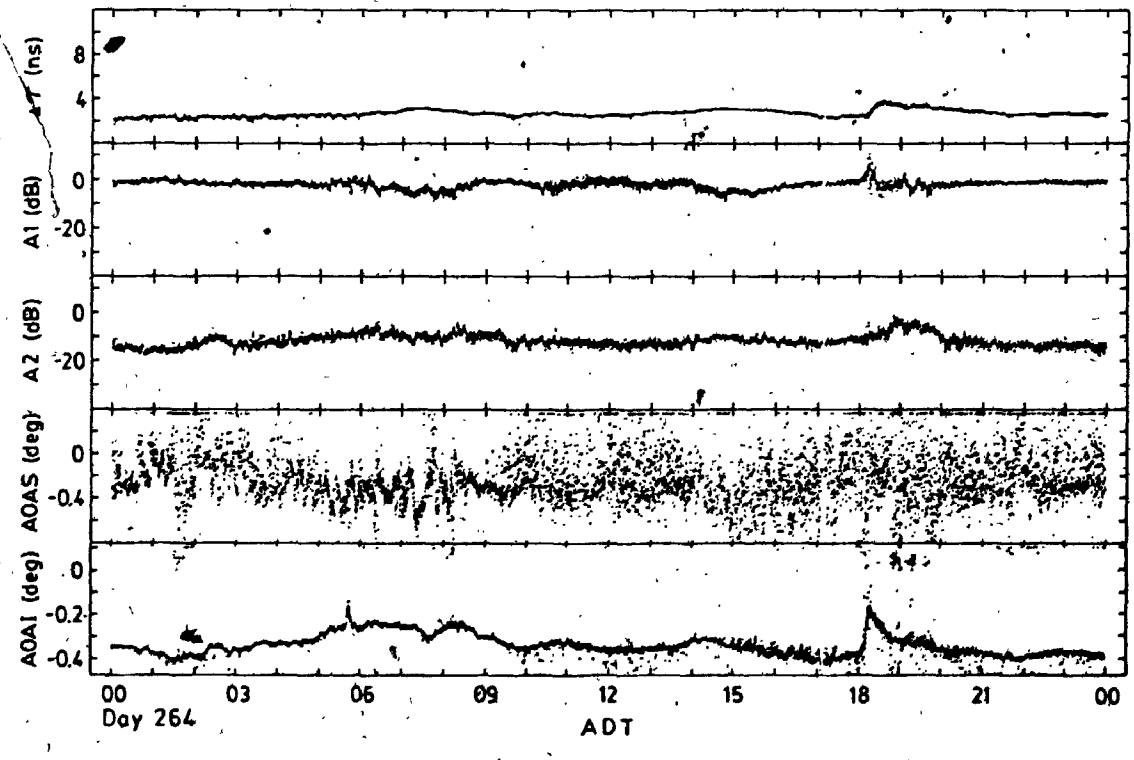
Δτ (ns)
8
4
A1 (dB)
0
-20
A2 (dB)
0
-20
AOAS (deg)
0
-0.4
AOAI (deg)
0
-0.2
-0.4
00
03
06
09
12
15
18
21
00
Day 264
ADT

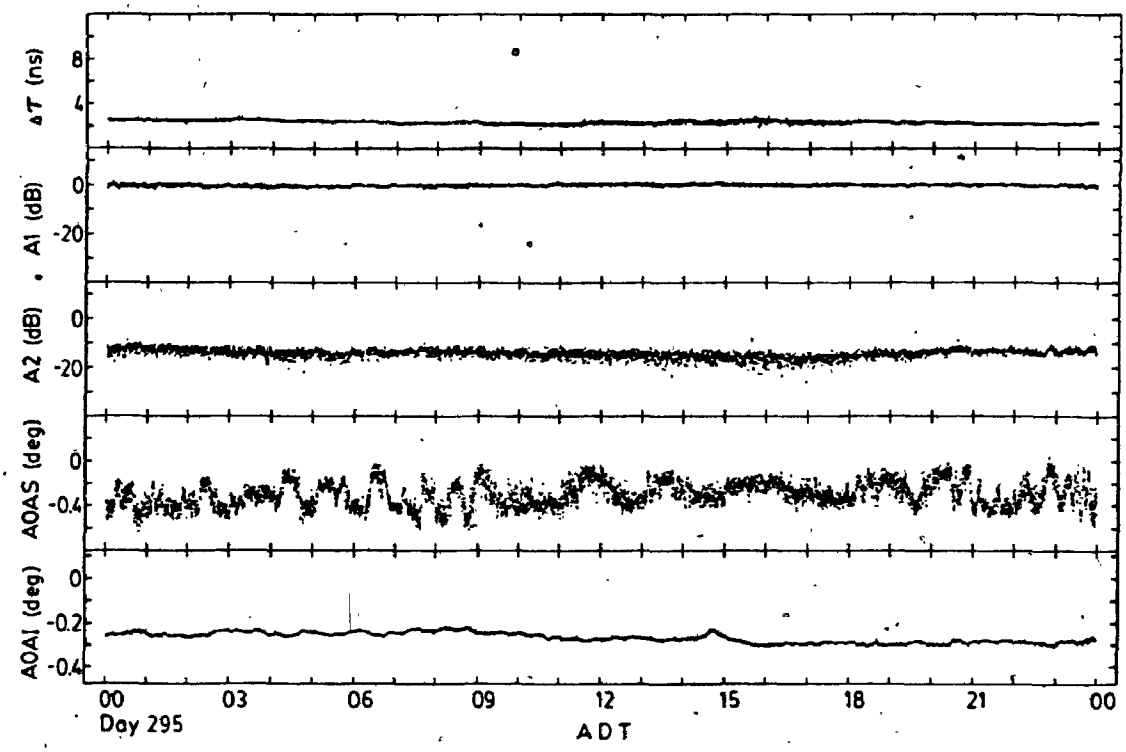
ΔT (ns)
8
4
A1 (dB)
0
-20
A2 (dB)
0
-20
AOAS (deg)
0
-0.4
AOAI (deg)
0
-0.2
-0.4
00
03
06
09
12
15
18
21
00
Day 295
ADT

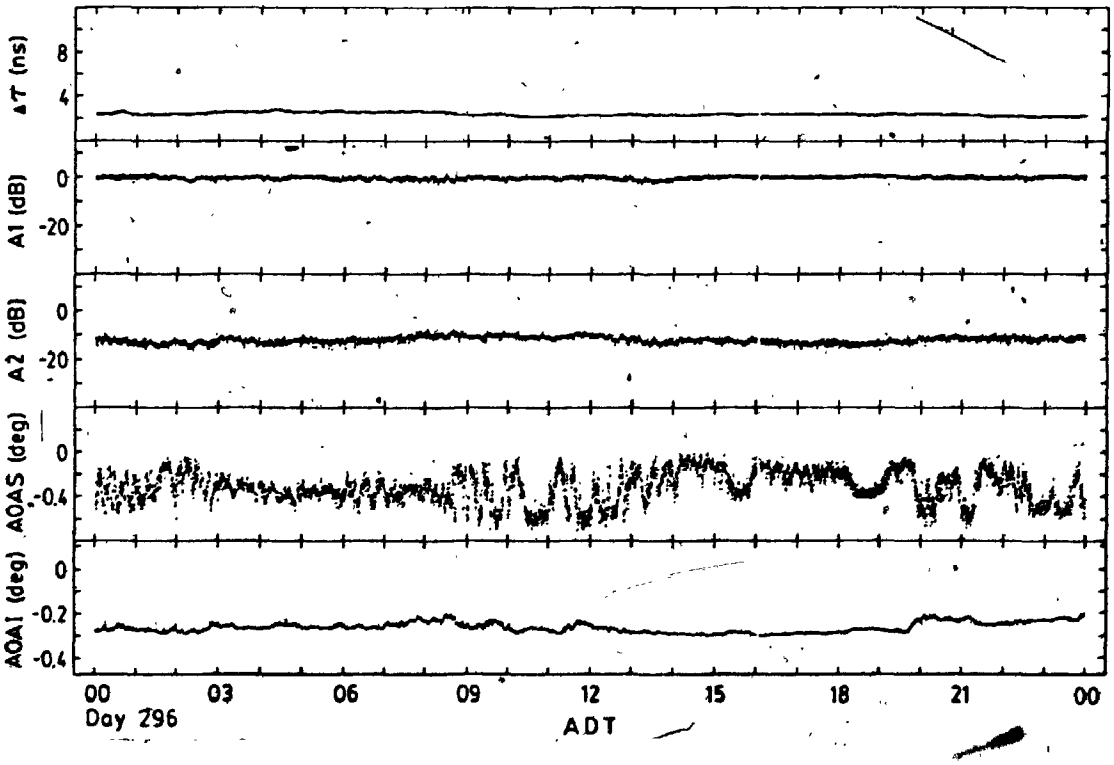
ΔT (ns)
8
4
A1 (dB)
0
-20
A2 (dB)
0
-20
AOAS (deg)
0
-0.4
AOAI (deg)
0
-0.2
-0.4
00
03
06
09
12
15
18
21
00
Day 296
ADT

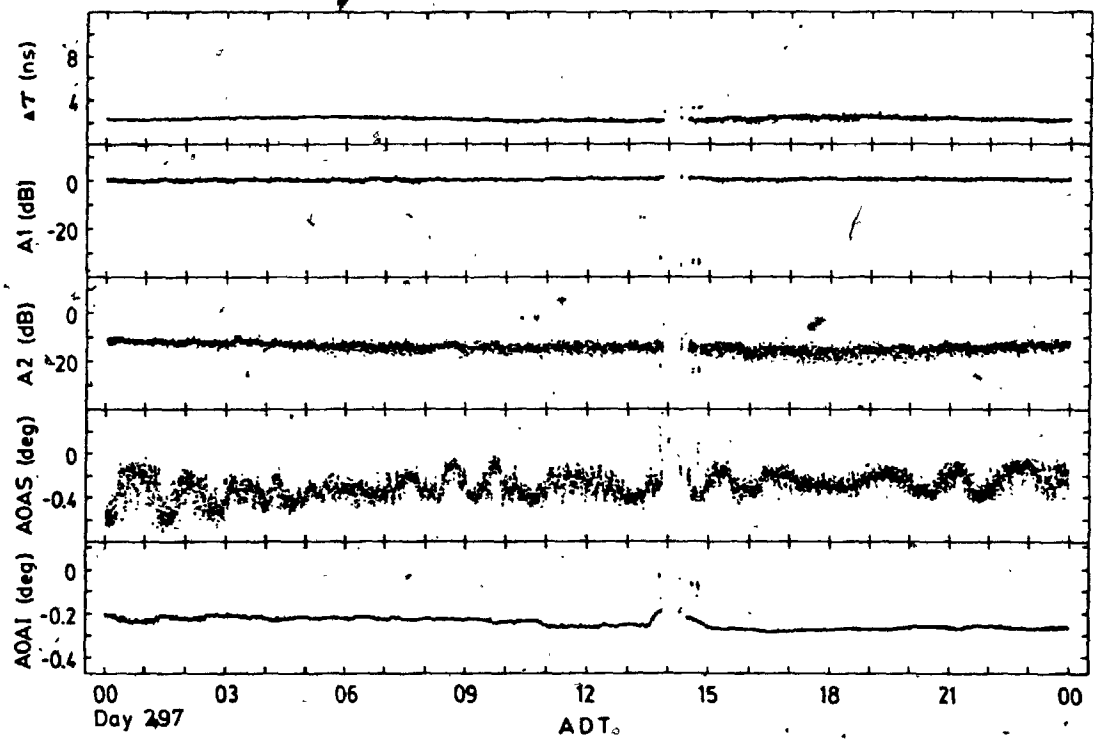
Δτ (ns)
8
4
A1 (dB)
0
-20
A2 (dB)
0
-20
AOAS (deg)
0
-0.4
AOAI (deg)
0
-0.2
-0.4
00
03
06
09
12
15
18
21
00
Day 297
ADT

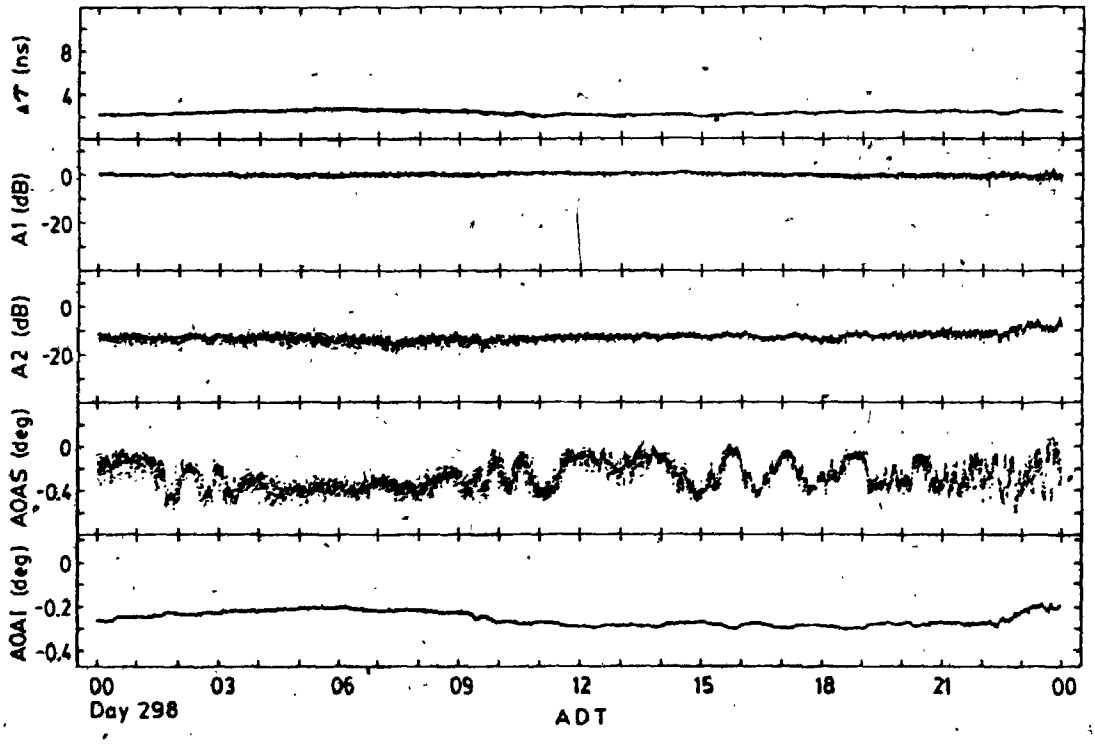
Δτ (ns)
8
4
A1 (dB)
0
-20
A2 (dB)
0
-20
AOAS (deg)
0
-0.4
AOAI (deg)
0
-0.2
-0.4
00
03
06
09
12
15
18
21
00
Day 298
ADT

APPENDIX 7

Summary of Results of the 1981 Experiment

The ray path characteristics of the two strongest rays during the thirty-five days in the 1981 experiment are summarized in the following pages. These characteristics include:

(a) Relative delay time (absolute value), $\Delta\tau$, between the rays given in nanoseconds.

(b) Main ray (strongest ray) amplitude, A1, given in dB relative to the median value during non-fading periods.

(c) Second ray (weaker ray) amplitude, A2, given in dB relative to the same reference level as in (b).

(d) Main ray angle-of-arrival. Two estimates of this parameter are obtained from the relative phase records. These are:

  (i) AOAS - estimated from the slope of the phase record.

  (ii) AOAI - estimated from the intercept of the phase record.

In most cases, the correct main ray AOA is given by AOAI rather than by AOAS. This is because the value of AOAS is often contaminated by the presence of short delay rays and was included mainly for identifying the occurrence of such short delay rays.

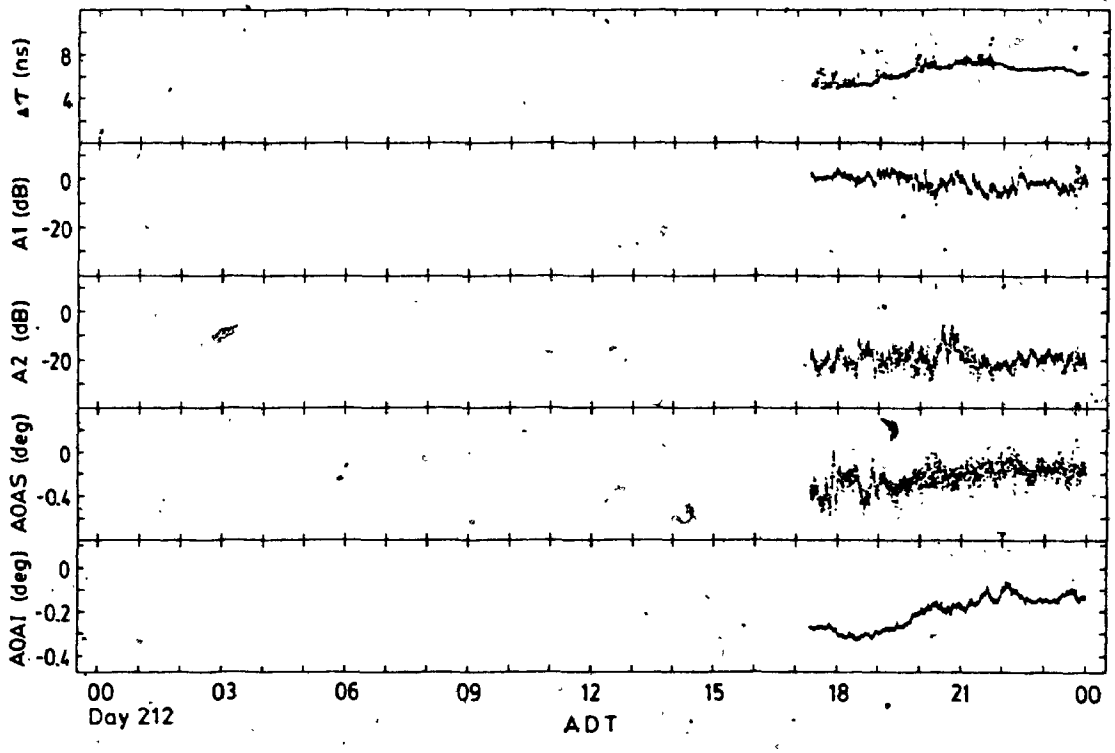
ΔT (ns)
8
4
A1 (dB)
0
-20
A2 (dB)
0
-20
AOAS (deg)
0
-0.4
AOAI (deg)
0
-0.2
-0.4
00
03
06
09
12
15
18
21
00
Day 212
ADT

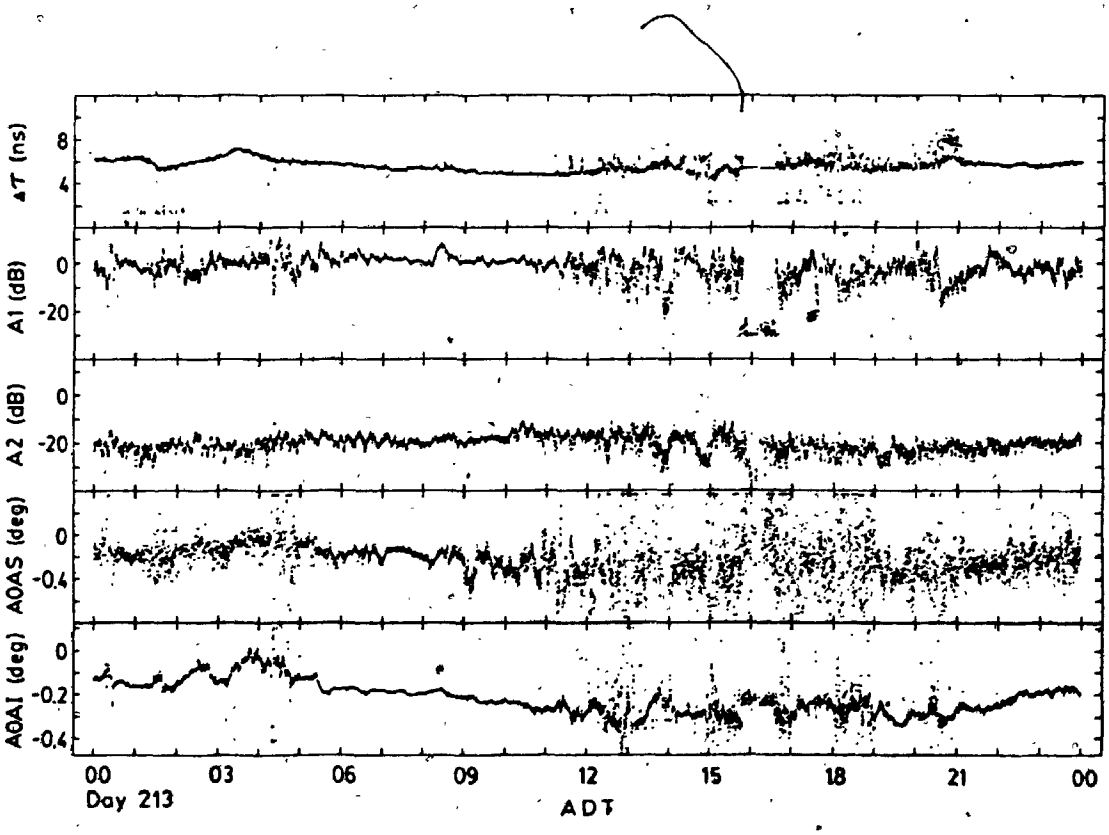
ΔT (ns)
8
4
A1 (dB)
0
-20
A2 (dB)
0
-20
AOAS (deg)
0
-0.4
AOAI (deg)
0
-0.2
-0.4
00
03
06
09
12
15
18
21
00
Day 213
ADT

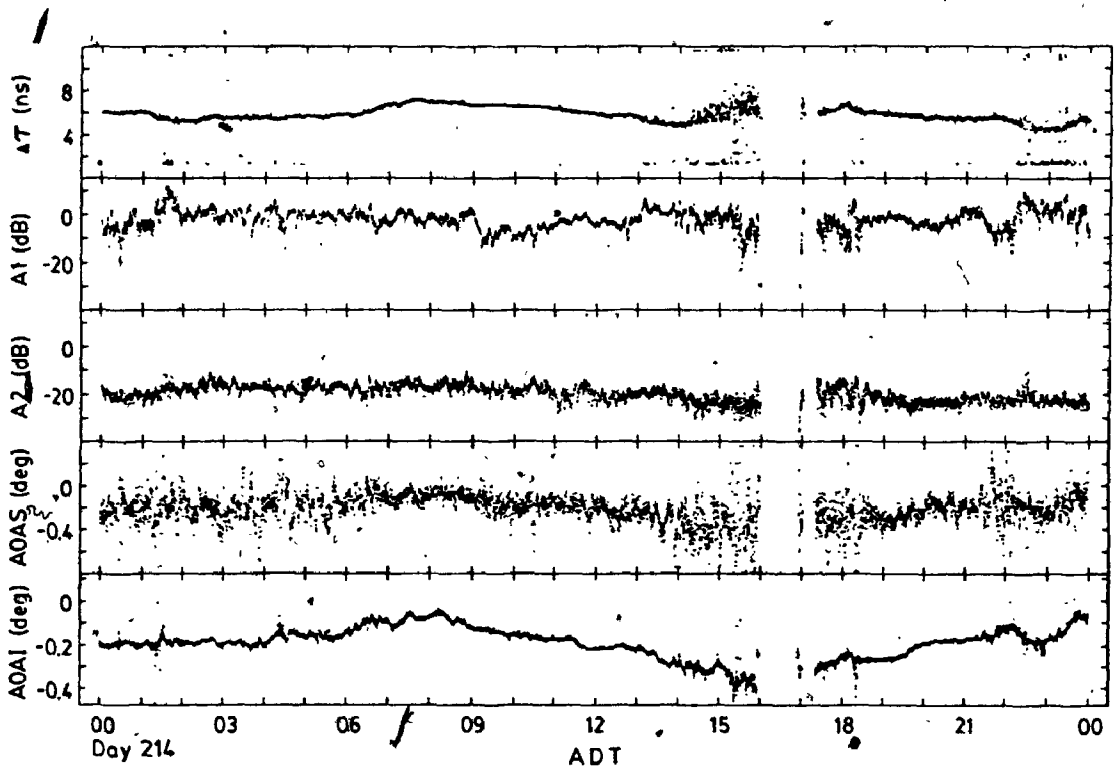
ΔT (ns)
8
4
A1 (dB)
0
-20
A2 (dB)
0
-20
AOAS (deg)
0
-0.4
AOAI (deg)
0
-0.2
-0.4
00
03
06
09
12
15
18
21
00
Day 214
ADT

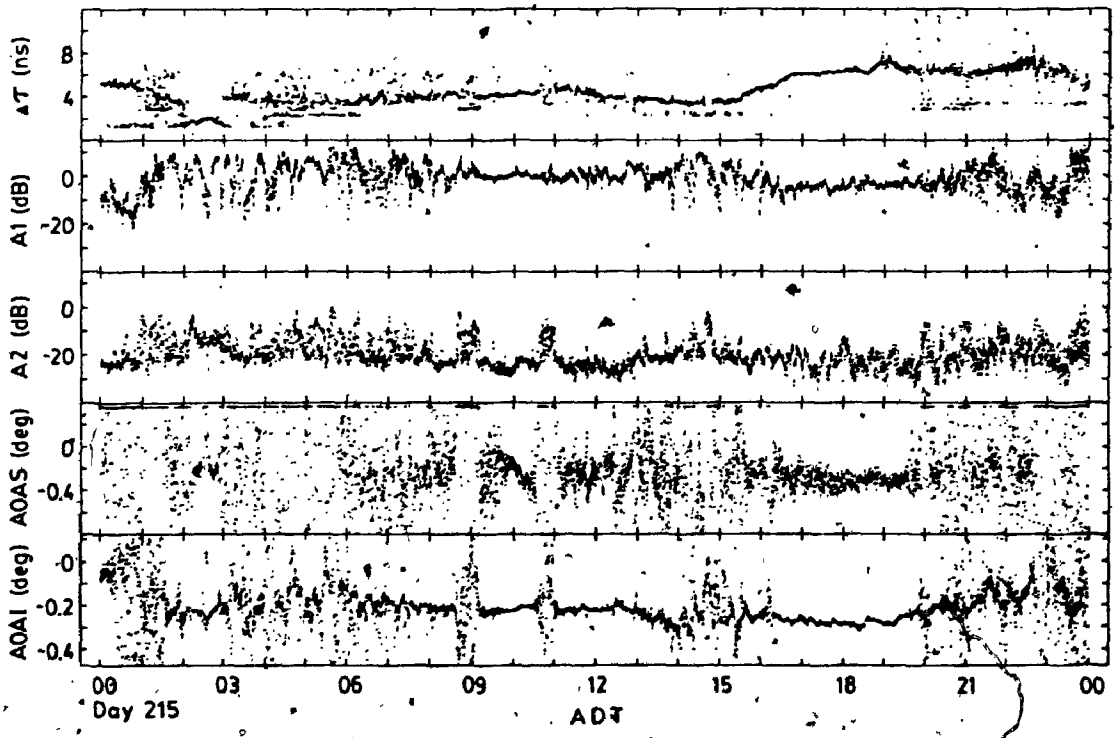
ΔT (ns)
8
4
A1 (dB)
0
-20
A2 (dB)
0
-20
AOAS (deg)
0
-0.4
AOAI (deg)
0
-0.2
-0.4
00
03
06
09
12
15
18
21
00
Day 215
ADT

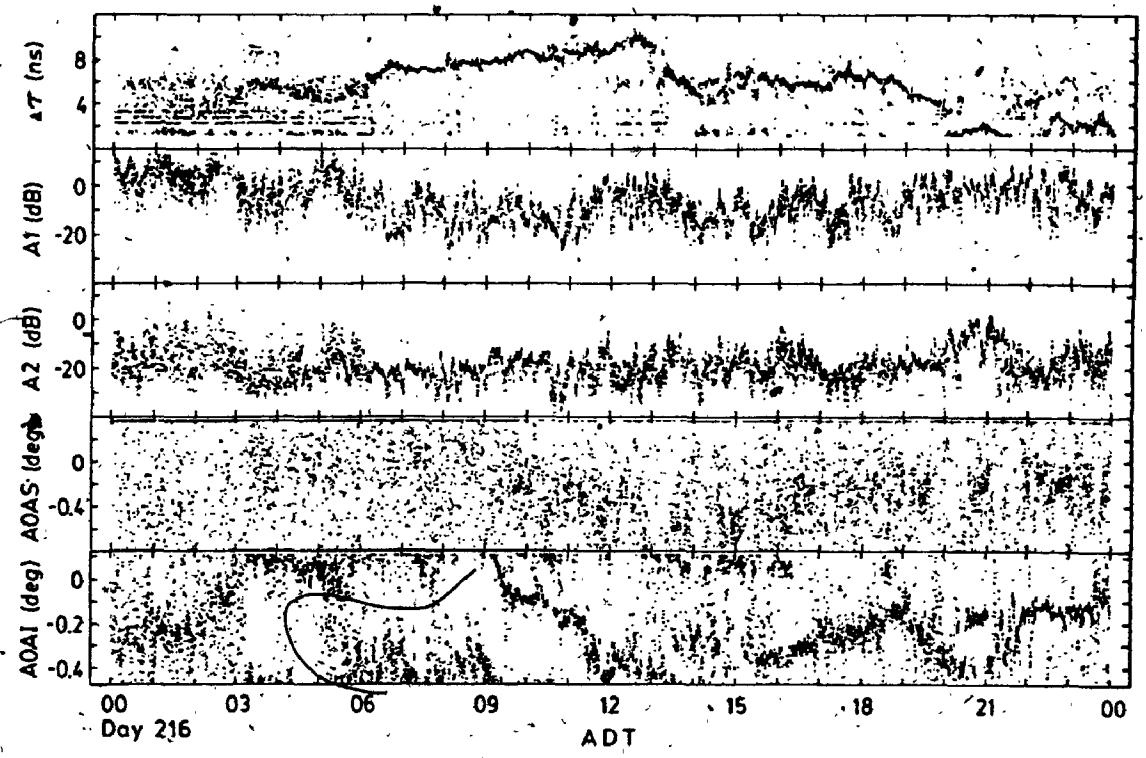
Δτ (ns)
8
4
A1 (dB)
0
-20
A2 (dB)
0
-20
AOAS (deg)
0
-0.4
AOAI (deg)
0
-0.2
-0.4
00
03
06
09
12
15
18
21
00
Day 216
ADT

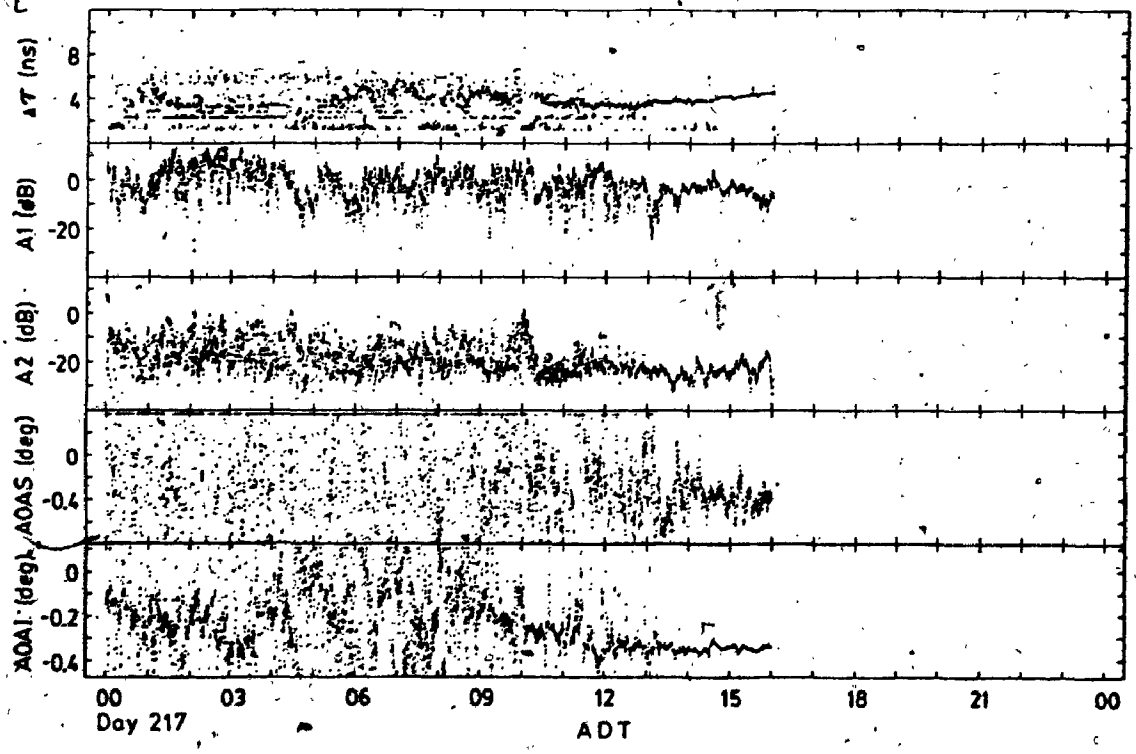
Δτ (ns)
8
4
A1 (dB)
0
-20
A2 (dB)
0
-20
AOAS (deg)
0
-0.4
AOAI (deg)
0
-0.2
-0.4
00
03
06
09
12
15
18
21
00
Day 217
ADT

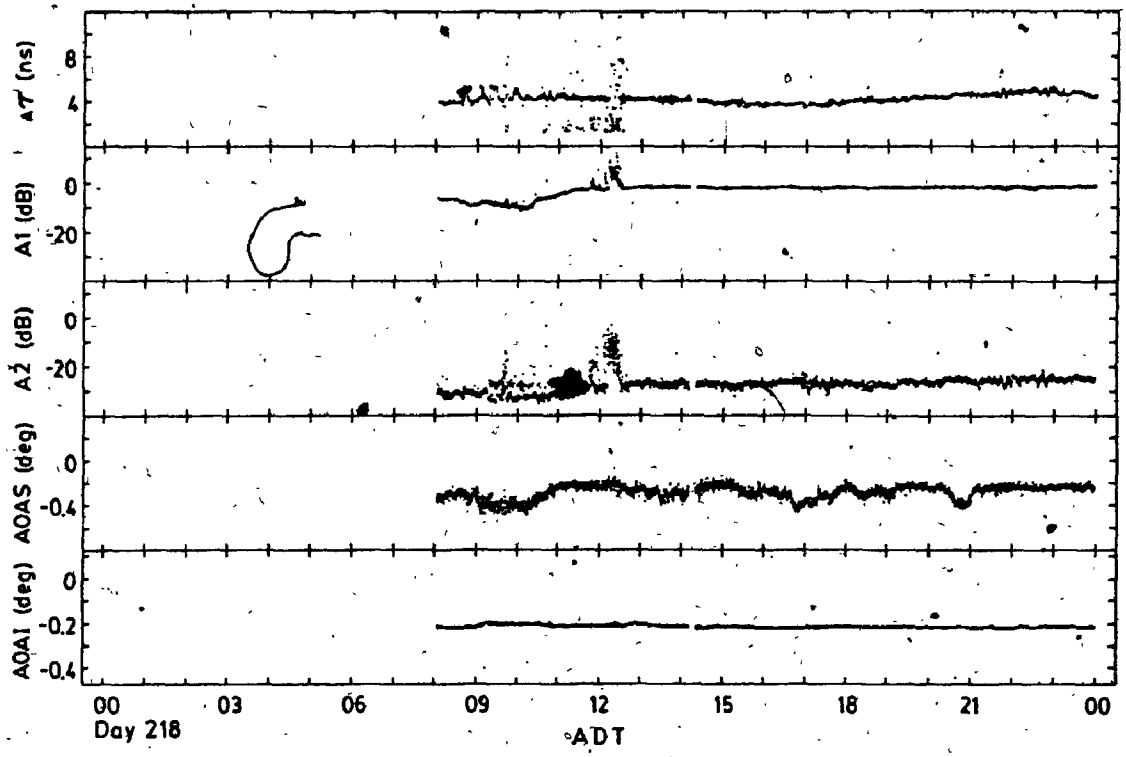
Δτ (ns)
8
4
A1 (dB)
0
-20
A2 (dB)
0
-20
AOAS (deg)
0
-0.4
AOAI (deg)
0
-0.2
-0.4
00
03
06
09
12
15
18
21
00
Day 218
ADT

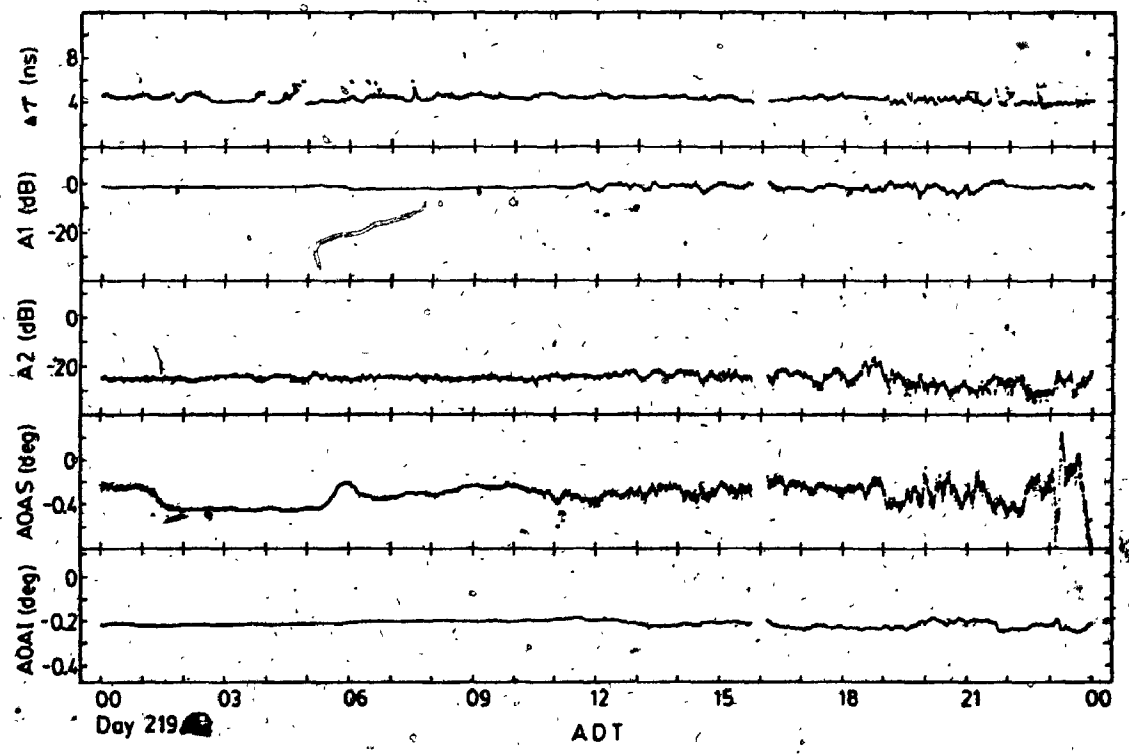
Δτ (ns)
8
4
A1 (dB)
0
-20
A2 (dB)
0
-20
AOAS (deg)
0
-0.4
AOAI (deg)
0
-0.2
-0.4
00
03
06
09
12
15
18
21
00
Day 219
ADT

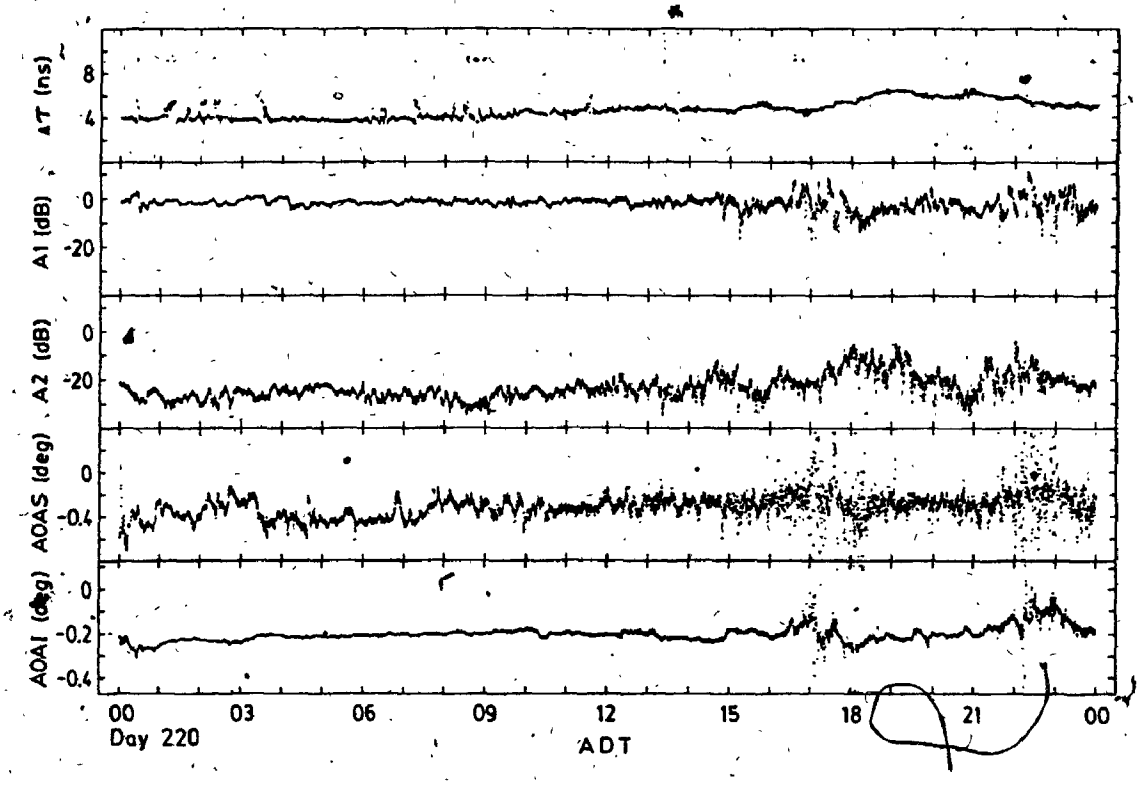
ΔT (ns)
8
4
A1 (dB)
0
-20
A2 (dB)
0
-20
AOAS (deg)
0
-0.4
AOAI (deg)
0
-0.2
-0.4
00
03
06
09
12
15
18
21
00
Day 220
ADT

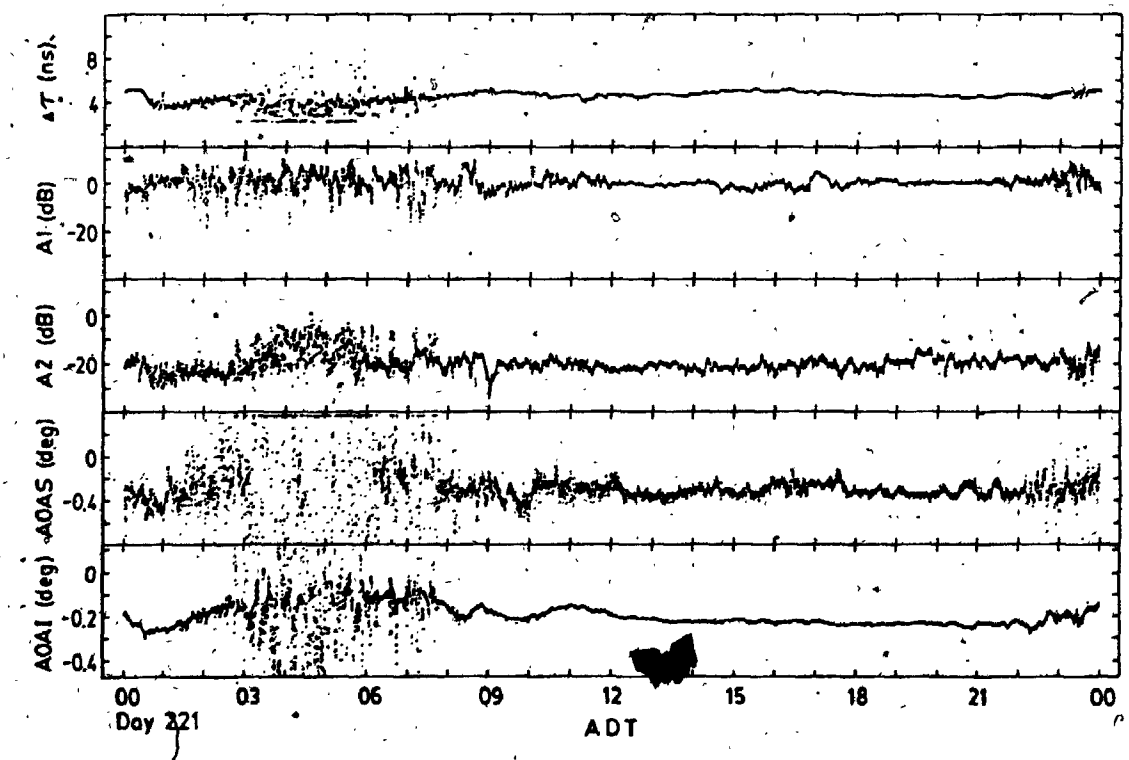
ΔT (ns)
8
4
A1 (dB)
0
-20
A2 (dB)
0
-20
AOAS (deg)
0
-0.4
AOAI (deg)
0
-0.2
-0.4
00
03
06
09
12
15
18
21
00
Day 221
ADT

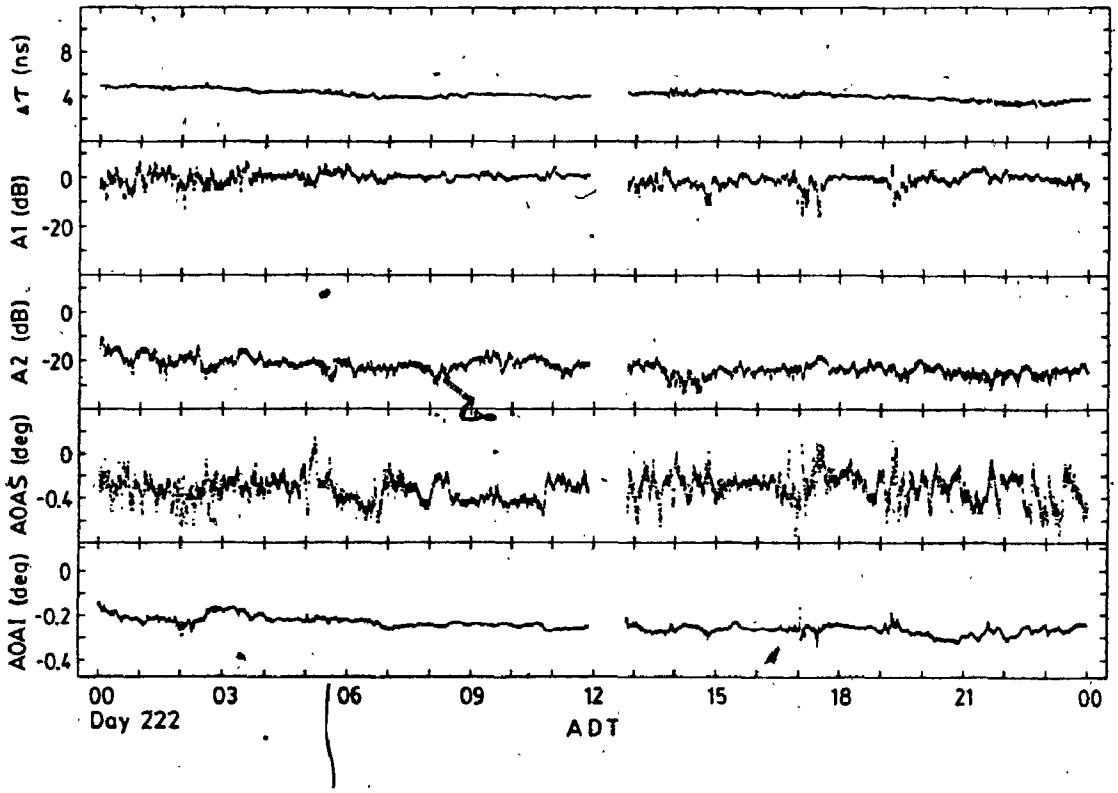
Δτ (ns)
8
4
A1 (dB)
0
-20
A2 (dB)
0
-20
AOAS (deg)
0
-0.4
AOAI (deg)
0
-0.2
-0.4
00
03
06
09
12
15
18
21
00
Day 222
ADT

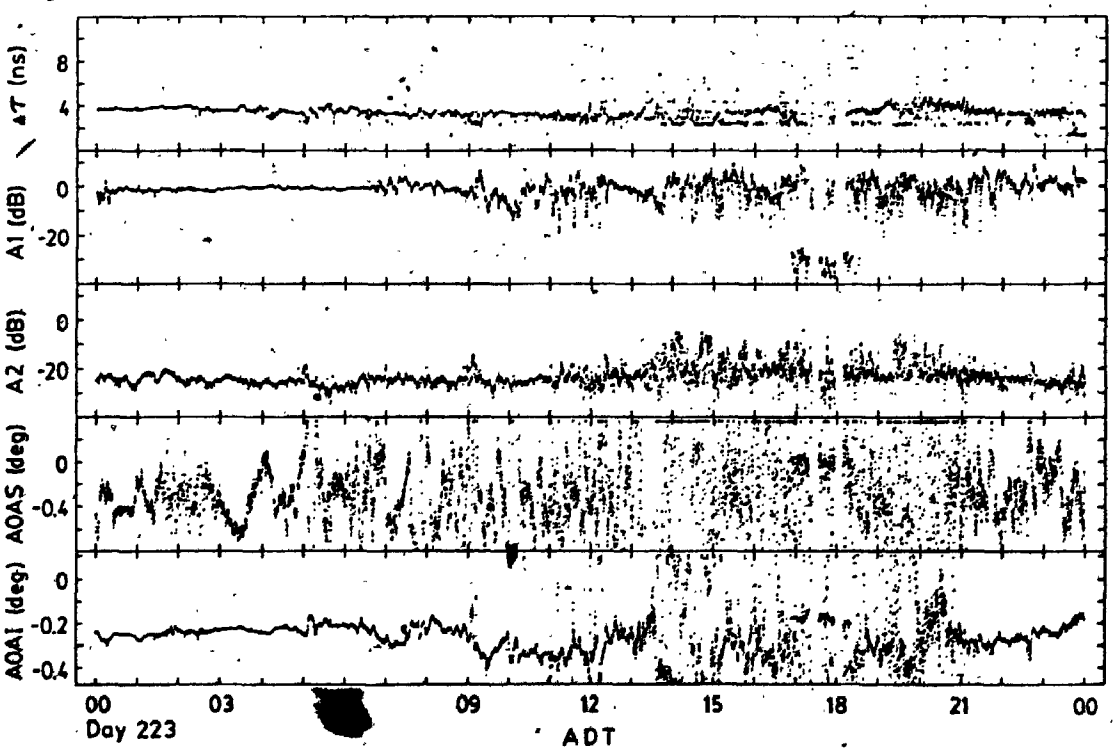
Δτ (ns)
8
4
A1 (dB)
0
-20
A2 (dB)
0
-20
AOAS (deg)
0
-0.4
AOAI (deg)
0
-0.2
-0.4
00
03
09
12
15
18
21
00
Day 223
ADT

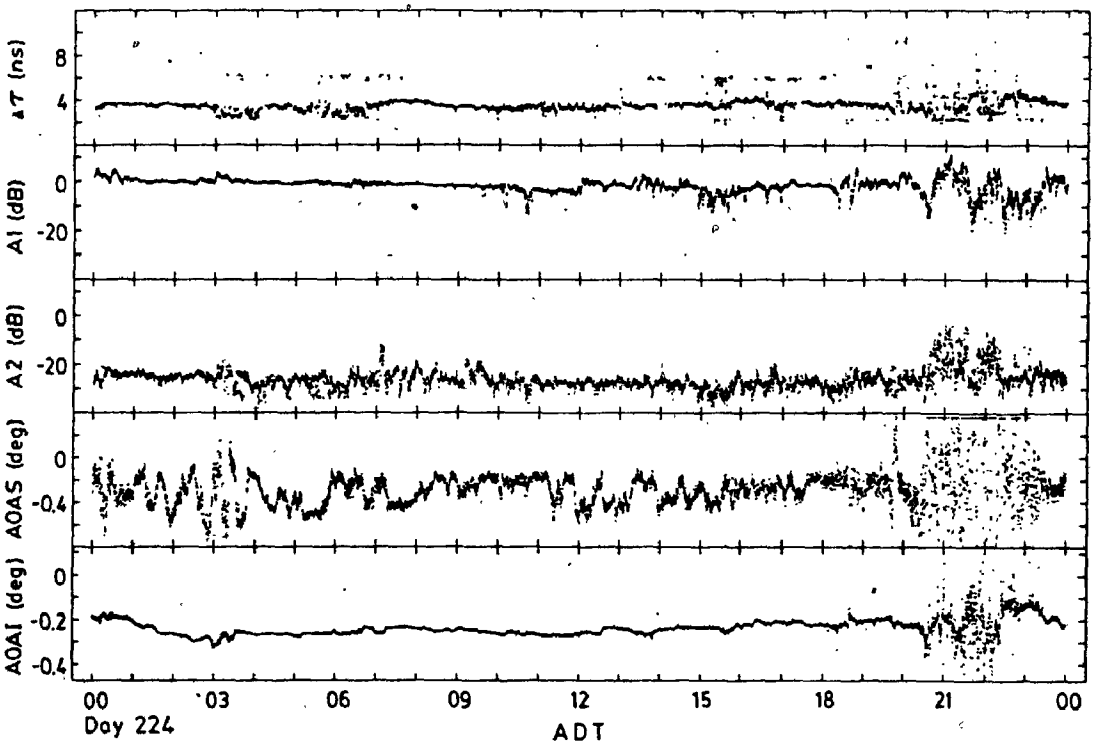
Δτ (ns)
8
4
A1 (dB)
0
-20
A2 (dB)
0
-20
AOAS (deg)
0
-0.4
AOAI (deg)
0
-0.2
-0.4
00
03
06
09
12
15
18
21
00
Day 224
ADT

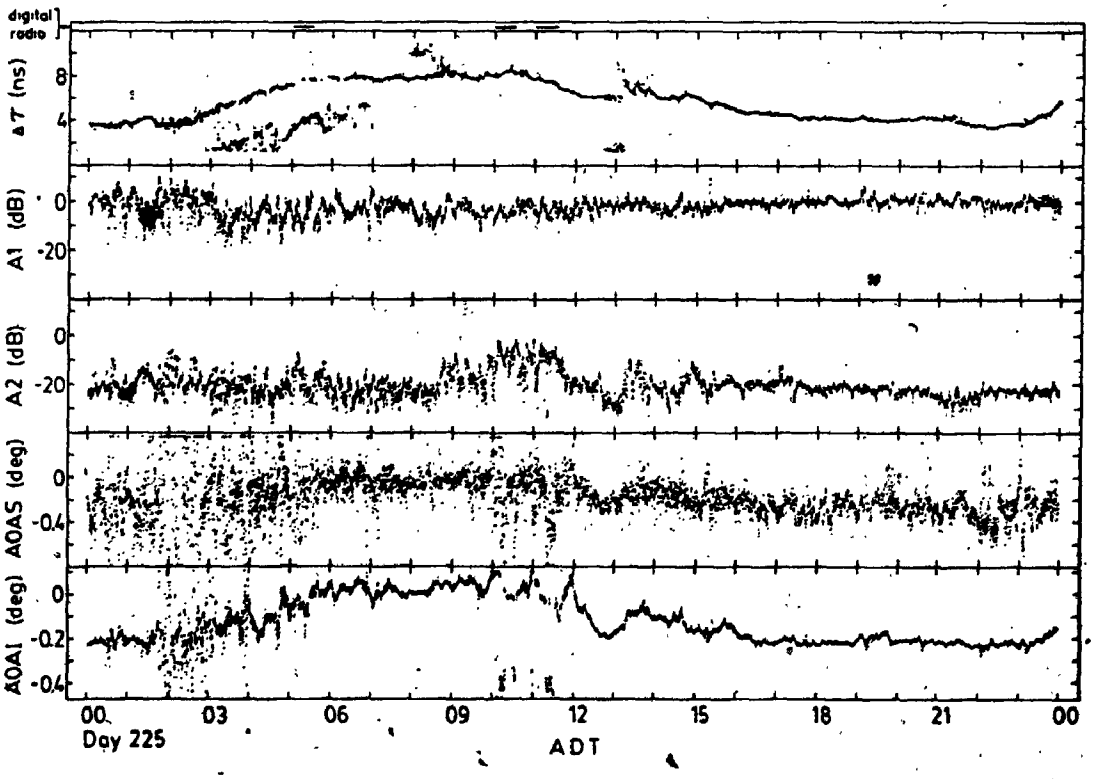
digital radio
Δτ (ns)
8
4
A1 (dB)
0
-20
A2 (dB)
0
-20
AOAS (deg)
0
-0.4
AOAI (deg)
0
-0.2
-0.4
00
03
06
09
12
15
18
21
00
Day 225
ADT

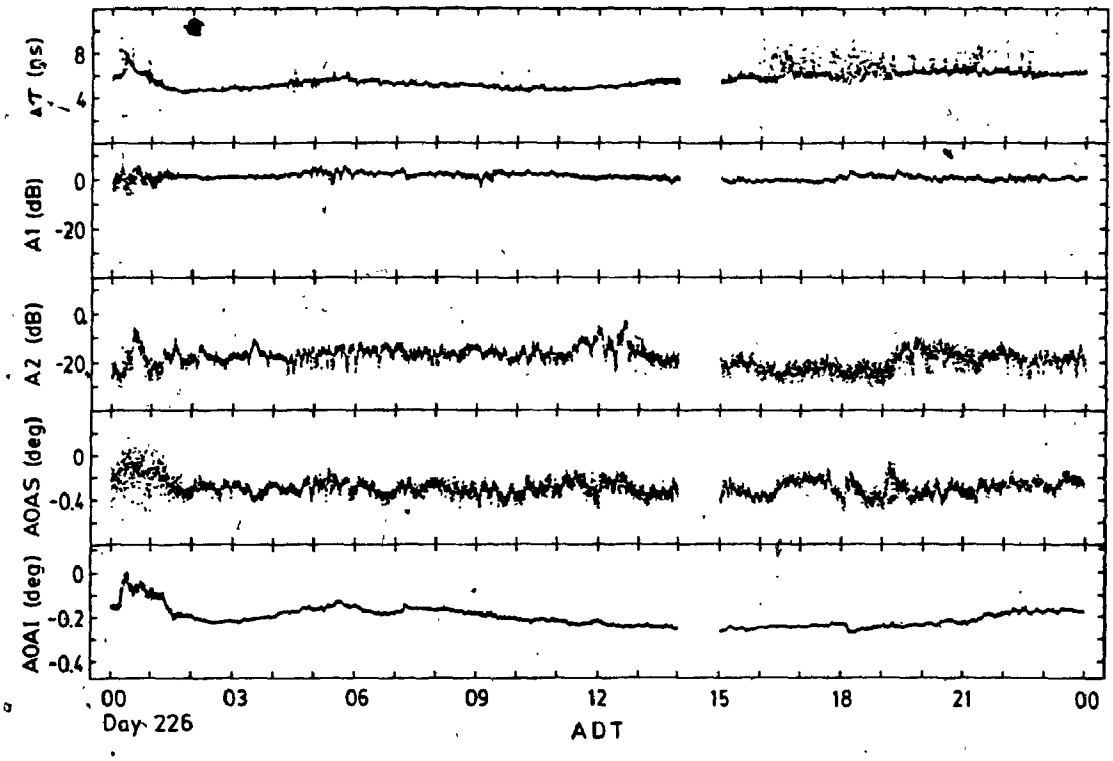
ΔT (ns)
8
4
A1 (dB)
0
-20
A2 (dB)
0
-20
AOAS (deg)
0
-0.4
AOAI (deg)
0
-0.2
-0.4
00
03
06
09
12
15
18
21
00
Day 226
ADT

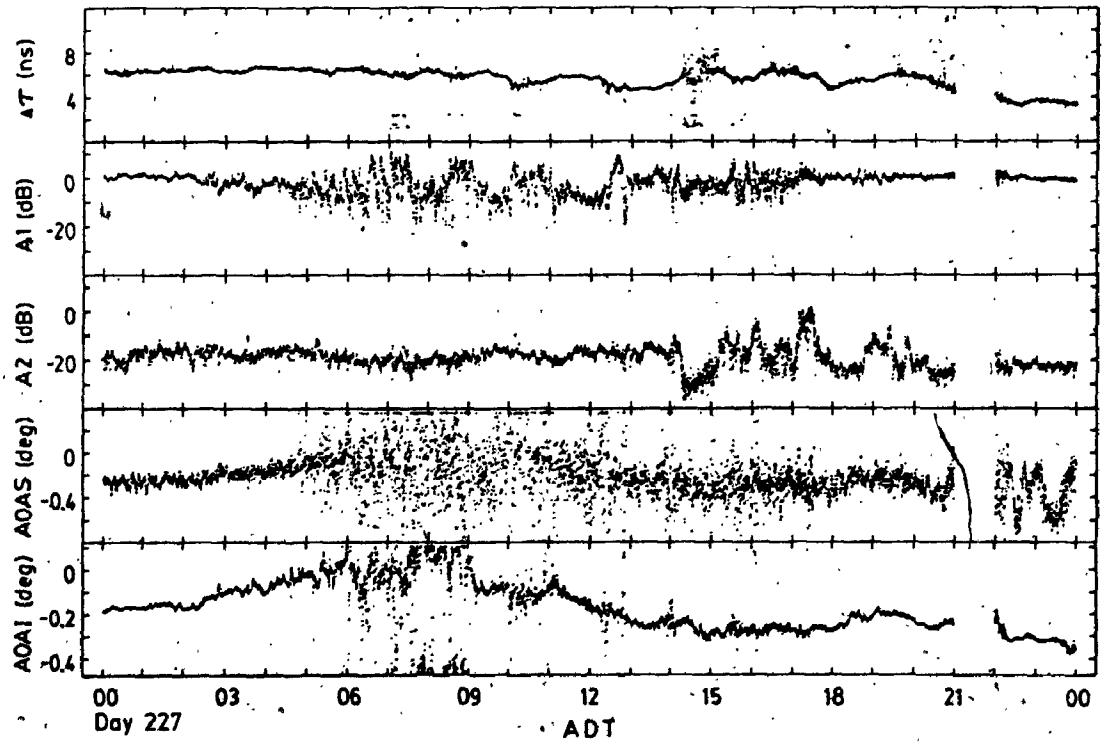
ΔT (ns)
8
4
A1 (dB)
0
-20
A2 (dB)
0
-20
AOAS (deg)
0
-0.4
AOAI (deg)
0
-0.2
-0.4
00
03
06
09
12
15
18
21
00
Day 227
ADT

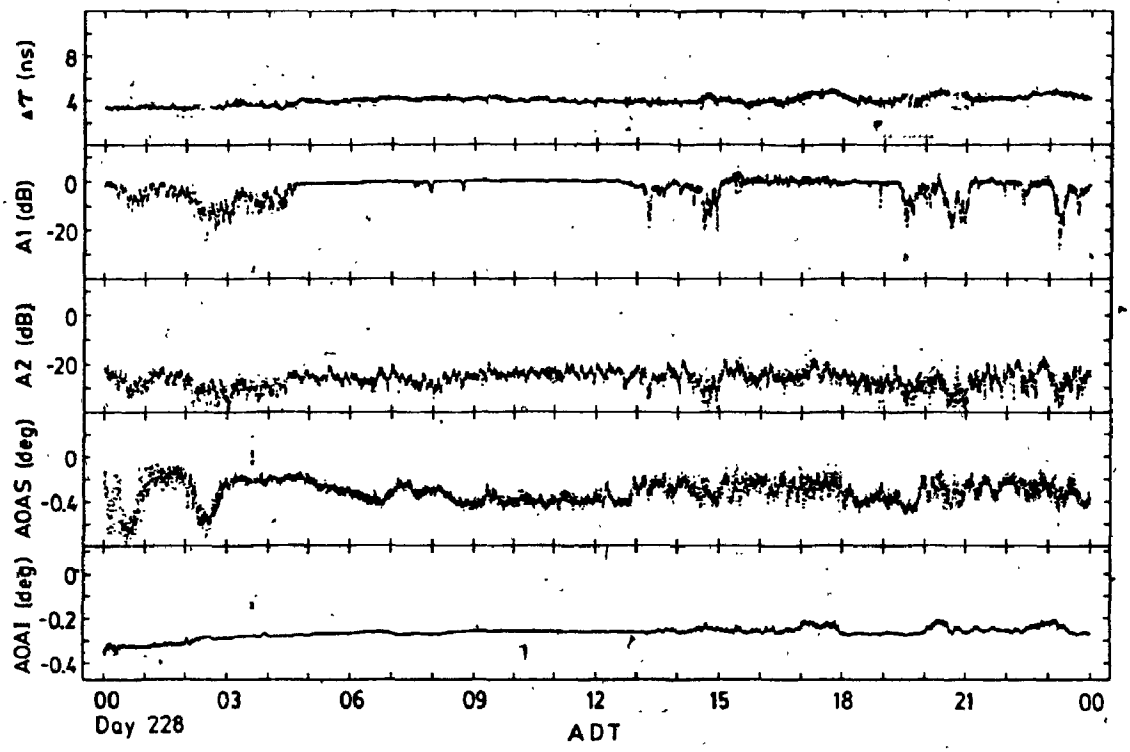
Δτ (ns)
8
4
A1 (dB)
0
-20
A2 (dB)
0
-20
AOAS (deg)
0
-0.4
AOAI (deg)
0
-0.2
-0.4
00
03
06
09
12
15
18
21
00
Day 228
ADT

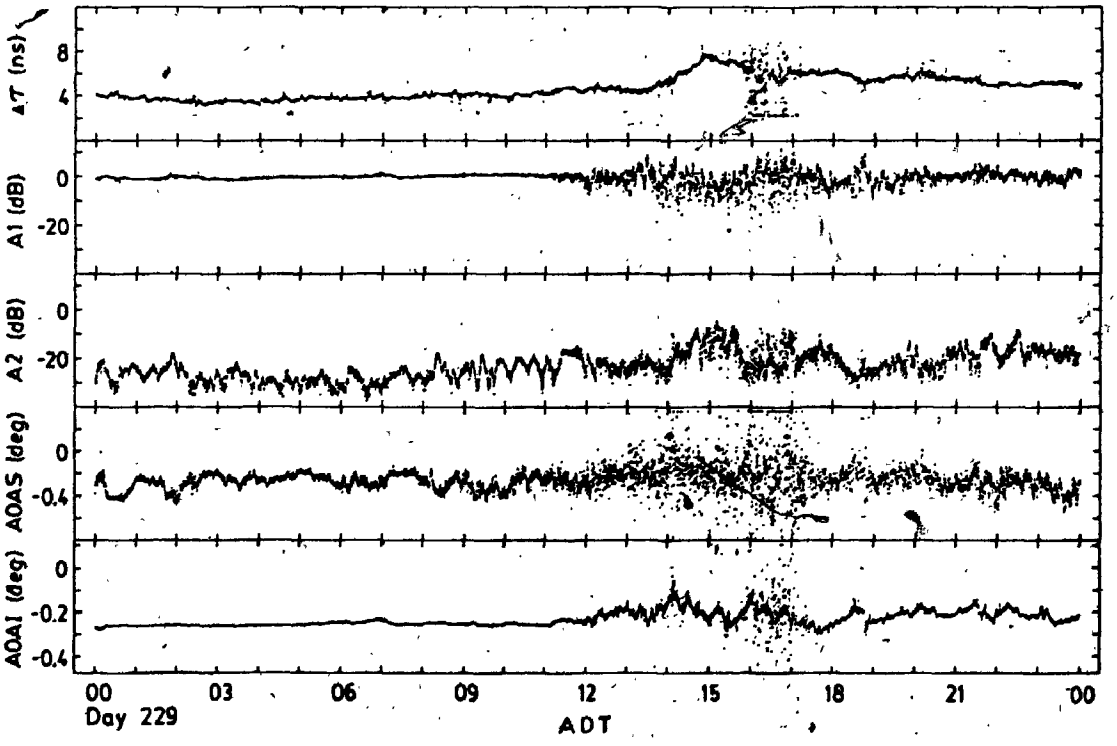
Δτ (ns)
8
4
A1 (dB)
0
-20
A2 (dB)
0
-20
AOAS (deg)
0
-0.4
AOAI (deg)
0
-0.2
-0.4
00
03
06
09
12
15
18
21
00
Day 229
ADT

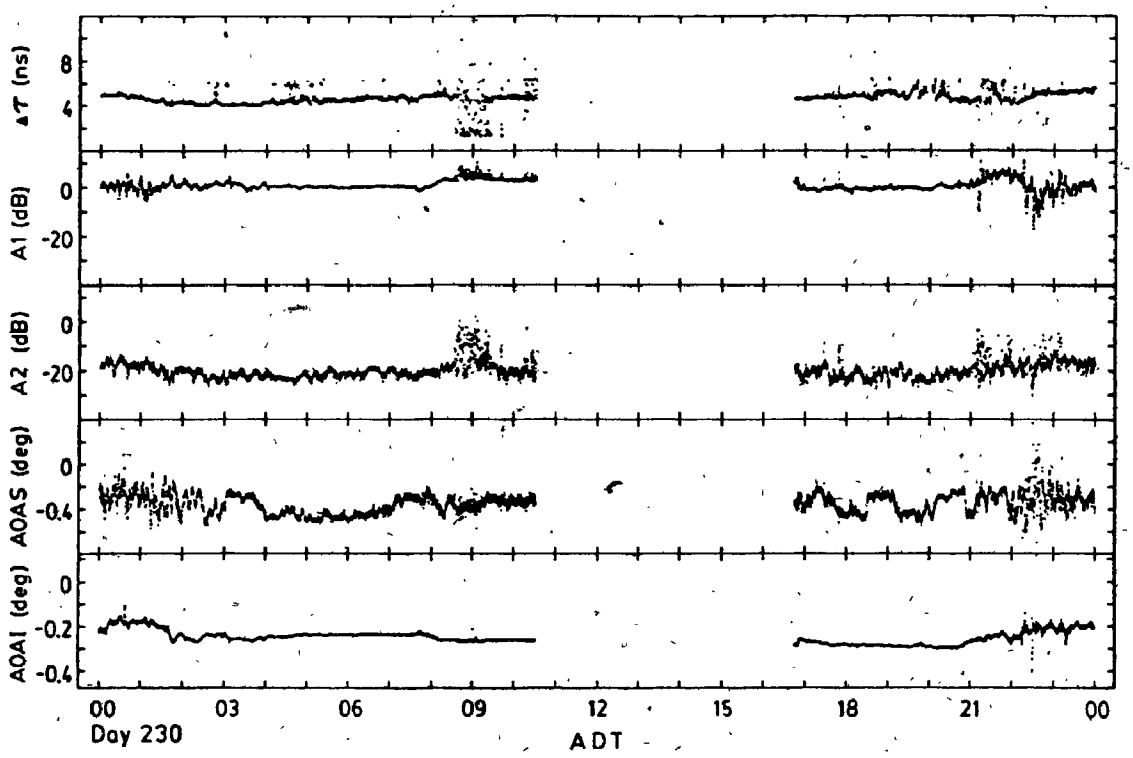
ΔT (ns)
8
4
A1 (dB)
0
-20
A2 (dB)
0
-20
AOAS (deg)
0
-0.4
AOAI (deg)
0
-0.2
-0.4
00
03
06
09
12
15
18
21
00
Day 230
ADT

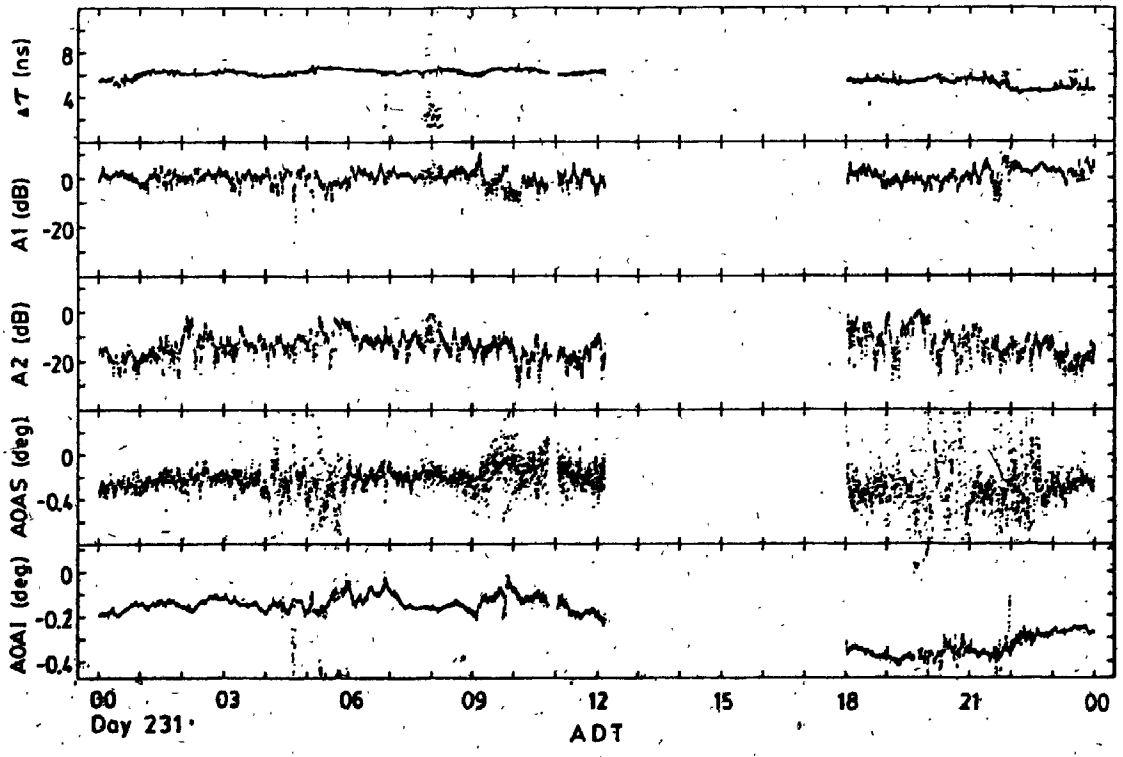
ΔT (ns)
8
4
A1 (dB)
0
-20
A2 (dB)
0
-20
AOAS (deg)
0
-0.4
AOAI (deg)
0
-0.2
-0.4
00
03
06
09
12
15
18
21
00
Day 231
ADT

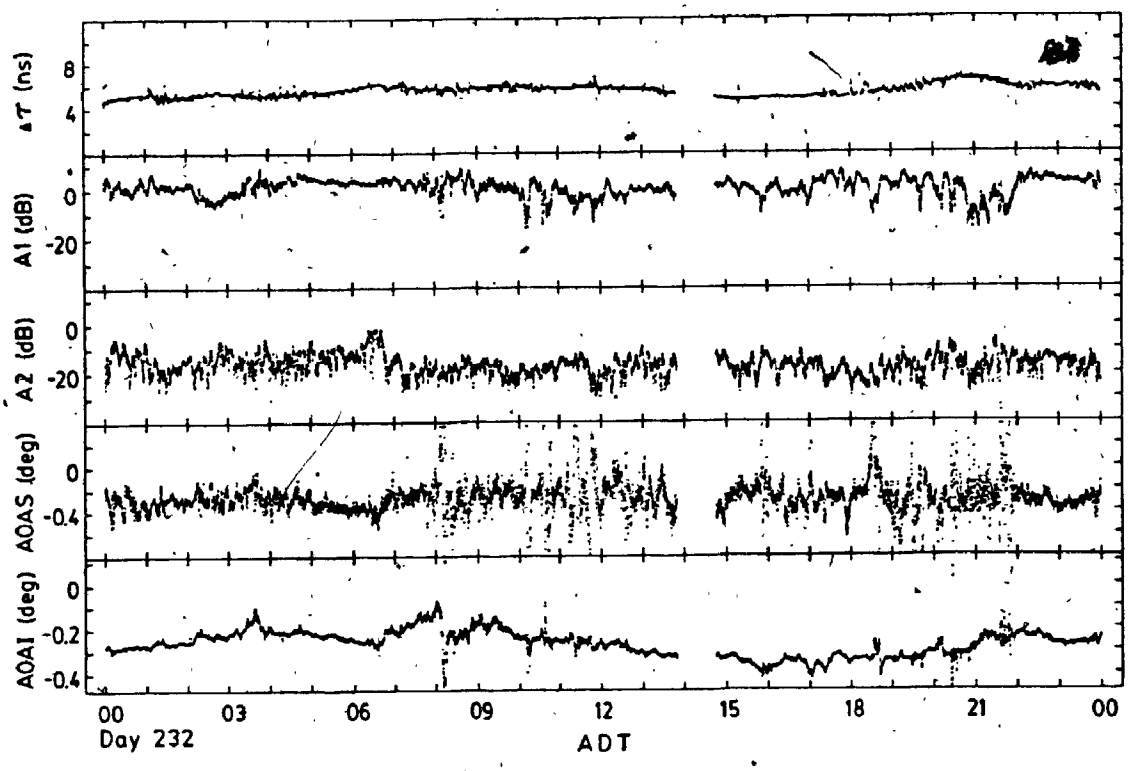
Δτ (ns)
8
4
A1 (dB)
0
-20
A2 (dB)
0
-20
AOAS (deg)
0
-0.4
AOAI (deg)
0
-0.2
-0.4
00
03
06
09
12
15
18
21
00
Day 232
ADT

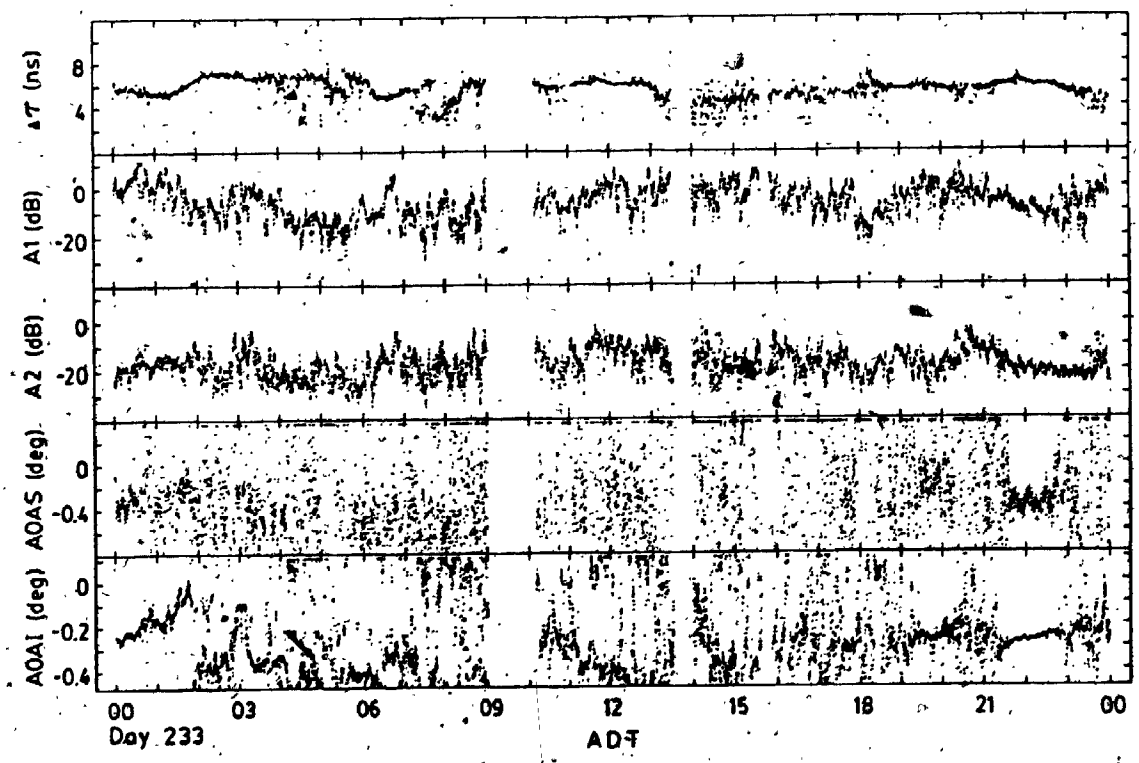
Δτ (ns)
8
4
A1 (dB)
0
-20
A2 (dB)
0
-20
AOAS (deg)
0
-0.4
AOAI (deg)
0
-0.2
-0.4
00
03
06
09
12
15
18
21
00
Day 233
ADT

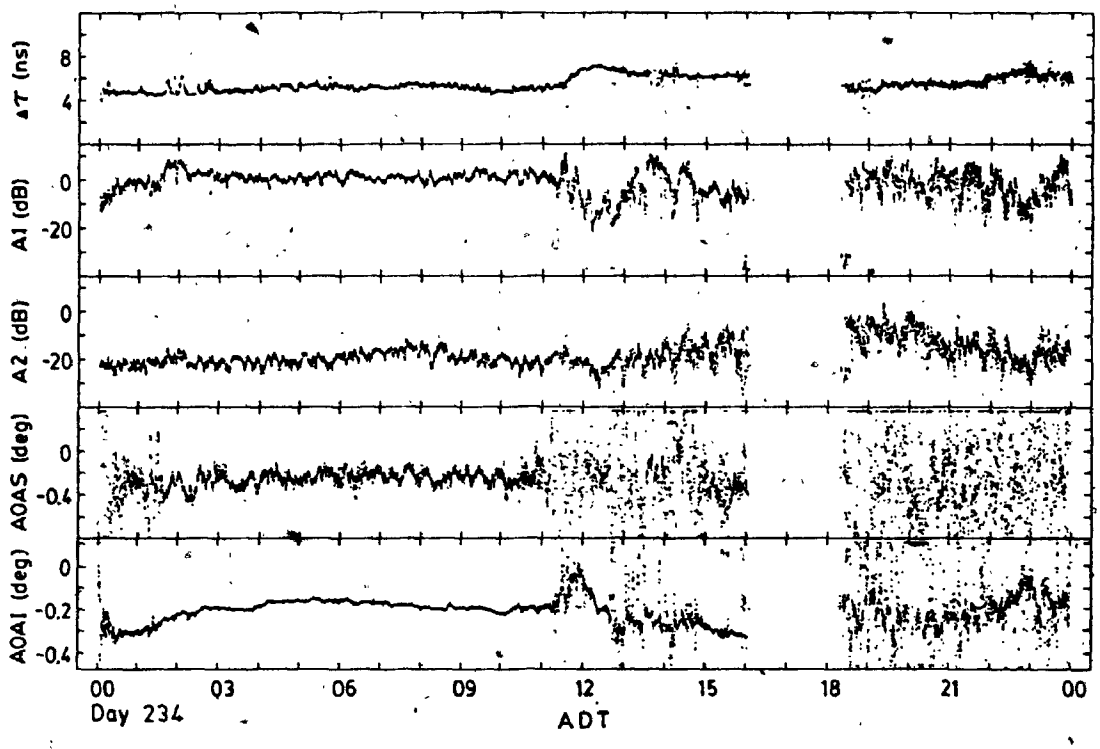
Δτ (ns)
8
4
A1 (dB)
0
-20
A2 (dB)
0
-20
AOAS (deg)
0
-0.4
AOAI (deg)
0
-0.2
-0.4
00
03
06
09
12
15
18
21
00
Day 234
ADT

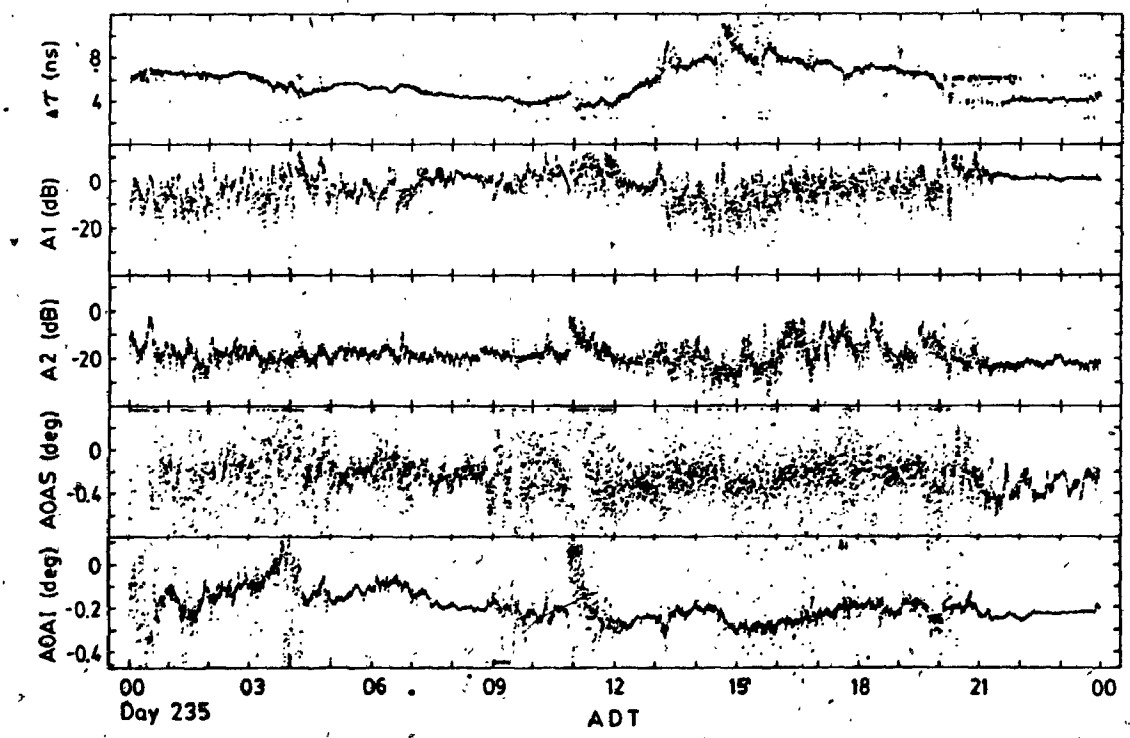
Δτ (ns)
8
4
A1 (dB)
0
-20
A2 (dB)
0
-20
AOAS (deg)
0
-0.4
AOAI (deg)
0
-0.2
-0.4
00
03
06
09
12
15
18
21
00
Day 235
ADT

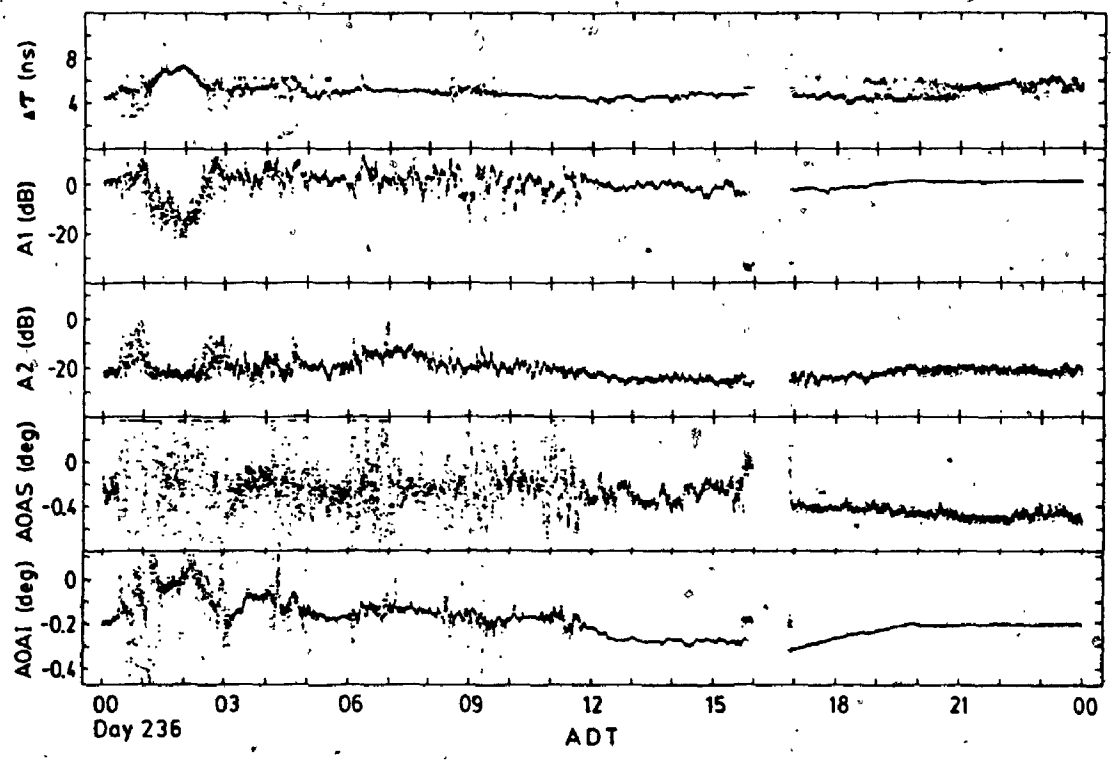
Δτ (ns)
8
4
A1 (dB)
0
-20
A2 (dB)
0
-20
AOAS (deg)
0
-0.4
AOA1 (deg)
0
-0.2
-0.4
00
03
06
09
12
15
18
21
00
Day 236
ADT

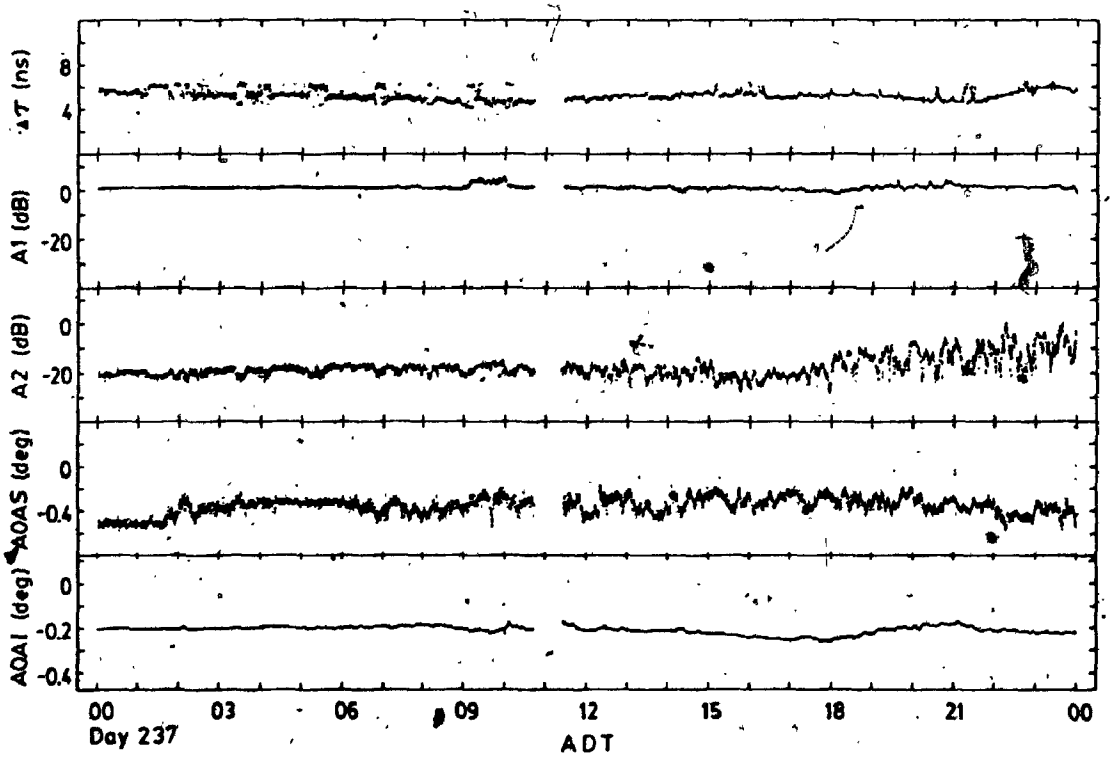
Δτ (ns)
8
4
A1 (dB)
0
-20
A2 (dB)
0
-20
AOAS (deg)
0
-0.4
AOA1 (deg)
0
-0.2
-0.4
00
03
06
09
12
15
18
21
00
Day 237
ADT

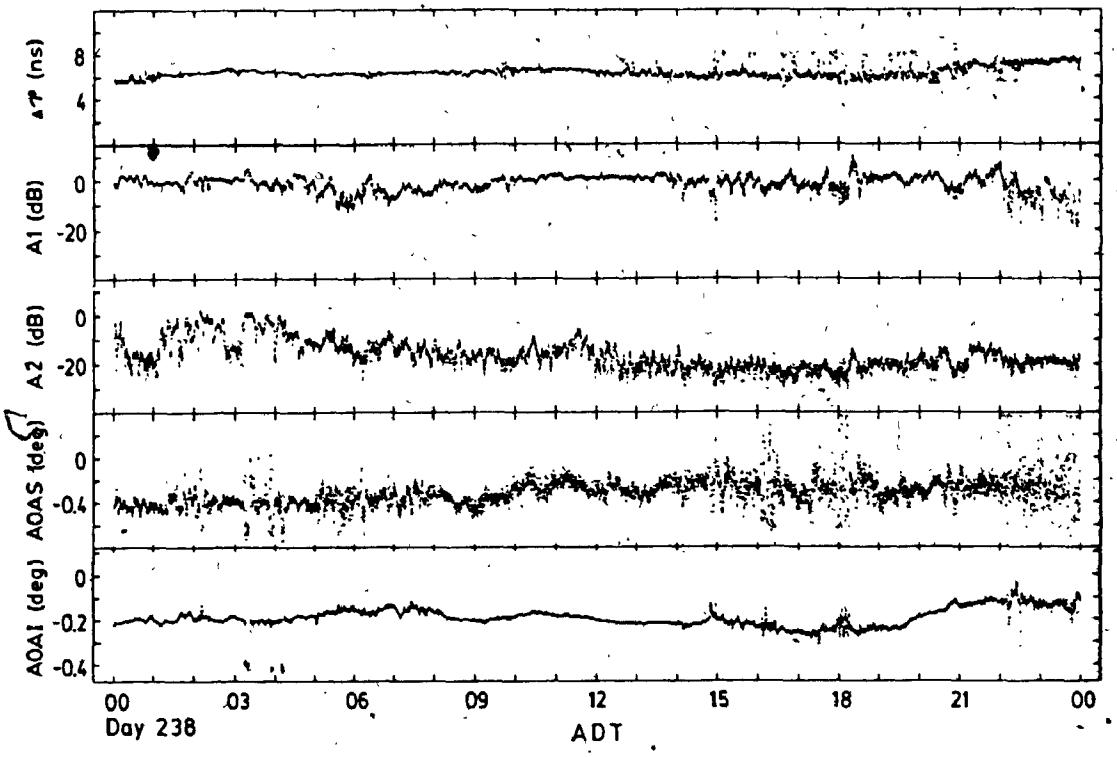
Δτ (ns)
8
4
A1 (dB)
0
-20
A2 (dB)
0
-20
AOAS (deg)
0
-0.4
AOAI (deg)
0
-0.2
-0.4
00
03
06
09
12
15
18
21
00
Day 238
ADT

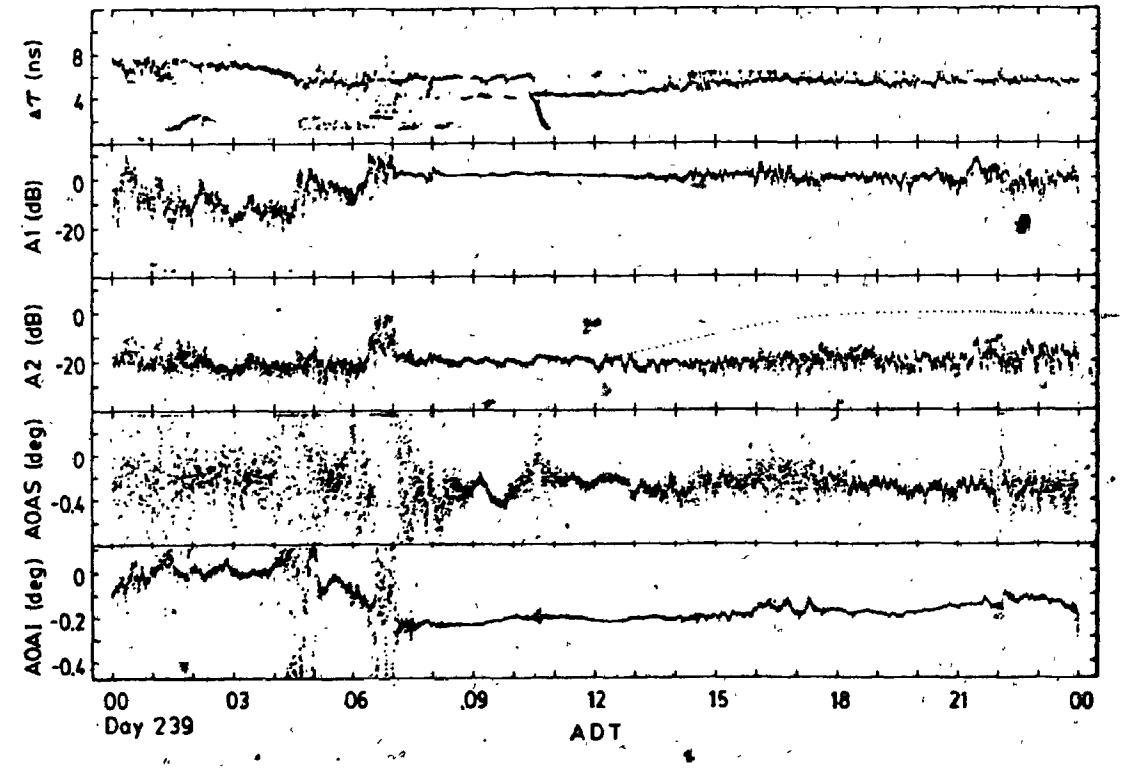
Δτ (ns)
8
4
A1 (dB)
0
-20
A2 (dB)
0
-20
AOAS (deg)
0
-0.4
AOAI (deg)
0
-0.2
-0.4
00
03
06
09
12
15
18
21
00
Day 239
ADT

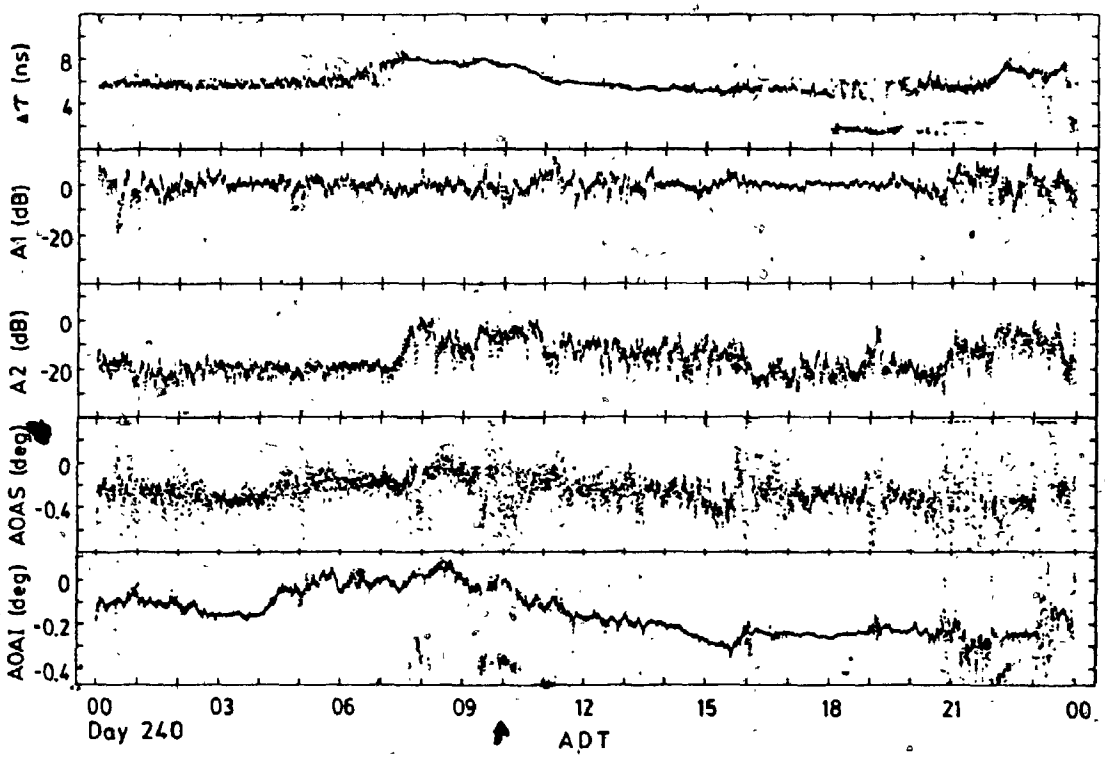
ΔT (ns)
8
4
A1 (dB)
0
-20
A2 (dB)
0
-20
AOAS (deg)
0
-0.4
AOAI (deg)
0
-0.2
-0.4
00
03
06
09
12
15
18
21
00
Day 240
ADT

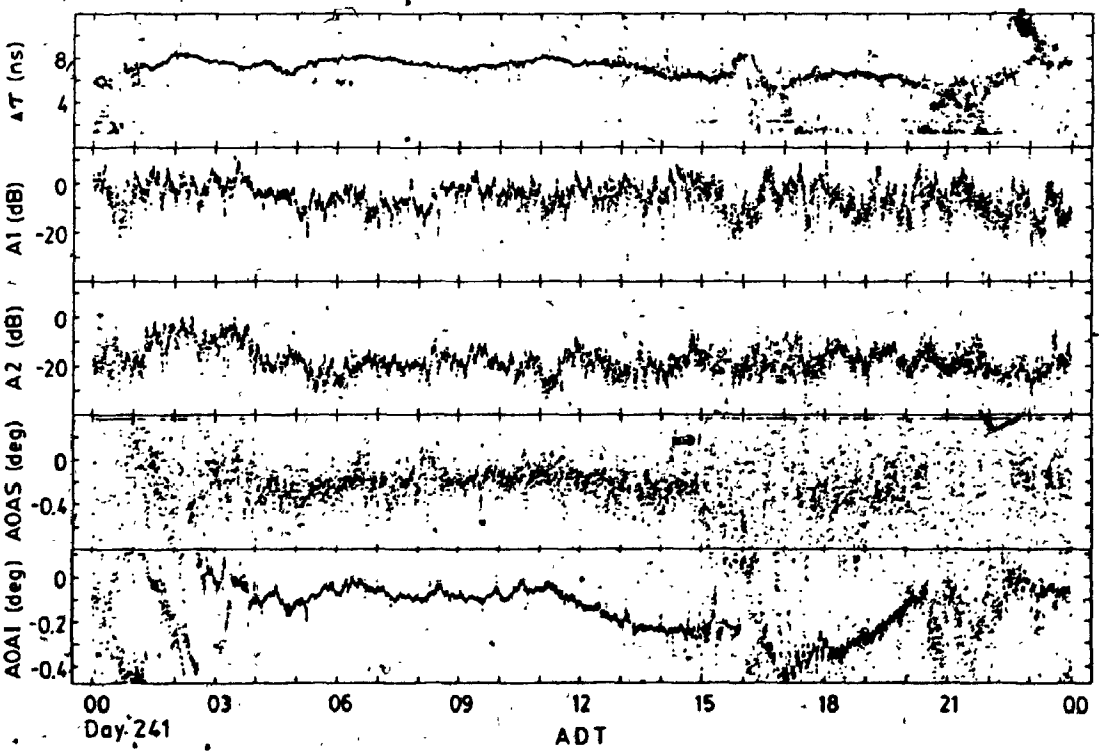
ΔT (ns)
8
4
A1 (dB)
0
-20
A2 (dB)
0
-20
AOAS (deg)
0
-0.4
AOAI (deg)
0
-0.2
-0.4
00
03
06
09
12
15
18
21
00
Day 241
ADT

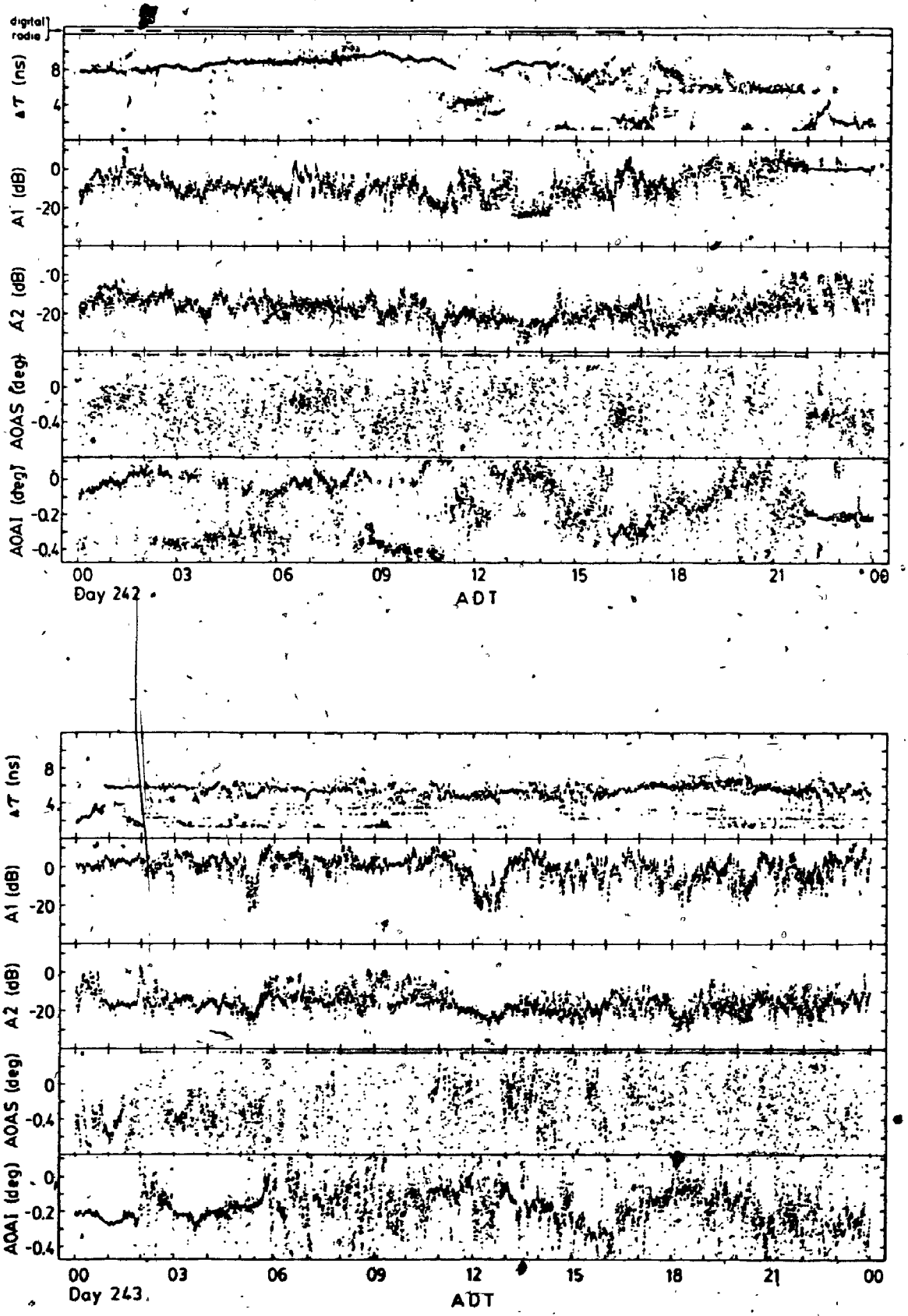
digital radio
ΔT (ns)
A1 (dB)
A2 (dB)
AOAS (deg)
AOAI (deg)
00
03
06
09
12
15
18
21
00
Day 242
ADT
Day 243

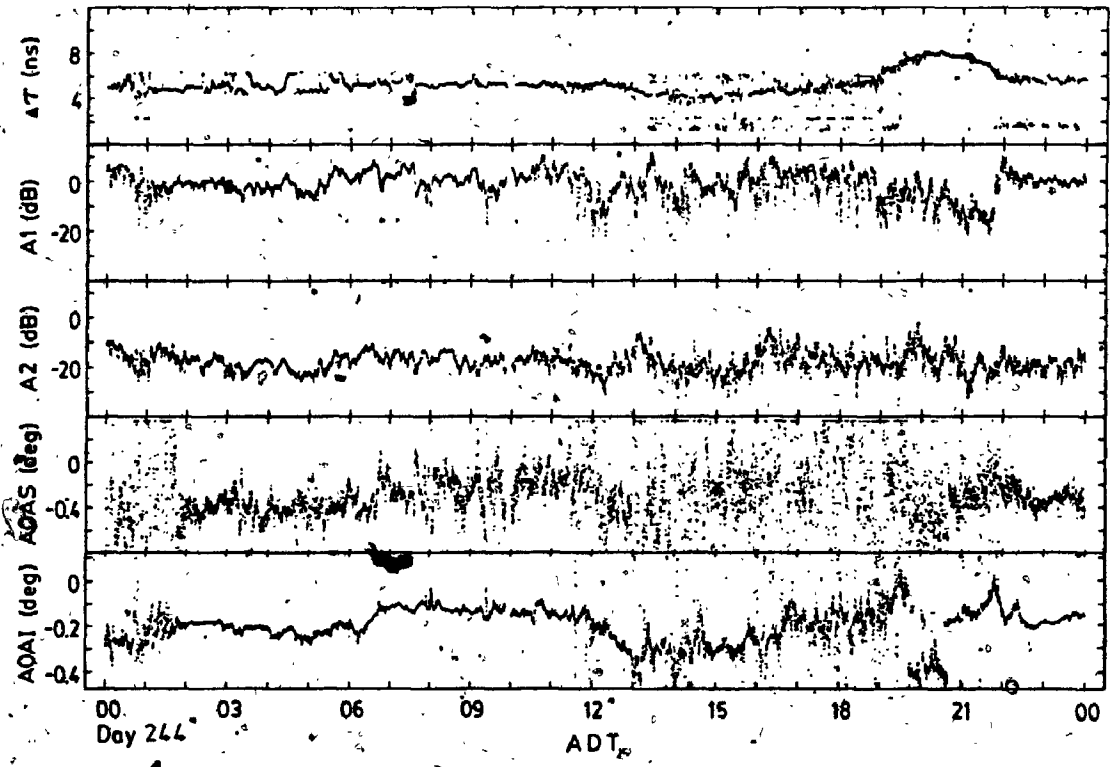
Δτ (ns)
8
4
A1 (dB)
0
-20
A2 (dB)
0
-20
AOAS (deg)
0
-0.4
AOAI (deg)
0
-0.2
-0.4
00
03
06
09
12
15
18
21
00
Day 244
ADT

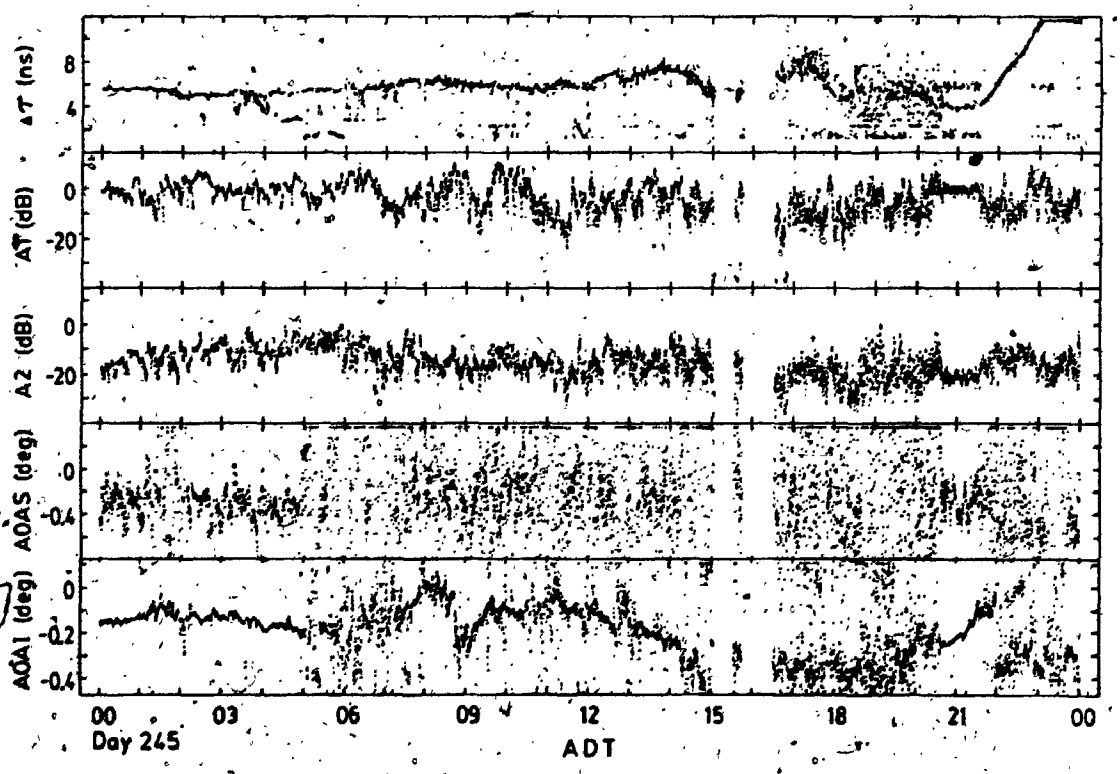
Δτ (ns)
8
4
AT (dB)
0
-20
A2 (dB)
0
-20
AOAS (deg)
0
-0.4
AOAI (deg)
0
-0.2
-0.4
00
03
06
09
12
15
18
21
00
Day 245
ADT

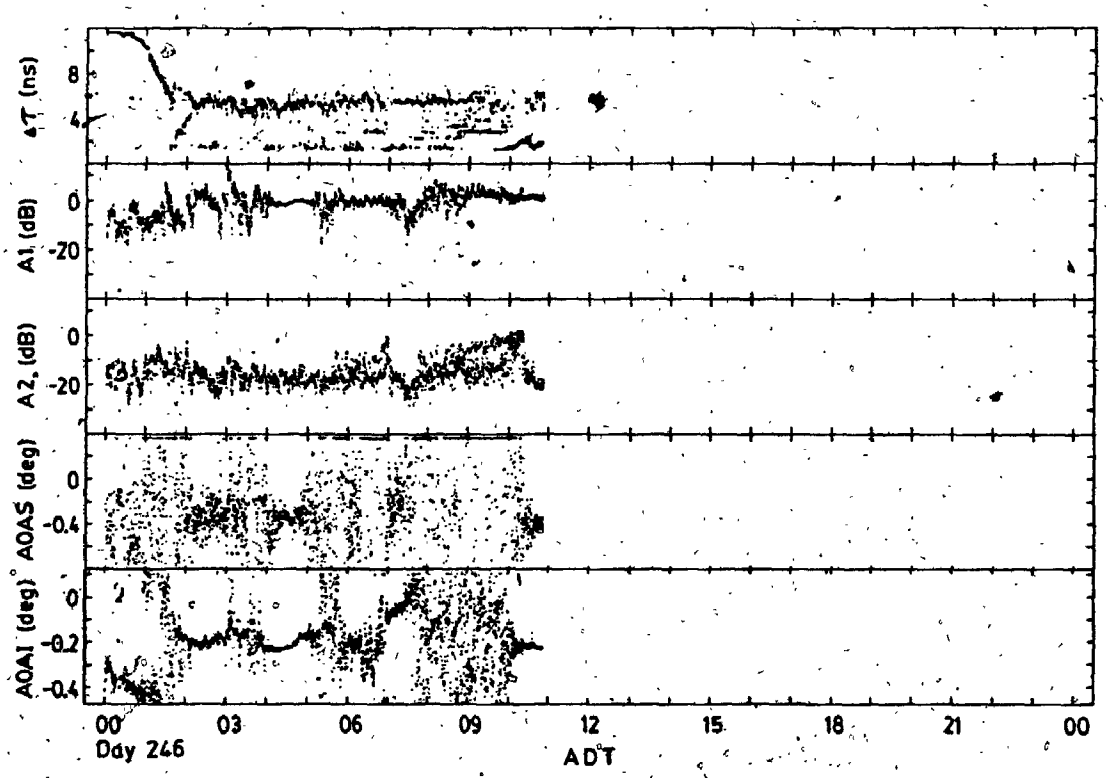
ΔT (ns)
8
4
A1 (dB)
0
-20
A2 (dB)
0
-20
AOAS (deg)
0
-0.4
AOAI (deg)
0
-0.2
-0.4
00
03
06
09
12
15
18
21
00
Day 246
ADT

REFERENCES

[1] Smith, E.K.Jr. and S. Weintraub, "The constants in the equation for atmospheric refractive index at radio frequencies," Proc. I.R.E., vol. 41, pp. 1035-1037, Aug. 1953.

[2] Hall, M.P.M., Effects of the Troposphere on Radio Communication. IEE, London, 1979.

[3] Segal, B. and R.E. Barrington, "Tropospheric refractivity atlas for Canada," CRC Report no. 1315-E, Ottawa, Dec. 1977.

[4] Sharpless, W.M., "Measurement of the angle-of-arrival of microwaves," Proc. I.R.E., pp. 838-845, 1946.

[5] Crawford, A.B. and W.M. Sharpless, "Further observations of the angle-of-arrival of microwaves," Proc. I.R.E., pp. 845-848, 1946.

[6] Bell, J., "Propagation measurements at 3, 6, and 11 GHz over a line-of-sight radio path," Proc. IEEE, vol. 114, pp. 545-549, 1967.

[7] Webster, A.R. and T. Ueno, "Tropospheric microwave propagation -- an X-band diagnostic system," IEEE Trans. Antennas Propagat., vol. AP-28, pp. 693-699, 1980.

[8] Webster, A.R. and W.I. Lam, "Microwave angle-of-arrival measurements under anomalous tropospheric propagation conditions," Ann. des. Telecomm., vol. 35, pp. 474-478, 1980.

[9] Webster, A.R., "Angle-of-arrival considerations in microwave communication systems," IEEE Trans. Antennas Propagat., vol. AP-30(4), pp. 800-802, 1982.

[10] Webster, A.R., "Raypath parameters in tropospheric multipath propagation," IEEE Trans. Antennas Propagat., vol. AP-30(4), pp. 796-800, 1982.

[11] Bean, B.R. and E.J. Dutton, Radio Meteorology. NBS Monograph 92, Washington D.C., 1966.

[12] Dougherty, H.T. and B.A. Hart, "Recent progress in duct propagation predictions," IEEE Trans. Antennas Propagat., vol. AP-27(4), pp. 542-548, 1979.

[13] Chang, H.T., "The effect of tropospheric layer structures on long range VHF radio propagation," IEEE Trans. Antennas Propagat., vol. AP-19(6), pp. 751-756, Nov. 1971.

[14] Sheppard, P.A., "Structure and refractive index of lower atmosphere," in Meteorological Factors in Radio Wave Propagation. Physical Society and Royal Meteorological Society, London, 1946.

[15] Lane, J.A., "Small-scale variations of radio refractive index in the troposphere," Parts 1 and 2, Proc. IEE, vol. 115, no. 9, pp. 1227-1234, Sept. 1968.

[16] Ikegami, F., M. Haga, T. Fukuda, and H. Yoshida, "Experimental studies on atmospheric ducts and microwave fading," Review of the Elect. Comm. Lab., vol. 14, pp. 505-533, July-Aug. 1966.

[17] Gossard, E.E., "Clear wether meteorological effects on propagation at frequencies above 1 GHz," Radio Sci., vol. 16, no. 5, pp. 589-608, Sept.-Oct. 1981.

[18] Booker, H.G. and W. Walkinshaw, "The mode theory of tropospheric refraction and its relation to waveguides and diffraction," in Meteorological Factors in Radio Wave Propagation. Physical Society and Royal Meteorological Society, London, 1946.

[19] Kerr, D.E., Propagation of Short Radio Waves. Book pp. 9-22, McGraw Hill, New York, 1951.

[20] Livingston, D.C., Physics of Microwave Propagation. Prentice Hall, New York, 1970.

[21] Beckmann, P., Probability in Communication Engineering. Harcourt, Brace and World, New York, 1967.

[22] Nakagami, M., "The m-Distribution -- a general formula of intensity distribution of rapid fading," in Statistical Methods in Radio Wave Propagation. Pergamon Press, New York, 1960.

[23] White, R.F., Engineering Considerations for Microwave Communications Systems. Lenkurt Electric Co. Inc., June 1970.

[24] Beckmann, P. and A. Spizzichino, The Scattering of Electromagnetic Waves from Rough Surfaces. MacMillan, New York, 1963.

[25] Webster, A.R., P.A. Forsyth, and T. Ueno, "A study for the development and testing of a microwave diagnostic system," Final report, DSS Contract No. 01SU.36001-6-2317. CRC, Ottawa, Canada, Sept. 1977.

[26] Ueno, T., A Prototype Microwave Propagation Diagnostic System. M.E.Sc. Thesis, The University of Western Ontario, London, Canada, 1978.

[27] Farn, B., "A system monitor for an INTEL-8080 based microcomputer," ES 400 Report. The University of Western Ontario, London, Canada, 1978.

[28] Barnett, W.T., "Multipath fading effects on digital radio," IEEE Trans. Comm., vol. COM-27(12), pp. 1842-1848, Dec. 1979.

[29] Anderson, C.W., S.G. Barber, and R.N. Patel, "The effect of selective fading on digital radio," IEEE Trans. Comm., vol. COM-27(12), pp. 1870-1876, Dec. 1979.

[30] N.B. Tel., "Digital radio, Otter Lake - Aylesford test hop," Engineering report no. 530, Saint John, NB., Canada, Jan. 1980.

[31] Deygout, J., "Multiple knife-edge diffraction of microwaves," IEEE Trans. Antennas Propagat., vol. AP-14(4), pp. 480-489, July 1966.

[32] Beauchamp, K.G. and C.K. Yuen, Digital Methods for Signal Analysis. George Allen & Unwin Ltd., London, 1979.

[33] Brigham, E.O., The Fast Fourier Transform. Prentice Hall, New Jersey, 1974.

[34] Feher, K., Digital Communications: Microwave Applications. Prentice Hall, New Jersey, 1981.

[35] Greenstein, L.J. and B.A. Czekaj-Augun, "Performance comparisons among digital radio techniques subjected to multipath fading," IEEE Trans. Comm., vol. COM-30(5), pp. 1184-1197, May 1982.

[36] Surveys and Mapping Branch, Map 21A/14 (1976) and Map 21H/5 (1966), Series A791, scale 1:50,000. Department of Energy, Mines and Resources, Canada.

[37] Skolnik, M.I., Radar Handbook. Chapter 26, McGraw Hill, New York, 1970.

[38] McAllister, L.G., J.R. Pollard, A.R. Mahoney, and P.J.R. Shaw, "Acoustic sounding -- a new approach to the study of atmospheric structure," Proc. IEEE, vol. 57-4, pp. 579-587, Apr. 1969.

[39] Norton, K.A., L.E. Vogler, W.V. Mansfield, and P.J. Short, "The probability distribution of the amplitude of a constant vector plus a Rayleigh-distributed vector," Proc. I.R.E., vol. 43, pp. 1354-1361, Oct. 1955.

[40] Foldes, G., "The lognormal distribution and its applications to atmospheric studies," in Statistical Methods of Radio Wave Propagation. Pergamon Press, New York, 1960.

[41] Meyer, D.P. and H.A. Mayer, Radar Target Detection. Academic Press, New York, 1973.

[42] Mitchell, R.L., Radar Signal Simulation. Artech House Inc., Massachusetts, 1976.

[43] Webster, A.R., "Angles-of-arrival and delay times on terrestrial line-of-sight microwave links," IEEE Trans. Antennas Propagat., vol. AP-31(1), pp. 12-17, Jan.1983.

[44] Webster, A.R. and W.I. Lam, "Microwave propagation across the Bay of Fundy," Discussion paper presented at Maritime Tel. & Tel., N.S., Canada, June 1982.

[45] Lin, S.H., "Statistical behaviour of a fading signal," BSTJ, vol. 50(10), pp. 3211-3270, Dec. 1971.

[46] International Radio Consultative Committee (CCIR), "Propagation data required for line-of-sight radio-relay systems," XV-th Plenary Assembly, Report 338-3 (mod. F), Geneva, 1982.

[47] Stephansen, E.T., "Clear-air propagation on line-of-sight radio paths: a review," Radio Sci., vol. 16(5), pp. 609-629, Sept. 1981.

[48] Babler, G.M., "A study of frequency selective fading for a microwave line-of-sight narrowband radio channel," BSTJ, vol. 51(3), pp. 731-757, Mar. 1972.

[49] Barnett, W.T., "Multipath propagation at 4, 6, and 11 GHz," BSTJ, vol. 51(2), pp. 321-361, Feb. 1972.

[50] Vigants, A., "Number and duration of fades at 6 and 4 GHz," BSTJ, vol. 50(3), pp. 815-841, Mar. 1971.

[51] Ruthroff, C.L., "Multiple-path fading on line-of-sight microwave radio systems as a function of path length and frequency," BSTJ, vol. 50(7), pp. 2375-2399, Sept. 1971.

[52] Stephansen, E.T. and G.E. Mogensen, "Experimental investigation of some effects of multipath propagation on a line-0f-sight path at 14 GHz," IEEE Trans. Comm., vol. COM-27(3), pp. 643-647, Mar. 1979.

[53] Albrecht, P.B., D.R. Wortendyke, and R.R. Larsen, "Signal level distributions and fading for a long over-water link at 5 GHz," IEEE Trans. Antennas Propagat., vol. AP-30(3), pp. 479-483, May 1982.

[54] Gudmandsen, P. and B.F. Larsen, "Statistical data for microwave propagation measurements on two oversea paths in Denmark," I.R.E. Trans. Antennas Propagat., pp. 255-259, July 1957.

[55] Oetting, J.D., "A comparison of modulation techniques for digital radio," IEEE Trans. Comm., vol. COM-27(12), pp. 1752-1762, Dec. 1979.

[56] Lundgren, C.W. and W.D. Rummler, "Digital radio outage due to selective fading -- observation vs prediction from laboratory simulation," BSTJ, vol. 58(5), pp. 1073-1100, May-June 1979.

[57] Morais, D.H., A. Sewerinson, and K. Feher, "The effects of the amplitude and delay slope components of frequency selective fading on QPSK, offset QPSK, and 8PSK systems," IEEE Trans. Comm., vol. COM-27(12), pp. 1849-1853, Dec. 1979.

[58] Ramadan, M., "Availability prediction of 8PSK digital microwave systems during multipath propagation," IEEE Trans. Comm., vol. COM-27(12), pp. 1862-1869, Dec. 1979.

[59] Hartmann, P.R. and E.W. Allen, "An adaptive equalizer for correction of multipath distortion in a 90 Mb/s 8PSK system," ICC-79 Confer. Record, vol. 1, pp. 5.6.1-5.6.4, June 1979.

[60] Komaki, S., I. Horikawa, K. Morita, and Y. Okamoto, "Characteristics of a high capacity 16-QAM digital radio system in multipath fading," IEEE Trans. Comm., vol. COM-27(12), pp. 1854-1861, Dec. 1979.

[61] Greenstein, L.J., "A multipath fading channel model for terrestrial digital radio systems," IEEE Trans. Comm., vol. COM-26(8), pp. 1247-1250, Aug. 1978.

[62] Rummler, W.D., "A new selective fading model: application to propagation data," BSTJ, vol. 58(5), pp. 1037-1071, May-June 1971.

[63] Jakes, W.C., "An approximate method to estimate an upper bound on the effect of multipath delay distortion on digital transmission," IEEE Trans. Comm., vol. COM-27(1), pp. 76-81, Jan 1979.

[64] Greenstein, L.J. and V.K. Prabhu, "Analysis of multipath outage with applications to 90-Mbit/s PSK systems at 6 and 11 GHz," IEEE Trans. Comm., vol. COM-27(1), pp. 68-75, Jan. 1979.

[65] Rummler, W.D., "A comparison of calculated and observed performance of digital radio in the presence of interference," IEEE Trans. Comm., vol. COM-30(7), pp. 1693-1700, July 1982.

[66] Wang, Y.Y., "Simulation and measured performance of a space diversity combiner for 6 GHz digital radio," IEEE Trans. Comm., vol. COM-27(12), pp. 1896-1907, Dec. 1979.

[67] Morgan, D.R., "Adaptive multipath cancellation for digital data communications," IEEE Trans. Comm., vol. COM-26(9), pp. 1380-1390, Sept. 1978.

[68] Pothier, M.P., "1981 Bay of Fundy test hop, Otter Lake - Nictaux South," Final report, Maritime Tel. & Tel., 1983.

END

1 9H0 3 1 8 4

FIN